https://doi.org/10.15388/vu.thesis.689
https://orcid.org/0000-0003-0818-4740

VILNIUS UNIVERSITY
CENTER FOR PHYSICAL SCIENCES AND TECHNOLOGY

Rūta Aukštakojytė

Synthesis and Investigation of Graphene-Based Materials and their Application in the Dopamine Electrochemical Sensing

DOCTORAL DISSERTATION

Natural Sciences,
Chemistry (N 003)

VILNIUS 2024

The dissertation was prepared between 2020 and 2024 at Vilnius University. The research was supported by Research Council of Lithuania.

Academic supervisor – Assoc. Prof. Dr. Justina Gaidukevič (Vilnius University, Natural Sciences, Chemistry, N 003).
Academic consultant – Prof. Dr. Jurgis Barkauskas (Vilnius University, Natural Sciences, Chemistry, N 003).

This doctoral dissertation will be defended in a public meeting of the Dissertation Defence Panel:

Chairman – Prof. Dr. Rimantas Ramanauskas (Center for Physical Sciences and Technology, Natural Sciences, Chemistry, N 003).
Members:
Assoc. Prof. Dr. Inga Grigoravičiūtė (Vilnius University, Natural Sciences, Chemistry, N 003),
Dr. Olga Kizinievič (Vilnius Gediminas Technical University, Technological Sciences, Materials Engineering, T 008),
Dr. Teresė Rauckytė-Žak (University of Science and Technology in Bydgoszcz, Natural Sciences, Chemistry, N 003),
Assoc. Prof. Dr. Živilė Stankevičiūtė (Vilnius University, Natural Sciences, Chemistry, N 003).

The dissertation shall be defended at a public meeting of the Dissertation Defence Panel at 2 p. m. on 29th November 2024 in Inorganic Chemistry Auditorium of the Institute of Chemistry of the Faculty of Chemistry and Geosciences (Vilnius University). Address: Naugarduko Str. 24, 141, Vilnius, Lithuania, phone: +370 (5) 219 3105; e-mail: info@chgf.vu.lt.

The text of this dissertation can be accessed at the libraries of Vilnius University and of Center for Physical Sciences and Technology as well as on the website of Vilnius University:
www.vu.lt/lt/naujienos/ivykiu-kalendorius

https://doi.org/10.15388/vu.thesis.689
https://orcid.org/0000-0003-0818-4740

VILNIAUS UNIVERSITETAS
FIZINIŲ IR TECHNOLOGIJOS MOKSLŲ CENTRAS

Rūta Aukštakojytė

Grafeninių medžiagų sintezė, tyrimas ir taikymas dopamino elektrocheminiam nustatymui

DAKTARO DISERTACIJA

Gamtos mokslai,
Chemija (N 003)

VILNIUS 2024

Disertacija rengta 2020–2024 metais Vilniaus universitete.
Mokslinius tyrimus rėmė Lietuvos mokslo taryba.

Mokslinė vadovė – doc. dr. Justina Gaidukevič (Vilniaus universitetas, gamtos mokslai, chemija, N 003).
Mokslinis konsultantas – prof. dr. Jurgis Barkauskas (Vilniaus universitetas, gamtos mokslai, chemija, N 003).

Gynimo taryba:
Pirmininkas – prof. dr. Rimantas Ramanauskas (Fizinių ir technologijos mokslų centras, gamtos mokslai, chemija, N 003).
Nariai:
doc. dr. Inga Grigoravičiūtė (Vilniaus universitetas, gamtos mokslai, chemija, N 003),
dr. Olga Kizinievič (Vilniaus Gedimino technikos universitetas, technologijos mokslai, medžiagų inžinerija, T 008),
dr. Teresė Rauckytė-Žak (Bydgoščiaus Jono ir Andriaus Sniadeckių technikos ir gamtos mokslų universitetas, gamtos mokslai, chemija, N 003),
doc. dr. Živilė Stankevičiūtė (Vilniaus universitetas, gamtos mokslai, chemija, N 003).

Disertacija ginama viešame Gynimo tarybos posėdyje 2024 m. lapkričio 29 d. 14.00 val. Vilniaus universiteto Chemijos ir geomokslų fakulteto Chemijos instituto Neorganinės chemijos auditorijoje. Adresas: Naugarduko g. 24, 141, Vilnius, Lietuva, tel. +370 (5) 219 3105; el. paštas info@chgf.vu.lt.

Disertaciją galima peržiūrėti Vilniaus universiteto, Fizinių ir technologijos centro bibliotekose ir Vilniaus universiteto interneto svetainėje adresu:
https://www.vu.lt/naujienos/ivykiu-kalendorius

TABLE OF CONTENT

LIST OF ABBREVIATIONS

3D	Three-dimensional
AA	Ascorbic acid
BB	Bismarck brown
BET	Brunauer-Emmett-Teller
CA	Citric acid
ChA	Chronoamperometry
CV	Cyclic voltammetry
DA	Dopamine
DI	Deionized
DQ	Dopamine-o-quinone
DPV	Differential pulse voltammetry
DSC	Differential scanning colorimetry
DTG	Derivative thermogravimetry
EDX	Energy dispersive X-ray spectroscopy
FTIR	Fourier transform infrared spectroscopy
FWHM(G)	Width of G band of sample under investigation
FWHM(G_0)	Width of G band of unmodified pristine graphene
GCE	Glassy carbon electrode
GO	Graphene oxide
LOD	Limit of detection
MA	Malonic acid
N-rGO	Nitrogen-modified reduced graphene oxide
ORR	Oxygen reduction reaction
P-rGO	Phosphorus-modified reduced graphene oxide
PB	Phosphate buffer
rGO	Reduced graphene oxide
RS	Relative standard deviation
SEM	Scanning electron microscopy
TEM	Transmission electron microscopy
TG	Thermogravimetry
UA	Uric acid
XPS	X-ray photoelectron spectroscopy
XRD	X-ray diffraction
WE	Working electrode
A	Cross section area (m^2)
A_g	Geometric area of the GCE electrode (cm^2)
C_p	Specific heat ($J\ kg^{-1}\ K^{-1}$)
$d\alpha/dt$	Reaction rate

E	Potential (V)
E_a	Activation energy (J mol^{-1})
H	Amount of heat (J)
I	Current (A)
I_D	Intensity of the D band in the Raman spectra
I_G	Intensity of the G band in the Raman spectra
$k(T)$	Rate constant at temperature T (min^{-1})
l	Length of the sample (m)
l_C	Photon coherence length (32 nm)
L_α	Average in-plane crystallite size (nm)
m	Sample mass (g)
n	Reaction order
R	Universal gas constant (J $(mol\ K)^{-1}$)
s	Slope of the calibration plot
T	Temperature (K)
t	Time (s)
T_m	Maximum temperature value of the DSC curve (K)
T_{onset}	Onset temperature (K)
W	Heat flow used in DSC (W/g)
Z	Pre-exponential factor
α	Fraction of reacted material
β	Heating rate (K min^{-1})
ΔBE	Binding energy (eV)
ΔE_p	Separation of cathodic and anodic peak potentials (mV)
ΔH	Enthalpy (J g^{-1})
ρ	Resistivity (Ω m)
σ	Standard deviation of the anodic peak current of the blank signal
σ_c	Electrical conductivity (S m^{-1})

INTRODUCTION

Since A. Geim and K. Novoselov received the 2010 Nobel Prize in Physics for their ground-breaking work on graphene, this carbon material has attracted extraordinary interest across a broad scientific community [1]. Due to its unique two-dimensional honeycomb structure, graphene exhibits attractive physicochemical and thermomechanical properties, leading to the promising development of next-generation materials as well as energy technologies, biomedical tools, environmental safeguards, and electronic devices. This carbon material has also substantially intensified global interest in other graphene-based derivatives, prompting in-depth exploration of innovative production techniques, modifications, and diverse applications [2,3].

Recently, graphene-based materials, such as graphene oxide (GO) and reduced graphene oxide (rGO), have displayed remarkable promise as active electrode materials for electrochemical sensors. This is attributed to their long-term stability, cost-effectiveness, biocompatibility, hydrophilicity, and environmentally friendly nature [4]. Pure graphene, lacking surface functional groups and featuring a zero band gap, faces limitations in the effective electrochemical performance for sensing applications [5]. However, the introduction of heteroatoms (N, P, S, or B) into graphene and rGO matrices allows precise control over electronic structure, chemical, and textural characteristics, leading to the creation of electrocatalytically active sites. This modification significantly improves the charge transfer at the interface between an electrode and electrolyte, resulting in enhanced sensor performance [6,7]. Heteroatoms-modified rGO-based electrodes have been successfully applied in glucose, uric acid (UA), ascorbic acid (AA), H_2O_2, nitrite, serotonin, and hydrazine electrochemical sensing [8–13].

Despite worldwide attention, the field of graphene-based sensors remains in its early developmental stage, facing several key challenges that need addressing, and most of them are related to the design of a sensor. Typically, graphene-based electrochemical sensors are designed with noble/transition metal nanoparticles (Au, Pd) or their oxides (MnO, NiO, CoO, Fe_2O_3, and ZnO) for high efficiency and excellent electrochemical sensing abilities [1]. Nevertheless, the high cost, complex surface chemistry, agglomeration, and potential toxic effects deter their sustainable use in combination with graphene-based derivatives. Furthermore, the existing metal-free graphene-based sensors still suffer from poor sensitivity, limited selectivity, narrow linear range of detection, and delayed response times [14]. To address these issues, more efforts must be devoted to the investigation and improvement of scalable and cheap synthesis methodologies of graphene-based materials.

Functionalizing them with heteroatoms can optimize their structural characteristics for superior sensing performance, including a low limit of detection (LOD), wide linear detection range, high sensitivity, improved reproducibility, repeatability, and stability, all while using metal-free electrodes. Therefore, in this dissertation, significant emphasis has been placed on exploring novel methods for modifying graphene-based materials and thoroughly investigating their thermal, chemical, electrical, structural, and electrochemical properties to develop cost-effective, versatile, and highly active electrode materials, capable of detecting dopamine (DA). DA is a vital neurotransmitter for human well-being. Its irregular levels in blood can potentially lead to the development of nervous system disorders such as senile dementia, schizophrenia, attention deficit hyperactivity syndrome, Parkinson's, and Alzheimer's diseases [4,15]. Hence, precise, sensitive, and rapid DA determination is crucial for the early diagnosis and treatment of these aforementioned conditions.

THE AIM AND SCIENTIFIC TASKS OF THE THESIS

The aim of this PhD thesis was to prepare a range of graphene-based materials, to modify their structure with heteroatoms and to study the influence of the functionalities on the properties of the obtained products and electrochemical performance in the detection of DA. In order to achieve the main goal, the following tasks were formulated:

1. To synthesize GO and study its thermal properties and the kinetic parameters of the thermal reduction reaction in the absence and presence of carbon suboxide using the Borchardt-Daniels, Kissinger, and Ozawa models.
2. To prepare P- and N-modified rGO samples by the thermal and hydrothermal reduction of GO with malonic acid/P_2O_5 and organic dye Bismarck brown additives, respectively.
3. To evaluate the changes in structural and electrical properties between prepared graphene-based materials using various spectroscopic, electrical, and microscopic methods.
4. To design and electrochemically test novel and metal-free electrochemical sensors based on N- and P-modified rGO samples for dopamine detection in model systems.

NOVELTY, ORIGINALITY AND IMPORTANCE OF THE THESIS

To the best of our knowledge, the malonic acid (MA) and P_2O_5 additives applied in this research have not been used so far in the process of the thermal decomposition of GO. This innovative approach leverages the unique chemical properties of MA and P_2O_5, where MA can be dehydrated to produce carbon suboxide (C_3O_2) in the presence of a strong dehydrating agent like P_2O_5 at 150 °C. For the first time, we have demonstrated that the thermal reduction of GO using C_3O_2 is a promising approach for restoring the conjugated aromatic structure of rGO in a safer and more controlled way. This proposed mixture of additives has effectively lowered not only the reduction temperature of GO (up to 125 °C), but also enthalpy and activation energy of thermal decomposition of GO. This may be considered as a prospective way to manage the process of GO thermal reduction more precisely. Additionally, we have shown that this mixture not only facilitates the reduction of GO but also introduces phosphorus functionalities into the rGO. This rGO modification has also led to the development of a novel electrochemical platform for the efficient determination of DA with a low LOD and relatively high sensitivity. Additionally, the kinetics of GO thermal decomposition have been investigated both with and without the addition of MA and P_2O_5 additives, employing the Borchardt-Daniels, Kissinger, and Ozawa models. Notably, the Ozawa method has been utilized for the first time to determine the activation energy of the GO thermal reduction reaction.

Furthermore, beyond functionalizing rGO with phosphorus, novel metal-free rGO samples modified with nitrogen have been successfully synthesized using a simple one-pot hydrothermal treatment of GO in the presence of the Bismarck brown (BB) dye, which served as a nitrogen source for the first time in this context. We have systematically investigated the effects of BB concentration on the structural and electrochemical characteristics of the final samples. Also, we have demonstrated that synthesized N-modified rGO samples can be used as prospective electrode materials for the highly selective electrochemical detection of DA, achieving an impressively lower LOD, a wider linear working range, and higher sensitivity compared to other previously developed metal-free N-modified graphene-based sensors for DA detection. Undoubtedly, this work makes a significant contribution to future developments in a new type of sensing platform that could enable the sensitive detection of various analytes and will inevitably focus on the technology of new conductive materials, especially the new graphene-based materials.

STATEMENTS FOR DEFENSE

1. The use of carbon suboxide changes the thermal stability of GO and influences the decrease in the enthalpy and activation energy of its thermal reduction reaction.
2. The simultaneous restoration of π-conjugation and incorporation of phosphorus-containing functionalities into rGO can be achieved by using the mixture of malonic acid and P_2O_5 during the thermal reduction of GO. By employing this mixture, structural, electrical, and electrochemical properties of rGO can be controlled.
3. Metal-free nitrogen-modified rGO, prepared by the hydrothermal treatment of GO with the dye Bismarck brown, as well as phosphorus-modified rGO, obtained by the thermal reduction of GO in the presence of malonic acid and P_2O_5, are promising electrode materials for the sensitive and selective electrochemical detection of DA.

1. LITERATURE SURVEY

1.1. Graphene-based materials

Different hybridization states of carbon (sp, sp^2, and sp^3) provide the formation of a broad spectrum of structures, ranging from small molecules to long chains. This also enables various structural modifications and composites to achieve the desired electrical, optical, thermal, mechanical, and electrochemical properties of graphene-based materials. They include both traditional carbon materials such as graphite and the new range of substances such as graphene and its derivatives (GO, rGO, and functionalized GO/rGO), single- and multi-walled carbon nanotubes, carbon nanofiber, fullerenes, and carbon dots (Fig. 1). They can be made primarily from sp^2-hybridized carbon (such as graphene, carbon nanotubes, and graphite) or sp^2- and sp^3-hybridized carbons in various ratios (such as GO and rGO) [3,16].

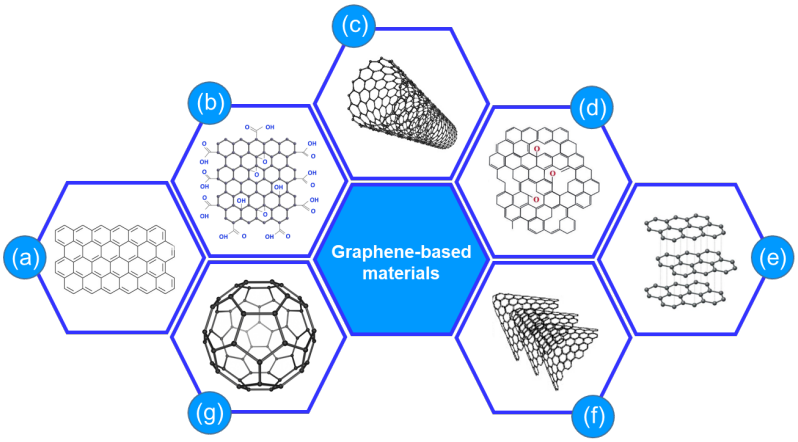

Fig. 1. Graphene-based materials: graphene (a), graphene oxide (b), carbon nanotube (c), reduced graphene oxide (d), graphite (e), carbon nanofibers (f), and fullerene (g).

1.1.1. Reduced graphene oxide

Reduced graphene oxide possesses properties between graphene and GO that makes it an attractive carbon material in the applications of energy storage systems, (bio)sensors, fuel cells, Li^+ ion batteries, and supercapacitors [17–19]. Metal-free rGO exhibits relatively good electrical conductivity and adsorption properties as well shows a high specific surface area, thermal stability, thermal conductivity, and mechanical strength. Due to the presence

of some functional groups on the surface, rGO results in a good dispersion in numerous solvents and serve as a platform for the immobilization of various (bio)molecules. Structural defects, such as sp^3 defects, carbon vacancies, dislocations, and grain boundaries, serve as electroactive centers that ensure the high electrochemical and catalytic performance of rGO [20]. Several synthesis strategies of rGO have been proposed, which could mainly be categorized into the chemical, electrochemical, hydrothermal, and thermal reduction of GO. Since this dissertation involves the thermal and hydrothermal treatment of GO, these methods will be discussed in greater depth.

Thermal reduction. Thermal reduction of GO can be defined as a disproportionation reaction, during which reduced (rGO) and oxidized (CO, CO_2) forms of carbon are produced [21]. GO exhibits numerous oxygen-containing functionalities such as hydroxyl, epoxy, carbonyl, carboxyl groups, esters, lactones, and ketones on its surface and edges. Exfoliation (separation of graphene sheets) occurs when the decomposition rate of these functional groups in aGO exceeds the diffusion rate of the gases released from the thermal reduction treatment. Due to the high gas pressure formed at that time, van der Waals forces are broken, resulting in rGO monolayers [20].

The final properties of thermally reduced GO, including the C/O ratio, number of layers, surface area, and number of structural defects, mostly depend on the synthesis temperature, pressure, atmosphere, and oxidation degree of GO. GO can be thermally reduced in air, vacuum, inert (N_2, Ar, He) or reducing atmosphere [20,22]. For example, the use of the H_2 and Ar mixture leads to a higher C/O ratio compared to that of the rGO sample obtained only under the Ar atmosphere [23]. Thermal reduction of GO under NH_3 atmosphere can also be carried out, however, in this way, nitrogen-doped graphene is obtained [24]. Since all oxygen-containing functional groups exhibit different thermal stability [20], the choice of temperature also has a particularly significant influence on the ratio of C/O. For instance, at temperatures higher than 750 °C, the C/O ratio can vary from 2 to 13 and by reducing temperatures up to 500 °C, the highest achievable C/O ratio could be up to 7 [22]. Although the graphene sheets obtained by the thermal reduction are typically wrinkled due to the release of CO and CO_2, the high-quality graphene monolayers with minimal defects can be prepared at high temperatures of 2000 °C and 2400 °C, with corresponding C/O values of 35.1 and 39.8, respectively. Raman spectroscopy indicates that the samples obtained at 2000 °C and 2400 °C show I_D/I_G ratios (0.15 and 0.14, respectively) close to that of the pristine graphite ($I_D/I_G = 0.12$), indicating the full restoration of the π-conjugation [25]. Nevertheless, a successful reduction

of GO is possible not only at high temperatures but also at low temperatures (around 300 °C) by creating a high vacuum, as it increases the mechanical driving force, which allows the more efficient separation of graphene sheets [21]. Although the reduction temperature and atmosphere have the greatest influence on the composition of rGO, the structure of the resulting material also depends on the GO employed. GO can be synthesized using various chemical methods, with the most popular being Brodie, Staudenmaier, Hummers, and its modifications [26]. Each synthesis method yields GO with varying amounts of oxygen-containing functional groups, structural disorders, morphology, and elemental composition. The efficiency of thermal reduction depends on the degree of oxidation achieved in GO. The higher it is, the more effective the synthesis. Among the mentioned graphite oxidation methods, the product with the lowest C/O ratio is obtained by a modified Hummers' method [20].

The use of carbon sources in the thermal reduction of GO can also restore the π-conjugated bond system. It is known that higher temperature leads to more effective graphitization, which restores the structure characteristic to graphene. Y. Liang et al. have carried out the GO reduction not only using high temperature (1000 °C) but also by introducing acetylene (C_2H_2) into the reduction system, creating transparent and highly conductive graphene-based electrode coatings. In this synthesis, C_2H_2 has acted as an additional carbon source and enhanced graphitization. The conductivity of rGO has increased over 4 times, from 247 S cm^{-1} to 1031 S cm^{-1}, in Ar and C_2H_2 atmospheres, respectively [27]. Thus, it can be confidently stated that by selecting the appropriate carbon additives, it is possible to enhance the restoration of sp^2-hybridized carbon atoms during the thermal reduction of GO.

Hydrothermal reduction. The reduction of GO through the hydrothermal route generally occurs at low temperatures (< 200 °C) and high pressure, resulting in the porous 3D material. Typically, this synthesis is performed in a Teflon-line autoclave or a batch reactor. Under hydrothermal conditions, the superheated water behaves as a strong electrolyte with high diffusion and dielectric constants. Within this environment, water acts as an efficient catalyst, which readily promotes the decomposition of oxygen-containing functionalities on the GO surface [28,29]. The chemical composition, morphology, and dispersibility of rGO might be controlled by changing the synthesis parameters such as the initial concentration of GO, temperature, reaction time, and pH. X. Xu et al. have found that hydrothermal treatment of 0.5 g mL^{-1} of GO for 12 hours yields only a black powdery material, while treatment of 1.0 mg mL^{-1} and 2.0 mg mL^{-1} of GO results in mechanically stable rGO samples (Fig. 2 (a)). The GO (2.0 mg mL^{-1})

reduction performed for different reaction times (1, 2, 4, 6, and 12 hours) has also resulted in a notable decrease in the apparent sizes of the 3D rGO structures within the first 6 hours (Fig. 2 (b)) [30].

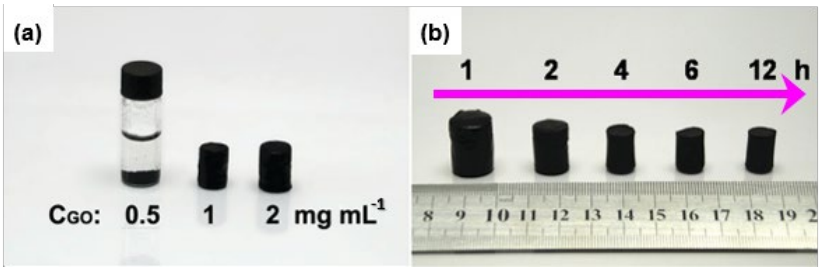

Fig. 2. rGO samples obtained by the hydrothermal reduction of GO dispersions with different concentration at 180 °C for 12 hours (a). rGO structures prepared by the hydrothermal reduction of 2 mg mL^{-1} of GO at 180 °C for different reaction times (b). Modified version from [30].

The mechanical strengths and electrical conductivities of the rGO structures also increase with reaction time [30]. This can be explained as follows. Prior to reduction, the GO sheets are randomly dispersed in water, owing to their pronounced hydrophilicity and the electrostatic repulsion effect. Upon undergoing hydrothermal reduction, the GO sheets change to a hydrophobic state, attributed to the restoration of their conjugated domains and the decomposition of oxygen-containing functionalities. The interplay between hydrophobicity and π-π interactions leads to the 3D random stacking of flexible graphene sheets. If the concentration of GO is sufficiently high, timely cross-linking takes place through the partial overlapping of flexible graphene sheets. Subsequently, a satisfactory number of cross-linking sites are generated, leading to the formation of a 3D network characterized by pore sizes, varying from submicrometer to several micrometers [30,31]. C. Bosch-Navarro et al. have also investigated the influence of pH (pH = 3, 5, 7, 9, and 11) on the morphology of rGO (Fig. 3) under hydrothermal conditions. They have determined that the size of the rGO sheets decreases from tens of micrometers (in the case of GO) to smaller sheets with sizes varying between 1 and 10 μm (in the case of rGO) with a decrease of pH. At lower values of pH (pH = 3, 5, and 7), the short- and long-length multiwall-nanotubes have also been achieved [32].

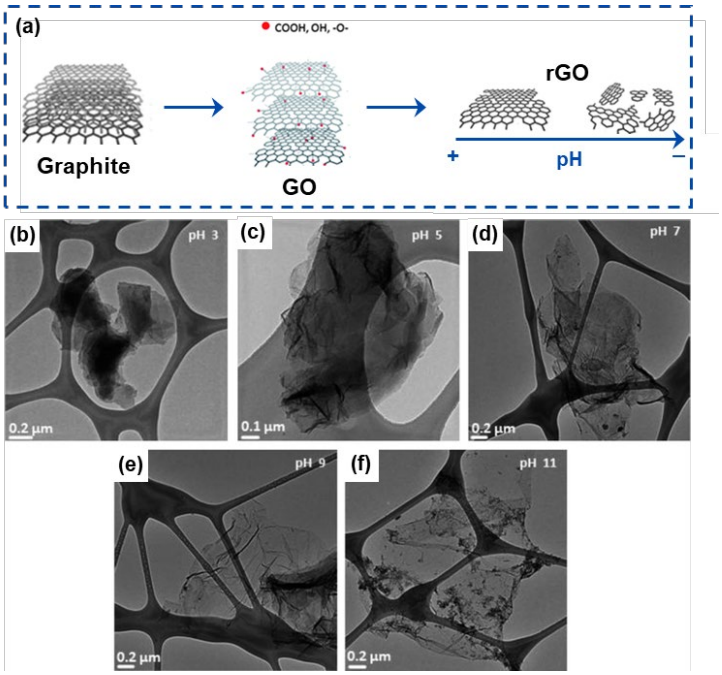

Fig. 3. HR-TEM images for the rGO obtained at pH = 3 (b), pH = 5 (c), pH = 7 (d), pH = 9 (e), and pH = 11 (f). Modified version from [32].

The drying process of the rGO sample significantly influences the final 3D structure. When subjected to typical thermal conditions, the 3D rGO hydrogel will undergo significant volume shrinkage and structural cracking. This occurs primarily due to the substantial capillary pressure resulting from solvent evaporation and the structural thickness. Capillary pressure can be managed through freeze-drying or supercritical CO_2 drying methods. In these processes, water is substituted by ice or supercritical CO_2 liquid, as they do not interact favorably with graphene walls [31].

1.1.2. Nitrogen-modified reduced graphene oxide

The doping process can modulate structural, electronic, magnetic, thermal, optical, chemical, and electrochemical properties of rGO, significantly broadening the range of its potential applications. Typically, rGO is modified with heteroatoms such as B, N, P, and S. Halogens (F, Cl, Br, and I), metals (Ga, Fe and Cr) and silicon have also been shown to serve as dopants for graphene-based materials [33,34]. Several sections of this PhD thesis focus on studying the rGO doping with N- and P-containing functionalities, therefore, a comprehensive review including the structure, synthesis, properties, and

potential applications of nitrogen-modified rGO (N-rGO) and phosphorus-modified rGO (P-rGO) has been further performed.

The N atom is an ideal dopant for graphene-based materials. Nitrogen exhibits a comparable atomic radius (0.70 Å) with carbon (0.77 Å) and possesses a more negative electronegativity (3.04) than carbon (2.55), thereby facilitating its incorporation into the carbon basal plane through substitutional doping [35]. N-containing bonding configurations such as pyridinic-N, pyrrolic-N, graphitic-N, and N-oxides of pyridinic-N are the most common bonds in N-modified graphene-based materials as shown in Fig. 4 [33].

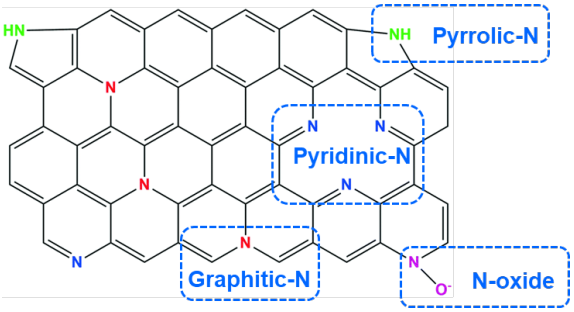

Fig. 4. Typical N-containing bonding configurations in graphene-based materials.

In general, pyridinic-N forms bonds with two carbon atoms located at the edges or defects of graphene, contributing a one p electron to the π-system. Pyrrolic-N denotes nitrogen atoms that contribute two p electrons to the π-system, forming bonds within the five-membered ring structure, as in pyrrole. Graphitic-N refers to nitrogen atoms that replace carbon atoms within a hexagonal ring structure [36]. In N-oxides, the nitrogen atom bonds with two carbon atoms and one oxygen atom and forms a hexagonal ring structure. In this configuration, the nitrogen atom possesses a partially positive charge, and the oxygen atom remains partially negatively charged [37]. Due to the similar bond lengths of C–N (1.41 Å) and C–C (1.42 Å), both sp^2-hybridized pyridinic-N and graphitic-N minimally affect the structure of graphene. Conversely, the presence of sp^3-hybridized pyrrolic-N induces distortions in the planar symmetry of graphene. Pyridinic-N bonding configuration exhibits the highest stability in the presence of monovacancy defects, whereas both pyridinic-N and graphitic-N configurations dominate in the presence of Stone-Wales and divacancy defects [33]. Pyridinic-N and pyrrolic-N bonding configurations are capable of increasing the catalytic activity, wettability, and biocompatibility of graphene-based derivatives, when graphitic-N accelerates

the mobility of the charge carriers because of the contribution of nitrogen p electrons to the graphene π-system. Regarding the electrochemical performance of the N-rGO, pyridinic-N, pyrrolic-N, and N-oxides groups are responsible for increasing the overall energy density through reversible redox reactions, whereas graphitic-N improves the conductivity of the material [38].

Synthesis of N-doped graphene and its derivatives primarily involves two methods, categorized as direct synthesis (chemical vapor deposition, segregation growth, solvothermal, and arc discharge) and post-synthesis treatment (thermal, hydrothermal, microwave, and plasma-assisted techniques). Direct synthesis is the common approach for the preparation of high-quality graphene with homogenous doping. However, the low yield, complexity, high cost of the equipment, and the use of metal catalysts limit their application to fundamental studies. The post-treatment method presents an attractive strategy to obtain nitrogen-doped graphene-based materials owing to its convenience for the simple, inexpensive, and large-scale production as well the versatile functional groups capabilities [39]. The most promising scalable post-synthesis doping strategies usually employ GO as a starting carbon material. In this work, the N-rGO samples have been prepared by the hydrothermal treatment of GO in the presence of the organic diazo dye Bismarck brown at 180 °C for 12 hours. However, the variety of N-containing sources can also be used to obtain N-rGO via hydrothermal reduction of GO, as presented in Table 1.

Table 1. Hydrothermal reduction conditions for producing N-rGO.

Nitrogen source	Temperature (ºC)	Reaction time (hours)	N content (at.%)	Application of N-rGO	Reference
amitrole	180	8	13.4	DA detection	[40]
ammonia	180	15	7.77	water treatment	[41]
ammonia	200	24	–	NO gas sensor	[5]
ammonia and melamine	180	3	3.86	fuel cell	[42]
glucosamine hydrochloride	180	12	6.3	supercapacitors	[43]
Urea	180	12	10.13	supercapacitors	[44]
Urea	150	12	5.0	supercapacitors	[45]
Bismarck brown	180	12	3.8 and 10.6	DA detection	This work

N-rGO has found the applications in the various sensors for the detection of a range of substances, including DA [46], glucose [47], H_2O_2 [24], nitrite [11], guanine [48], methylene blue [49], and methyl parathion [50]. Also, it demonstrates efficient catalytic activity in supercapacitors [44], Li^+ ion batteries [51], solar [52], and fuel cells [42].

1.1.3. Phosphorus-modified reduced graphene oxide

Due to its larger size compared to nitrogen, phosphorus-doping causes a higher degree of structural distortions in rGO. When phosphorus is introduced into rGO, the sp^2-hybridized carbon transforms into the sp^3 state and phosphorus forms a pyramidal-like structure with three carbon atoms. In this configuration, P protrudes from the graphene plane by 1.33 Å accompanied by a 24.6% increase in the P–C bond length compared to the C–C bond length of pristine graphene (Fig. 5 (a)) [53]. These lattice distortion-induced defects can function as the active site for the oxygen reduction reaction (ORR) [54].

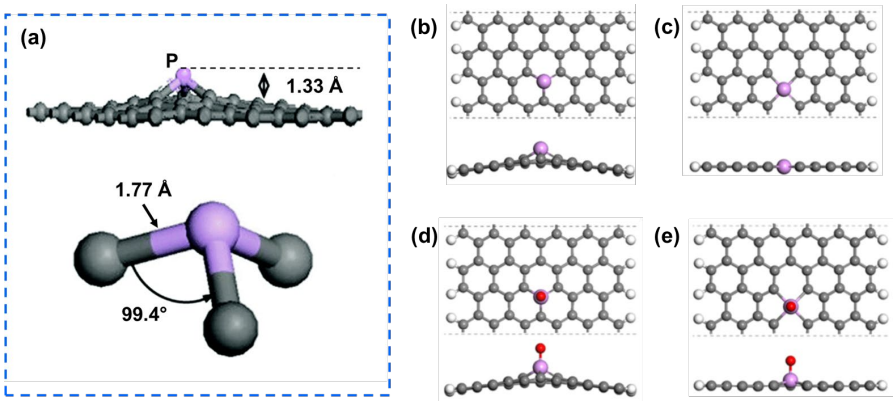

Fig. 5. Optimized geometrical structure of P-doped graphene (a). Adapted from [33]. The three-coordinated (b), four-coordinated (c), oxidized three-coordinated (d), and oxidized four-coordinated phosphorus-doped graphene structure. Modified from [55].

Unlike nitrogen, which has an electronegativity of 3.04, the electronegativity of phosphorus (2.19) is significantly lower than that of carbon (2.55). As a result, the polarity of the C–P bond is opposite to that of the C–N bond. Moreover, distinct effects from P-doping, in contrast to N-doping, may also emerge due to the presence of the additional orbital of phosphorus ($3s^23p^3$) [33]. The prevalent model for P-rGO structure involves phosphorus in a sp^3-hybridized state, though models incorporating sp^3d (four-

coordinated), sp^3 (oxidized), and sp^3d (oxidized) phosphorus have also been proposed (Fig. 5 (b−e)). Due to sp^3d-hybridization of phosphorus, a four-membered ring framework exhibits a square pyramidal structure, which is not only relatively flat but also stable. Additionally, phosphorus readily oxidizes when exposed to air within the carbon matrix containing phosphorus. Consequently, structures featuring P−O bonds can be constructed based on the aforementioned configurations [55].

The synthesis of P-rGO remains challenging in comparison to N-rGO, primarily due to the relatively large atomic radius of phosphorus. Electrochemical method, microwave-assisted solvothermal treatment, and thermolysis have been studied for the P-rGO preparation [56]. However, the typical method for preparing P-rGO involves the thermal reduction of GO in the presence of P-containing compounds such as $NH_4H_2PO_4$, triphenylphosphine (TPP), phosphoric acid, 1-butyl-3-methlyimidazolium hexafluorophosphate ($BmimPF_6$), and phytic acid. The phosphorus content in P-rGO prepared via the thermal treatment of GO generally ranges from 1.16 to 9.86 at.% [56]. Table 2 presents the synthesis conditions of the P-rGO samples prepared by the thermal reduction of GO.

Table 2. Thermal reduction conditions for producing P-rGO.

Phosphorus source	Temperature (°C)	Reaction time (hours)	P content (at.%)	Annealing atmosphere	Application of P-rGO	Reference
TPP	1000	1	1.32	Ar	ORR and Li^+ ion batteries	[57]
TPP	400–800	–	2.09–1.55	Ar	NH_3 detection	[58]
$BmimPF_6$	550 1000	2 1	1.16	Ar	ORR catalysts	[59]
H_3PO_4	800	2	2.18	Ar/H_2	electrocatalysis	[60]
H_3PO_4	600	0.5	8.27	Ar	–	[61]
Phytic acid	900	1	6.1	Ar	pseudocapacitors	[62]
MA and P_2O_5	800	1	1.84, 2.74	Ar	DA detection	This work

P-containing bonds such as C–P=O, C–P–O, and C–O–P can be found in P-rGO. However, the most stable structure in P-rGO is the C–P=O configuration, which plays a crucial role in stabilizing the electrochemical

interface between the electrode and the electrolyte. These characteristics allow the electrode based on P-doped rGO to demonstrate an expanded potential window of 1.5 V in an aqueous electrolyte and significantly improve cyclic stability with extremely low leak current [63]. In addition, the P-rGO materials possess a high surface area and enhanced catalytic activity for ORR [56]. As presented in the Table 2, P-rGO exhibits potential applications as an electrode material in both energy storage devices and sensors.

1.2. Thermal decomposition of graphene oxide (GO)

Due to the high amount of heat released during thermal decomposition, GO is classified into the class of energetic materials, such as ammonium nitrate, nitroglycerin, 2,4,6-trinitrotoluene, octogen, and nitrocellulose. Such compounds are characterized by the ability, under external stimuli (heat or electric current), to rapidly convert large amounts of chemical potential energy into kinetic energy, leading to detonation or deflagration [21]. During the thermal reduction of GO, approximately from 40% to 60% of the gases are released, and as the mass of GO increases, so do the limitations on mass and heat transfer, leading to the uncontrolled self-heating and ultimately, explosion of the sample [64]. Therefore, in order to safely apply the thermal reduction method of GO in industry, it is important to understand the kinetics and thermochemistry aspects of this uncontrolled exothermic reaction.

1.2.1. Thermochemistry and kinetics of GO

The n^{th}-order Kissinger, Ozawa, and Borchardt-Daniels models can be used to evaluate the degree of reaction and activation energy of thermal GO decomposition using differential scanning calorimetry (DSC) data [65]. The equations describing these models are listed in Table 3.

Table 3. Kinetic models used in the dissertation.

Models	**Equations**	
Borchardt-Daniels	$ln\left(\frac{d\alpha}{dt}\right) = \ln\big(k(T)\big) + n\ ln(1-\alpha)$ (**Eqn. 1**)	[66]
Kissinger	$\ln\left(\frac{\beta}{T_m^2}\right) = \ln\left(\frac{ZR}{E_a}\right) - \frac{E_a}{RT_m}$ (**Eqn. 2**)	[66]
Ozawa	$ln(\beta) = constant - 1.052\left(\frac{E_a}{RT_m}\right)$ (**Eqn. 3**)	[67]

Borchardt-Daniels model. Due to its simplicity, the Borchardt-Daniels model is the most commonly used method to characterize the kinetic parameters of decomposition reactions. However, it is suitable only for determining the activation energy E_a, the pre-exponential factor Z, and the reaction order n of the exothermic reactions. This model can only be applied to reactions where $n \leq 2$. The Borchardt-Daniels equation (Eqn. 1) describes the dependence of the reaction rate on the fraction of reacted material at any given moment, where $d\alpha/dt$ represents the reaction rate (min^{-1}), α is the fraction of reacted material, $k(T)$ is the rate constant at temperature T (min^{-1}), and n is the reaction order. Plotting the logarithm of the reaction rate ($\ln(d\alpha/dt)$) against the logarithm of the fraction reacted ($\ln(1 - \alpha)$) yields a linear relationship, with a slope equal to n [66].

Kissinger model. The Kissinger method also allows the estimation of the activation energy E_a, pre-exponential factor Z, and reaction order n of thermally unstable materials. It is often used to investigate thermally hazardous materials, but the model is only suitable for reactions with reaction orders of $0.5 < n < 4$. The Kissinger model requires data obtained from the DSC by selecting multiple heating rates. Eqn. 3 corresponds to a linear function $y = mx + b$, where $y = \ln(\beta/T_m^2)$, $x = 1/T_m$, β is the heating rate ($K\ min^{-1}$), T_m is the maximum temperature value of the DSC peak (K). The activation energy E_a and the pre-exponential factor Z are calculated by plotting $\ln(\beta/T_m^2)$ vs. $1/T_m$, where the slope coefficient (m) is equal to E_a/R, and $b = \ln(ZR/E_a)$. The type of reaction is determined based on the shape of the exothermic peak of the sample, by measuring the time at which the full width at half maximum (t_{FWHM}) is reached [66].

Ozawa model. This model is used to evaluate the kinetic parameters of energetic materials, operating on the assumption that the reaction rate, under constant conversion, is a function of temperature. This method requires conducting a series of experiments using DSC equipment and varying heating rates $\beta = dT/dt$. According to Eqn. 2, a plot of $\ln(\beta)$ against $1/T_m$, where T_m is the maximum value of the DSC curve temperature (K), results in a straight line with a slope equal to $1.052\ E_a/R$, where E_a is the activation energy ($J\ mol^{-1}$), and R is the universal gas constant ($J\ (mol\ K)^{-1}$) [67].

Several studies investigate the kinetics of GO thermal decomposition. Y. Qui et al., using the Kissinger model, have calculated the E_a of 142 kJ mol^{-1} for the thermal decomposition of GO and found that the degree of reaction n is 0.7 [64]. Another scientific group has also carried out a kinetic analysis according to the same model, yielding a marginally different activation energy of 167 kJ mol^{-1} [68]. When considering the kinetic parameters of GO, particular attention is also paid to the analysis of the onset temperature (T_{onset})

of GO decomposition, as this value indicates the onset of spontaneous decomposition and defines the maximum temperature for safe storage and use of GO. Studies show that T_{onset} values range from 150 to 220 °C.

A typical thermochemical profile of the thermal decomposition of GO at a heating rate of 10 K min^{-1} is shown in Fig. 6.

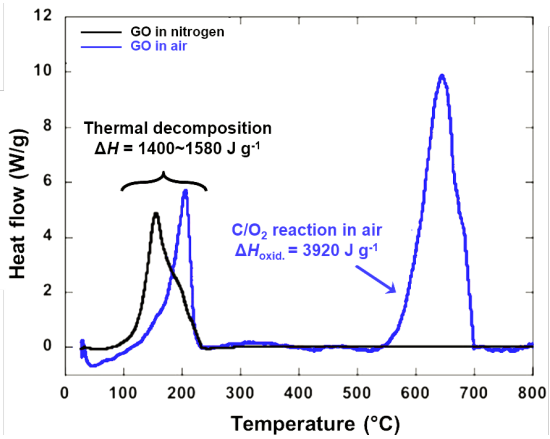

Fig. 6. DSC thermograms of the thermal reduction of GO in a N_2 atmosphere and in air. Adapted version from [64].

Fig. 6 presents that in a nitrogen atmosphere the decomposition of GO starts at lower temperatures ~ 100 °C compared to the air-heated GO data. In addition, when GO is heated in air, a second exothermic peak is observed in the DSC curve at ~ 550 °C, indicating the typical oxidation of defective carbonaceous materials obtained at low temperatures [64]. The enthalpy (ΔH) for this process is 3902 J g^{-1}. The ΔH of GO decomposition in inert environments can range from 1400 to 1700 J g^{-1}, while the enthalpies of the promising industrial energetic materials benzoyl peroxide and trinitrotoluene are 1602 J g^{-1} and 2305 J g^{-1}, respectively [21]. This is an unusual reaction for GO decomposition, as organic materials enriched in oxygenated functional groups, such as coal or biomass, are characterized by endothermic decomposition. Annealing of carbon surfaces is also normally an endothermic process, but there are a few exceptions in the case of ozonized fullerenes and carbon nanotubes oxidized with $KMnO_4$. It would appear that a common characteristic (high heat release) of exothermically decomposing oxidized carbons is due to the formation of oxygen-containing rings. For example, ozone forms highly reactive ozonide rings and $KMnO_4$ is known in synthetic organic chemistry as a catalyst for the formation of epoxy groups. GO is also

distinguished by its abundance of highly reactive epoxy groups compared to oxidized carbons. Therefore, the nature of the exothermic thermal decomposition of GO has been attributed to the epoxy groups in the base plane of the GO sheet [18].

1.2.2. The effect of additives on the GO reduction process

Salts and reducing agents change the thermal properties of GO. Specifically, the thermal reduction of GO, catalyzed by KOH, is notable for its impact on lowering the exothermic decomposition temperature. This catalytic effect is attributed to OH^- ions, which accelerate the decomposition process. Y. Qui et al. have carried out a study showing that an annealing of a mixture of GO and 1 wt.% of KOH in a N_2 atmosphere leads to a decomposition temperature of 128 °C. The researchers have also confirmed that the catalytic effect of KOH on the thermal decomposition reaction of GO is due to OH^- rather than K^+ ions, as K^+ ions only catalyze the combustion reaction of GO at ~ 500 °C. Furthermore, the results of the DSC study of GO dried in acidic medium (pH = 2) have shown that H^+ ions do not increase the thermal reactivity of GO. DSC studies of GO with other different additives (glutathione, citric acid (CA), AA, trolox, hydrazine, and $LiAlH_4$) have revealed that partial chemical reduction decreases the enthalpy of thermal decomposition but increases the reactivity of GO due to the reduction of the T_{onset} temperature value [64].

In this dissertation, the impact of carbon suboxide (C_3O_2) on the kinetics of thermal decomposition of GO has been studied. C_3O_2 is a molecule of linear structure and can be synthesized by the dehydration reaction between malonic acid and phosphorus pentoxide at the temperature of 150 °C [69]:

$$3\ C_3H_4O_4 + P_4O_{10} \rightarrow 3\ C_3O_2 + 4\ H_3PO_4 \quad \textbf{(Eqn. 4)}$$

C_3O_2 is stable below –35 °C, but it spontaneously polymerizes at standard temperature and pressure (0 °C and 1 atm) [70,71]. Most importantly, C_3O_2 thermally decomposes to elemental carbon and two carbon monoxide molecules above 16 °C [72]. For this reason, it is used as a source of atomic carbon for the synthesis of carbon nanotubes [73]. H. B. Palmer et al. have demonstrated that C_3O_2 is also a suitable starting material for the successful preparation of carbon films due to its useful rate and lower temperature of decomposition compared to most hydrocarbons [74]. As discussed in the Section 1.1.1., structural disorders can also be repaired by using a supplemental carbon source, therefore, C_3O_2 is expected to be an alternative

carbon source in the thermal reduction of GO to restore the conjugated aromatic structure of rGO.

1.3. Electrochemical sensors for dopamine detection

To date, numerous reports on DA detection using highly sensitive techniques such as mass spectrometry [75], fluorescence spectrophotometry [76], fluorimetry [77], capillary electrophoresis [78], and high-performance liquid chromatography [79] have been reported. Nevertheless, these methods require well-qualified staff, tedious sample preparation methods, expensive and complex instrumentation setups, which extend the detection time of analytes [80]. In contrast, considering the fast determination of redox-active molecules, electrochemical sensors have attracted considerable attention for DA detection due to their advantages, including high sensitivity, rapid response time, reproducibility, time-saving, cost-effectiveness, and simple operational procedures [81].

An electrochemical sensor typically consists of two key components, such as a chemical recognition system and a physicochemical transducer. The main principle in the detection of analytes by electrochemical sensors involves the measurement of electric current generated by redox reactions in the electrochemical system. These reactions take place at the electrode surface interface, where the recognition element interacts with the target analyte, exhibiting a specific electrochemical activity. The electrode facilitates charge transfer, leading to the generation of current. Consequently, this current is transmitted through the conduction system of the electrodes to the signal analysis system for amplification and converted into a measurable electrochemical signal (Fig. 7.) [82,83].

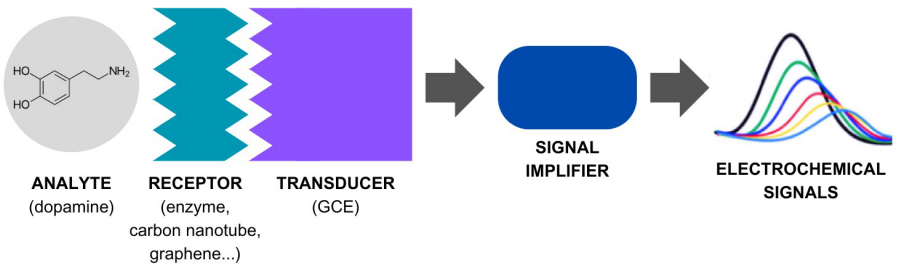

Fig. 7. The schematic diagram of the electrochemical sensor.

An excellent electrochemical sensor should have high selectivity, low LOD, and short response time. The receptor and the signal transducer of the

sensor helps to promote its ultimate performance and expand its application in various fields [82]. Given the ease of DA oxidation, numerous electrochemical methods have been developed for its detection, such as amperometry, cyclic voltammetry (CV), linear sweep voltammetry, chronoamperometry (ChA), and differential pulse voltammetry (DPV) [84].

1.3.1. Dopamine and its electro-oxidation mechanism

DA is a catecholamine neurotransmitter with a benzene ring, two hydroxyl groups, and an amine group. DA acts in both the central nervous system and the peripheral nervous system and plays an important role in functions such as neuromodulation, motor control, reward, motivation, blood pressure regulation, central nervous, and immune systems. DA can be found in various biofluids such as blood, urine, eye fluids, and cerebral spinal fluid. The typical concentrations of DA in human's blood range from 0.01 to 1 μM. Nevertheless, its abnormal levels are associated with the development of nervous system disorders such as senile dementia, schizophrenia, depression, attention deficit hyperactivity disorder, Parkinson's and Alzheimer's diseases [12,84].

DA is a highly redox active molecule, that makes it capable of efficient electrochemical detection without using enzymes. Under physiological conditions in nervous tissues and body fluids, DA occurs in the protonated form. The initial oxidation of DA yields dopamine-o-quinone (DQ) through a two-electron process. Subsequently, the DQ can further undergo a ring-closure reaction, resulting in the formation of lucodopachrome, which can be oxidized to dopachrome through a two-electron pathway (Fig. 8) [85,86]. Other electroactive species, such as AA and UA, also coexist in biofluids in much higher concentrations than DA. AA and UA usually interfere with the detection of DA due to their close oxidation potentials, complicating the selective sensing of DA [87,88]. Therefore, the detection of DA in the presence of AA and UA requires specific electrode surface modifications to achieved its accurate detection [88].

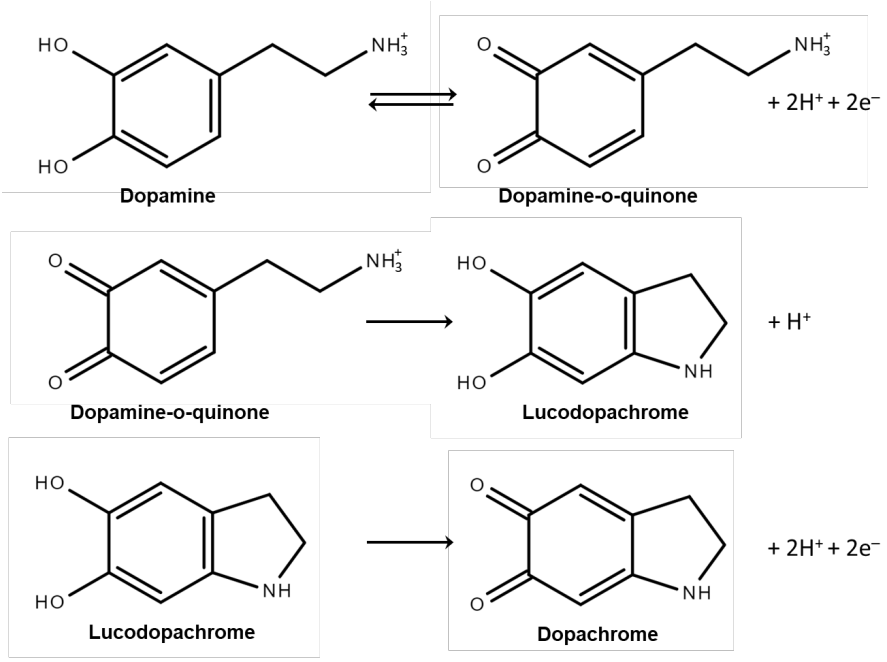

Fig. 8. Electro-oxidation mechanism of DA [86].

1.3.2. Sensors based on reduced graphene oxide

The bare working electrode (WE) exhibits poor selectivity and sensitivity due to its low effective surface area and poor electron transfer rate. Various materials have been proposed for the modification of WE to improve the electrochemical performance and selectivity of DA detection: nobel metal nanoparticles (Pt, Au); carbon-based derivatives (graphene, rGO, GO, single-wall or multi-wall carbon nanotubes); conductive polymers (polypyrrole, poly(2-naphtol)); metal oxides (NiO, ZnO, Fe_3O_4) [4].

Recently, graphene-based derivatives, such as GO and rGO, have shown considerable potential as active electrode materials for electrochemical devices. Their long-term stability, cost-effectiveness, biocompatibility, and environmentally friendly characteristics contribute to this promise [4]. Furthermore, the improved mechanical strength and remarkable electrical and thermal conductivity make them suitable nanomaterials for various electrochemical and biological applications. Specifically, carbon-based materials possess substantial double-layer electrical capacities, leading to high signal-to-noise ratios as a desired characteristic for any type of sensor [85]. In the context of detecting DA, sensors utilizing rGO typically incorporate noble or transition metal nanoparticles (Au, Pd) or their oxides (MnO, NiO, CoO,

Fe_2O_3, ZnO, and $CuCo_2O_4$). Despite the notable efficiency and electrochemical sensing capabilities of rGO/metal nanocomposites, their high expense and potential toxicity deter their widespread use in conjunction with graphene-based derivatives, particularly concerning sustainability parameters.

The present studies show only several works regarding the electrochemical detection of DA using metal-free rGO without any additives [89–91]. rGO modified with heteroatoms exhibits the greater promise for DA sensing due to the ability to tune the electronic structure, physicochemical and structural characteristics. This kind of modification also enhances the surface catalytic active sites, thereby improving charge transfer at the interface between a WE and an electrolyte [6]. Z. H. Sheng et al. have prepared N-doped rGO by thermal reduction of GO with the addition of melamine as a nitrogen-containing precursor and designed the DA sensor with a linear range of 0.5–170 μM and a LOD of 250 nM for DA in the presence of AA and UA [92]. H. Zhang and co-workers have also presented the DA sensor based on N-rGO with a LOD of 0.1 μM in the detection range of 1–60 μM toward DA, simultaneously determining AA and UA [9]. Furthermore, the study reported by S. Ai et al. has revealed that the non-metal N-doped rGO aerogel synthesized by the hydrothermal reduction of GO with aniline exhibits excellent electrochemical characteristics toward DA (LOD = 0.1 μM; the linear range of 1–250 μM), confirming the highly promising sensing abilities of the metal-free N-rGO-modified electrode [46]. Moreover, the P-rGO based electrochemical sensor has exhibited prominent DA sensing performances and selectivity due to the important role of P-doping in improving the electrocatalytic activity of graphene toward DA oxidation [93]. rGO modified with S has been demonstrated to possess high electrocatalytic activity toward the redox reaction of DA, resulting in high selectivity, high sensitivity (3.94 μM μA^{-1}) and low LOD (15 nM at S/N = 3) with a linear range of 0.2–12 μM [94].

2. EXPERIMENTAL

2.1. Materials and reagents

Graphite powder (particle size ≥ 50 μm, purity ≥ 99.5%), potassium persulfate ($K_2S_2O_8$, purity 99.99%), sodium nitrate ($NaNO_3$, purity ≥ 99%), phosphorus pentoxide (P_2O_5, purity ≥ 99%), potassium permanganate ($KMnO_4$, purity ≥ 99%), malonic acid ($CH_2(COOH)_2$, purity 99%), chromium(VI) oxide (CrO_3, purity 99.99%), boric acid (H_3BO_3, purity ≥ 99.5%), dopamine hydrochloride ($(HO)_2C_6H_3CH_2CH_2NH_2 \cdot HCl$, purity 98%), ascorbic acid ($C_6H_8O_6$, ≥ 99%), citric acid ($C_6H_8O_7$, ≥ 99.5%), and uric acid ($C_5H_4N_4O_3$, purity ≥ 99%) were purchased from Merck (Darmstadt, Germany). Phosphate buffer (PB) solution (pH = 7.0, c = 0.1 mol L^{-1} and pH = 7.2, c = 0.1 mol L^{-1}) was prepared using sodium phosphate dibasic (Na_2HPO_4, purity ≥ 99%, Sigma-Aldrich, Steinheim, Germany) and sodium phosphate monobasic (NaH_2PO_4, purity ≥ 99%, Sigma-Aldrich, Steinheim, Germany). Sulfuric acid (H_2SO_4, purity ≥ 98%) and hydrogen peroxide (H_2O_2, 30% weight) were obtained from Eurochemicals (Bratislava, Slovakia). Nafion (5% weight) was purchased from Alfa Aesar (Kandel, Germany). Bismarck brown ($C_{18}H_{18}N_8 \cdot 2HCl$, ≥ 99%) was purchased from Sigma-Aldrich, Steinheim, Germany.

2.2. GO synthesis

In this study, GO was prepared employing three different techniques. One GO sample was prepared by the traditional Hummers' synthesis method, while remaining two GO samples underwent the modified Hummers' synthesis methods, involving a two-stage approach: initial pre-oxidation of natural graphite powder followed by the traditional Hummers' method (see Fig. 9).

GO_1 synthesis. GO_1 was prepared by the traditional Hummers' method [95]. Natural graphite powder (6 g) was added into the mixture with cold (3 °C) concentrated H_2SO_4 (240 mL) and $NaNO_3$ (3 g). Then, $KMnO_4$ (30 g) was gradually added maintaining a temperature of 20 °C. The resulting mixture was left at room temperature for 3 days. After the specified time, the mixture was stirred at 35 °C with a magnetic stirrer for 1 hour and 246 mL of deionized (DI) water was carefully added. The hot suspension was kept at 70 °C for 15 minutes. After all the operations were completed, 840 mL of DI water and 20 mL of conc. H_2O_2 was added. The resulting suspension was filtered through a Buchner funnel and washed with 0.5 L of 10 wt.% HCl.

GO_2 synthesis. Pre-oxidation of the graphite powder was performed by the synthesis protocol described in the work of X. Yan et al. [96]. In a typical experiment, natural graphite powder (6.0 g) was mixed with $K_2S_2O_8$ (5.0 g) and P_2O_5 (5.0 g) in the 98 wt.% H_2SO_4 (24.0 mL) media and heated to 80 °C for 4.5 hours using a hot plate. After that, the mixture was cooled to the room temperature and diluted with 1.0 L of DI water. The resulting pre-oxidized graphite was filtered, air-dried at room temperature to a constant weight and oxidized following the Hummers' method as mentioned earlier.

GO_3 synthesis. In this synthesis of GO, the pre-oxidation of graphite was carried out according to the new approach proposed in our laboratory [97]. In this method, graphite powder (2.0 g) was added to the mixture of 98 wt.% H_2SO_4 (11.0 mL) and H_3BO_3 (0.78 g) with steady and vigorous stirring. Later, CrO_3 (2.1 g) was gradually added and the reaction mixture was maintained for 2 hours at 45−55 °C. Afterwards, the resulting suspension was washed with warm DI water to remove the excess of H_3BO_3. Further oxidation of this pre-oxidized graphite was performed using the same traditional Hummers' method as described above.

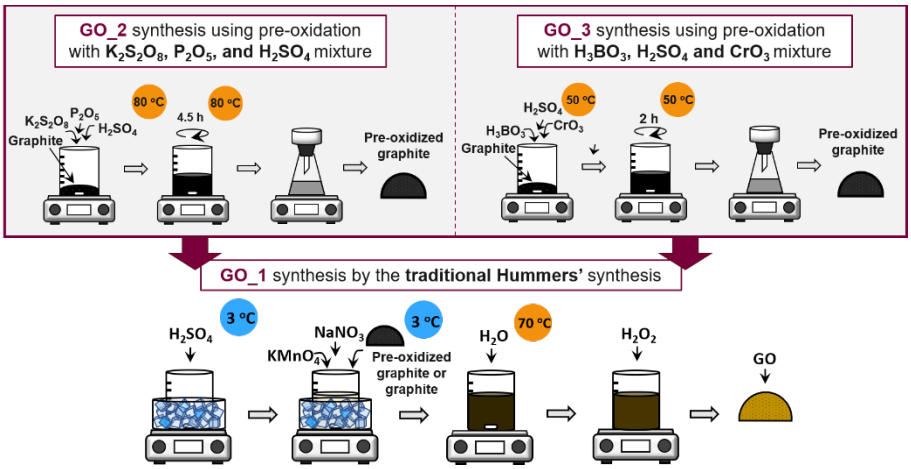

Fig. 9. Synthesis scheme of the GO_1, GO_2, and GO_3 samples.

The GO suspensions (GO_1, GO_2, and GO_3) formed in the reactions were transferred into a dialysis tubing cellulose membrane with a cut-off molecular weight of 10,000–20,000 Da for further purification and dialyzed against DI water until the pH value of the dialysate became ~5. After purification, the resulting GO samples were dried in air to a constant weight.

2.3. Modified-rGO synthesis

2.3.1. Phosphorus-modified rGO synthesis

GO_1 or GO_3 mixed with malonic acid (MA) and phosphorus pentoxide was ground in an agate mortar for 10 min. The weight ratios of GO and MA used in this mechanochemical synthesis were 1:0.05 and 1:0.10. The amount of phosphorus pentoxide was calculated according to Eqn. 4. The solid mixtures prepared after grinding were initially annealed in the tubular furnace exposing them at 100 °C for 10 min. The samples obtained were then treated by thermal shock at 800 °C for 5 min. The whole heat treatment process (at temperatures of 100 °C and 800 °C) was carried out under an argon atmosphere with a flow rate of 60 mL min^{-1}. After cooling, the thermally reduced GO samples were thoroughly washed with DI water and dried in air. The thermal reduction of the GO samples without additives was also performed under the same synthesis conditions. The samples obtained were labelled rGO_1 and rGO_2, respectively. Whereas, the thermally reduced GO_1 and GO_3 samples with the addition of MA and phosphorus pentoxide were named according to the ratio of added MA. For example, if GO_1 was thermally reduced by adding 5 wt.% or 10 wt.% of MA, this synthesized product was denoted as rGO_1_5 or rGO_1_10, respectively.

2.3.2. Nitrogen-modified rGO synthesis

GO_2 was also reduced by the one-pot hydrothermal treatment. To prepare a homogeneous suspension, GO_2 (500 mg) was dispersed in 50 mL of DI water in the presence of 20 wt.% or 50 wt.% Bismarck brown (BB) and ultrasonicated for 1 hour. The prepared suspensions were transferred to Teflon-lined stainless-steel autoclaves with a capacity of 90 mL and were heated at a temperature of 180 °C for 12 hours. After the reaction time, the autoclaves were kept for cooling at room temperature. The resulting black powders were washed with DI water and dried in air at the ambient atmosphere. Samples synthesized with 20 wt.% and 50 wt.% of BB were denoted as rGO__BB20 and rGO_BB_50, respectively. Pure rGO without BB was also prepared under the same synthesis conditions and named as rGO_2.

2.4. Characterization methods

Brunauer-Emmett-Teller (BET) analysis. N_2 adsorption-desorption measurements were performed using a BET analyzer TriStar II 3020 (Micromeritics, Norcross, GA, USA) at 77 K. All materials were outgassed

for two hours at 90 °C or 120 °C in a N_2 environment prior to gas sorption experiments. The BET model was applied to determine the specific surface area S_{BET}, while the pore volume distribution was estimated using the Barrett-Joyner-Halenda (BJH) method.

Energy dispersive X-ray spectroscopy (EDX). EDX analysis was performed by a scanning electron microscope (TM3000; Hitachi, Tokyo, Japan) equipped with an EDX detector.

Electrical conductivity measurements. A Keithley 2601 source meter (GlobalTech Sourcing, North Hampton, NH, USA) was applied for the conductivity measurement. The electrical conductivity of the samples obtained was determined using a cell made in our laboratory. The experiments were carried out at room temperature (22 °C) and a relative humidity of 40%. Approximately 0.02 g of graphene-based powder samples were placed in a glass cylinder of 2.86 mm in diameter between two copper electrodes. We assume that the electrical contact area between the electrode and the powder was the same as the inner area of a cylinder. The sample was gradually pressed by reducing the distance between the electrodes, and the resistance was determined. The resistivity (ρ) was determined using the following equation:

$$\rho = R\frac{A}{l} \textbf{ (Eqn. 5)}$$

where R is a resistance (Ω), A – a cross section area (m^2), and l – the length of the sample (m). Current-voltage characteristic curves were linear in a voltage range of ±1 V for all samples tested.

Fourier transform infrared spectroscopy (FTIR). Measurements were performed by an FTIR spectrometer (PerkinElmer, Inc., Waltham, MA, USA). Infrared spectra were recorded in the range of 700–4000 cm^{-1} using the KBr pellet technique in transmission mode. The spectral resolution was set at 4 cm^{-1}.

Raman spectroscopy. Raman spectra were recorded using an inVia Raman spectrometer (Renishaw, Wotton-under-Edge, UK) equipped with a thermoelectrically cooled (−70 °C) CCD camera in the range of 300–3300 cm^{-1}. He-Ne gas laser provided an excitation beam at 532 nm with power restricted to 1 mW. The integration time was selected as 100 s. The 20×/0.40NA objective (Leica, Wetzlar, Germany) was used during the all measurements. The Raman frequencies were calibrated by the silicon peak at 520.7 cm^{-1}. The average in-plane crystallite size L_α was determined according to the following equations [98]:

$$L_\alpha = 2.4 \cdot 10^{-10} \cdot \lambda_L^4 \cdot \left[\frac{I_D}{I_G}\right]^{-1} \textbf{(Eqn. 6)}$$

$$L_\alpha = \frac{l_c}{2} \ln\left[\frac{C}{FWHM(G) - FWHM(G_0)}\right] \textbf{(Eqn. 7)}$$

where λ_L is the wavelength of the laser radiation used for the excitation of the Raman analysis, I_D and I_G – the intensities of the D and G bands in the Raman spectra, respectively, l_C – a photon coherence length (32 nm), $C = 95$ cm^{-1}, FWHM(G) and FWHM(G_0) – the width of the G band of the sample under investigation and undoped pristine graphene (15 cm^{-1}), respectively.

Scanning electron microscopy (SEM). SEM imaging was carried out using a Hitachi SU-70 microscope at an accelerating voltage of 10.0 kV at magnifications of 50,000. The samples were coated with 10 nm of silver using a Q150T ES Turbo-Pumped Sputter Coater (Quorum, Washington, DC, USA) before SEM microscopy.

Transmission electron microscopy (TEM). The analysis was performed using a TECNAI G2 F20 X-TWIN microscope equipped with an Orius SC1000B CCD camera (Gatan, Pleasanton, CA, USA) with a Schottky-type field emission electron source using an accelerating voltage of 200 kV.

Thermogravimetry (TG), derivative thermogravimetry (DTG), and differential scanning colorimetry (DSC). TG/DTG and DSC experiments were performed using a Thermal analyzer STA6000 (PerkinElmer, USA) under non-isothermal heating mode. The prepared samples were heated at three heating rates β: 2.5 °C min^{-1}, 5 °C min^{-1}, and 10 °C min^{-1} from room temperature to 300 °C. The ambient nitrogen atmosphere was used with a flow rate of 20 mL min^{-1}. The average mass of the samples was about 5 mg.

X-ray photoelectron spectroscopy (XPS). XPS analysis was carried out with a Kratos Axis Supra (Kratos analytical, Manchester, UK) spectrometer. Monochromatic Al Kα radiation ($h\nu$ = 1486.69 eV) was used as an X-ray source. The XPS spectra were recorded at a pass energy of 20 eV and calibrated using the carbon 1s line at 284.6 eV. The raw XPS spectrum was deconvoluted by curve fitting peak components using the software CASAXPS. Symmetric Gaussian–Lorentzian functions were used to approximate the line shapes of the fitting components after Shirley-type background subtraction.

X-ray diffraction (XRD). The crystallographic information of the synthesized products was obtained using a MiniFlex II X-ray diffractometer

(Rigaku, Tokyo, Japan). XRD patterns were recorded in the 2θ range from 5° to 60° using CuKα λ = 1.5406 Å radiation with a step of 0.010°.

2.5. Determination of kinetic parameters

For the kinetic analysis of the thermal GO reduction, GO_2 (0.1 g), MA (0.01 g), and P_2O_5 (0.009 g) were grounded in an agate mortar for 10 min. The prepared mixture was named GO_2_MA_P.

Determination of enthalpy. The enthalpy of the thermal decomposition reaction (ΔH) of GO was calculated based on the obtained results of DSC analysis. For this purpose, the amount of heat released during decomposition was equated to the integrated area of the DSC peak:

$$\int \left(\frac{dH}{dt}\right) dt = \Delta H \text{ (Eqn. 8)}$$

where H is the amount of heat (J) and t is time (s).

Determination of activation energy. The activation energy (E_a) of the thermal decomposition of GO was calculated using the obtained DSC curves and three different methods: Kissinger, Ozawa, and Borchardt-Daniels. Kissinger and Ozawa methods are model-free and based upon a series of experiments, in which solid samples are heated at several different heating rates while the reaction exothermic peak is recorded. The Kissinger method is based on the following equation:

$$\ln\left(\frac{\beta}{T_m^2}\right) = \ln\left(\frac{ZR}{E_a}\right) - \frac{E_a}{RT_m} \text{ (Eqn. 9)}$$

where E_a is the activation energy, β – the heating rate, T_m – the maximum peak temperature of DSC curve, Z – the Arrhenius frequency factor, R – the universal gas constant (8.314 J mol^{-1} K^{-1}). The E_a can be evaluated as a slope from Kissinger's $\ln(\beta/T_m^2)$ plot versus $1/T_m$.

In the Ozawa method, a linear relation between heating rates and temperature can be expressed as:

$$\log(\beta) \cong 0.4567 \cdot \frac{E_a}{R} \cdot \frac{1}{T_m} \text{ (Eqn. 10)}$$

where E_a is the activation energy, β – the heating rate, T_m – the peak temperature, and R – the universal gas constant. The apparent value of E_a can be determined from a slope by plotting $\log(\beta)$ versus $1/T_m$.

The Borchardt-Daniels model allows a rapid determination of kinetic parameters based on a single scan by DSC. This approach considers that the reaction follows n^{th} order kinetics and obeys Arrhenius behavior. The Borchardt-Daniels method gives the following equation:

$$\ln\left(\frac{d\alpha}{dt}\right) = \ln\big(k(T)\big) \cdot n\, ln(1-\alpha) \quad \textbf{(Eqn. 11)}$$

where dα/dt is the reaction rate, α – the fractional conversion, $k(T)$ – the specific reaction rate constant at temperature T, and n – the reaction order. The activation energy E_a can be obtained from the slope of $\ln(k(T))$ versus $1/T$ by fitting the n values.

2.6. Electrochemical measurements

Electrochemical measurements were performed under ambient conditions at a temperature of 22 °C and a relative humidity of 40%, using a potentiostat/galvanostat CompactStat instrument (Ivium Technologies, The Netherlands). All electrochemical measurements were conducted in a three-electrode system composed of an auxiliary platinum wire electrode, a reference Ag/AgCl electrode, and working electrodes (Ø 3 mm, 0.07065 cm^2). The working electrode was constructed by coating the active rGO-based material onto the surface of a glassy carbon electrode (GCE) previously polished with alumina powder (0.05 μm, Kemet, UK) and ultrasonicated in DI water and ethanol for 1 hour. For the preparation of rGO-based active material/GCE electrodes, 1 mg of rGO_1_10 (or rGO_3_10, rGO_BB20, rGO_BB50) sample was dispersed in 1 mL of the mixture of DI water and Nafion (V_{water}:V_{Nafion} = 9:1) by sonicating in an ultrasonic bath for 2 h. After that, 10 μL of the suspension (1.0 mg mL^{-1}) obtained were drop-casted onto the surface of GCE and left to dry in air at the room temperature for 1 hour.

The study of P-modified rGO. Cyclic voltammetry (CV) and differential pulse voltammetry (DPV) were used to investigate the electrochemical behavior of dopamine at the modified GCE/rGO_1_10-based or GCE/rGO_3_10-based electrode. The impact of the scan rate was determined cycling the potential from − 0.2 to + 0.8 V (vs Ag/AgCl) in the 0.1 M PB solution (pH = 7.2) from 10 to 180 mV s^{-1}. The start potential of − 0.4 V, the end potential of + 0.6 V, the potential step of 5 mV, the scan rate 50 mV s^{-1}, the pulse time of 10 ms, and the pulse amplitude of 50 mV were

used for the DPV electrochemical analysis. In the interference study, 200 μM of UA were added to the electrochemical system.

The study of N-modified rGO. CV and chronoamperometry (ChA) were used to investigate the electrochemical behavior of DA at the modified GCE/N-rGO_20 or N-rGO_50-based electrodes. The impact of the scanning rate was observed cycling the potential from – 1.0 to + 1.0 V (vs Ag/AgCl) in a 0.1 M PB solution (pH = 7.0) from 10 to 120 mV s^{-1}. ChA measurements were performed in 0.1 M PB (pH = 7.0) by successively adding DA with a constant stirring of 300 rpm. The chronoamperometric response was measured at a constant potential of + 0.3 V. In the interference study, 0.05 mM of AA, 0.05 mM of CA, 0.05 mM of H_2O_2, and 0.05 mM of UA were added to the electrochemical system.

The LOD of DA has been calculated according to the equation:

$$LOD = \frac{3\sigma}{s} \textbf{ (Eqn. 12)}$$

σ is a standard deviation of the anodic peak current of the blank signal and s signifies the slope of the calibration plot obtained using ChA results. The sensitivity of the electrodes toward DA has been determined by the following equation:

$$sensitivity = \frac{s}{A_g} \textbf{ (Eqn. 13)}$$

where A_g is the geometric area (cm^2) of the GCE electrode.

3. RESULTS AND DISSCUSIONS

3.1. Impact of carbon suboxide on the kinetics of thermal decomposition of GO

GO is an energetic material that releases a significant amount of energy during thermal decomposition. Consequently, to assess the kinetic parameters of this decomposition both with and without C_3O_2, in this part of the PhD thesis, a thermal analysis (TG/DTG/DSC) has been performed. The TG/DTG/DSC curves have been recorded for two samples: GO_2 and GO_2_MA_P. The TG and DTG data at three different heating rates of 2.5, 5, and 10 °C min^{-1} from room temperature to 300 °C are shown in Fig. 10.

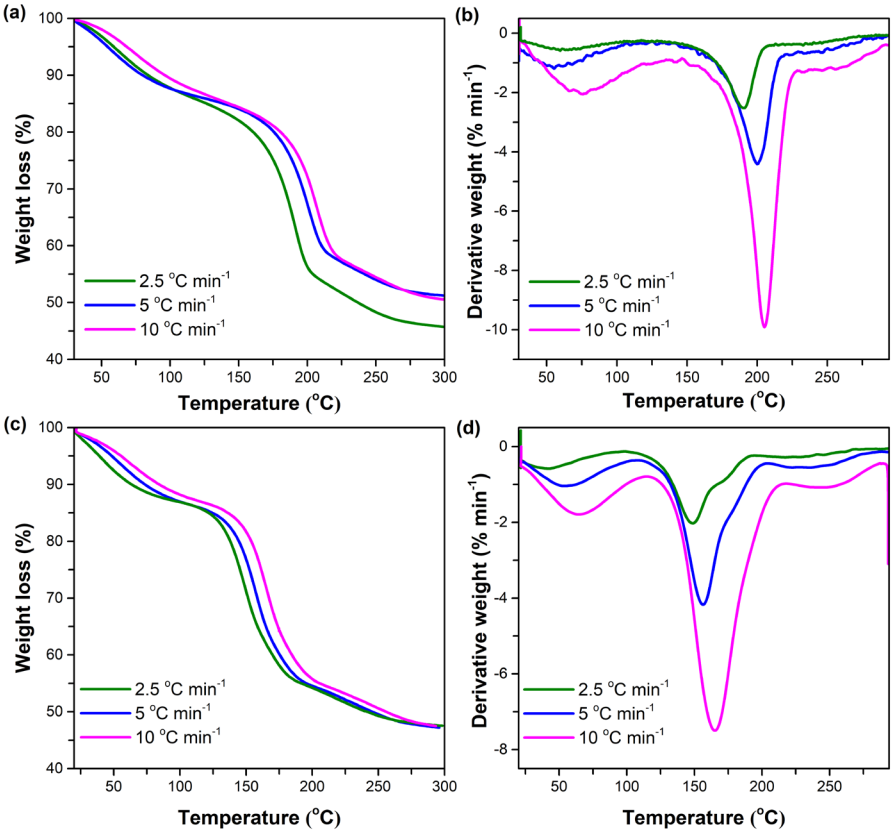

Fig. 10. TG curves of GO_2 (a) and GO_2_MA_P (c) and DTG curves of GO_2 (b) and GO_2_MA_P (d) at heating rates of 2.5, 5, and 10 °C min^{-1}.

Thermal properties of GO_2 under ambient atmosphere are presented in Fig. 10 (a) and (b). From the TG curves, it can be observed that the thermal reduction of GO_2 occurs in three stages. These results are in good agreement with those found in the literature [99,100]. The first stage (up to 100 °C) is associated with the evaporation of adsorbed or intercalated water molecules. In the second step, the major loss of weight occurring between 100 °C and 250 °C results from the removal of labile oxygen functionalities, including hydroxyl, lactone, and carboxyl, forming CO and CO_2 gases [99]. The final step (> 300 °C) could be attributed to the decomposition of stable oxygen-containing functional groups such as phenol, quinone, carbonyl and the degradation of graphitic GO network [100]. It has been noticed that the heating rate affects the thermal profile of samples by changing the position of the TG curve and the peak positions in DTG curves. Fig. 10 (a) shows that the residual weight after thermal decomposition of GO_2 increases with increasing heating rate, which indicates the increase in thermal stability. Mass losses (measured at 240 °C) of 50.56%, 44.92%, and 44.42% have been recorded for heating rates of 2.5, 5, and 10 °C min^{-1}, respectively. These observed differences are most likely due to the fact that the faster heating rate does not ensure the same temperature to the whole sample [101]. This trend suggests that the lower heating rate is more favorable for the production of high-quality rGO as the higher reduction degree is achieved. At higher heating rates, the decomposition process also slightly shifts towards the higher temperatures. This shift also could be assigned to the limitations of heat transfer [101].

The shapes of TG curves of the GO_2_MA_P sample are in general similar to that of pure GO_2. Nevertheless, each stage of decomposition of GO_2_MA_P is slightly shifted to lower temperatures. The shift can be more accurately observed using DTG curves (Fig. 10 (b) and (d)). The dehydration of the GO_2_MA_P sample starts at lower temperatures (50–90 °C) in comparison with that of pure GO_2 (60–100 °C). The second stage, the deoxygenation of GO_2, occurs in the temperature range 90–200 °C, while the decomposition of pure GO_2 starts at higher temperature (100–250 °C). Moreover, in TG curves of GO_2_MA_P sample, a decreasing trend in the mass loss with the increase in heating rate from 2.5 °C min^{-1} to 5.0 °C min^{-1} and then further to 10.0 °C min^{-1} is determined as in the case of pure GO_2. Mass losses (measured at 210 °C) of 46.86%, 46.40%, and 45.38% are recorded for heating rates of 2.5, 5.0, and 10.0 °C min^{-1}, respectively. Comparing the mass loss values and DTG curves of GO_2 and GO_2_MA_P samples, one can conclude that the use of C_3O_2 additive in the reduction process can provide new possibilities in the decomposition of GO_2 by

reducing the temperature of the process. The successful low-temperature reduction of GO_2 under ambient atmosphere could open new possibilities for the safe, large-scale production of graphene and the development of graphene-based composites.

In order to obtain a better understanding of the reaction that occurs during the thermal decomposition of pure GO_2 and GO_2 with C_3O_2 additive, the kinetic (activation energy E_a and reaction order n) and thermodynamic (reaction heat ΔH) parameters have been determined using the DSC analysis. The DSC curves of GO_2, GO_2_MA_P, and the mixture of malonic acid and phosphorus pentoxide are displayed in Fig. 11.

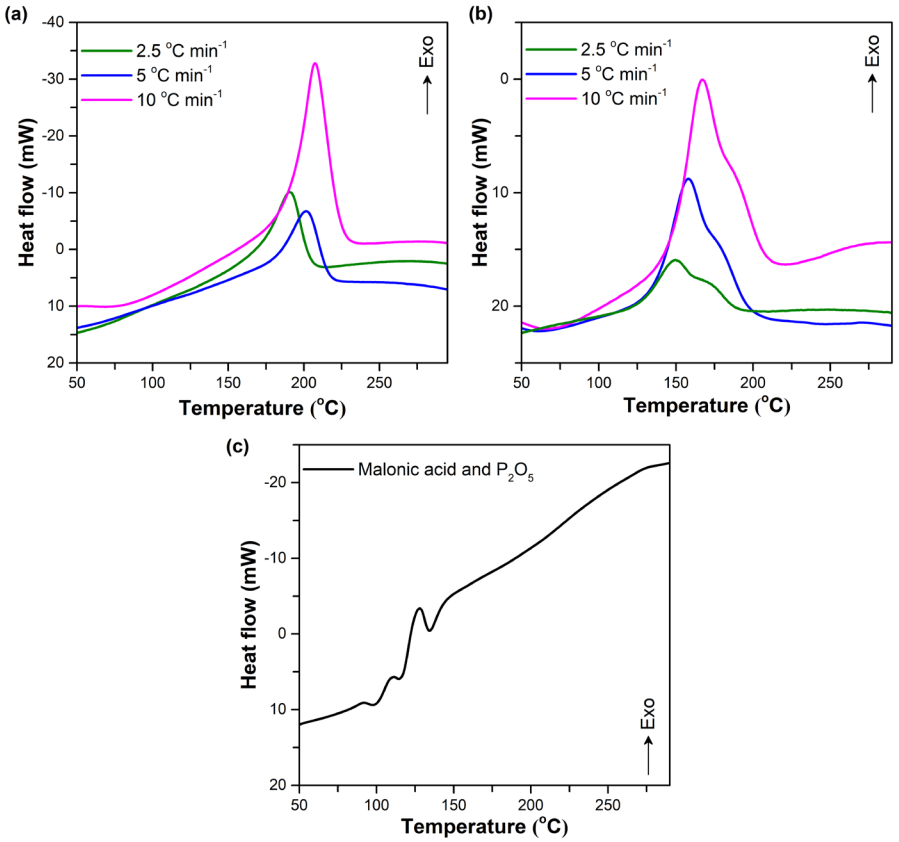

Fig. 11. DSC curves of GO_2 (a), GO_2_MA_P (b) at heating rates of 2.5, 5, and 10 °C min^{-1}, and the mixture of malonic acid and P_2O_5 (c) at the heating rate of 10 °C min^{-1}.

DSC results of GO_2 and GO_2_MA_P are in line with the studies obtained from TG/DTG. The faster heating rates β cause a marked shift in the

peak maxima T_m of decomposition reaction to higher temperatures. As it has been mentioned above, this shift is due to the heat transfer limitations at higher heating rates [101]. At a lower heating rate, the sample comes quickly into equilibrium with the external furnace temperature at any point with an increase in temperature. However, at a faster heating rate, equilibrium reaches slowly, and as such, the curve moves toward the high-temperature region. In addition, in the DSC results presented in Fig. 11 (b) the shoulder in the temperature range of 160–200 °C is observed. We are to assume that this shoulder in the DSC thermograms of GO_2_MA_P could correspond to the decomposition of non-reacted GO_2. We suppose that the amount of C_3O_2 reacted with GO_2 is non-stoichiometric, since some part of gaseous C_3O_2 formed during the reaction between MA and P_2O_5 has not react with GO_2 and has been able to evaporate. Moreover, the amount of used mixture of MA and P_2O_5 is less comparing to the stoichiometric conditions. Thus, we consider that not the whole amount of GO_2 reacts with C_3O_2 and the decomposition of the non-reacted amount of GO_2 occurs in a different manner compared to that of pure GO_2 without additives. The thermodynamic parameter (ΔH) and the temperatures (T_{onset} and T_m) at the peak of the DSC exotherm are summarized in Table 4. The value of T_{onset} specifies the practical start of thermal reduction of GO_2 and it is reported to be in the range of 150–220 °C [64]. Moreover, in this study, a significant shift of T_{onset} to lower temperatures is observed using an additive. The addition of C_3O_2 can reduce the T_{onset} up to 125 °C at the heating rate of 2.5 °C min^{-1}, indicating the decreased reduction temperature of GO_2. Determined ΔH values of pure GO_2 are similar to those reported in [21,102]. An average value of the enthalpy of the GO_2 decomposition is 1487.18 J g^{-1}. In addition, from Table 4, it can be noted that the amount of energy released is reduced using C_3O_2 in the reaction mixture. As a result, the average ΔH of GO_2 is decreased by 303.85 J g^{-1} with an additive of C_3O_2. Furthermore, these results show that heating rate affects the ΔH values and exhibits an important role for ensuring the safe process of thermal reduction of GO_2. The enthalpy increases with increasing the heating rate for pure GO_2 and GO_2_MA_P samples. The enthalpy determined using heating rate range of 2.5 °C min^{-1} and 10 °C min^{-1} varied respectively between 1449.52 J g^{-1} and 1534.12 J g^{-1} for GO and between 1083.47 J g^{-1} and 1296.88 J g^{-1} for GO_2_MA_P. There might be various reasons for this increase. The first hypothesis is related to the instrumental property since the decomposition enthalpies linearly depends on to the heating rate. The heat flow (W) used in DSC is related to sample mass (m), the specific heat (C_p), and the heating rate (β) by equation $W = \beta \cdot m \cdot C_p$ [103]. Increasing the scanning rate during DSC measurements would increase the apparent

intensity of endotherms or exotherms since DSC measures the heat flow as a function of time and temperature [103,104]. A second hypothesis that could clarify the increase of decomposition enthalpy with the heating rate is associated with GO structural changes occurring during thermal decomposition. In different stages of reduction process GO suffers complex restructurings such as endothermic dehydration, the release of CO, CO_2, and other carbon-containing gaseous products, the partial recovery of sp^2-hybridized carbon structure, and the rearrangement of carbon framework, where more complex carbonaceous structures and defects are formed [99,100]. All of these circumstances may vary the enthalpy value recorded during DSC analysis. Furthermore, the DSC curve of the mixture of MA and P_2O_5 presented in Fig. 11 (c) shows that this mixture does not have influence on the DSC of GO_2_MA_P. It could be explained by the positions of the peaks. The DSC peaks of the mixture of malonic acid and P_2O_5 observed in the temperature range of 85–140 °C are not visible in the DSC data of GO_2_MA_P. Furthermore, the amount of the mixture used in the investigation was relatively low that also reduced the possibility of system error during the DSC investigation [105,106].

Table 4. Parameters of DSC peaks and determined values of decomposition enthalpy at the heating rates of 2.5, 5, and 10 °C min^{-1}.

Sample	β (°C min^{-1})	T_{onset} (°C)	T_m (°C)	ΔH (J g^{-1})
GO_2	2.5	166	190	1449.52
	5	173	201	1477.89
	10	186	207	1534.12
GO_2_MA_P	2.5	125	149	1083.47
	5	133	158	1169.65
	10	140	167	1296.88

Further, the Borchardt-Daniels model has been applied with three heating rates (2.5, 5, and 10 °C min^{-1}) for the kinetic parameters (activation energy E_a and reaction order n) evaluation of the thermal decomposition of GO_2 and GO_2_MA_P. The Borchardt-Daniels fitting plots of $\ln(k(T))$ vs. $1/T_m$ and kinetic parameters are shown in Fig. 12 and Table 5, respectively. These results show a positive relationship between heating rate and activation energy. The values of E_a increase with increasing the heating rate for both studied samples. This is because model fitting kinetic method, namely Borchardt-Daniels method, generally involves a single heating rate, and the disadvantage is that activation energy varies with heating rate. This

discrepancy is likely due to the higher thermal lag appeared at the higher heating rate.

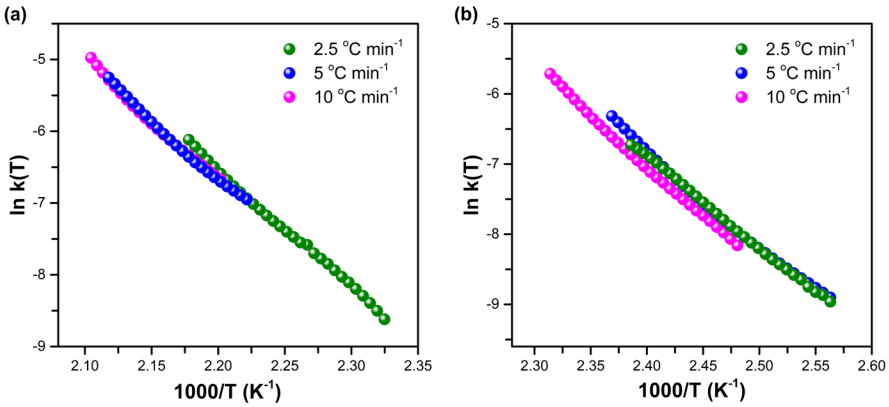

Fig. 12. The E_a determination for GO_2 (a) and GO_2_MA_P (b) using the Borchardt-Daniels approach.

Table 5. Determined values of activation energy for GO_2 and GO_2_MA_P by different kinetic models

	Borchardt-Daniels			Kissinger		Ozawa	
	β (°C min^{-1})	E_a (kJ mol^{-1})	R^2	E_a (kJ mol^{-1})	R^2	E_a (kJ mol^{-1})	R^2
GO_2	2.5	134.9	0.9980	141.5	0.9682	142.1	0.9713
	5	137.8	0.9941				
	10	143.1	0.9931				
GO_2_MA_P	2.5	107.5	0.9991	114.0	0.9999	115.2	0.9999
	5	110.7	0.9948				
	10	115.8	0.9990				

The most significant observation to emerge from the analysis was that, the addition of C_3O_2 to the reaction mixture results in a decrease of E_a by approximately 27 kJ mol^{-1} at all heating rates comparing to that of pure GO_2. Supposedly, it shows that carbon suboxide molecules catalyze the thermal decomposition reaction of GO_2 and increase the reactivity of GO_2. Moreover, it should be noted that pure GO_2 exhibits higher thermal stability than GO_2_MA_P due to the greater value of E_a for GO_2. The apparent reaction order for both GO_2 and GO_2_MA_P is the same (n = 0.7), which is in agreement with the value of GO_2 reported in [64,107] The fractional

value of n demonstrates a complex mechanism of the thermal reduction reaction of both GO_2 and GO_2_MA_P. Also, the value $n = 0.7$ can be assigned to the fact that the extensive release of CO and CO_2 take place directly into the space between the basal planes of graphene. The mechanism of this operation can be designed including consecutive zero-order and first-order stages. The zero-order reaction could occur in the conditions when the energy consumed in the thermal reduction reaction comes through the basal graphene plane. Thus, the reaction rate should be constant and not depend on the reagent concentration (i.e., the concentration of oxygen functionalities). The first-order reaction could originate in the case when the energy is absorbed directly by an oxygen-containing functional group. In this situation the reaction rate linearly depends only on the concentration of the reagent [107]. The same reaction order for GO_2 and GO_2_MA_P reduction reveals the same mechanism for both processes.

To compare the values of activation energy E_a for GO_2 and GO_2_MA_P, the thermal decomposition is studied by other isoconversional (i.e., model-free) kinetic models such as Kissinger and Ozawa. The linear fitting plots of $\ln(\beta/T_m^2)$ vs $1/T_\mathrm{m}$ and $\log(\beta)$ vs $1/T_\mathrm{m}$ are displayed in Fig. 13. The activation energy E_a of GO_2 and GO_2_MA_P can be evaluated as a slope from those displayed fitting plots. By comparing the results presented in Table 5, it is found that the E_a values obtained by both Kissinger and Ozawa method are quite similar. E_a values of GO_2 from Kissinger and Ozawa approaches are estimated to be 141.5 kJ mol^{-1} and 142.1 kJ mol^{-1}, respectively. The difference between both values is 0.6 kJ mol^{-1}, which is acceptable in the error region. The error related to these models depends on the selected baseline to determine the peak temperature. Moreover, observed E_a values of pure GO_2 are similar to those reported previously [64,68,108]. The values of E_a for GO_2_MA_P decomposition are found to be 114.0 kJ mol^{-1} and 115.2 kJ mol^{-1} from Kissinger and Ozawa methods, respectively. Also, it is noticed the same trend that the addition of C_3O_2 decreases the activation energy of GO_2 by approximately 27 kJ mol^{-1} in both methods. Besides, it is observed that the activation energy evaluated by the Borchardt-Daniels' method is slightly different from those calculated by Ozawa and Kissinger's models. According to the literature [109], this variation of activation energy is due to assumptions made in these approaches and the simplicity of Borchardt-Daniels' method. This method is based on a single scan by DSC and it is assumed that the kinetic parameters depend on the heating rate. Nevertheless, it has the benefits of its straightforward and rapid determination of a broad kinetic information. Meanwhile, for the isoconversional methods, it is considered that the kinetic parameters do not

depend on the heating rate, and the observed value of activation energy demonstrates the average value for the overall process.

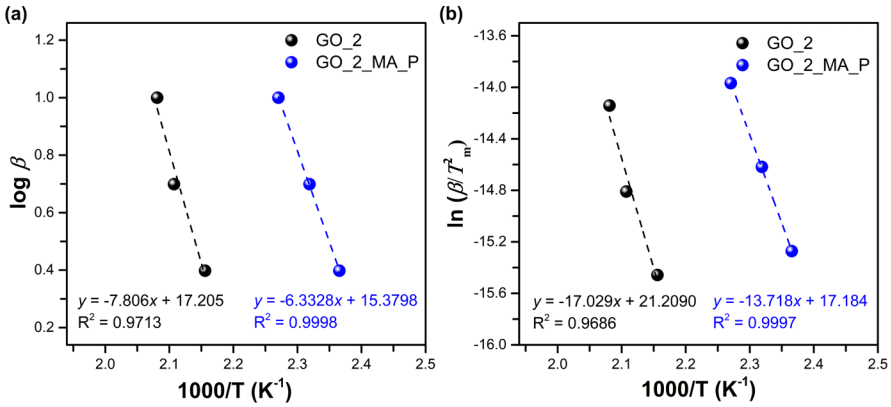

Fig. 13. The E_a determination of GO_2 and GO_2_MA_P using Ozawa (a) and Kissinger methods (b).

GO_2 and GO_2_MA_P samples have been also thermally annealed at 250 °C temperature to investigate the primary structural differences between reduced products with and without C_3O_2. From X-ray diffractograms it has been studied that the use of C_3O_2 in the thermal reduction of GO leads to the more pronounced conversion to graphite structure as evidenced by a sharper and more prominent peak corresponding to the (002) plane. Raman spectra have also confirmed a more effective restoration of π-conjugated system in rGO in the presence of C_3O_2 compared to that of pure rGO due to the shift of G mode and a slight decrease in I_D/I_G ratio. It could be concluded, that a positive impact of C_3O_2 on the structural properties of reduced GO at relative low reduction temperature has been achieved. These results are detailed in our 1st publication.

3.2. Characterization of P-modified rGO

In this section, the impact of the MA and P_2O_5 mixture on the structural and electrical properties of rGO samples annealed at 800 °C temperature have been studied. Consequently, the thermal reduction of two GO samples (such as GO_1 and GO_3) using the different amounts of MA and P_2O_5 has been performed.

The elemental composition of the synthesized GO and rGO samples is presented in Fig. 14 (a, b). As can be seen, GO_1 and GO_3 contain carbon, oxygen, and sulfur atoms. The origin of sulfur is associated with the presence of HSO_4^- and SO_4^{2-} residuals, introduced during the oxidation treatment of pristine graphite. Moreover, the C/O ratio of GO_1 is determined to be 1.66 indicating the higher oxidation degree compared to that of GO_3 (C/O = 1.95). After thermal treatment of GO samples without MA and P_2O_5 additives, only carbon and oxygen elements are identified for rGO_1 and rGO_3 and the ratio of C/O significantly increased up to 11.66 and 8.68 for rGO_1 and rGO_3, respectively. Besides, from Fig. 14 (a, b), it can be noted that the relative concentration of oxygen has been reduced from 33.6 at.% and 37.4 at.% for GO_1 and GO_3, respectively, to 7.9 at.% for rGO_1 and 9.6 at.% for rGO_3, suggesting a partial reduction of the GO samples. On the contrary, the samples obtained after thermal reduction of GO using a mixture of MA and P_2O_5 consist of carbon, oxygen, and phosphorus atoms. The similar tendency of the increasing of C/O values is observed for all rGO samples obtained using additives in the reduction process. The determined C/O values for rGO_1_5, rGO_1_10, rGO_3_5, and rGO_3_10 are 8.68, 7.02, 7.71, and 6.24, respectively. Supposedly, phosphorus functionalities enter the structure of rGO samples due to the formation of H_3PO_4 in the reaction between MA and P_2O_5 (Eqn. 4). As can be seen in Fig. 14 (a, b), the content of phosphorus varies from 0.3 at.% to 2.3 at.%, while the highest content of P (2.3 at.%) is determined in the rGO_3_10 sample. It should be noted that the phosphorus-doping level in this sample is much higher than other previously synthesized phosphorus-doped rGO samples reported in the literature [57–59,110]. Furthermore, the results obtained from the elemental analysis show that the amount of oxygen increases with an increase of the additives content used in the thermal reduction process. In the case of rGO_1 samples, the oxygen contents are 10.3 at.% and 12.3 at.% for rGO_1_5 and rGO_1_10, respectively, while in the case of rGO_3 samples, the oxygen contents are 11.4 at.% and 13.5 at.% for rGO_3_5 and rGO_3_10 samples, respectively. It could be a consequence of introducing oxygen-containing phosphate groups (O–P or O=P) into the graphene structure.

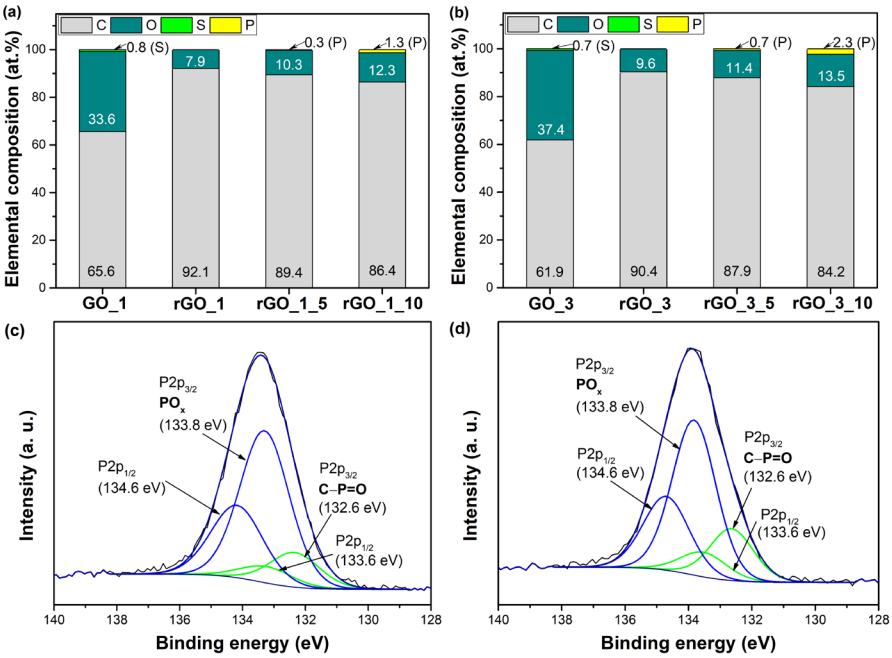

Fig. 14. Elemental composition of GO_1 and thermally reduced samples derived from GO_1 (a), GO_3 and thermally reduced samples derived from GO_3 (b) based on EDX results. The P2p XPS spectra of rGO_1_10 (c) and rGO_3_10 (d) samples.

The P2p XPS spectrum could provide detailed information on the phosphorus-containing functional groups presented on the surface of samples. As only two samples, rGO_1_10 and rGO_3_10, exhibited a higher amount of phosphorus, they were selected for a P2p peak deconvolution analysis, and the results are presented in Fig. 14 (c, d). It can be noted that for both samples, deconvolution of the P2p region presents an inseparable doublet with $P2p_{1/2}$ and $P2p_{3/2}$ components at ΔBE = 0.8 eV and an area ratio of 1:2. A low energy doublet with the energy of the $P2p_{3/2}$ component of 132.6 eV is assigned to the C–P=O bonds. An intense doublet with the $P2p_{3/2}$ component located at approximately 133.8 eV corresponds to the higher oxidation state of phosphorus [111]. Regarding the content of specific phosphorus-containing functionalities in the samples, it can be noticed that the reduction of GO in the presence of the MA and P_2O_5 additive leads to the formation of mainly the higher oxidation state of phosphorus (PO_x), as the relative concentration of these groups in the rGO_3_10 sample is 74.9 at.% and in the case of the rGO_1_10 sample is 81.4 at.%. The content of the C–P=O groups was

considerably lower (25.1 at.% for rGO_3_10 and 18.6 at.% for rGO_1_10). Overall, these results confirm the partial reduction of GO samples and present a new kind of dopant for the successful insertion of phosphorus functionalities in the thermally reduced GO structure.

The behavior of the MA and P_2O_5 additive used to repair the π-conjugated system and defective sites of the graphene network during the annealing process have been evaluated in detail by using Raman spectroscopy analysis. This technique is employed as a non-destructive, high-resolution, and fast tool to investigate the vibrational properties, the lattice structure, purity, defects, doping, and strain of carbon allotropes [112]. The Raman spectra of graphite, GO_1, GO_3, and thermally reduced GO_1 and GO_3 samples are shown in Fig. 15.

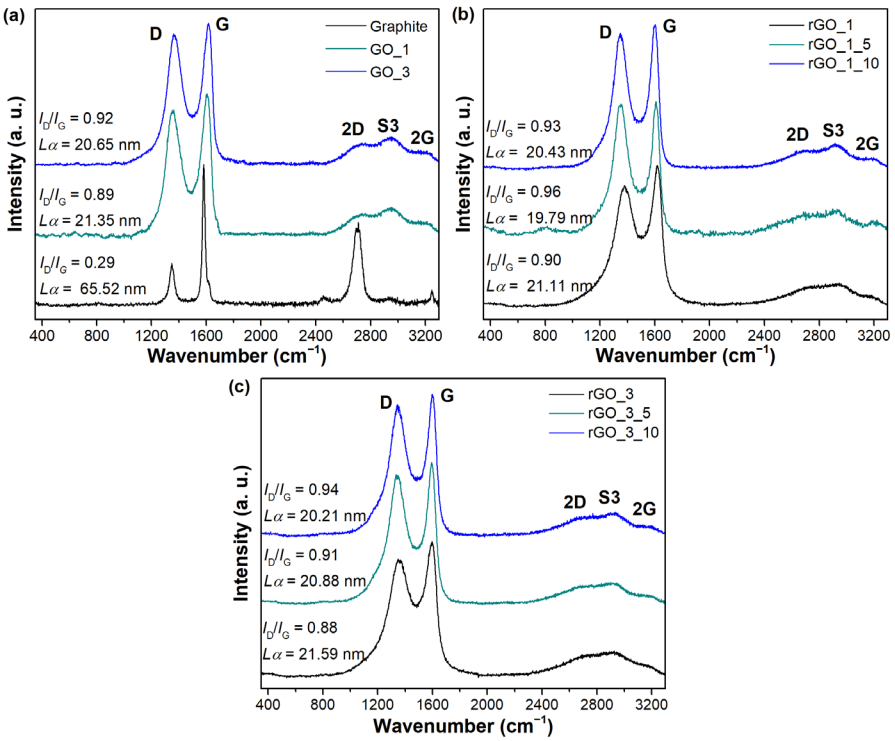

Fig. 15. Raman spectra of graphite, GO_1, and GO_3 (a), thermally reduced samples derived from GO_1 (b), and thermally reduced samples derived from GO_3 (c). The excitation wavelength is 532 nm.

Fig. 15 shows that recorded Raman spectra are similar between all synthesized samples. Each Raman spectrum consists of two dominant peaks

located at ~1360 cm^{-1} and ~1600 cm^{-1}, corresponding to the D and G bands, which are typical modes of graphitic materials, respectively. The D band can be visualized as a breathing vibration of six-membered aromatic rings; defects and various disorders, such as carbon vacancies, grain boundaries, dislocations, sp^3 defects, armchair, or zigzag edges, are required for activation of this mode. The G band is associated with in-plane vibrations of pairs of sp^2-hybridized carbon atoms. This mode is always allowed in Raman spectra.

The intensity ratio of the D and G modes (I_D/I_G) characterizes the degree of structural disorder in graphene-derived material. The number of defects decreases with a decrease in the I_D/I_G value [113,114]. Furthermore, the ratio of I_D/I_G could be used to determine an average crystallite size L_α (Eqn. 6) [98]. The second order bands are observed in the range of 2500–3300 cm^{-1}. The S3 peak located at ~2900 cm^{-1} is an overtone derived from the combination of D and G modes, while the 2G peak at ~3180 cm^{-1} is attributed to an overtone of the G band. The 2D band (also called the G' band) at ~2700 cm^{-1} is a second-order band of the D peak. It is called the 2D band since it involves two of the same phonons responsible for the D band but it does not require the presence of the defects in the structure in contrast with the D band [115]. The value of I_{2D}/I_G (intensities ratio of 2D and G bands) defines the number of graphene layers in the structure. The number of layers increases with an increase of the G band intensity and the decrease of the 2D intensity [116]. In this study, the much higher intensity of the G peak is observed in all Raman spectra of synthesized samples compared to that of the 2D band. This suggests the multilayer structure in all obtained thermally reduced GO products. As can be seen in Fig. 15 (a), the ratio of I_D/I_G is found to be 0.89 and 0.92 for GO_1 and GO_3 samples, respectively. The higher I_D/I_G value for GO_3 indicates that this sample has a more defective structure than GO_1 due to the higher number of sp^3 defects and other disorders generated by the attachment of oxygen-containing functional groups to the graphene layers. Furthermore, the D and G bands in the GO_3 spectrum are shifted to higher wavenumbers compared to that of GO_1, indicating a greater disruption of the conjugated structure after the oxidation process in the GO_3 sample. Meanwhile, Fig. 15 (b, c) indicates that the values of I_D/I_G for rGO samples obtained during thermal reduction of GO with MA and P_2O_5 additives varies from 0.91 to 0.96 and are slightly higher in comparison with those of pure GO. This increase might be due to the removal of functional groups and the high release of gaseous products during thermal reduction that causes disorders in the structure, such as vacancies, dislocations, armchair, and zigzag edges. Furthermore, from Fig. 15 (b, c) it can be noted that the thermal treatment of GO in the presence of additives causes a slightly higher I_D/I_G value than that

of the thermal treatment of GO without additives. The value of the I_D/I_G could rise due to the presence of phosphorus atoms in the structure of the rGO samples, which were effectively introduced during thermal treatment of GO in the presence of the MA and P_2O_5 mixture. These phosphorus atoms could be attached to the graphene layer in the form of C–P–O or C–P=O bonds generating sp^3 defects and, also, may be able to replace carbon atoms creating new point defects in the structure due to the higher atomic radius of P than that of C atoms. Nonetheless, this slight increase of I_D/I_G does not detract from the benefits of the use of carbon suboxide in the thermal reduction of GO since lower values of I_D/I_G are obtained compared to the results investigated by other authors [57,59,116,117]. Furthermore, the values of L_α vary from 19.79 to 21.59 nm between all synthesized samples showing that the crystallite size remains similar during the thermal treatment in the presence and absence of the addition of MA and P_2O_5 mixture.

The morphology of thermally reduced GO samples was studied using SEM analysis at 50,000× magnification (Fig. 16). SEM images of the GO_1 and GO_3 samples (Fig. 16 (a, e)) present a well-ordered layered structure with folds and wrinkles. This is a consequence of the oxidative treatment of graphite by the attachment of oxygen functional groups. After thermal reduction of the pure GO_1 sample (Fig. 16 (b)), the layers agglomerate and form carbon derivatives of about 1 μm in size. The heat treatment of GO_1 with the mixture of MA (5 wt.%) and P_2O_5 (Fig. 16 (c)) leads to irregular stacking of graphene layers with multiple folds. The further increase of additives in the thermal reduction of GO_1 creates a corrugated morphology, as can be seen in Fig. 16 (d). These obtained folded sheets could be related not only to the reduction process but also to the insertion of phosphorus into the rGO_1_5 and rGO_1_10 structures, because the phosphorus atoms form a pyramid-like structure in the graphene sheet due to increased bond length and decreased bond angle. After the reduction of pure GO_3 (Fig. 16 (f)), no agglomerates are observed, but the graphene layers are disrupted into smaller randomly arranged sheets. The rGO_3_10 sample is composed of numerous thin layers that are randomly stacked together, forming a porous network. Furthermore, as can be seen from Fig. 16 (g, h), both reduced GO_3 samples in the presence of additives (rGO_3_5 and rGO_3_10) exhibit nanosheets with folded and crumpled features that could also be attributed to the doping of rGO with phosphorus atoms.

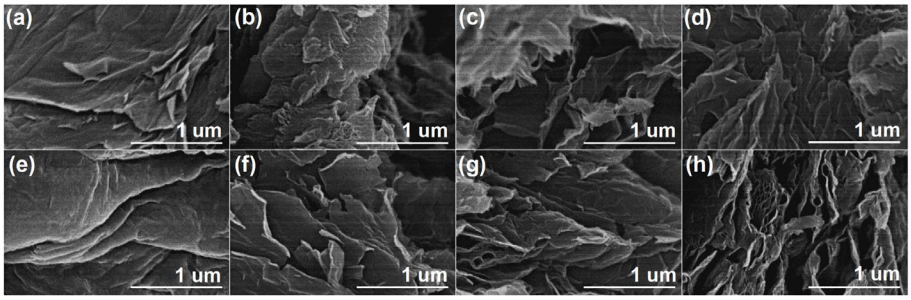

Fig. 16. SEM images of GO_1 (a), rGO_1 (b), rGO_1_5 (c), rGO_1_10 (d), GO_3 (e), rGO_3 (f), rGO_3_5 (g), and rGO_3_10 (h) samples.

Electrical conductivity is one of the key characteristics determining the successful application of rGO in various electrochemical systems such as (bio)sensors, supercapacitors, fuel cells, etc. The electrical behavior of non-metallic powders, including carbonaceous compounds, could be estimated by monitoring the electrical conductivity of bulk materials under compression [118]. Consequently, in this study, the relationship between electrical conductivity (σ_c) on the logarithmic scale and bulk density (ρ_{bulk}) was determined. The results presented in Fig. 17 reveal that the electrical conductivity of prepared carbon materials increases with the increasing of ρ_{bulk} value. This trend is in accordance with the electrical conductivity and resistivity results of graphene, graphite, graphite oxide, carbon black, and carbon nanotubes reported in [118–120]. By compressing a bulk material, closer contact between particles is achieved, leading to higher electrical conductivity because higher electron mobility is ensured in the sample. Following this, the highest electrical conductivity is established with maximum values of bulk density when the most compact arrangement of particles is obtained. The electrical conductivity of pristine graphite is dependent on the compression of the sample as well. From Fig. 17 (a), it can be noted that graphite is a good electrical conductor. Log electrical conductivity varies in the range 1.47–3.53 S m^{-1}, approaching the theoretical values [120]. Besides, the maximum value of ρ_{bulk} for graphite powder is found to be 2.03 g cm^{-3}, which is a similar result to the theoretical value of its density reported in the literature (ρ = 2.26 g cm^{-3}) [121]. Meanwhile, the electrical conductivity of both synthesized GO_1 and GO_3 samples is significantly lower than that of graphite. This decrease is certainly due to the existence of a large number of oxygen-containing functional groups in the backbone of the graphene sheet. Upon oxidation treatment of graphite, its band gap significantly broadens due to the disruption of the sp^2-hybridized carbon

network and the attachment of numerous oxygen-containing functionalities to the surface that inhibit the effective electron transport. Furthermore, higher resistivity is estimated in the case of GO_3, which proves the higher degree of oxidation for GO_3 compared to that of GO_1.

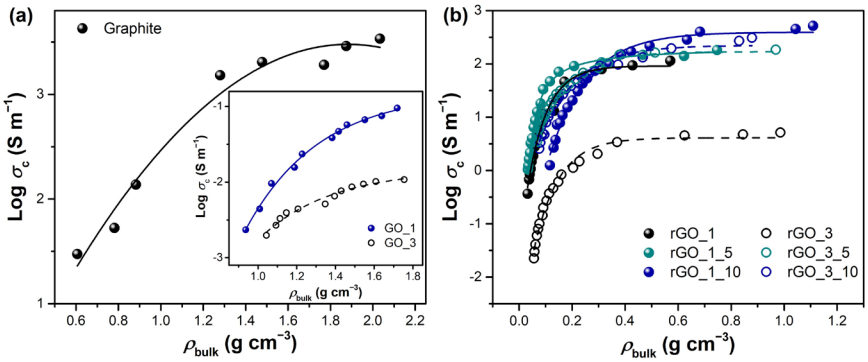

Fig. 17. Electrical conductivity dependence on bulk density for graphite (a) and thermally reduced GO samples (b). The inset in (a) demonstrates the relationship between electrical conductivity and bulk density for GO_1 and GO_3 samples.

Fig. 17 (b) represents the dependence of electrical conductivity on bulk density for thermally reduced GO samples. It should be noted that the bulk density values for all annealed compounds are significantly decreased compared to those of their precursors (GO_1 and GO_3). This drastic change in density indicates the porous structure of products after thermal treatment. The highest bulk density corresponds to the rGO_1_10 sample (ρ_{bulk} = 1.11 g cm^{-3}), while the lowest density value is determined for the rGO_1 product (ρ_{bulk} = 0.57 cm^{-3}). Furthermore, a remarkable enhancement of electrical conductivity is observed after the thermal decomposition process of GO in the presence of the MA and P_2O_5 mixture. The higher the amount of additives used in the thermal reduction reaction, the higher the conductivity achieved. In addition, higher electrical conductivity values in the case of rGO samples are achieved at lower densities than that of graphite. This makes these materials promising in the production of supercapacitor electrodes. Log conductivity (S m^{-1}) appears to be in the range of –0.43–2.05 for rGO_1, 0.01–2.25 for rGO_1_5, 0.09–2.72 for rGO_1_10, –1.65–0.71 for rGO_3, 0.53–2.26 for rGO_3_5, and 0.40–2.48 for rGO_3_10, showing the semi-conductor properties of samples. These electrical conductivity values of rGO

are similar to previous reports found in the literature [119,122]. It should be highlighted that the most obvious advantage of the use of additives is observed in the set of thermally reduced GO_3 samples. As can be seen from Fig. 17 (b), rGO_3 without additives shows the worst conductivity between all reduced products, but the addition of MA and P_2O_5 enhances electrical conductivity extremely in rGO_3_5 and rGO_3_10. These reduced samples exhibit values close to the reduced GO_1 products with additives indicating the achieved effective recovery of π-conjugated system. Moreover, it could be clearly seen that the addition of MA (10 wt.%) and P_2O_5 in the thermal reduction of GO leads to the highest values of electrical conductivity between all reduced samples. This suggests that carbon suboxide used in the thermal reduction reaction of GO could repair the sp^2-hybridized carbon structure and improve electron mobility. However, the presence of phosphorus atoms observed by EDX and Fourier transform infrared spectroscopy (FTIR) analysis (presented in the 2nd publication) could also influence the electrical behavior of the rGO_1_5, rGO_1_10, rGO_3_5, and rGO_3_10 samples because phosphorus atoms are capable of modulating the electronic structure and decreasing the resistivity of graphene-based derivatives. The incorporation of phosphorus species may increase the density of charge carries in the carbon product due to the contribution of phosphorus electrons to the graphene π-conjugated system [123]. Overall, the obtained electrical conductivity data indicate that the thermal reduction of GO with the use of the MA and P_2O_5 mixture has a positive impact on electronic properties of the final products. The relatively high conductivity at low values of bulk density demonstrates the possibility of applying thermally reduced GO samples for metal-free and cheap carbon-based electrode materials.

GO and rGO samples with and without the mixture of MA and P_2O_5 additives have been also investigated by XRD, FTIR, and TEM. These results can be found in our 2nd publication. In summary, the XRD results reveal that MA and P_2O_5 additives are responsible for the recovery of π-conjugation in rGO as the XRD pattern presents peaks corresponding to (002) graphitic-lattice planes, suggesting the formation of the sp^2-like carbon structure. FTIR spectra further supports this due to the presence of C=C bonds and also confirm the formation of O=P and O–P–O bonds in rGO samples treated with MA and P_2O_5. From TEM images, it is determined, that the morphology of rGO samples is multi-layered with corrugations and folds.

3.3. Electrochemical detection of dopamine using P-modified rGO

In this part of dissertation, synthesized thermally reduced GO samples, such as rGO_1_10 and rGO_3_10, exhibiting the highest content of phosphorus and highest electrical conductivity, have been applied as metal-free electrode materials for selective and sensitive electrochemical detection of DA. Initially, the XPS analysis has been performed to investigate C- and P-containing functionalities and specify the P content with the results obtained using EDX. The XPS findings have demonstrated that the phosphorus content in rGO_1_10 and rGO_3_10 amounts to 1.84 at.% and 2.74 at.%, respectively, slightly exceeding values determined by EDX. Subsequently, GCE, GCE/rGO_1_10, and GCE/rGO_3_10 electrodes have been fabricated and tested by CV in the presence and absence of 52 μM DA. CV curves show that GCE/rGO_1_10 and GCE/rGO_3_10 electrodes exhibit enhanced electrocatalytic activity toward the DA redox reactions compared to the bare GCE. These results are comprehensively discussed in our 3rd publication.

Further in this study, the effect of the potential scan rate on the redox reaction of DA has been investigated. The results are presented in Fig. 18. Fig. 18 (a) shows the CV of 52 μM DA on the surface of the GCE/rGO_1_10 electrode at different potential scan rates from 10 to 180 mV s^{-1}. As seen, the anodic and cathodic peak currents of the DA gradually enhance with the increase in the scan rate. Moreover, the E_{pc} is slightly shifted toward lower potential values, while the anodic peak, corresponding to oxidation of DA, is slightly shifted toward higher potential values, which indicates that the electron transfer is a rather slow process than the high scan rates. A minor increase in the separation of cathodic and anodic peak potentials (ΔE_p), suggests a quasi-reversible redox system. The calculated ΔE_p value of GCE/rGO_1_10 at a scan rate of 180 mV s^{-1} is approximately 136 mV. The graphs of the cathodic and anodic peak currents against the scan rate (Fig. 18 (b)) have shown linear relationships in the range of 10 to 120 mV s^{-1}, with regression equations of $I_{pa}(\mu A) = 0.050v + 0.943$ ($R^2 = 0.963$) and $I_{pc}(\mu A) = -0.130v - 1.006$ ($R^2 = 0.986$), which proves that the electrochemical process is a surface adsorption-controlled reaction. Later, at higher scan rates, the relationships became non-linear, suggesting that the mechanism of the redox reaction of DA has been changed, probably because of the transition from reversible to irreversible dependence.

From Fig. 18 (c), it can be seen that the GCE/rGO_3_10 electrode demonstrates the same trend of the increase in anodic and cathodic peak currents with the increasing scan rate as in the case of the rGO/rGO_1_10 modified electrode. Moreover, the plots of the cathodic and anodic peak

currents against the scan rate (Fig. 18 (d)) have linear relationships the entire tested scan rate range, indicating an adsorption-controlled mechanism. The linear equation for GCE/rGO_3_10 is $I_{pa}(\mu A) = 0.0305v + 0.8203$ ($R^2 = 0.973$) and $I_{pc}(\mu A) = -0.0286v - 0.5392$ ($R^2 = 0.976$). Furthermore, as Fig. 18 (c) shows, there is no shift in the position of the redox peaks. The separation of the cathodic and anodic peak potentials (ΔE_p) of the voltammograms is independent of the scan rates, demonstrating the electrochemical reversibility of the process and fast electron transfer.

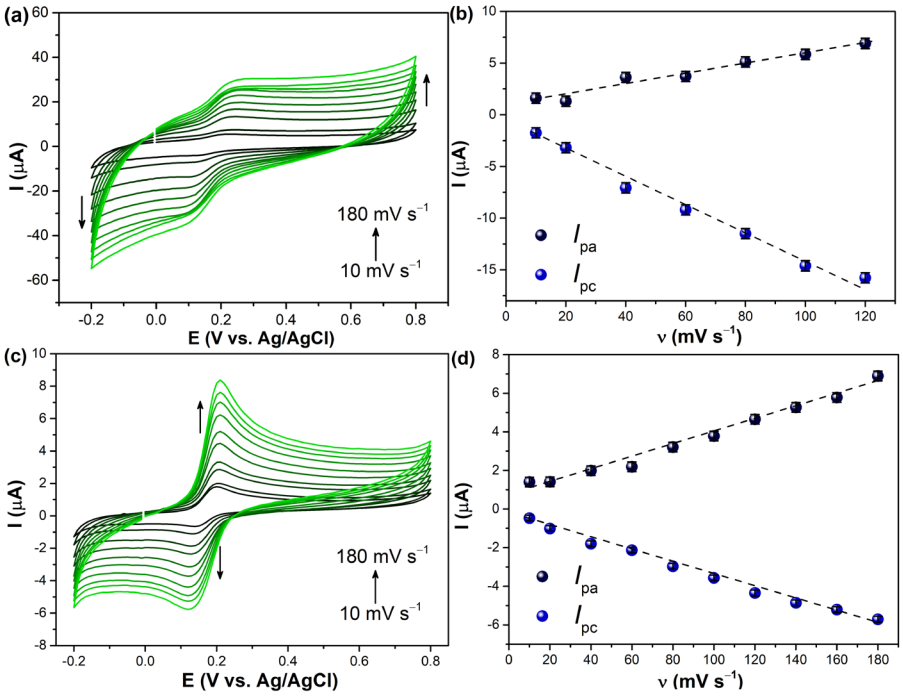

Fig. 18. CV curves at different scan rates and linear variation of anodic and cathodic peak currents vs. scan rates of GCE/rGO_1_10 (a, b) and GCE/rGO_3_10 (c, d). Supporting electrolyte: 0.1 M PB pH = 7.2, c(DA) = 52 μM.

The DPV study has been performed for the quantitative analysis of DA on GCE/rGO_1_10 and GCE/rGO_3_10 modified electrodes because of the higher sensitivity and selectivity than CV [124]. The DPV responses of the prepared GCE/rGO_1_10 and GCE/rGO_3_10 sensors with various concentrations of DA (0–500 μM) are depicted in Fig. 19. From the data shown in Fig. 19 (a), it is apparent that in the case of the GCE/rGO_1_10 sensor, one peak at approximately + 0.19 V is presented and can be attributed

to the oxidation of DA. Also, it must be noted that with the increase in the DA concentration, the peak at +0.19 V gradually increases in a range from 0 μM to 42 μM and reaches a plateau after the addition of a higher amount of DA (Fig. 19 (c)). The linear regression equation is $I_{pc}(\mu A) = 0.1515c(DA) - 0.7021$ ($R^2 = 0.976$). The sensitivity is 2.14 μA μM^{-1} cm^{-2}. The LOD is 0.27 μM based on a 3σ/s. Moreover, at higher concentrations of dopamine (104–500 μM), oxidation peak shifts toward higher potential values (+0.19 V to +0.31 V). One reasonable explanation for this shift can be explained by the adsorption of DA or its by-products on the electrode surface. This might result in an increase in the thickness of a layer, and a higher voltage is acquired for electron transfer [125].

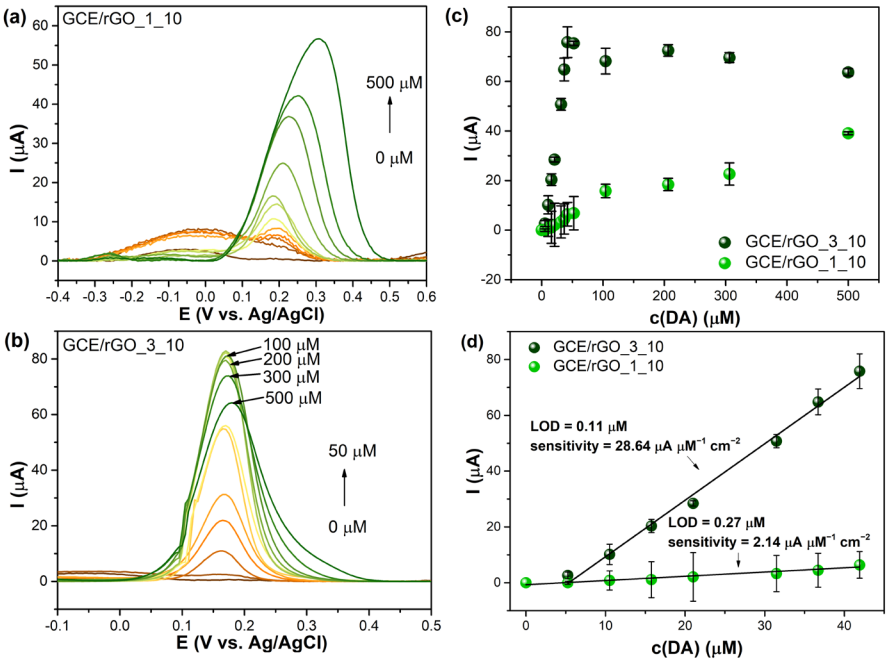

Fig. 19. DPV responses of successive additions of DA into PB solution (pH = 7.2) on GCE/rGO_1_10 (a) and GCE/rGO_3_10 (b). Typical calibration plots corresponding to DA additions (c). Calibration curves in low concentration range (d).

Fig. 19 (b) shows the DPV curves of DA with a variety of different concentrations (from 0 μM to 500 μM) recorded on the GCE/rGO_3_10 sensor. It is clearly visible that the current responses increase with the rise of

the DA concentration in the range of 0 μM to 42 μM. Fig. 19 (d) displays excellent linearity of the calibration curve obtained from the oxidation peak current and at different concentrations of dopamine ranging from 5 μM to 42 μM. The linear regression equation is $I_{pc}(\mu A) = 2.0232c(DA) - 10.876$ ($R^2 = 0.993$). The estimated LOD of DA is 0.11 μM, while the sensitivity is 28.64 μA μM^{-1} cm^{-2}. Whereas, at higher concentrations of DA (from 104 μM to 500 μM), the intensity of the anodic peak decreases and the oxidation peak moves slightly to higher potential values. This shift in potential and decrease in peak current can be explained by the increase in the layer thickness due to the adsorption of DA, its by-products, or impurities on the catalyst surface, and increased blockage of the rGO-based electrode pores and active sites, which are responsible for the electrode kinetics. Similar trends have been reported by Wei Sun et al. in their work on methanol sensors [126].

To sum up, DPV results are in line with CV ones and prove that rGO_1_10 and rGO_3_10 samples are promising electrode materials for DA sensing. However, the determined LOD of DA and sensitivity of GCE/rGO_3_10 are much better than those of GCE/rGO_1_10. The difference in results can be explained by a slightly higher amount of P-containing functional groups on the rGO_3_10 surface. It has been published that a great number of defective / active sites created by doped heteroatoms strongly contribute to improving the sensing performance of modified graphene-based electrodes [33]. Moreover, the proposed GCE/rGO_3_10 electrode possesses a comparable or impressively lower LOD than other previously developed rGO-based sensors [89,127–130]. On the contrary, in comparison to some rGO/metal nanoparticle or rGO/polymer modified electrodes, the GCE/rGO_1_10 electrode exhibits worse analytical characteristics [131,132]. Functionalization of rGO-based electrode materials with various nanomaterials such as metal oxides, quantum dots, and metal nanoparticles effectively improved the analytical performance of sensors. Nonetheless, the development of pure metal-free rGO electrodes for the sensing of neurotransmitters has drawn the most attention in the past few years. The main reason is that rGO/metal nanoparticles or rGO/polymers modified electrodes suffer from numerous disadvantages, e.g. adsorption of the analyte, high-cost, toxicity, environmentally harmful, and complicated surface chemistry.

The selectivity of the GCE/rGO_3_10 electrode has been evaluated using DPV carried out in the presence of UA. According to the literature, the oxidation process of UA occurs at the potential similar to that of DA [133]. As a result, the presence of UA in the electrochemical cell may influence the results of the analysis. Unfortunately, the GCE/rGO_1_10 sensor response for

dopamine has changed chaotically and decreased in the presence of UA (data not shown). Consequently, Fig. 20 shows the DPV responses of the GCE/rGO_3_10 sensor towards DA and UA changing the concentrations of both molecules from 0 µM to 306 µM

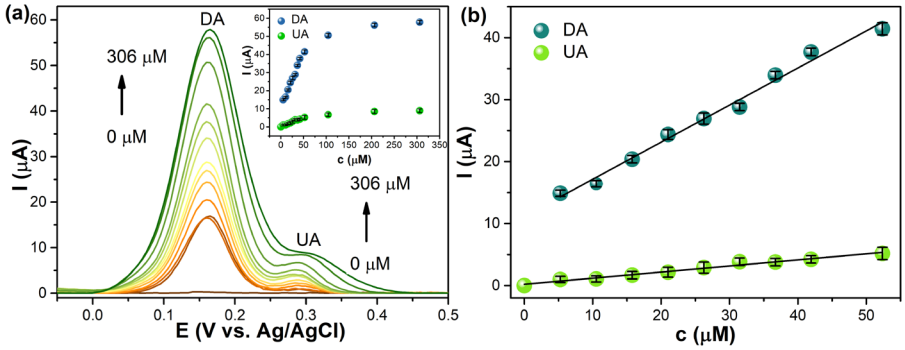

Fig. 20. DPV responses of simultaneous additions of DA and UA into PB solution pH 7.2 on GCE/rGO_3_10 (a); Calibration plot is depicted in inset. Calibration curves in low concentration range (b).

As seen, the oxidation peaks of these two analytes remain well-separated when the concentration is increasing, showing that there is no mutual disturbance for the DA and UA contemporaneously detection. Moreover, even in the presence of higher concentrations of UA, the DA oxidation peak is still well developed. The results of this study indicate that the GCE/rGO_3_10 sensor shows effective detection of DA with good selectivity. Also, the current signals of DA and UA are linearly enhanced with the increase of their concentration in the range of 5–52 µM. The linear regression equations for DA and UA are $I_{DA} = 0.5984c(DA) + 11.167$ ($R^2 = 0.990$) and $I_{UA} = 0.0985c(UA) + 0.2035$ ($R^2 = 0.980$), respectively. Meanwhile, the LODs of simultaneous determination is 0.12 µM and 0.15 µM for DA and UA, respectively. The sensitivity of GCE/rGO_3_10 to DA and UA in the binary mixture is 8.47 µA μM^{-1} cm^{-2} and 1.40 µA μM^{-1} cm^{-2}, respectively. The sensitivity at the GCE/rGO_3_10 modified electrode in the presence of UA (8.47 µA μM^{-1} cm^{-2}) decreases approximately three times from the sensitivity at GCE/rGO_3_10 in the absence of interferant (28.64 µA μM^{-1} cm^{-2}). This indicates that the presence of UA in the same mixture has an effect on the detection of DA. On the other hand, these results suggest that the GCE/rGO_3_10 sensor still possesses acceptable selectivity for the simultaneous determination of DA and UA species.

The long-term stability of the GCE/rGO_3_10 modified electrode has also been investigated. The electrode has been stored dry at room temperature between measurements. Fig. 21 shows the current response obtained after the addition of 21 μM of DA to PB (pH = 7.2). Measurements have been made during 15 days of the electrode storage period. The GCE/rGO_3_10 modified electrode activity has decreased by around 5.27% and 40.24% after 2 days and 3 days of storage, respectively. After 10 days of electrode storage, the current has dropped by 69.66%. Additionally, it is seen that the electrode retained approximately 32% of the original current at the end of two weeks. The loss of activity (~69.66%) during 10 days of storage could be a consequence of poisoning of the electrode surface by adsorbed dopamine or intermediate species on its surface. One more reasonable explanation for this decrease can be attributed to the insufficient adhesion of the active material onto the GCE, and after the consecutive washing of the electrode, the active material could be partially leach from the surface. The relative standard deviation of the oxidation peak currents by three successive measurements is 2.28%. This result revealed a good reproducibility of the GCE/rGO_3_10 modified electrode.

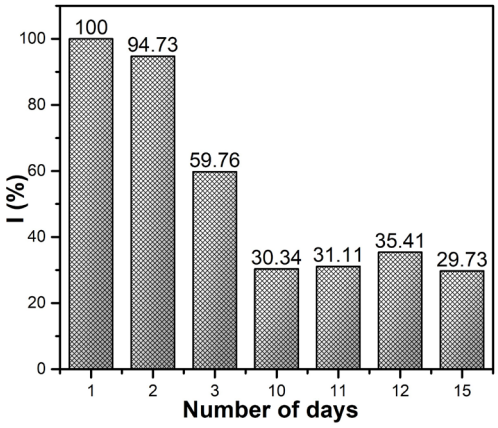

Fig. 21. Stability of the GCE/rGO_3_10 sensor tested over 15 days period.

Electrochemical studies using CV and DPV showed that the rGO_3_10 sample significantly improves the oxidation peak current of DA, demonstrating its higher sensitivity to the determination of DA than that on rGO_1_10.

3.4. Structural characterization of N-modified rGO and its application in electrochemical detection of dopamine

In this PhD thesis, rGO samples modified with nitrogen have been also investigated for electrochemical sensing of DA. In order to prepare N-rGO samples, the one-pot hydrothermal treatment of GO_2 using two different concentrations of the diazo dye Bismarck brown (BB), namely 20 wt.% (rGO_BB20) and 50 wt.% (rGO_BB50), has been carried out. BB has been used as a nitrogen source for the rGO modification for the first time.

XPS analysis has been carried out to examine the chemical nature, composition, and nitrogen-doping configurations of graphene-based materials synthesized. The results of the elemental composition presented in Fig. 22 show that GO_2 contains C (66.4 at.%), O (31.9 at.%), S (0.9 at.%), and N (0.8 at.%) elements. The presence of sulfur and nitrogen in the GO_2 structure could be associated with residual substances such as nitrates and sulphates used in the chemical oxidation of graphite. Hydrothermal treatment of GO_2 results in a notable decrease in oxygen content (from 31.9 at.% for GO_2 to 12.1 at.% for rGO_2), indicating a partial reduction of oxygen-containing functionalities in rGO_2. On the contrary, hydrothermal treatment of GO_2 using BB leads to the simultaneous reduction process as well as the incorporation of N species into the structure of the rGO_BB20 and rGO_BB50 samples. From Fig. 22 it is observed that the content of N-containing functionalities increases in accordance with N-precursor concentration (3.8 at.% for rGO_BB20 and 10.6 at.% for rGO_BB50). The similar N content in the hydrothermally reduced GO samples has also been reported by other authors, revealing the effectiveness of the BB additive as a nitrogen source in modifying rGO.

Although the C/O ratio has increased drastically from 2.08 for GO_2 to 6.5 for rGO_BB20 and 8.1 for rGO_BB50 after hydrothermal treatment in the presence of BB, residual oxygen-containing functional groups still remain in the structure. Nevertheless, the presence of oxygen species might induce the appropriate wettability of the N-rGO material, which is favorable for the suitable accessibility of an electrolyte during the electrochemical measurements. Furthermore, the existence of oxygen-containing functional groups with the negative charge on the N-rGO surface can assist in the attraction of cationic DA molecules, which may have a beneficial impact on the sensor performance [40].

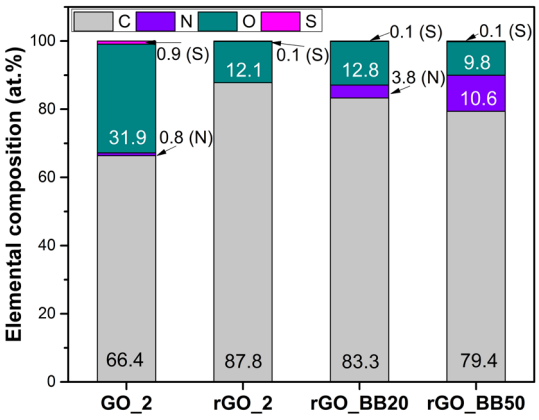

Fig. 22. Surface elemental composition (at.%) for GO_2, rGO_2, rGO_BB20, and rGO_BB50 samples determined by the XPS analysis.

The oxygen and nitrogen-containing functionalities on the surface of graphene derivatives have been studied in detail using the high resolution C1s and N1s XPS spectra. The C1s XPS spectra of prepared samples are provided in our 4th publication. In order to study the structural differences between the rGO_BB20 and rGO_BB50 samples, the N1s XPS spectra have been deconvoluted into five components, as shown in Fig. 23. The assignment of the first component aligns with pyridinic-N (398.0 eV), the second one covers amide-N or pyridone (399.1 eV), when the remaining peaks are attributed to pyrrolic-N (400.5 eV), graphitic-N (402.6 eV), and nitrogen oxides (404.8 eV) [134]. As could be seen from the relative amount of nitrogen bands presented in Fig. 23, in the rGO_BB20 sample nitrogen primarily exists as the pyridinic groups (45.0%), whereas the rGO_BB50 sample demonstrates both pyridinic (40.7%) and amine groups (35.7%) as prevailing nitrogen configurations.

Furthermore, the rGO_BB20 sample exhibits a higher amount of pyrrolic-N (16.1%) and graphitic-N (6.1%) groups compared to those of rGO_BB50. The graphitic nitrogen is doped into the graphitic basal plane and replaces one of the carbon atoms in the six-numbered ring. This kind of bond configuration is able to improve the electrical conductivity in the rGO material as a result of the induced electron transfer rate. The pyrrolic and pyridinic nitrogen are mainly located at the edges of graphene nanosheets, forming five- and six-membered rings, respectively. The presence of these structural defects in the graphene sheet has the potential to improve electron transfer rates in redox reactions and consequently enhance the electrochemical capabilities for DA detection [50].

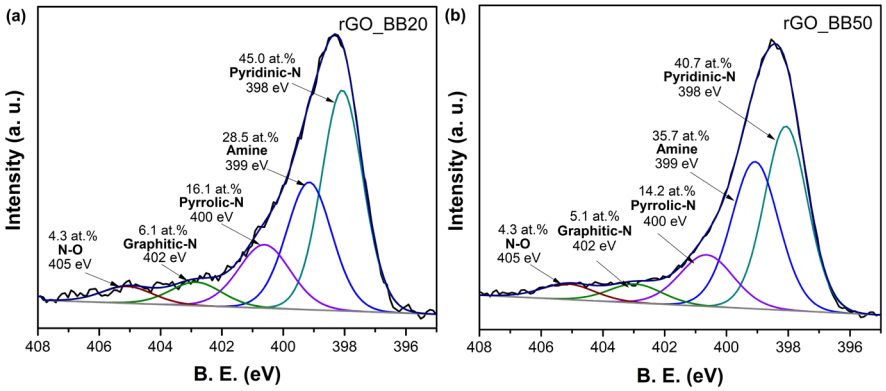

Fig. 23. The N1s XPS spectra for rGO_BB20 (a) and rGO_BB50 (b) samples.

Raman spectroscopy is a highly sensitive technique to identify the microstructure of graphene-based derivatives. Therefore, Raman spectra for graphite, GO_2, and reduced GO_2 samples have been recorded and presented in Fig. 24. Each spectrum exhibits two characteristic peaks located around 1350 cm^{-1} and 1600 cm^{-1}, corresponding to the D and G bands, respectively. The D band is associated with defects (vacancies, edges, sp^3-hybridized carbon, heteroatom doping and functionalities) and the G band represents the in-plane vibrations of the sp^2-hybridized carbon domains [35]. Important quantitative information about the structure of carbon material can be extracted from the analysis of full width at half maximum of G band, FWHM(G) [135–137]. Therefore, the Raman spectra in the frequency range from 1000 cm^{-1} to 1800 cm^{-1} have been fitted by 3–5 Gaussian or Lorentzian-Gaussian form components (Fig. 24). Besides the well-known D and G components (Lorentzian-Gaussian form), an additional Gaussian form bands located at 1275 cm^{-1} (D*) and 1520 cm^{-1} (D") have been introduced [138,139]. The D" band has been previously related with amorphization of carbon material. Fitting the Raman spectra from samples rGO_BB20 and rGO_BB50 has required to introduce additional bands at 1160 and 1166 cm^{-1}, respectively (Fig. 23 (d) and (e)).

The important structural parameter in sp^2-hybridization layered carbon material is an average in-plane crystallite size L_a [136,138]. The experimentally obtained FWHM(G) value can be used to determine the L_a using Eqn. 7 [135,140]. The parameters of G band and estimated L_a values are given in Table 6.

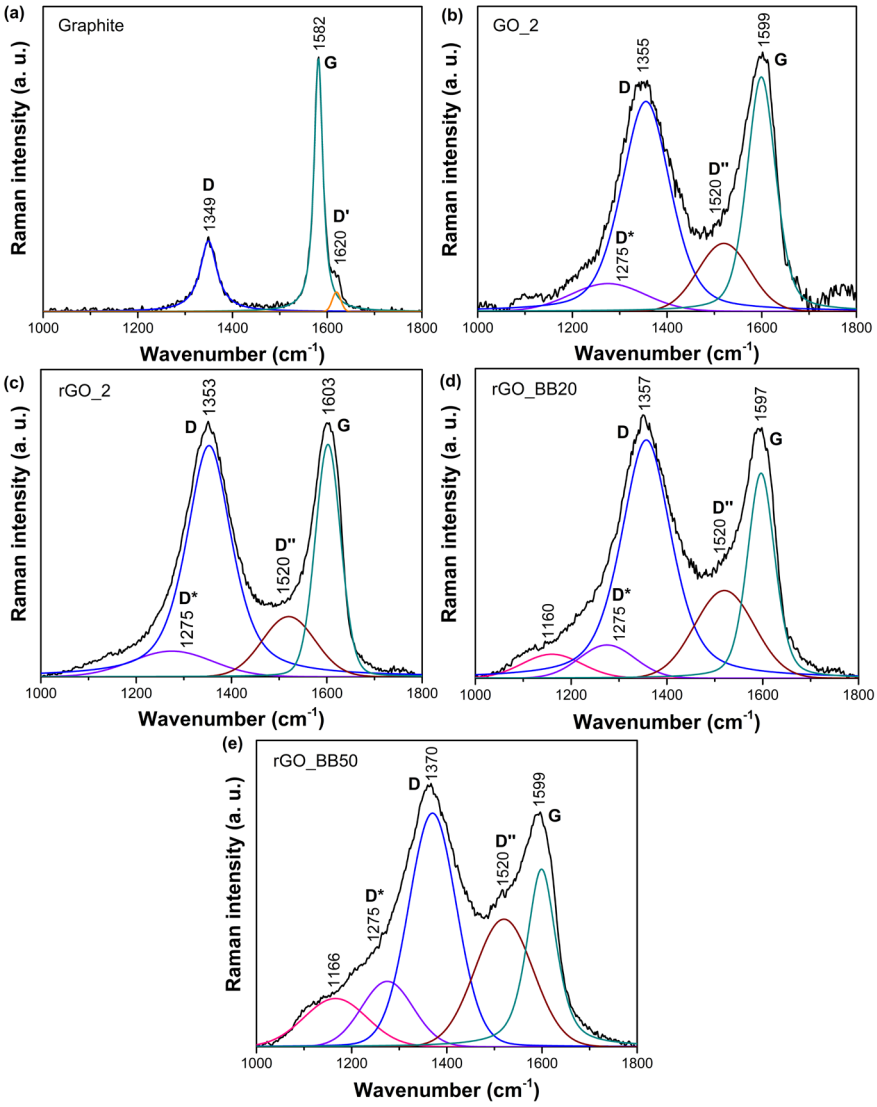

Fig. 24. Raman spectra for graphite with fitted Lorentzian-Gaussian (D and G bands) and Gaussian (D' band) form components (a), GO_2 with fitted Gaussian (D* and D" bands) and Lorentzian-Gaussian (D and G bands) form components (b), rGO_2 with fitted Gaussian (D* and D" bands) and Lorentzian-Gaussian (D and G bands) form component (c), rGO_BB20 with fitted Gaussian (D*, D", and 1160 cm^{-1} bands) and Lorentzian-Gaussian (D and G bands) form components (d), and rGO_BB50 with fitted Gaussian (D*, D", and 1160 cm^{-1} bands) and Lorentzian-Gaussian (D and G bands) form components (e) samples. Excitation wavelength is 532 nm (0.4 mW).

As could be seen in Table 6, after oxidative treatment of pristine graphite, the FWHM(G) value increases significantly from 21.2 cm^{-1} for graphite to 71.4 cm^{-1} for GO_2. Higher values of FWHM(G) mean the higher sp^3 defects as well as reduction in particle size, due to the attachment of an abundance of oxygen-containing groups such as hydroxyl, epoxy, carboxyl, and carbonyl groups. Following the hydrothermal reduction of GO_2, the decrease of the FWHM(G) value from 71.4 cm^{-1} to 62.7 cm^{-1} reflects the partial restoration of the sp^2-hybridization due to the removal of oxygen moieties. The modification with nitrogen results in the further increase of FWHM(G) values to 67.2 cm^{-1} and 72.4 cm^{-1} for rGO_BB20 and rGO_BB50, respectively, indicating the interrupted carbon lattice and induced higher defective degrees due to the incorporation of nitrogen species in the structure. These results are in a good agreement with the studies reported elsewhere [9,141]. Moreover, a slight red shift of the G band (from 1602 cm^{-1} to 1594 cm^{-1}) for both nitrogen-modified rGO samples provides additional evidence for the formation of chemical bonds between C and N in the carbon honeycomb network [142]. Depending on the sample treatment the L_a varies from 8.1 to 43.7 nm. The largest in-plane crystallite size values have been obtained for graphite (43.7 nm). High L_a values are also characteristic for rGO_2 sample (11.0 nm). The intensity ratio I(D")/I(G) can be employed to probe amorphization of studied carbon samples (Table 6). The highest content of amorphous phase has been found in the sample rGO_BB50 (0.72).

Table 6. G-peak full with at half maximum FWHM(G), average crystallite size L_a, and intensity ratio I(D") / I(G) of carbon-based samples.

Sample	FWHM(G) (cm^{-1})	L_a (nm)	I(D") / I(G)
GO_2	71.4	8.3	0.29
rGO_2	62.7	11.0	0.26
Graphite	21.2	43.7	0
rGO_BB20	67.2	9.6	0.43
rGO_BB50	72.4	8.1	0.72

Not only elemental composition but also the surface morphology of materials considerably impacts their application in electrochemical sensing devices, as electrochemical reactions, including adsorption and diffusion, take place specifically on the surface of the electrode. Fig. 25 shows SEM micrographs of the GO_2, rGO_2, rGO_BB20, and rGO_BB50 samples. Fig. 25 (a) represents a typical morphology of GO with irregular, wrinkled layers and multiple folds. After hydrothermal reduction of GO (Fig. 25 (b)),

the resultant material forms a highly porous structure with a wide range of pore sizes. From Fig. 25 (c) and (d) it could be seen that the morphology of N-rGO samples is corrugated due to the presence of foreign nitrogen atoms and is highly dependent on the BB content used during the hydrothermal synthesis. In the case of rGO_BB20, the pores have become larger compared to that of rGO and their consistent formation between the layers is not observed in all areas of the surface. On the contrary, in the presence of 50 wt.% BB graphene nanosheets partially aggregate and form a small number of pores. The restacking of layers could be associated with a high content of nitrogen (10.6 at.%) since the similar trend has been noticed in other studies [143].

The differences in porous nature and surface area between reduced GO_2 samples have been further investigated by BET analysis. Fig. 25 (e) and (f) show N_2 adsorption-desorption isotherms at 77 K and pore distribution curves for the rGO_2, rGO_BB20, and rGO_BB50 samples, respectively. As can be seen in Fig. 25 (e), N_2 adsorption-desorption curves of reduced GO_2 samples can be characterized by IV-type isotherms, according to the classification defined by IUPAC, which is a typical signature of mesopores. The hysteresis loop (H2-type) for rGO_2 indicates the ink-bottle-shaped pores, while hysteresis loops (H3-type) for rGO_BB20 and rGO_BB50 suggest the presence of slit type pores between parallel layers of graphene. The pore distribution curves obtained by the BJH model (Fig. 25 (f)) also confirm the presence of mesopores with predominant pore widths in the range of 2.5–5 nm for all reduced GO_2 samples. The value of the BET surface area (S_{BET}) is determined to be 241 $m^2\ g^{-1}$ for pure rGO_2 which is significantly lower than the theoretical value for fully exfoliated and isolated graphene sheets (2630 $m^2\ g^{-1}$) [144]. After BB-assisted hydrothermal treatment of GO_2, S_{BET} drastically decreases to 52 $m^2\ g^{-1}$ and 29 $m^2\ g^{-1}$ for rGO_BB20 and rGO_BB50, respectively. This drastic reduction in the BET surface area for the nitrogen-modified rGO samples is probably attributed to the inability of N_2 molecules to access the interlamellar space of the samples because of the aggregation of graphene sheets [119]. The divergence in S_{BET} could also be a result of a possible adsorption of the BB dye on the rGO_2 surface or the blocking of some pores between the graphene layers. Despite the low surface area, the rGO_BB20 and rGO_BB50 samples still provide a great advantage for electrochemistry studies due to their mesoporous characteristics.

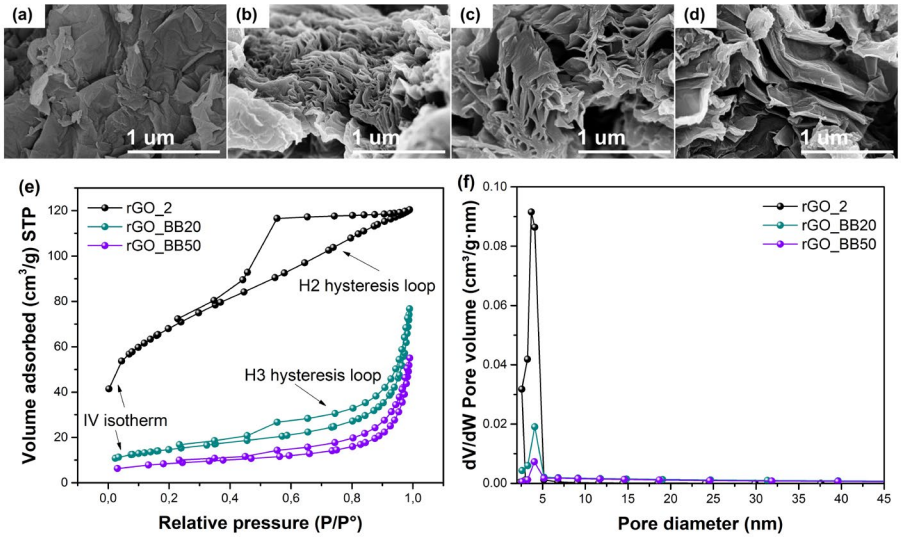

Fig. 25. SEM micrographs for the GO_2 (a), rGO_2 (b), rGO_BB20 (c), and rGO_BB50 (d) samples. N_2 adsorption-desorption curves (e) and pore distribution curves (f) for the rGO_2, rGO_BB20, and rGO_BB50 samples.

The conductive properties of electrode materials are crucial in electrochemical sensing devices. This study assesses the electrical performance of the synthesized materials by observing changes in electrical conductivity during compression. Fig. 26 shows the calculated electrical conductivity against bulk density for GO_2 and reduced GO_2 samples in the presence and absence of BB.

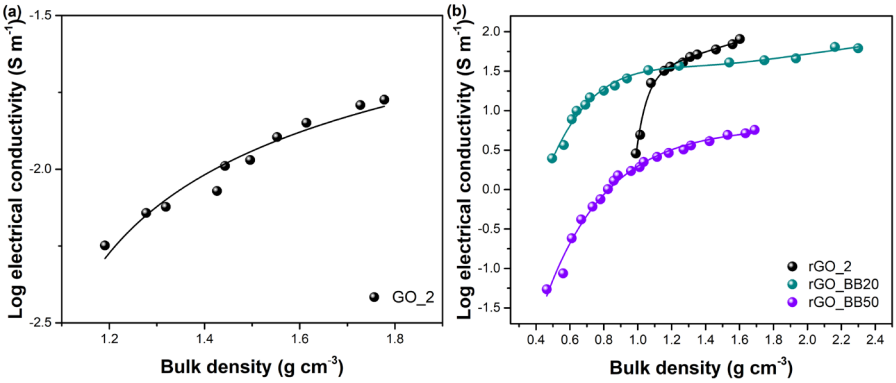

Fig. 26. The relationship between electrical conductivity and bulk density for GO_2 (a) rGO_2, rGO_BB20, and rGO_BB50 (b).

The findings indicate that as bulk densities increase for the carbon-based materials synthesized, there is a corresponding rise in electrical conductivity. When a bulk substance is compressed, the enhanced particle-to-particle contact leads to greater electrical conductivity, as denser samples facilitate electron transfer more effectively [145]. Consequently, the highest electrical conductivity occurs when achieving the most compact arrangement of particles, leading to the peak values in bulk density. A similar trend of the results is observed in studies of other bulk carbon-based derivatives such as carbon foam, reduced GO, carbon nanotubes, and graphene [119,146,147]. From Fig. 26 (a) it could be seen that the determined log conductivity for GO_2 varies from –2.24 to –1.77 S m^{-1}, indicating electrically insulating behavior of GO_2. GO_2 becomes an insulator since the π-conjugated system is interrupted due to the alteration suffered by the hybridization of carbon atoms from sp^2 to sp^3 during the oxidation. The hydrothermal reduction of pure GO_2 leads to the partially recovered π-conjugation that result in an enhanced log electrical conductivity from 0.46 S m^{-1} to 1.91 S m^{-1} with increasing of bulk density. The relationships presented in Fig. 26 (b) also show that rGO_2 samples in the presence of BB exhibit electrical conductivity in the ranges of 0.40 – 1.79 S m^{-1} and –1.26 – 0.76 S m^{-1} for rGO_BB20 and rGO_BB50, respectively. The negligible reduction in conductivity for rGO_BB20 compared to that of unmodified rGO_2 is related to the insertion of pyridinic-N in the basal plane and the creation of disorders in the structure. Although N-doping provides additional energy levels, thus favoring a higher number of electrons for conductivity, it also creates defects throughout the graphene layer, hampering the electron motion [148]. Following this, the most drastic change in conductivity has been established for rGO_BB50 as a result of a highest number of defects due to the nitrogen insertion in the structure as well as a relatively low concentration of graphitic-N species.

Structural and morphological studies have shown that the nitrogen-modified rGO materials prepared in this study exhibit appropriate and promising characteristics for their successful application in the electrochemical sensing of DA. The impact of the scan rate (v) on the electrochemical behavior of the N-modified electrodes toward DA detection has been analyzed, and the results obtained are shown in Fig. 27.

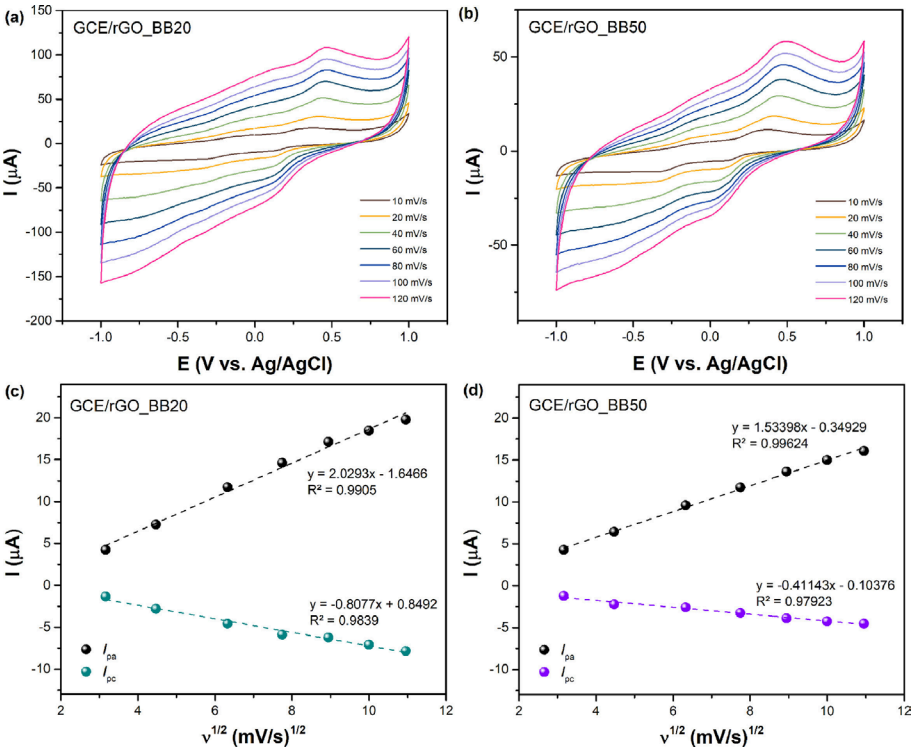

Fig. 27. CV curves at different scan rates and linear variation of anodic and cathodic peak currents vs. square root of scan rate for GCE/rGO_BB20 (a, c) and GCE/rGO_BB50 (c, d) in 0.1 M PB (pH = 7.0) with 99 μM dopamine.

Fig. 27 (a, b) present CV curves at different scanning rates from 10 to 120 mV s^{-1} with 99 μM DA for both N-modified GCE. It is determined that all anodic and cathodic peaks show the enhancement in current response in correspondence of increasing scanning rate, implying a high charge transfer occurred between the redox reaction centers and the surface of the N-modified electrodes. As the scan rate rises, the anodic current increases alongside a slight shift in the peak potential toward the positive side. Simultaneously, the cathodic current rises with a slight shift in the peak potential toward the negative side, indicating a deceleration in the charge transfer process due to the increased scanning rate [149].

For a more circumstantial comprehension of the process controlling the electrochemical reaction, the current dependence on the scanning rate (not shown) and the square root of scanning rate has been plotted (Fig. 27 (c, d)). It demonstrates the linear dependence was obtained only in the case of the square root of the scanning rate in the range of 10–120 mV s^{-1} with linear

regression equations of $I_{pa}(\mu A) = 2.0293v - 1.6466$ ($R^2 = 0.9905$) and $I_{pc}(\mu A) = -0.8077v + 0.8492$ ($R^2 = 0.9839$) for GCE/rGO_BB20, as well as $I_{pa}(\mu A) = 1.471v + 0.024$ ($R^2 = 0.9965$) and $I_{pc} = -0.3901\nu - 0.2276$ ($R^2 = 0.9874$) for GCE/rGO_BB50. These results suggest that the kinetics of the electrochemical reactions on the GCE/rGO_BB20 and GCE/rGO_BB50 electrodes is a diffusion-controlled process. The electrochemically active surface area (ECSA) of the N-modified electrodes has been determined by the linear regression curves derived from the Randles-Sevcik equation [150]. The electroactive area is found to be 0.3092 cm^2 and 0.2336 cm^2 for GCE/rGO_BB20 and GCE/rGO_BB50, respectively, which was larger than the geometric area in four and three times. ECSA is correlated with the results of the BET surface area, since the higher value of surface area has been determined for the sample with a lower content of nitrogen.

The analytic performance of the GCE/rGO_BB20 and GCE/rGO_BB50 electrodes has been further examined using chronoamperometry. This involved successive additions of DA to the 0.1 M PB solution under an applied potential of +0.3 V. This optimal potential has been determined through chronoamperometry measurements conducted at various applied potentials (data not shown). As presented in Fig. 28 (a), the anodic current progressively increases with the addition of DA and reaches stability within a few seconds using both N-modified electrodes. Nevertheless, much higher current responses are recorded for GCE/rGO_BB20, confirming its suitability for the determination of DA compared to that of GCE/rGO_BB50. Two linear calibration curves corresponding to the lower and higher concentration regions could be obtained for both proposed modified electrodes, as presented in Fig. 28 (c, d). In the lower concentration range (0–15 μM), GCE/rGO_BB20 and GCE/rGO_BB50 exhibit linear regression equations, which could be represented as $I(\mu A) = 0.04264c(DA) + 0.00216$ ($R^2 = 0.998$) and $I(\mu A) = 0.02795c(DA) - 0.01823$ ($R^2 = 0.986$), respectively. In the linear range of 0–15 μM, LOD is estimated to be 45 nM with a sensitivity of 0.61 μA μM^{-1} cm^{-2} for GCE/rGO_BB20 and 149 nM with a sensitivity of 0.39 μA μM^{-1} cm^{-2} for GCE/rGO_BB50.

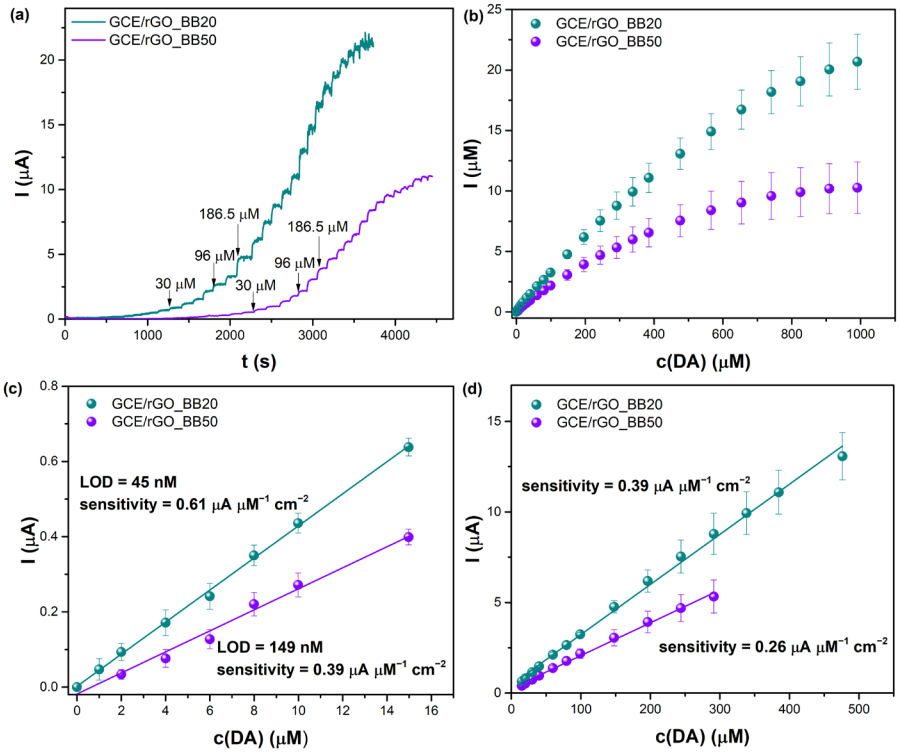

Fig. 28. Chronoamperograms (a) and calibration curves in different concentration ranges (b, c, d) for GCE/rGO_BB20 and GCE/rGO_BB50 in 0.1 M PB (pH = 7.0). The applied potential of +0.3 V, 300 rpm.

Fig. 28 (b, d) distinctly illustrates that GCE/rGO_BB20 possesses a much wider linear detection range (15–476 μM), compared to that of the GCE/rGO_BB50 electrode (15–291 μM) and N-rGO-based sensors reported elsewhere [9,92,151]. The calibration plot in *c*(DA) = 15–476 μM follows the equation of $I(\mu A) = 0.02767c(DA) + 0.46357$ ($R^2 = 0.996$) with a sensitivity of 0.39 μA μM^{-1} cm^{-2} for GCE/rGO_BB20. In the range of 15–291 μM, GCE/rGO_BB50 exhibits $I(\mu A) = 0.01813c(DA) + 0.25497$ ($R^2 = 0.995$) with a sensitivity = 0.26 μA μM^{-1} cm^{-2}. All these observations show that the electrode modified with rGO_BB20 exhibits higher sensitivity and a lower limit of detection compared to those of GCE/rGO_BB50. Several reasons for the better sensing performances of GCE/rGO_BB20 can be distinguished. First, the higher surface area and ECSA for the GCE/rGO_BB20 electrode increases the adsorption capacities toward DA. Second, the higher electrical conductivity ensures a higher charge transfer between the redox reaction center and the electrode's surface. Third, the GCE/rGO_BB20 electrode

demonstrates the highest sensitivity, since the protonated groups in DA molecules are more attracted to the surface of the electrode as a result of the larger concentration of electronegative oxygen-containing functional groups. One more reasonable explanation for the enhanced electrochemical response at the GCE/rGO_BB20 sensor could be attributed to the elevated content of graphitic-N groups on its surface.

As reported in the literature, the increased nucleophilicity of the carbon atom neighboring graphitic-N in a material brings forth several advantages for electrochemical sensing [152]. This phenomenon fosters increased adsorption of analyte molecules on the electrode surface, enhances electrical conductivity, and consequently results in superior electrochemical activity, thereby improving sensing performance. Comparing the existing N-rGO sensors with and without metal particles, the rGO_BB20-modified sensor also exhibits preferable analytical characteristics in terms of LOD and linear range than non-metal electrodes (GCE/NG [92], GCE/N-rGO-Ur [151], GCE/N-rGO-180-8/NH_3 [40], and GCE/N-rGO/polyethylenimine [153]) or even metal-assisted materials (GCE/N-rGO-Au [154], GCE/N-RGO/MnO [155], and GCE/Fe_2O_3/N-rGO [156]). Our results represent a notable improvement in the electrochemical performance since sensors with high sensitivity usually operate within an especially restricted linear range, while GCE/rGO_BB20 presented in this report possesses two linear ranges of 0–15 μM and 15–476 μM with a detection limit of 45 nM. Therefore, the results achieved suggest promising applications of GCE/rGO_BB20 to detect DA in a wider linear concentration range that is important in the medicine and food industry.

Determining the interference of different compounds at identical oxidation potentials is a key aspect in assessing selectivity. In this study, the selectivity of the prepared GCE/rGO_BB20 and GCE/rGO_BB50 electrodes toward DA has been investigated by recording the chronamperometric current response of DA with various interfering molecules such as AA, CA, H_2O_2, and UA. The results obtained are depicted in Fig. 29. As illustrated in Fig. 28, the well-defined chronamperometric responses using both modified electrodes have been recorded only with the additions of 0.05 mM DA, while no significant changes in current have been observed in the presence of 0.05 mM AA, 0.05 mM CA, 0.05 mM H_2O_2, and 0.05 mM UA at regular intervals at the working potential of +0.3 V. It indicates that GCE/rGO_BB20 and GCE/rGO_BB50 exhibit outstanding selectivity and anti-interference property for the DA detection. The strong electrostatic attraction between DA and N-rGO materials, which causes more DA molecules to absorb on the surface of the sensor, results in an amplified and specific response of DA,

which may be the most possible cause of the selective detection of DA. Additionally, Nafion is a cation-exchanger polymer which could increase the selectivity of DA by deflecting electronegative AA, CA, and UA away from the sensor [156].

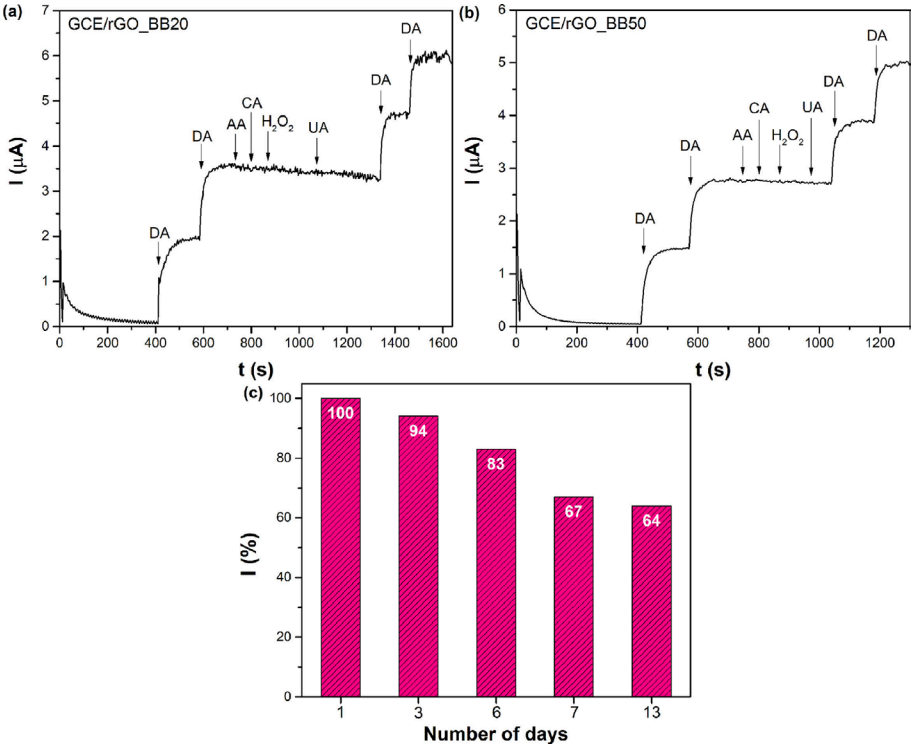

Fig. 29. Interference of 0.05 mM AA, 0.05 mM CA, 0.05 mM H_2O_2, and 0.05 mM UA on the response of 0.05 mM DA in 0.1 M PB solution at +0.3 V for GCE/rGO_BB20 (a) and GCE/rGO_BB50 (b). Stability of GCE/rGO_BB20 tested over the 13 days of electrode storage period (c).

Finally, the stability of the GCE/rGO_BB20 sensor has been explored by assessing the current response following the introduction of 30 μM DA into the PB solution (pH = 7.0) over a 13-day period. The sensor has been kept in the air at room temperature during the intervals between measurements. As seen in Fig. 29 (c), the peak current remains at 94% of its initial current response after 3 days of measurements, showing a slight decrease in electrochemical activity. Although the sensing performance of the proposed sensor further decreases by 17%, 33%, and 36% after 6, 7, and 13 days, respectively, the active sites are still exposed for the detection of DA. The

decline in observed activity during measurements might be due to the active electrode sites getting blocked by adsorbed analytes or intermediate substances on their surface. Additionally, this reduction is likely a result of the active material being washed away from the GCE surface during electrode cleaning. Nevertheless, these results confirm that the GCE/rGO_BB20 electrode demonstrates great stability in the detection of DA over a period of six days, which would be extended in changing polymers used for rGO_BB20 immobilization on the electrode surface.

CONCLUSIONS

1. The kinetics of GO thermal reduction with and without carbon suboxide has been thoroughly evaluated using Borchardt-Daniels, Ozawa, and Kissinger models. The results of kinetics indicate that the use of carbon suboxide in the thermal reduction of GO changes the thermal stability of GO and lowers its reduction temperature up to 125 °C. This additive also causes a decrease in the enthalpy and activation energy, but does not influence the reaction order. This reveals the complex mechanism of GO thermal decomposition that consists of simultaneous zero-order and first-order stages. Furthermore, it has been determined that parameters such as E_a and ΔH of the GO thermal reduction reaction depend on the heating rate.

2. The structural and electrical properties of the rGO samples depend on the amount of MA and P_2O_5 additive used and the type of GO. The use of the mixture of MA and P_2O_5 in thermal reduction of GO leads to the incorporation of a relatively high content of phosphorus (0.3–2.3 at.% determined by EDX) in rGO. The results of Raman spectroscopy and electrical conductivity show that the best recovery of sp^2 hybridized carbon system is achieved, using the mixture which has 10 wt.% of MA and GO prepared by the traditional Hummers' method (the sample named as rGO_1_10).

3. Phosphorus-modified rGO samples, prepared by the thermal reduction of GO in the presence of MA and P_2O_5, show prospective electrochemical activity in detecting dopamine. The better electrochemical performance toward dopamine has been achieved, using the GCE/rGO_3_10 electrode, compared to that of GCE/rGO_1_10. From the DPV studies, it is determined that the GCE/rGO_3_10 modified electrode shows a fairly wide linear range (5–42 μM), low LOD value (0.11 μM) and high sensitivity (28.64 μA μM^{-1} cm^{-2}) toward detection of DA. Moreover, it is observed that the presence of UA in the electrochemical cell causes a slightly lower sensor response for DA. Nonetheless, the proposed GCE/rGO_3_10 modified electrode still possesses acceptable selectivity and is capable of detecting DA simultaneously. Simultaneous LOD (0.12 μM) and sensitivity (8.47 μA μM^{-1} cm^{-2}) are obtained for DA, while for UA the corresponding values are 0.15 μM and 1.40 μA μM^{-1} cm^{-2}, respectively. Our proposed sensors exhibit preferable analytical characteristics in terms of LOD and sensitivity compared to previously reported non-metal or even metal-assisted rGO materials.

4. Nitrogen-modified rGO samples have been prepared by a facile hydrothermal treatment of GO using the Bismarck brown additive as a nitrogen source. Quantitative XPS analysis shows the successful incorporation of nitrogen-containing functional groups into the structure of graphene-based material, as evidenced by an increase in the nitrogen content in rGO_BB20 (3.8 at.%) and rGO_BB50 (10.6 at.%). Notably, the rGO_BB20 sample exhibits a higher concentration of pyrrolic-N (16.1 at.%) and graphitic-N (6.1 at.%) groups compared to rGO_BB50. Raman spectroscopy analysis reveals that the sample rGO_BB50 exhibits the highest content of amorphous phase and an increased number of defects. Electrical conductivity measurements demonstrate that the pure rGO sample exhibits the highest electrical conductivity among both N-rGO samples. The slight decrease in conductivity for rGO_BB20 and rGO_BB50 compared to unmodified rGO can be attributed to the higher structural disorders in the basal plane.

5. Electrochemical measurements have revealed that both GCE modified with rGO_BB20 and rGO_BB50 possess outstanding selectivity towards the detection of DA in the presence of AA, UA, CA and H_2O_2. However, compared to the GCE/rGO_BB50 sensor, the proposed GCE/rGO_BB20 sensor exhibits superior electrochemical performance in terms of DA sensing as it shows a low value of LOD (45 nM) and a high sensitivity (0.61 μA μM^{-1} cm^{-2}) in a linear detection range (0–15 μM), and the sensitivity of 0.39 μA μM^{-1} cm^{-2} in the wide linear detection range of 15–476 μM. Considering the facile preparation route and excellent experimental results, rGO_BB20 may be used as an alternative metal-free electrode material in the construction of a sensing platform for the determination of DA. This sensor shows improved analytical performance, offering a lower LOD and a wider linear range compared to earlier reported N-doped graphene-based sensors.

SUMMARY IN LITHUANIAN / SANTRAUKA

ĮVADAS

Nuo tada, kai 2010 m. A. Geimui ir K. Novoselovui buvo skirta Nobelio fizikos premija už novatorišką grafeno atradimą, ši anglinė medžiaga susilaukė ypatingo dėmesio plačioje mokslo bendruomenėje [1]. Grafenas dėl unikalios dvimatės heksagoninės struktūros pasižymi išskirtinėmis fizikinėmis, cheminėmis ir termomechaninėmis savybėmis, kurios leidžia kurti perspektyvias naujos kartos medžiagas, energetikos technologijas, biomedicinos įrankius, aplinkos apsaugos priemones ir elektronikos prietaisus. Grafeno atradimas taip pat reikšmingai sustiprino pasaulinį susidomėjimą kitais grafeno dariniais, paspartinant jų gilesnį inovatyvių gamybos metodų, modifikacijų ir įvairių taikymo sričių tyrinėjimą [2,3].

Pastaruoju metu grafeniniai dariniai, tokie kaip grafeno oksidas (GO) ir redukuotas grafeno oksidas (rGO), yra perspektyvios elektrodinės medžiagos ir rodo išskirtinį potencialą, kuriant elektrocheminius jutiklius. Tai siejama su jų ilgalaikiu stabilumu, biologiniu suderinamumu, hidrofiliškumu, sintezės ekonomiškumu ir ekologiškumu [4]. Dėl paviršiaus funkcinių grupių trūkumo, hidrofobiškumo ir nulinės draustinės juostos vertės gryno grafeno efektyvus elektrocheminis veikimas jutikliuose yra ribotas [5]. Tačiau heteroatomų (N, P, S arba B) įterpimas į grafeno ir rGO struktūrą leidžia tiksliai kontroliuoti jų elektronines, paviršiaus chemines ir tekstūrines savybes, taip sukuriant naujas elektrokatalitiškai aktyvias vietas. Tokia modifikacija žymiai pagerina krūvio pernašą elektrodo ir elektrolito tarpfazinėje riboje, todėl pagerėja jutiklio jautris [6,7]. Heteroatomais modifikuoto rGO pagrindu sukurti elektrodai buvo sėkmingai pritaikyti gliukozės, šlapimo rūgšties (UA), askorbo rūgšties (AA), H_2O_2, nitritų, serotonino ir hidrazino elektrocheminiam aptikimui [8–13].

Nepaisant pasaulinio dėmesio, grafeninių jutiklių sritis tebėra ankstyvojoje vystymosi stadijoje ir susiduria su keliais svarbiais iššūkiais, kuriuos reikia išspręsti. Dauguma iš jų yra susiję su jutiklio sandara. Paprastai, siekiant užtikrinti puikias jutiklio savybes, grafeniniai elektrocheminiai jutikliai yra tobulinami įvedant įvairias nanomedžiagas, tokias kaip tauriųjų ir pereinamųjų metalų nanodaleles (Au, Pd) arba jų oksidus (MnO, NiO, CoO, Fe_2O_3 ir ZnO) [1]. Vis dėlto metalo nanodalelių tvarų naudojimą kartu su grafeno dariniais riboja aukšta jų sintezės kaina, sudėtinga paviršiaus chemija, aglomeracija ir galimas toksinis poveikis. Kita vertus, esami bemetaliai grafeniniai jutikliai vis dar pasižymi mažu jautriu, ribotu selektyvumu, nepakankama analitės aptikimo riba (LOD), siauru tiesiniu analitės

koncentracijos intervalu ir uždelstu atsako laiku [14]. Todėl, siekiant išspręsti šias problemas, reikia skirti daugiau pastangų bemetalių grafeninių medžiagų pigios ir našios sintezės bei modifikacijos metodikų tyrimui ir tobulinimui. Funkcionalizuojant grafenines medžiagas heteroatomais galima optimizuoti struktūrines charakteristikas taip, kad būtų pasiekti geresni jutiklio parametrai, įskaitant žemą LOD vertę, platų tiesinį analitės koncentracijos intervalą, didelį jautrį, geresnį atkuriamumą, selektyvumą, atsikartojamumą ir stabilumą, net ir naudojant bemetalius elektrodus. Todėl šioje disertacijoje daug dėmesio skiriama naujų grafeninių junginių modifikavimo metodų tyrinėjimui, terminių, cheminių, elektrinių, struktūrinių ir elektrocheminių savybių analizei, siekiant sukurti ekonomiškai efektyvias, universalias ir pasižyminčias aukštu elektrocheminiu aktyvumu elektrodines medžiagas dopamino (DA) nustatymui. Dopaminas – tai hormonas ir neurotransmiteris, kuris atlieka svarbų vaidmenį organizmo judesių koordinavime, nuotaikos reguliavime, dėmesio valdyme bei kitose neurologinėse funkcijose. Normali DA pusiausvyra organizme yra gyvybiškai svarbi ne tik fizinei, bet ir psichologinei gerovei. Bet kokie DA koncentracijos nukrypimai nuo normos kraujyje gali sukelti nervų sistemos sutrikimus, tokius kaip senatvinė demencija, šizofrenija, dėmesio deficito hiperaktyvumo sindromas, Parkinsono ir Alzheimerio ligos [4,15]. Todėl tikslus, jautrus ir greitas DA nustatymas yra labai svarbus ankstyvai šių sutrikimų diagnozei ir gydymui.

DISERTACIJOS TIKSLAS IR UŽDAVINIAI

Šios disertacijos tikslas – susintetinti įvairias grafenines medžiagas, modifikuoti jų struktūrą heteroatomais ir ištirti funkcinių grupių įtaką paruoštų bandinių savybėms ir elektrocheminiam aktyvumui nustatant dopaminą. Šiam tikslui įgyvendinti buvo iškelti tokie uždaviniai:

1. Susintetinti GO, ištirti jo termines savybes ir taikant Borchardt-Daniels, Kissinger ir Ozawa modelius nustatyti terminės redukcijos reakcijos kinetinius parametrus, nesant ir esant anglies suboksidui;
2. Paruošti P- ir N- modifikuotus rGO bandinius, termiškai ir hidrotermiškai redukuojant GO su malono rūgšties / P_2O_5 ir organinio dažo Bismarko rudojo priedais;
3. Įvairiais spektroskopiniais, elektriniais ir mikroskopiniais metodais įvertinti paruoštų grafeninių medžiagų struktūrinių ir elektrinių savybių pokyčius;
4. Suformuoti ir elektrochemiškai ištirti naujus, bemetalius N- ir P-modifikuotų rGO bandinių elektrocheminius jutiklius, skirtus dopamino aptikimui modelinėse sistemose.

DISERTACIJOS ORIGINALUMAS, NAUJUMAS IR SVARBA

Pirmą kartą malono rūgšties (MA) ir P_2O_5 mišinys buvo panaudotas GO terminio skilimo procese. Šis novatoriškas metodas yra pagrįstas unikaliomis MA ir P_2O_5 mišinio cheminėmis savybėmis, kai 150 °C temperatūroje MA dehidratuojasi iki anglies suboksido (C_3O_2), veikiant stipriam dehidratoriui P_2O_5. Šiame darbe pirmą kartą įrodėme, kad GO terminė redukcija naudojant C_3O_2 yra perspektyvus būdas atkurti konjuguotą aromatinę rGO struktūrą saugesniu ir labiau kontroliuojamu būdu. MA ir P_2O_5 mišinys efektyviai sumažino ne tik GO redukcijos temperatūrą (iki 125 °C), bet ir GO terminio skilimo entalpiją bei aktyvacijos energiją. Taip pat įrodėme, kad naudojant šį mišinį, ne tik palengvinama GO redukcija, bet ir prijungiamos fosforo funkcinės grupės rGO struktūroje. Tokia rGO modifikacija fosforu leido sukurti naują elektrocheminę platformą, pasižyminčią maža LOD verte ir palyginti dideliu jautriu, efektyviam DA nustatymui. Be to, taikant Borchardt-Daniels, Kissinger ir Ozawa modelius buvo ištirta GO terminio skilimo kinetika, redukcinėje aplinkoje nesant ir esant MA ir P_2O_5 mišiniui. Pažymėtina, kad pirmą kartą Ozawa metodas buvo panaudotas GO terminės redukcijos reakcijos aktyvacijos energijai nustatyti.

Siekiant susintetinti naujus bemetalius azotu modifikuotus rGO (N-rGO) bandinius, naudojant greitą ir paprastą GO hidroterminį apdorojimą, pirmą kartą azoto šaltiniu buvo panaudotas organinis dažas Bismarko rudasis (BB). Sistemingai ištyrėme BB koncentracijos poveikį galutinių grafeninių medžiagų struktūrinėms ir elektrocheminėms savybėms. Taip pat įrodėme, kad paruoštus N-rGO mėginius galima naudoti kaip perspektyvias elektrodines medžiagas labai selektyviam elektrocheminiam DA nustatymui. Lyginant su anksčiau sukurtais bemetaliais azotu modifikuotais grafeno jutikliais, mūsų pasiūlytas jutiklis pasižymėjo žymiai mažesnė LOD verte, platesniu tiesiniu analitės koncentracijos intervalu ir didesniu jautriu. Neabejotinai šis darbas reikšmingai prisideda prie naujo tipo jutiklių platformos, kuri leistų jautriai aptikti įvairias analites, kūrimo ir tobulinimo, bei neišvengiamai sutelks dėmesį į naujų laidžių medžiagų, o ypač į naujų grafeninių darinių, vystymąsi.

Anglies suboksido poveikis GO terminio skilimo kinetikai

GO terminės savybės ir terminės redukcijos kinetika, nesant ir esant anglies suboksidui (C_3O_2), ištirta termogravimetrijos (TA), diferencinės termogravimetrijos (DTG) ir diferencinės skenuojančios kalorimetrijos (DSC) metodais, parenkant tris skirtingus temperatūros kėlimo greičius: β = 2,5 °C min^{-1}, β = 5 °C min^{-1} ir β = 10 °C min^{-1}. Terminės redukcijos kinetiniai parametrai įvertinti Borchardt-Daniels, Kissenger ir Ozawa metodais. Tyrimui įgyvendinti buvo susintetintas GO_2, remiantis modifikuota Hummers sintezės metodika [96], ir paruoštas homogenizuotas GO_2, MA ir P_2O_5 mišinys (žymėjimas GO_2_MA_P). Šis mišinys pasirinktas dėl to, kad kaitinant MA ir P_2O_5 150 °C temperatūroje susidaro C_3O_2.

1 pav. pateiktos GO_2 ir GO_2_MA_P mėginių DSC kreivės, iš kurių nustatyta, kad tiriamųjų bandinių terminis skilimas yra egzoterminis. DSC rezultatai taip pat rodo, kad GO_2 terminės redukcijos pradžios temperatūra T_{onset} reikšmingai sumažėja, naudojant C_3O_2 priedą. Remiantis literatūroje pateiktais duomenimis, T_{onset} vertė varijuoja 150–200 °C temperatūros intervale [64], tačiau šiame darbe, pridėjus C_3O_2, T_{onset} vertė sumažėja iki 125 °C, esant 2,5 °C min^{-1} temperatūros kėlimo greičiui. Be to, nustatyta, kad vidutinė GO_2 terminės redukcijos reakcijos entalpija lygi 1487,18 J g^{-1}, o esant C_3O_2, ši vertė sumažėja apie 303,85 J g^{-1}.

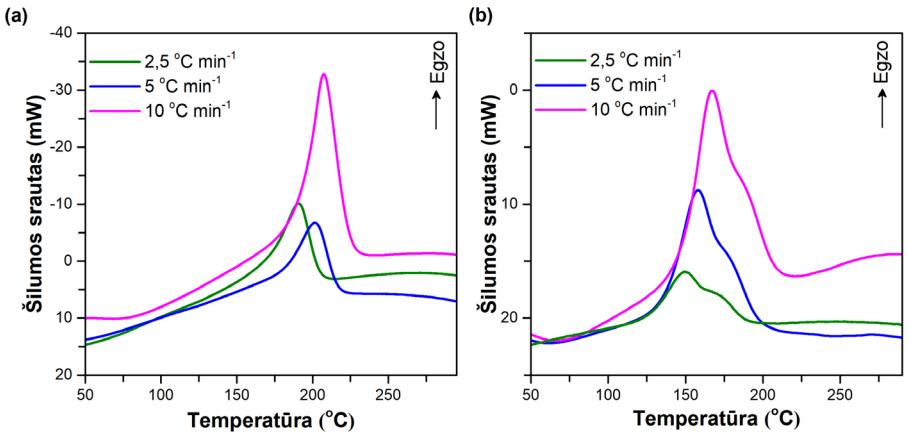

1 pav. GO_2 (a) ir GO_2_MA_P (b) DSC kreivės, esant 2,5, 5, ir 10 °C min^{-1} temperatūros kėlimo greičiams.

Naudojant Borchardt-Daniels modelį, buvo nustatyta, kad vidutinė GO_2 terminio skilimo aktyvacijos energija yra 138,6 kJ mol^{-1} ir ji sumažėja apie 27 kJ mol^{-1}, naudojant C_3O_2 priedą. Tai rodo, kad C_3O_2 katalizuoja GO_2 terminės redukcijos reakciją ir padidina GO_2 reaktyvumą. Remiantis Borchardt-Daniels metodu, apskaičiuota ne tik E_a vertė, bet ir terminio skilimo reakcijos laipsnis. Gauta, kad abiejų tiriamųjų mėginių (GO_2 ir GO_MA_P) terminio skilimo reakcijos laipsnis yra vienodas ir lygus 0,7, o tai parodo, kad C_3O_2 pridėjimas nepakeičia GO_2 terminio skilimo mechanizmo.

GO_2 ir GO_2_MA_P mėginių terminės redukcijos reakcijos aktyvacijos energija taip pat apskaičiuota, naudojant Kissinger ir Ozawa metodus. Gautieji duomenys taip pat patvirtino, kad GO_2 bandinio terminio skilimo reakcijos E_a vertės sumažėja, esant C_3O_2: nuo 141,5 kJ mol^{-1} iki 114,0 kJ mol^{-1} (Kissinger metodas) ir nuo 142,1 kJ mol^{-1} iki 115,2 kJ mol^{-1} (Ozawa metodas).

P-rGO mėginių charakterizavimas

Fosforu modifikuoti rGO (P-rGO) bandiniai gauti, termiškai redukuojant homogenizuotą GO, MA ir P_2O_5 mišinį horizontalioje vamzdinėje krosnyje 800 °C temperatūroje 30 min Ar atmosferoje. Šioje dalyje buvo naudojami du GO mėginiai (GO_1 gautas pagal tradicinę Hummers metodiką [95] ir GO_3 susintetintas pagal modifikuotą Hummers metodiką [97]) ir skirtingi MA ir P_2O_5 kiekiai. Iš viso paruošti keturi skirtingi P-rGO mėginiai: rGO_1_5, rGO_1_10, rGO_3_5 ir rGO_3_10. Nemodifikuoti rGO bandiniai (rGO_1 ir rGO_3) taip pat buvo susintetinti tomis pačiomis sąlygomis. Gautieji grafeniniai mėginiai charakterizuoti energinės dispersijos Rentgeno spektroskopijos (EDX), Rentgeno fotoelektroninės spektroskopijos (XPS), Raman spektroskopijos metodais. Taip pat atlikti visų mėginių elektrinio laidumo matavimai.

EDX analizės rezultatai rodo, kad, naudojant MA ir P_2O_5 mišinį GO terminės redukcijos metu, į rGO struktūrą yra įterpiamos P turinčios funkcinės grupės. Nustatyta, kad bandiniuose P kiekis varijuoja nuo 0,3 at.% iki 2,3 at.%, o didžiausiu P kiekiu pasižymi rGO_3_10 mėginys (2,3 at.%). P2p XPS spektrai rodo, kad naudojant MA ir P_2O_5 priedą daugiausiai prijungiamos didesnio oksidacijos laipsnio fosforo grupės (PO_x), kadangi šių grupių koncentracija siekia 81,4 at.% ir 74,9 at.% atitinkamai rGO_1_10 ir rGO_3_10 mėginiuose.

Iš gautų Raman spektrų apskaičiuotos D ir G modų intensyvumo santykio I_D/I_G vertės, kurios nurodo grafeninės medžiagos defektiškumą. Kuo šis santykis didesnis, tuo defektiškesnė struktūra [113,114]. Nustatyta, kad P

modifikuotų rGO mėginių I_D/I_G vertės yra šiek tiek didesnės už rGO_1 ir rGO_3 ir varijuoja nuo 0,91 iki 0,96. Didžiausias struktūrinių defektų kiekis nustatytas rGO_3_10 mėginyje.

Grafeninių medžiagų elektrinės savybės įvertintos, remiantis 2 pav. pateiktomis elektrinio laidumo priklausomybėmis nuo piltinio tankio logaritminėje skalėje. Nustatyta, kad elektrinis laidumas didėja, didėjant medžiagos piltiniam tankiui. Didžiausiu elektriniu laidumu pasižymi produktai, kurių redukcijoje buvo naudojama 10 masės % MA, o mažiausiu – rGO mėginiai be priedų. Tai įrodo, kad MA ir P_2O_5 priedo naudojimas GO terminėje redukcijoje leidžia efektyviau atstatyti π-konjuguotų ryšių sistemą ir pagerinti elektronų mobilumą.

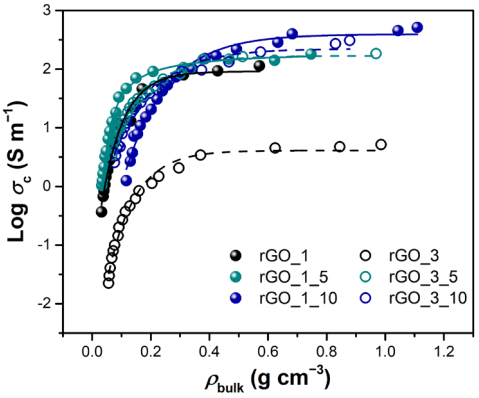

2 pav. Grafeninių medžiagų: rGO_1, rGO_1_5, rGO_1_10, rGO_3, rGO_3_5 ir rGO_3_10 elektrinio laidumo priklausomybės nuo piltinio tankio logaritminėje skalėje.

Dopamino elektrocheminis aptikimas naudojant P-rGO

Mėginiai, turintys didžiausią P kiekį ir pasižymintys didžiausiu elektriniu laidumu (rGO_1_10 ir rGO_3_10), buvo pritaikyti, kuriant bemetalį, jautrų ir selektyvų elektrocheminį jutiklį DA nustatymui. Elektrocheminiai tyrimai atlikti, naudojant trijų elektrodų celę, kurią sudarė pagalbinis Pt elektrodas, palyginamasis Ag/AgCl (KCl, 3 M) ir darbinis stikliškosios anglies elektrodas (GCE), padengtas tiriamaja rGO_1_10 ar rGO_3_10 medžiaga. Elektrocheminis aktyvumas dopaminui įvertintas ciklinės voltamperometrijos (CV) ir diferencinės impulso voltamperometrijos (DPV) metodais.

Iš CV kreivių, gautų skleidžiant skirtingų potencialų greičiu, nustatyta, kad naudojant GCE/rGO_1_10 elektrodą, DA redokso reakcija yra dalinai

grįžtama, o naudojant GCE/rGO_3_10 – grįžtama. Iš gautųjų tiesinių srovės stiprio priklausomybių nuo potencialo skleidimo greičio nustatyta, kad elektrocheminė reakcija yra kontroliuojama paviršiaus adsorbcijos, naudojant abu tiriamuosius elektrodus.

Iš DPV rezultatų buvo nubrėžtos tiesinės srovės stiprio priklausomybės nuo DA koncentracijos. Jos pavaizduotos 3 pav. Nustatyta, kad jutiklis suformuotas iš GCE/rGO_3_10 elektrodo turėjo mažiausią DA aptikimo ribą (0,11 μM) ir didžiausią jautrį (28,64 μA μM^{-1} cm^{-2}), lyginant su GCE/rGO_1_10. Kadangi GCE/rGO_3_10 pasižymėjo geresnėmis analitinėmis savybėmis, buvo įvertintas šio elektrodo selektyvumas ir stabilumas. Selektyvumui įvertinti į elektrocheminę celę buvo įpiltas žinomas interferuojančios analitės UA kiekis (200 μM). Nustatyta, kad esant UA, šiek tiek padidėja DA aptikimo riba (0,13 μM) ir sumažėja elektrodo jautris (4,94 μA μM^{-1} cm^{-2}). Nepaisant to, GCE/rGO_3_10 elektrodas vis tiek pasižymi geru elektrocheminiu atsaku į DA.

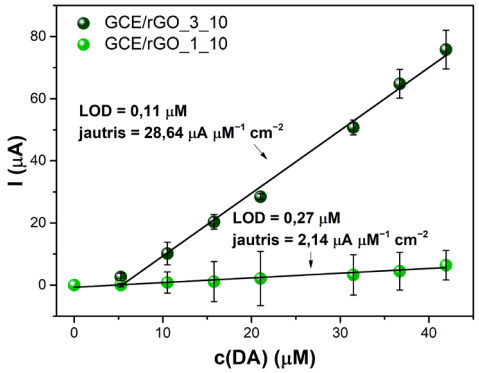

3 pav. GCE/rGO_1_10 ir GCE/rGO_3_10 elektrodų srovės stiprio pokyčio priklausomybės nuo dopamino koncentracijos.

Siekiant įvertinti jutiklio stabilumą, elektrocheminiai matavimai buvo kartoti 15 dienų. Nustatyta, kad po dviejų ir trijų dienų GCE/rGO_3_10 modifikuoto elektrodo aktyvumas atitinkamai sumažėjo maždaug 5,27 % ir 40,24 %. Po dešimt dienų elektrodo srovė sumažėjo 69,66 %. Be to, pastebėta, kad po dviejų savaičių elektrodas išlaikė apie 32 % pradinės srovės. Toks stabilumo sumažėjimas siejamas su elektrodo paviršiaus dezaktyvacija, kadangi jo paviršiuje adsorbuojasi DA ir jo šalutiniai produktai. Stabilumo sumažėjimas galėjo atsirasti ir dėl prastos adhezijos tarp tiriamosios medžiagos ir elektrodo paviršiaus.

N-rGO struktūrinė analizė ir taikymas dopamino elektrocheminiam nustatymui

Siekiant susintetinti N-rGO mėginius (rGO_BB20 ir rGO_BB50), GO_2 suspensija su 20 arba 50 masės % BB dažo buvo redukuojama hidroterminės sintezės reaktoriuje 180 °C temperatūroje 12 val. Nemodifikuotas rGO_2 bandinys gautas, remiantis ta pačia metodika. Gautieji mėginiai išanalizuoti XPS, Raman spektroskopijos, Brunauer-Emmett-Teller (BET) analizės metodais ir elektrinio laidumo matavimais.

XPS analizės duomenys rodo, kad hidroterminės GO_2 redukcijos metu, naudojant BB dažą, yra sėkmingai įterpiamas azotas rGO_BB20 (3,8 at.% N) ir rGO_BB50 (10,6 at.% N) mėginiuose. Iš gautųjų rGO_BB20 ir rGO_BB50 bandinių N1s XPS spektrų nustatyta, kad azotas prisijungęs piridininio-N, amido ar piridono, pirolinio-N, grafitinio-N ir azoto oksidų konformacijose. Nustatyta, kad rGO_BB20 mėginyje vyrauja piridininio-N (45,0 %), o rGO_BB50 bandinyje – piridininio-N (40,7 %) ir amino (35,7 %) funkcinės grupės. Be to, nustatyta, kad rGO_BB20 pasižymi didesniu pirolinio-N ir grafitinio-N kiekiu, lyginant su rGO_BB50, o didesnė šių azoto konformacijų koncentracija gali lemti didesnį grafeninės medžiagos elektrocheminį aktyvumą [50].

Iš gautųjų Raman spektrų buvo apskaičiuoti G smailės puspločiai (FWHM(G)). Didesnės FWHM(G) vertės rodo didesnį sp^3 defektų kiekį mėginyje ir mažesnes medžiagos daleles. Nustatyta, kad po hidroterminės redukcijos FWHM(G) sumažėja nuo 71,4 cm^{-1} (GO_2) iki 62,7 cm^{-1} (rGO_2), o tai patvirtina dalinį rGO_2 sp^2 anglies hibridizacijos atkūrimą dėl deguoninių funkcinių grupių skilimo. Po rGO_2 modifikavimo azotu, FWHM(G) padidėja iki 67,2 cm^{-1} ir 72,4 cm^{-1} atitinkamai rGO_BB20 ir rGO_BB50 mėginiuose. Šis padidėjimas parodo suardytą anglies tinklo struktūrą ir išaugusį defektų skaičių dėl prisijungusių azoto funkcinių grupių. Raman spektruose matomas raudonasis G juostos poslinkis (nuo 1602 cm^{-1} iki 1594 cm^{-1}) abiejuose azotu modifikuotuose rGO_2 mėginiuose taip pat papildomai pagrindžia cheminių ryšių tarp C ir N susidarymą [142].

Redukuotų GO_2 mėginių porėtumas ir paviršiaus ploto skirtumai buvo išanalizuoti BET analizės metodu. Nustatyta, kad visų mėginių N_2 adsorbcijos-desorbcijos izotermos pagal IUPAC nomenklatūrą priskiriamos IV tipui, kuris nurodo, kad medžiagos sudarytos iš mezoporų. Porų pasiskirstymo kreivės, gautos pagal BJH modelį, taip pat patvirtina 2–5 nm dydžio mezoporų buvimą redukuotuose GO_2 mėginiuose. Be to, nustatyta, kad rGO_2 pasižymi didesniu BET paviršiaus plotu (241 $m^2\ g^{-1}$) nei rGO_BB20 (52 $m^2\ g^{-1}$) ir rGO_BB50 (29 $m^2\ g^{-1}$) bandiniai. Tikėtina, kad toks

BET paviršiaus ploto sumažėjimas atsiranda dėl modifikacijos metu įvestų azoto funkcinių grupių gebėjimo blokuoti mažiausias poras, dėl kurių N_2 dujos negali įsiterpti tarp rGO plokštumų.

Elektrinės medžiagų savybės įvertintos, remiantis elektrinio laidumo priklausomybėmis nuo piltinio tankio logaritminėje skalėje. Nustatyta, kad rGO_BB20 elektrinis laidumas yra nežymiai mažesnis už rGO_2. rGO_BB20 laidumo sumažėjimas, palyginti su nemodifikuotu rGO_2, yra nereikšmingas ir susijęs su piridininio azoto įterpimu bazinėje plokštumoje bei struktūrinių defektų padidėjimu. rGO_BB50 rodo mažiausias elektrinio laidumo vertes, kadangi šiame bandinyje nustatyta mažiausia grafitinio-N koncentracija ir didžiausias defektų kiekis.

Susintetinti N-rGO mėginiai taip pat buvo pritaikyti, kuriant elektrocheminį DA jutiklį. Elektrocheminis paruoštų elektrodų (GCE/rGO_BB20 ir GCE/rGO_BB50) aktyvumas dopaminui įvertintas naudojant trijų elektrodų celę ir taikant CV ir chronoamperometrijos (ChA) metodus.

Iš srovės stiprio priklausomybės nuo kvadratinės šaknies iš potencialo skleidimo greičio nustatyta, kad elektrocheminės reakcijos kinetika yra difuzijos kontroliuojamas procesas. Remiantis Randles-Sevcik lygtimi [150] apskaičiuota, kad GCE/rGO_BB20 ir GCE/rGO_BB50 elektrodų elektrochemiškai aktyvus paviršiaus plotas (ECSA) atitinkamai lygus 0,3092 cm^2 ir 0,2336 cm^2. ECSA koreliuoja su BET paviršiaus ploto rezultatais, kadangi didesnė paviršiaus ploto vertė nustatyta mėginiui su mažesniu azoto kiekiu.

Iš gautųjų chronoamperogramų buvo nubrėžtos kalibracinės kreivės (4 pav.) dviejuose tiesiniuose koncentracijų ruožuose abiem tiriamiesiems elektrodams. Nustatyta, kad 0−15 μM koncentracijų intervale GCE/rGO_BB20 elektrodas pasižymi mažesne aptikimo riba (45 nM) ir didesniu jautriu (0,61 $\mu A\ \mu M^{-1}\ cm^{-2}$), lyginant su GCE/rGO_BB50 elektrodu. GCE/rGO_BB20 taip pat pasižymi platesniu tiesiniu analitės koncentracijos intervalu (15−476 μM), lyginant tiek su GCE/rGO_BB50 (15–291 μM), tiek su kitais literatūroje pateiktais azotu modifikuotais grafeniniais elektrodais [9,93,151]. Be to, nustatyta, kad abu tiriamieji elektrodai yra selektyvūs DA, kadangi elektrocheminis atsakas į kitas interferuojančias molekules tokias, kaip citrinų rūgštis (CA), H_2O_2, AA ir UA, neužfiksuotas.

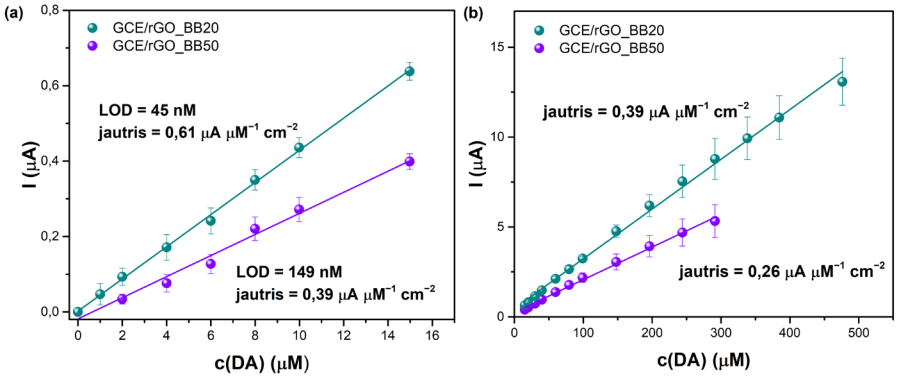

4 pav. GCE/rGO_BB20 ir GCE/rGO_BB50 elektrodų kalibracinės kreivės skirtingų koncentracijų intervaluose.

IŠVADOS

1. GO terminės redukcijos kinetika, naudojant ir nenaudojant anglies suboksido, nuodugniai įvertinta, taikant Borchardt-Daniels, Kissinger ir Ozawa modelius. Rezultatai parodė, kad naudojant anglies suboksidą GO terminėje redukcijoje pasikeičia GO terminis stabilumas ir sumažėja jo redukcijos temperatūra iki 125 °C. Įvedus šį priedą, taip pat sumažėja reakcijos entalpija ir aktyvacijos energija, o reakcijos laipsnis išlieka nepakitęs ir lygus 0,7. Tai atskleidžia sudėtingą GO terminio skilimo mechanizmą, kurį sudaro vienu metu vykstančios nulinės ir pirmojo laipsnio reakcijos. Be to, nustatyta, kad GO terminės redukcijos reakcijos E_a ir ΔH priklauso nuo temperatūros kėlimo greičio.

2. rGO bandinių struktūrinės ir elektrinės savybės priklauso nuo naudojamo MA ir P_2O_5 priedo kiekio bei GO tipo. Ištyrus paruoštus mėginius EDX metodu nustatyta, kad naudojant MA ir P_2O_5 mišinį GO terminėje redukcijoje, į rGO įterpiamas palyginti didelis fosforo kiekis (0,3–2,3 at.%). Raman spektroskopijos ir elektrinio laidumo rezultatai parodė, kad geriausiai atkuriama sp^2 hibridizuota anglies sistema yra naudojant mišinį, kuriame yra 10 masės % MA ir GO, paruošto tradiciniu Hummers sintezės metodu (mėginys pavadintas rGO_1_10).

3. Fosforu modifikuoti rGO mėginiai, gauti termiškai redukuojant GO ir pridedant MA ir P_2O_5, pasižymėjo perspektyviu elektrocheminiu aktyvumu nustatant DA. Atlikus elektrocheminius matavimus nustatyta, kad jutiklis, suformuotas iš GCE/rGO_3_10 mėginio, turėjo geresnius elektrocheminius

parametrus, palyginti su GCE/rGO_1_10 elektrodu. Remiantis DPV tyrimais, nustatyta, kad GCE/rGO_3_10 modifikuotas elektrodas pasižymėjo platesniu tiesiniu analitės koncentracijos intervalu (5–42 μM), maža LOD verte (0,11 μM) ir dideliu jautriu (28,64 μA μM^{-1} cm^{-2}) nustatant DA. Ištyrus jutiklio selektyvumą, pastebėta, kad UA buvimas elektrocheminėje celėje lemia šiek tiek mažesnį jutiklio atsaką į DA. Nepaisant to, GCE/rGO_3_10 modifikuotas elektrodas vis tiek pasižymėjo priimtinu selektyvumu ir gali tuo pat metu aptikti tiek DA, tiek UA, pasiekiant LOD (0,12 μM) ir jautrį (8,47 μA μM^{-1} cm^{-2}) dopaminui, o šlapimo rūgščiai atitinkamai 0,15 μM ir 1,40 μA μM^{-1} cm^{-2}. Mūsų pasiūlyti jutikliai turėjo geresnes elektrochemines savybes, lyginant su anksčiau aprašytais bemetaliais ir net metaliniais rGO jutikliais.

4. Azotu modifikuoti rGO bandiniai buvo paruošti hidrotermiškai apdorojant GO ir kaip azoto šaltinį naudojant Bismarko rudąjį. Atlikus paruoštų mėginių kiekybinę XPS analizę nustatyta, kad funkcionalizavus rGO, jo paviršiuje yra prisijungusios azoto funkcinės grupės. Azoto kiekis rGO_BB20 buvo lygus 3,8 at.%, o rGO_BB50 – 10,6 at.%. XPS analizės metodas taip pat parodė, kad rGO_BB20 bandinyje, palyginti su rGO_BB50, yra didesnė pirolinio-N (16,1 %) ir grafitinio-N (6,1 %) grupių koncentracija. Raman spektroskopijos analizė parodė, kad rGO_BB50 bandinyje yra daugiausia amorfinės fazės ir daugiau struktūrinių defektų. Elektrinio laidumo matavimai parodė, kad nemodifikuotas rGO bandinys pasižymėjo didžiausiu elektriniu laidumu, lyginant su paruoštais N-rGO mėginiais. Nedidelį rGO_BB20 ir rGO_BB50 laidumo sumažėjimą, palyginti su nemodifikuotu rGO, galima paaiškinti didesniais struktūriniais defektais bazinėje plokštumoje.

5. Atlikus elektrocheminius matavimus nustatyta, kad abu elektrocheminiai jutikliai, suformuoti naudojant rGO_BB20 ir rGO_BB50 mėginius, pasižymėjo išskirtiniu selektyvumu nustatomajai DA analitei. Tačiau, GCE/rGO_BB20 jutiklis pasižymėjo platesniu tiesiniu analitės koncentracijos intervalu 0–15 μM ir 15–476 μM bei mažesne LOD verte (45 nM). Apskaičiuotas jautris 0–15 μM ruože buvo lygus 0,61 μA μM^{-1} cm^{-2}, o 15–476 μM – 0,39 μA μM^{-1} cm^{-2}. Atsižvelgiant į nesudėtingą paruošimo būdą ir puikius eksperimentinių tyrimų rezultatus, rGO_BB20 gali būti naudojamas kaip alternatyvi bemetalė elektrodinė medžiaga, kuriant DA jutiklį. Šis mėginys pasižymėjo geresnėmis analitinėmis savybėmis palyginti su anksčiau aprašytais azotu modifikuotais grafeniniais junginiais.

REFERENCES

[1] J. Molina, F. Cases, L.M. Moretto, Graphene-based materials for the electrochemical determination of hazardous ions, Anal. Chim. Acta. 946 (2016) 9–39. https://doi.org/10.1016/j.aca.2016.10.019.

[2] M. Uddin, M.H. Kabir, A. Ali, M. Hossain, M.U. Khandaker, S. Mandal, A. Arifutzzaman, D. Jana, Graphene-like emerging 2D materials: recent progress, challenges and future outlook, RSC Adv. 13 (2023) 33336–33375. https://doi.org/10.1039/d3ra04456d.

[3] Ababay Ketema Worku, Delele Worku Ayele, Recent advances of graphene-based materials for emerging technologies, Results Chem. 5 (2023) 100971. https://doi.org/10.1016/j.rechem.2023.100971.

[4] S. Lakard, I.A. Pavel, B. Lakard, Electrochemical biosensing of dopamine neurotransmitter: A review, Biosensors. 11 (2021). https://doi.org/10.3390/bios11060179.

[5] Y.S. Chang, F.K. Chen, D.C. Tsai, B.H. Kuo, F.S. Shieu, N-doped reduced graphene oxide for room-temperature NO gas sensors, Sci. Rep. 11 (2021) 1–12. https://doi.org/10.1038/s41598-021-99883-9.

[6] A.F. Quintero-Jaime, J. Quílez-Bermejo, D. Cazorla-Amorós, E. Morallón, Metal free electrochemical glucose biosensor based on N-doped porous carbon material, Electrochim. Acta. 367 (2021). https://doi.org/10.1016/j.electacta.2020.137434.

[7] S. Kaushal, M. Kaur, N. Kaur, V. Kumari, P.P. Singh, Heteroatom-doped graphene as sensing materials: A mini review, RSC Adv. 10 (2020) 28608–28629. https://doi.org/10.1039/d0ra04432f.

[8] B.A. Hussein, A.A. Tsegaye, G. Shifera, A.M. Taddesse, A sensitive non-enzymatic electrochemical glucose sensor based on a ZnO/Co3O4/reduced graphene oxide nanocomposite, Sensors and Diagnostics. 2 (2023) 347–360. https://doi.org/10.1039/d2sd00183g.

[9] H. Zhang, S. Liu, Electrochemical sensors based on nitrogen-doped reduced graphene oxide for the simultaneous detection of ascorbic acid, dopamine and uric acid, J. Alloys Compd. 842 (2020) 155873. https://doi.org/10.1016/j.jallcom.2020.155873.

[10] B. Patella, M. Buscetta, S. Di Vincenzo, M. Ferraro, G. Aiello, C. Sunseri, E. Pace, R. Inguanta, C. Cipollina, Electrochemical sensor based on rGO/Au nanoparticles for monitoring H2O2 released by human macrophages, Sensors Actuators, B Chem. 327 (2021) 128901. https://doi.org/10.1016/j.snb.2020.128901.

[11] D. Chen, J. Jiang, X. Du, Electrocatalytic oxidation of nitrite using metal-free nitrogen-doped reduced graphene oxide nanosheets for sensitive detection, Talanta. 155 (2016) 329–335. https://doi.org/10.1016/J.TALANTA.2016.05.003.

[12] A. Cernat, G. Ştefan, M. Tertis, C. Cristea, I. Simon, An overview of the detection of serotonin and dopamine with graphene-based sensors, Bioelectrochemistry. 136 (2020).

https://doi.org/10.1016/j.bioelechem.2020.107620.
[13] H.A. Rahman, M. Rafi, B.R. Putra, W.T. Wahyuni, Electrochemical Sensors Based on a Composite of Electrochemically Reduced Graphene Oxide and PEDOT:PSS for Hydrazine Detection, ACS Omega. (2022). https://doi.org/10.1021/acsomega.2c06791.
[14] M. Coroş, S. Pruneanu, R.-I. Stefan-van Staden, Review—Recent Progress in the Graphene-Based Electrochemical Sensors and Biosensors, J. Electrochem. Soc. 167 (2020) 037528. https://doi.org/10.1149/2.0282003jes.
[15] Z.N. Huang, Jiao Zou, J. Teng, Q. Liu, M.M. Yuan, F.P. Jiao, X.Y. Jiang, J.G. Yu, A novel electrochemical sensor based on self-assembled platinum nanochains - Multi-walled carbon nanotubes-graphene nanoparticles composite for simultaneous determination of dopamine and ascorbic acid, Ecotoxicol. Environ. Saf. 172 (2019) 167–175. https://doi.org/10.1016/J.ECOENV.2019.01.091.
[16] N. Slepičková Kasálková, P. Slepička, V. Švorčík, Carbon nanostructures, nanolayers, and their composites, Nanomaterials. 11 (2021). https://doi.org/10.3390/nano11092368.
[17] A.A. Ensafi, H.A. Alinajafi, B. Rezaei, Thermally reduced graphene oxide/polymelamine formaldehyde nanocomposite as a high specific capacitance electrochemical supercapacitor electrode, J. Mater. Chem. A. 6 (2018) 6045–6053. https://doi.org/10.1039/c7ta10825g.
[18] R.K. Singh, R. Kumar, D.P. Singh, Graphene oxide: Strategies for synthesis, reduction and frontier applications, RSC Adv. 6 (2016) 64993–65011. https://doi.org/10.1039/c6ra07626b.
[19] I. Šakinyte, J. Barkauskas, J. Gaidukevič, J. Razumiene, Thermally reduced graphene oxide: The study and use for reagentless amperometric d-fructose biosensors, Talanta. 144 (2015) 1096–1103. https://doi.org/10.1016/j.talanta.2015.07.072.
[20] S. Pei, H.M. Cheng, The reduction of graphene oxide, Carbon N. Y. 50 (2012) 3210–3228. https://doi.org/10.1016/j.carbon.2011.11.010.
[21] Y. Qiu, F. Guo, R. Hurt, I. Külaots, Explosive thermal reduction of graphene oxide-based materials: Mechanism and safety implications, Carbon N. Y. 72 (2014) 215–223. https://doi.org/10.1016/J.CARBON.2014.02.005.
[22] G.T.T. Le, J. Manyam, P. Opaprakasit, N. Chanlek, N. Grisdanurak, P. Sreearunothai, Divergent mechanisms for thermal reduction of graphene oxide and their highly different ion affinities, Diam. Relat. Mater. 89 (2018) 246–256. https://doi.org/10.1016/j.diamond.2018.09.006.
[23] A. Kaniyoor, T.T. Baby, T. Arockiadoss, N. Rajalakshmi, S. Ramaprabhu, Wrinkled graphenes: A study on the effects of synthesis parameters on exfoliation-reduction of graphite oxide, J. Phys. Chem. C. 115 (2011) 17660–17669. https://doi.org/10.1021/jp204039k.
[24] J. Gaidukevic, R. Aukstakojyte, M. Kozłowski, J. Barkauskas, R.

Pauliukaite, A simple preparation of N-doped reduced graphene oxide as an electrode material for the detection of hydrogen peroxide and glucose, Electrochim. Acta. 446 (2023). https://doi.org/10.1016/j.electacta.2023.142113.

[25] C. Botas, P. Álvarez, C. Blanco, R. Santamaría, M. Granda, M.D. Gutiérrez, F. Rodríguez-Reinoso, R. Menéndez, Critical temperatures in the synthesis of graphene-like materials by thermal exfoliation-reduction of graphite oxide, Carbon N. Y. 52 (2013) 476–485. https://doi.org/10.1016/j.carbon.2012.09.059.

[26] O.C. Compton, S.T. Nguyen, Graphene oxide, highly reduced graphene oxide, and graphene: Versatile building blocks for carbon-based materials, Small. 6 (2010) 711–723. https://doi.org/10.1002/smll.200901934.

[27] Y. Liang, J. Frisch, L. Zhi, H. Norouzi-Arasi, X. Feng, J.P. Rabe, N. Koch, K. Müllen, Transparent, highly conductive graphene electrodes from acetylene-assisted thermolysis of graphite oxide sheets and nanographene molecules, Nanotechnology. 20 (2009). https://doi.org/10.1088/0957-4484/20/43/434007.

[28] M. Zhi, Q. Liu, H. Chen, S. Feng, Y. He, Study on efficient and green reduction of graphene oxide by a one-step hydrothermal method, J. Phys. Conf. Ser. 1213 (2019). https://doi.org/10.1088/1742-6596/1213/5/052047.

[29] Y. Zhou, Q. Bao, L.A.L. Tang, Y. Zhong, K.P. Loh, Hydrothermal dehydration for the “green” reduction of exfoliated graphene oxide to graphene and demonstration of tunable optical limiting properties, Chem. Mater. 21 (2009) 2950–2956. https://doi.org/10.1021/cm9006603.

[30] and G.S. Yuxi Xu, Kaixuan Sheng, Chun Li, Self-Assembled Graphene Hydrogel via a One-Step Hydrothermal Process, ACS Nano. 4 (2012) 3535–4332.

[31] R. Singh, S. Ullah, N. Rao, M. Singh, I. Patra, D.A. Darko, C.P.J. Issac, K. Esmaeilzadeh-Salestani, R. Kanaoujiya, V. Vijayan, Synthesis of Three-Dimensional Reduced-Graphene Oxide from Graphene Oxide, J. Nanomater. 2022 (2022). https://doi.org/10.1155/2022/8731429.

[32] C. Bosch-Navarro, E. Coronado, C. Martí-Gastaldo, J.F. Sánchez-Royo, M.G. Gómez, Influence of the pH on the synthesis of reduced graphene oxide under hydrothermal conditions, Nanoscale. 4 (2012) 3977–3982. https://doi.org/10.1039/c2nr30605k.

[33] X. Wang, G. Sun, P. Routh, D.H. Kim, W. Huang, P. Chen, Heteroatom-doped graphene materials: Syntheses, properties and applications, Chem. Soc. Rev. 43 (2014) 7067–7098. https://doi.org/10.1039/c4cs00141a.

[34] S. Ullah, Q. Shi, J. Zhou, X. Yang, H.Q. Ta, M. Hasan, N.M. Ahmad, L. Fu, A. Bachmatiuk, M.H. Rümmeli, Advances and Trends in Chemically Doped Graphene, Adv. Mater. Interfaces. 7 (2020) 1–23.

https://doi.org/10.1002/admi.202000999.
[35] D. Li, X. Duan, H. Sun, J. Kang, H. Zhang, M.O. Tade, S. Wang, Facile synthesis of nitrogen-doped graphene via low-temperature pyrolysis: The effects of precursors and annealing ambience on metal-free catalytic oxidation, Carbon N. Y. 115 (2017) 649–658. https://doi.org/10.1016/j.carbon.2017.01.058.
[36] R. Yadav, C.K. Dixit, Synthesis, characterization and prospective applications of nitrogen-doped graphene: A short review, J. Sci. Adv. Mater. Devices. 2 (2017) 141–149. https://doi.org/10.1016/j.jsamd.2017.05.007.
[37] N. Talukder, Y. Wang, B.B. Nunna, E.S. Lee, Nitrogen-doped graphene nanomaterials for electrochemical catalysis/reactions: A review on chemical structures and stability, Carbon N. Y. 185 (2021) 198–214. https://doi.org/10.1016/j.carbon.2021.09.025.
[38] A. Śliwak, B. Grzyb, N. Díez, G. Gryglewicz, Nitrogen-doped reduced graphene oxide as electrode material for high rate supercapacitors, Appl. Surf. Sci. 399 (2017) 265–271. https://doi.org/10.1016/j.apsusc.2016.12.060.
[39] S. Kumar, S. Gonen, A. Friedman, L. Elbaz, G.D. Nessim, Doping and reduction of graphene oxide using chitosan-derived volatile N-heterocyclic compounds for metal-free oxygen reduction reaction, Carbon N. Y. 120 (2017) 419–426. https://doi.org/10.1016/j.carbon.2017.05.071.
[40] P. Wiench, Z. González, R. Menéndez, B. Grzyb, G. Gryglewicz, Beneficial impact of oxygen on the electrochemical performance of dopamine sensors based on N-doped reduced graphene oxides, Sensors Actuators, B Chem. 257 (2018) 143–153. https://doi.org/10.1016/j.snb.2017.10.106.
[41] X. Wang, P. Tang, C. DIng, X. Cao, S. Yuan, X. Zuo, X. Deng, Simultaneous enhancement of adsorption and peroxymonosulfate activation of Nitrogen-doped reduced graphene oxide for bisphenol A removal, J. Environ. Chem. Eng. 5 (2017) 4291–4297. https://doi.org/10.1016/j.jece.2017.08.018.
[42] R.I. Jafri, N. Rajalakshmi, K.S. Dhathathreyan, S. Ramaprabhu, Nitrogen doped graphene prepared by hydrothermal and thermal solid state methods as catalyst supports for fuel cell, Int. J. Hydrogen Energy. 40 (2015) 4337–4348. https://doi.org/10.1016/j.ijhydene.2015.02.008.
[43] X. Fan, C. Yu, J. Yang, Z. Ling, J. Qiu, Hydrothermal synthesis and activation of graphene-incorporated nitrogen-rich carbon composite for high-performance supercapacitors, Carbon N. Y. 70 (2014) 130–141. https://doi.org/10.1016/j.carbon.2013.12.081.
[44] L. Sun, L. Wang, C. Tian, T. Tan, Y. Xie, K. Shi, M. Li, H. Fu, Nitrogen-doped graphene with high nitrogen level via a one-step hydrothermal reaction of graphene oxide with urea for superior

capacitive energy storage, RSC Adv. 2 (2012) 4498–4506. https://doi.org/10.1039/c2ra01367c.
[45] H.J. Lee, A. Abdellah, F.M. Ismail, C. Gumeci, N. Dale, J. Parrondo, D.C. Higgins, Understanding the impact of nitrogen doping and/or amine functionalization of reduced graphene oxide via hydrothermal routes for supercapacitor applications, Electrochim. Acta. 397 (2021) 139241. https://doi.org/10.1016/j.electacta.2021.139241.
[46] S. Ai, Y. Chen, Y. Liu, Q. Zhang, L. Xiong, H. Huang, L. Li, X. Yu, L. Wei, Facile synthesis of nitrogen-doped graphene aerogels for electrochemical detection of dopamine, Solid State Sci. 86 (2018) 6–11. https://doi.org/10.1016/j.solidstatesciences.2018.09.014.
[47] W. Raza, K. Ahmad, H. Kim, Nitrogen-doped graphene as an efficient metal-free catalyst for ammonia and non-enzymatic glucose sensing, J. Phys. Chem. Solids. 160 (2022) 110359. https://doi.org/10.1016/J.JPCS.2021.110359.
[48] G. Song, R. Zhang, X. Jiang, F. Liu, X. Liu, Nitrogen-doped reduced graphene oxide as a sensing platform for detection of guanine and application in cell necrosis, Chem. Pap. 74 (2020) 89–98. https://doi.org/10.1007/S11696-019-00856-0/FIGURES/6.
[49] S. Sharma, R. Kumar, R.M. Yadav, Polyacrylonitrile/N-doped graphene quantum dots nanocomposite activity as SERS nanosensors for detection of methylene blue, Mater. Today Commun. 36 (2023) 106860. https://doi.org/10.1016/j.mtcomm.2023.106860.
[50] Z. Chen, Y. Zhang, Y. Yang, X. Shi, L. Zhang, G. Jia, Hierarchical nitrogen-doped holey graphene as sensitive electrochemical sensor for methyl parathion detection, Sensors Actuators B Chem. 336 (2021) 129721. https://doi.org/10.1016/J.SNB.2021.129721.
[51] R. Kumar, S. Sahoo, E. Joanni, R.K. Singh, W.K. Tan, K.K. Kar, A. Matsuda, Recent progress in the synthesis of graphene and derived materials for next generation electrodes of high performance lithium ion batteries, Prog. Energy Combust. Sci. 75 (2019) 100786. https://doi.org/10.1016/j.pecs.2019.100786.
[52] L. Wei, P. Wang, Y. Yang, R. Luo, J. Li, X. Gu, Z. Zhan, Y. Dong, W. Song, R. Fan, Facile synthesis of nitrogen-doped reduced graphene oxide as an efficient counter electrode for dye-sensitized solar cells, J. Nanoparticle Res. 20 (2018). https://doi.org/10.1007/s11051-018-4203-9.
[53] H.M. Wang, H.X. Wang, Y. Chen, Y.J. Liu, J.X. Zhao, Q.H. Cai, X.Z. Wang, Phosphorus-doped graphene and (8, 0) carbon nanotube: Structural, electronic, magnetic properties, and chemical reactivity, Appl. Surf. Sci. 273 (2013) 302–309. https://doi.org/10.1016/j.apsusc.2013.02.035.
[54] X. Zhan, X. Tong, M. Gu, J. Tian, Z. Gao, L. Ma, Y. Xie, Z. Chen, H. Ranganathan, G. Zhang, S. Sun, Phosphorus-Doped Graphene Electrocatalysts for Oxygen Reduction Reaction, Nanomaterials. 12

(2022). https://doi.org/10.3390/nano12071141.
[55] N. Yang, X. Zheng, L. Li, J. Li, Z. Wei, Influence of Phosphorus Configuration on Electronic Structure and Oxygen Reduction Reactions of Phosphorus-Doped Graphene, J. Phys. Chem. C. 121 (2017) 19321–19328. https://doi.org/10.1021/acs.jpcc.7b06748.
[56] L. Feng, Z. Qin, Y. Huang, K. Peng, F. Wang, Y. Yan, Y. Chen, Boron-, sulfur-, and phosphorus-doped graphene for environmental applications, Sci. Total Environ. 698 (2020) 134239. https://doi.org/10.1016/j.scitotenv.2019.134239.
[57] C. Zhang, N. Mahmood, H. Yin, F. Liu, Y. Hou, Synthesis of phosphorus-doped graphene and its multifunctional applications for oxygen reduction reaction and lithium ion batteries, Adv. Mater. 25 (2013) 4932–4937. https://doi.org/10.1002/adma.201301870.
[58] F. Niu, L.-M. Tao, Y.-C. Deng, Q.-H. Wang, W.-G. Song, Phosphorus doped graphene nanosheets for room temperature NH3 sensing, New J. Chem. 38 (2014) 2269–2272. https://doi.org/10.1039/C4NJ00162A.
[59] R. Li, Z. Wei, X. Gou, W. Xu, Phosphorus-doped graphene nanosheets as efficient metal-free oxygen reduction electrocatalysts, RSC Adv. 3 (2013) 9978–9984. https://doi.org/10.1039/c3ra41079j.
[60] M. An, C. Du, L. Du, Y. Sun, Y. Wang, C. Chen, G. Han, G. Yin, Y. Gao, Phosphorus-doped graphene support to enhance electrocatalysis of methanol oxidation reaction on platinum nanoparticles, Chem. Phys. Lett. 687 (2017) 1–8. https://doi.org/10.1016/j.cplett.2017.08.058.
[61] X. Mu, B. Yuan, X. Feng, S. Qiu, L. Song, Y. Hu, The effect of doped heteroatoms (nitrogen, boron, phosphorus) on inhibition thermal oxidation of reduced graphene oxide, RSC Adv. 6 (2016) 105021–105029. https://doi.org/10.1039/c6ra21329d.
[62] X. Yu, L. Feng, H.S. Park, Highly flexible pseudocapacitors of phosphorus-incorporated porous reduced graphene oxide films, J. Power Sources. 390 (2018) 93–99. https://doi.org/10.1016/j.jpowsour.2018.04.032.
[63] Z. Bi, L. Huo, Q. Kong, F. Li, J. Chen, A. Ahmad, X. Wei, L. Xie, C.M. Chen, Structural Evolution of Phosphorus Species on Graphene with a Stabilized Electrochemical Interface, ACS Appl. Mater. Interfaces. 11 (2019) 11421–11430. https://doi.org/10.1021/acsami.8b21903.
[64] Y. Qiu, F. Collin, R.H. Hurt, I. Külaots, Thermochemistry and kinetics of graphite oxide exothermic decomposition for safety in large-scale storage and processing, Carbon N. Y. 96 (2016) 20–28. https://doi.org/10.1016/j.carbon.2015.09.040.
[65] M. Coros, C. Socaci, S. Pruneanu, F. Pogacean, M.C. Rosu, A. Turza, L. Magerusan, Thermally reduced graphene oxide as green and easily available adsorbent for Sunset yellow decontamination, Environ. Res. 182 (2020) 109047. https://doi.org/10.1016/j.envres.2019.109047.

[66] T. Chang, K.H. Hsueh, C.C. Liu, C.R. Cao, C.M. Shu, A Method to Derive the Characteristic and Kinetic Parameters of 1,1-Bis(tert-butylperoxy)cyclohexane from DSC Measurements, Processes. 10 (2022) 1–20. https://doi.org/10.3390/pr10051026.
[67] N. Koga, Ozawa's kinetic method for analyzing thermoanalytical curves: History and theoretical fundamentals, J. Therm. Anal. Calorim. 113 (2013) 1527–1541. https://doi.org/10.1007/s10973-012-2882-5.
[68] K. Yin, H. Li, Y. Xia, H. Bi, J. Sun, Z. Liu, L. Sun, Thermodynamic and Kinetic Analysis of Lowtemperature Thermal Reduction of Graphene Oxide, Nano-Micro Lett. 3 (2011) 51–55. https://doi.org/10.5101/nml.v3i1.p51-55.
[69] O. Bortolini, L. Pandolfo, C. Tomaselli, P. Traldi, Ion-molecule chemistry of carbon suboxide in an ion-trap mass spectrometer, Int. J. Mass Spectrom. 190–191 (1999) 171–179. https://doi.org/10.1016/s1387-3806(98)14292-6.
[70] P.A. Gerakines, M.H. Moore, Carbon suboxide in astrophysical ice analogs, Icarus. 154 (2001) 372–380. https://doi.org/10.1006/icar.2001.6711.
[71] N. Tsoureas, J.C. Green, F.G.N. Cloke, H. Puschmann, S.M. Roe, G. Tizzard, Trimerisation of carbon suboxide at a di-titanium centre to form a pyrone ring system, Chem. Sci. 9 (2018) 5008–5014. https://doi.org/10.1039/c8sc01127c.
[72] M. Allen, Carbon suboxide in Halley [6], Nature. 354 (1991) 272. https://doi.org/10.1038/354272a0.
[73] M. Shao, D. Wang, G. Yu, B. Hu, W. Yu, Y. Qian, The synthesis of carbon nanotubes at low temperature via carbon suboxide disproportionation, Carbon N. Y. 42 (2004) 183–185. https://doi.org/10.1016/j.carbon.2003.10.010.
[74] H.B. Palmer, W.D. Cross, Carbon films from carbon suboxide decomposition. Inhibition by carbon monoxide and the heat of formation of C2O, Carbon N. Y. 3 (1966) 475–481. https://doi.org/10.1016/0008-6223(66)90033-9.
[75] A. Scalbert, L. Brennan, O. Fiehn, T. Hankemeier, B.S. Kristal, B. van Ommen, E. Pujos-Guillot, E. Verheij, D. Wishart, S. Wopereis, Mass-spectrometry-based metabolomics: Limitations and recommendations for future progress with particular focus on nutrition research, Metabolomics. 5 (2009) 435–458. https://doi.org/10.1007/S11306-009-0168-0/TABLES/1.
[76] Z. Miao, W. Hou, M. Liu, Y. Zhang, S. Yao, BSA capped bi-functional fluorescent Cu nanoclusters as pH sensor and selective detection of dopamine, New J. Chem. 42 (2018) 1446–1456. https://doi.org/10.1039/c7nj03524a.
[77] Y. Liu, X. He, P. Ma, Y. Huang, X. Li, Y. Sun, X. Wang, D. Song, Fluorometric detection of dopamine based on 3-aminophenylboronic acid-functionalized AgInZnS QDs and cells imaging, Talanta. 217

(2020) 121081. https://doi.org/10.1016/J.TALANTA.2020.121081.
[78] A. Roychoudhury, K.A. Francis, J. Patel, S. Kumar, J. Ab, S. Basu, A decoupler-free simple paper microchip capillary electrophoresis device for simultaneous detection of dopamine, epinephrine and serotonin †, RSD Adv. 10 (2020) 25487–25495. https://doi.org/10.1039/d0ra03526b.
[79] A. Gottås, Ripel, F. Boix, V. Vindenes, J. Mørland, E.L. Øiestad, Determination of dopamine concentrations in brain extracellular fluid using microdialysis with short sampling intervals, analyzed by ultra high performance liquid chromatography tandem mass spectrometry, J. Pharmacol. Toxicol. Methods. 74 (2015) 75–79. https://doi.org/10.1016/J.VASCN.2015.06.002.
[80] Z. Liao, Y. Ma, S. Yao, J. Zhang, Y. Han, K. Xu, Honeycomb-patterned porous graphene film for electrochemical detection of dopamine, Appl. Surf. Sci. 605 (2022) 154725. https://doi.org/10.1016/J.APSUSC.2022.154725.
[81] S.K. Arumugasamy, S. Govindaraju, K. Yun, Electrochemical sensor for detecting dopamine using graphene quantum dots incorporated with multiwall carbon nanotubes, Appl. Surf. Sci. 508 (2020) 145294. https://doi.org/10.1016/J.APSUSC.2020.145294.
[82] K. Chen, W. Chou, L. Liu, Y. Cui, P. Xue, M. Jia, Electrochemical sensors fabricated by electrospinning technology: An overview, Sensors (Switzerland). 19 (2019). https://doi.org/10.3390/s19173676.
[83] H.C.A. Murthy, A.N. Wagassa, C.R. Ravikumar, H.P. Nagaswarupa, Functionalized metal and metal oxide nanomaterial-based electrochemical sensors, Elsevier Ltd., 2022. https://doi.org/10.1016/B978-0-12-823788-5.00001-6.
[84] G. Burns, M.Y. Ali, M.M.R. Howlader, Advanced functional materials for electrochemical dopamine sensors, TrAC - Trends Anal. Chem. 169 (2023) 117367. https://doi.org/10.1016/j.trac.2023.117367.
[85] G. Balkourani, A. Brouzgou, P. Tsiakaras, A review on recent advancements in electrochemical detection of dopamine using carbonaceous nanomaterials, Carbon N. Y. 213 (2023) 118281. https://doi.org/10.1016/j.carbon.2023.118281.
[86] N. Ndebele, P. Sen, T. Nyokong, Electrochemical detection of dopamine using phthalocyanine-nitrogen-doped graphene quantum dot conjugates, J. Electroanal. Chem. 886 (2021) 115111. https://doi.org/10.1016/j.jelechem.2021.115111.
[87] S.I. Kaya, S. Kurbanoglu, S.A. Ozkan, Nanomaterials-Based Nanosensors for the Simultaneous Electrochemical Determination of Biologically Important Compounds: Ascorbic Acid, Uric Acid, and Dopamine, Crit. Rev. Anal. Chem. 49 (2019) 101–125. https://doi.org/10.1080/10408347.2018.1489217.
[88] J.I. de Oliveira Filho, M.C. Faleiros, D.C. Ferreira, V. Mani, K.N. Salama, Empowering Electrochemical Biosensors with AI:

Overcoming Interference for Precise Dopamine Detection in Complex Samples, Adv. Intell. Syst. 5 (2023) 1–8. https://doi.org/10.1002/aisy.202300227.
[89] L. Yang, D. Liu, J. Huang, T. You, Simultaneous determination of dopamine, ascorbic acid and uric acid at electrochemically reduced graphene oxide modified electrode, Sensors Actuators, B Chem. 193 (2014) 166–172. https://doi.org/10.1016/j.snb.2013.11.104.
[90] J. Yu, T.H. Kim, A Facile Electrochemical Fabrication of Reduced Graphene Oxide-Modified Glassy Carbon Electrode for Simultaneous Detection of Dopamine, Ascorbic Acid, and Uric Acid, J. Electrochem. Sci. Technol. 8 (2017) 274–281. https://doi.org/10.33961/jecst.2017.8.4.274.
[91] B. Yu, D. Kuang, S. Liu, C. Liu, T. Zhang, Template-assisted self-assembly method to prepare three-dimensional reduced graphene oxide for dopamine sensing, Sensors Actuators, B Chem. 205 (2014) 120–126. https://doi.org/10.1016/j.snb.2014.08.038.
[92] Z.H. Sheng, X.Q. Zheng, J.Y. Xu, W.J. Bao, F. Bin Wang, X.H. Xia, Electrochemical sensor based on nitrogen doped graphene: Simultaneous determination of ascorbic acid, dopamine and uric acid, Biosens. Bioelectron. 34 (2012) 125–131. https://doi.org/10.1016/j.bios.2012.01.030.
[93] K. Chu, F. Wang, X. lin Zhao, X. wei Wang, Y. Tian, Electrochemical dopamine sensor based on P-doped graphene: Highly active metal-free catalyst and metal catalyst support, Mater. Sci. Eng. C. 81 (2017) 452–458. https://doi.org/10.1016/j.msec.2017.08.053.
[94] M. Li, C. Liu, H. Zhao, H. An, H. Cao, Y. Zhang, Z. Fan, Tuning sulfur doping in graphene for highly sensitive dopamine biosensors, Carbon N. Y. 86 (2015) 197–206. https://doi.org/10.1016/j.carbon.2015.01.029.
[95] W.S. Hummers, R.E. Offeman, Preparation of Graphitic Oxide, J. Am. Chem. Soc. 80 (1958) 1339. https://doi.org/10.1021/ja01539a017.
[96] X. Yan, J. Chen, J. Yang, Q. Xue, P. Miele, Fabrication of free-standing, electrochemically active, and biocompatible graphene oxide-polyaniline and graphene-polyaniline hybrid papers, ACS Appl. Mater. Interfaces. 2 (2010) 2521–2529. https://doi.org/10.1021/am100293r.
[97] J. Gaidukevic, R. Aukstakojyte, T. Navickas, R. Pauliukaite, J. Barkauskas, A novel approach to prepare highly oxidized graphene oxide: structural and electrochemical investigations, Appl. Surf. Sci. 567 (2021) 150883. https://doi.org/10.1016/j.apsusc.2021.150883.
[98] L.G. Cançado, K. Takai, T. Enoki, M. Endo, Y.A. Kim, H. Mizusaki, A. Jorio, L.N. Coelho, R. Magalhães-Paniago, M.A. Pimenta, General equation for the determination of the crystallite size La of nanographite by Raman spectroscopy, Appl. Phys. Lett. 88 (2006) 163106. https://doi.org/10.1063/1.2196057.

[99] K. Haubner, J. Murawski, P. Olk, L.M. Eng, C. Ziegler, B. Adolphi, E. Jaehne, The Route to Functional Graphene Oxide, ChemPhysChem. 11 (2010) 2131–2139. https://doi.org/10.1002/cphc.201000132.
[100] E. Aliyev, V. Filiz, M.M. Khan, Y.J. Lee, C. Abetz, V. Abetz, Structural characterization of graphene oxide: Surface functional groups and fractionated oxidative debris, Nanomaterials. 9 (2019). https://doi.org/10.3390/nano9081180.
[101] M. Yahiaoui, H. Hadoun, I. Toumert, A. Hassani, Determination of kinetic parameters of Phlomis bovei de Noé using thermogravimetric analysis, Bioresour. Technol. 196 (2015) 441–447. https://doi.org/10.1016/j.biortech.2015.07.082.
[102] M.J. McAllister, J.L. Li, D.H. Adamson, H.C. Schniepp, A.A. Abdala, J. Liu, M. Herrera-Alonso, D.L. Milius, R. Car, R.K. Prud'homme, I.A. Aksay, Single sheet functionalized graphene by oxidation and thermal expansion of graphite, Chem. Mater. 19 (2007) 4396–4404. https://doi.org/10.1021/cm0630800.
[103] J.C. Van Miltenburg, M.A. Cuevas-Diarte, The influence of sample mass, heating rate and heat transfer coefficient on the form of DSC curves, Thermochim. Acta. 156 (1989) 291–297. https://doi.org/10.1016/0040-6031(89)87197-7.
[104] P. Malumba, L. Doran, S. Danthine, C. Blecker, F. Béra, The effect of heating rates on functional properties of wheat and potato starch-water systems, LWT - Food Sci. Technol. 88 (2018) 196–202. https://doi.org/10.1016/j.lwt.2017.10.017.
[105] N. Kongkaew, W. Pruksakit, S. Patumsawad, Thermogravimetric Kinetic Analysis of the Pyrolysis of Rice Straw, Elsevier B.V., 2015. https://doi.org/10.1016/j.egypro.2015.11.552.
[106] Z. Yang, H. Peng, W. Wang, T. Liu, Crystallization behavior of poly(ε-caprolactone)/layered double hydroxide nanocomposites, J. Appl. Polym. Sci. 116 (2010) 2658–2667. https://doi.org/10.1002/app.
[107] J. Barkauskas, J. Gaidukevič, G. Niaura, Thermal reduction of graphite oxide in the presence of nitrogen-containing dyes, Carbon Lett. 31 (2021) 1097–1110. https://doi.org/10.1007/s42823-021-00228-3.
[108] I. Jung, D.A. Field, N.J. Clark, Y. Zhu, D. Yang, R.D. Piner, S. Stankovich, D.A. Dikin, H. Geisler, C.A. Ventrice, R.S. Ruoff, Reduction kinetics of graphene oxide determined by electrical transport measurements and temperature programmed desorption, J. Phys. Chem. C. 113 (2009) 18480–18486. https://doi.org/10.1021/jp904396j.
[109] M. V. Alonso, M. Oliet, J.M. Pérez, F. Rodríguez, J. Echeverría, Determination of curing kinetic parameters of lignin-phenol-formaldehyde resol resins by several dynamic differential scanning calorimetry methods, Thermochim. Acta. 419 (2004) 161–167. https://doi.org/10.1016/j.tca.2004.02.004.
[110] A.R. MacIntosh, G. Jiang, P. Zamani, Z. Song, A. Riese, K.J. Harris,

X. Fu, Z. Chen, X. Sun, G.R. Goward, Phosphorus and Nitrogen Centers in Doped Graphene and Carbon Nanotubes Analyzed through Solid-State NMR, J. Phys. Chem. C. 122 (2018) 6593–6601. https://doi.org/10.1021/acs.jpcc.7b11671.

[111] A. V. Okotrub, M.A. Kanygin, V.O. Koroteev, S.G. Stolyarova, D. V. Gorodetskiy, Y. V. Fedoseeva, I.P. Asanov, L.G. Bulusheva, A. Vyalikh, Phosphorus incorporation into graphitic material via hot pressing of graphite oxide and triphenylphosphine, Synth. Met. 248 (2019) 53–58. https://doi.org/10.1016/j.synthmet.2019.01.005.

[112] N. Sharma, V. Sharma, R. Vyas, M. Kumari, A. Kaushal, R. Gupta, S.K. Sharma, K. Sachdev, A new sustainable green protocol for production of reduced graphene oxide and its gas sensing properties, J. Sci. Adv. Mater. Devices. 4 (2019) 473–482. https://doi.org/10.1016/j.jsamd.2019.07.005.

[113] I. Sengupta, S. Chakraborty, M. Talukdar, S.K. Pal, S. Chakraborty, Thermal reduction of graphene oxide: How temperature influences purity, J. Mater. Res. 33 (2018) 4113–4122. https://doi.org/10.1557/jmr.2018.338.

[114] F.T. Johra, J.W. Lee, W.G. Jung, Facile and safe graphene preparation on solution based platform, J. Ind. Eng. Chem. 20 (2014) 2883–2887. https://doi.org/10.1016/j.jiec.2013.11.022.

[115] B. Ma, R.D. Rodriguez, A. Ruban, S. Pavlov, E. Sheremet, The correlation between electrical conductivity and second-order Raman modes of laser-reduced graphene oxide, Phys. Chem. Chem. Phys. 21 (2019) 10125–10134. https://doi.org/10.1039/c9cp00093c.

[116] R. Muzyka, S. Drewniak, T. Pustelny, M. Chrubasik, G. Gryglewicz, Characterization of graphite oxide and reduced graphene oxide obtained from different graphite precursors and oxidized by different methods using Raman spectroscopy, Materials (Basel). 11 (2018) 15–17. https://doi.org/10.3390/ma11071050.

[117] R. Kumar, A. Kaur, Chemiresistive gas sensors based on thermally reduced graphene oxide for sensing sulphur dioxide at room temperature, Diam. Relat. Mater. 109 (2020) 108039. https://doi.org/10.1016/j.diamond.2020.108039.

[118] B. Marinho, M. Ghislandi, E. Tkalya, C.E. Koning, G. de With, Electrical conductivity of compacts of graphene, multi-wall carbon nanotubes, carbon black, and graphite powder, Powder Technol. 221 (2012) 351–358. https://doi.org/10.1016/j.powtec.2012.01.024.

[119] J. Gaidukevič, R. Pauliukaitė, G. Niaura, I. Matulaitienė, O. Opuchovič, A. Radzevič, G. Astromskas, V. Bukauskas, J. Barkauskas, Synthesis of reduced graphene oxide with adjustable microstructure using regioselective reduction in the melt of boric acid: Relationship between structural properties and electrochemical performance, Nanomaterials. 8 (2018) 889. https://doi.org/10.3390/nano8110889.

[120] S. Rattanaweeranon, P. Limsuwan, V. Thongpool, V. Piriyawong, P. Asanithi, Influence of bulk graphite density on electrical conductivity, Procedia Eng. 32 (2012) 1100–1106. https://doi.org/10.1016/j.proeng.2012.02.061.
[121] C. Ayyappadas, O.S. Shanu, A. Vijayan, I.A. Mohammed, V. Vishnu, M. Shamnadh, Effect of graphene, SiC and graphite addition on hardness, microstructure and electrical conductivity of microwave sintered copper MMCs fabricated by powder metallurgy route, J. Phys. Conf. Ser. 1355 (2019) 012035. https://doi.org/10.1088/1742-6596/1355/1/012035.
[122] H. Park, S. Lim, D. Du Nguyen, J.W. Suk, Electrical measurements of thermally reduced graphene oxide powders under pressure, Nanomaterials. 9 (2019) 1–11. https://doi.org/10.3390/nano9101387.
[123] X. Fan, H. Xu, S. Zuo, Z. Liang, S. Yang, Y. Chen, Preparation and supercapacitive properties of phosphorus-doped reduced graphene oxide hydrogel, Electrochim. Acta. 330 (2020) 135207. https://doi.org/10.1016/j.electacta.2019.135207.
[124] G. Hussain, D.S. Silvester, Comparison of Voltammetric Techniques for Ammonia Sensing in Ionic Liquids, Electroanalysis. 30 (2018) 75–83. https://doi.org/10.1002/elan.201700555.
[125] A.U.H.A. Shah, A. Inayat, S. Bilal, Enhanced electrocatalytic behaviour of poy(Aniline-co-2-hydroxyaniline) coated electrodes for hydrogen peroxide electrooxidation, Catalysts. 9 (2019). https://doi.org/10.3390/catal9080631.
[126] W. Sun, G. Sun, W. Yang, S. Yang, Q. Xin, A methanol concentration sensor using twin membrane electrode assemblies operated in pulsed mode for DMFC, J. Power Sources. 162 (2006) 1115–1121. https://doi.org/10.1016/j.jpowsour.2006.07.033.
[127] T.K. Aparna, R. Sivasubramanian, M.A. Dar, One-pot synthesis of Au-Cu2O/rGO nanocomposite based electrochemical sensor for selective and simultaneous detection of dopamine and uric acid, J. Alloys Compd. 741 (2018) 1130–1141. https://doi.org/10.1016/j.jallcom.2018.01.205.
[128] F. Mahmood, Y. Sun, C. Wan, Biomass-derived porous graphene for electrochemical sensing of dopamine, RSC Adv. 11 (2021) 15410–15415. https://doi.org/10.1039/d1ra00735a.
[129] C. Wang, J. Du, H. Wang, C. Zou, F. Jiang, P. Yang, Y. Du, A facile electrochemical sensor based on reduced graphene oxide and Au nanoplates modified glassy carbon electrode for simultaneous detection of ascorbic acid, dopamine and uric acid, Sensors Actuators, B Chem. 204 (2014) 302–309. https://doi.org/10.1016/j.snb.2014.07.077.
[130] X. Zhang, Y.C. Zhang, L.X. Ma, One-pot facile fabrication of graphene-zinc oxide composite and its enhanced sensitivity for simultaneous electrochemical detection of ascorbic acid, dopamine

and uric acid, Sensors Actuators, B Chem. 227 (2016) 488–496. https://doi.org/10.1016/j.snb.2015.12.073.
[131] D. Kim, S. Lee, Y. Piao, Electrochemical determination of dopamine and acetaminophen using activated graphene-Nafion modified glassy carbon electrode, J. Electroanal. Chem. 794 (2017) 221–228. https://doi.org/10.1016/j.jelechem.2017.04.018.
[132] S.S. Choo, E.S. Kang, I. Song, D. Lee, J.W. Choi, T.H. Kim, Electrochemical detection of dopamine using 3D porous graphene oxide/gold nanoparticle composites, Sensors (Switzerland). 17 (2017). https://doi.org/10.3390/s17040861.
[133] P.S. Hung, G.R. Wang, W.A. Chung, T.T. Chiang, P.W. Wu, Green synthesis of ni@PEDOT and ni@PEDOT/au (Core@shell) inverse opals for simultaneous detection of ascorbic acid, dopamine, and uric acid, Nanomaterials. 10 (2020) 1–20. https://doi.org/10.3390/nano10091722.
[134] M. Ayiania, M. Smith, A.J.R. Hensley, L. Scudiero, J.S. McEwen, M. Garcia-Perez, Deconvoluting the XPS spectra for nitrogen-doped chars: An analysis from first principles, Carbon N. Y. 162 (2020) 528–544. https://doi.org/10.1016/j.carbon.2020.02.065.
[135] A. Jorio, A.G. Souza Filho, Raman Studies of Carbon Nanostructures, Annu. Rev. Mater. Res. 46 (2016) 357–382. https://doi.org/10.1146/ANNUREV-MATSCI-070115-032140.
[136] A. Jorio, L.G. Cançado, Perspectives on Raman spectroscopy of graphene-based systems: from the perfect two-dimensional surface to charcoal, Phys. Chem. Chem. Phys. 14 (2012) 15246–15256. https://doi.org/10.1039/C2CP42621H.
[137] J. Ribeiro-Soares, L.G. Cançado, N.P.S. Falcão, E.H. Martins Ferreira, C.A. Achete, A. Jorio, The use of Raman spectroscopy to characterize the carbon materials found in Amazonian anthrosoils, J. Raman Spectrosc. 44 (2013) 283–289. https://doi.org/10.1002/JRS.4191.
[138] J. Ribeiro-Soares, M.E. Oliveros, C. Garin, M. V. David, L.G.P. Martins, C.A. Almeida, E.H. Martins-Ferreira, K. Takai, T. Enoki, R. Magalhães-Paniago, A. Malachias, A. Jorio, B.S. Archanjo, C.A. Achete, L.G. Cançado, Structural analysis of polycrystalline graphene systems by Raman spectroscopy, Carbon N. Y. 95 (2015) 646–652. https://doi.org/10.1016/J.CARBON.2015.08.020.
[139] S. Claramunt, A. Varea, D. López-Díaz, M.M. Velázquez, A. Cornet, A. Cirera, The importance of interbands on the interpretation of the raman spectrum of graphene oxide, J. Phys. Chem. C. 119 (2015) 10123–10129. https://doi.org/10.1021/ACS.JPCC.5B01590/SUPPL_FILE/JP5B01590_SI_001.PDF.
[140] R. Trusovas, K. Ratautas, G. Račiukaitis, G. Niaura, Graphene layer formation in pinewood by nanosecond and picosecond laser irradiation, Appl. Surf. Sci. 471 (2019) 154–161.

https://doi.org/10.1016/J.APSUSC.2018.12.005.
[141] H. Zhang, T. Kuila, N.H. Kim, D.S. Yu, J.H. Lee, Simultaneous reduction, exfoliation, and nitrogen doping of graphene oxide via a hydrothermal reaction for energy storage electrode materials, Carbon N. Y. 69 (2014) 66–78. https://doi.org/10.1016/J.CARBON.2013.11.059.
[142] F.Y. Kong, L. Yao, R.F. Li, H.Y. Li, Z.X. Wang, W.X. Lv, W. Wang, Synthesis of nitrogen-doped reduced graphene oxide loading with Au-Ag bimetallic nanoparticles for electrochemical detection of daunorubicin, J. Alloys Compd. 797 (2019) 413–420. https://doi.org/10.1016/J.JALLCOM.2019.04.276.
[143] P. Bharathidasan, M.B. Idris, D.W. Kim, S.R. Sivakkumar, S. Devaraj, Enhanced capacitance properties of nitrogen doped reduced graphene oxide obtained by simultaneous reduction and nitrogen doping, FlatChem. 11 (2018) 24–31. https://doi.org/10.1016/j.flatc.2018.10.001.
[144] B.D. Ossonon, D. Bélanger, Synthesis and characterization of sulfophenyl-functionalized reduced graphene oxide sheets, RSC Adv. 7 (2017) 27224–27234. https://doi.org/10.1039/c6ra28311j.
[145] Y. Cheng, S. Zhou, P. Hu, G. Zhao, Y. Li, X. Zhang, W. Han, Enhanced mechanical, thermal, and electric properties of graphene aerogels via supercritical ethanol drying and high-Temperature thermal reduction, Sci. Rep. 7 (2017) 1–11. https://doi.org/10.1038/s41598-017-01601-x.
[146] M. Ghislandi, E. Tkalya, B. Marinho, C.E. Koning, G. De With, Electrical conductivities of carbon powder nanofillers and their latex-based polymer composites, Compos. Part A Appl. Sci. Manuf. 53 (2013) 145–151. https://doi.org/10.1016/j.compositesa.2013.06.008.
[147] Q. Yan, R. Arango, J. Li, Z. Cai, Fabrication and characterization of carbon foams using 100% Kraft lignin, Mater. Des. 201 (2021) 109460. https://doi.org/10.1016/J.MATDES.2021.109460.
[148] M. Steinmetz, D. Lima, R.R.L. Machado, U. Sundararaj, M. Arjmand, A.B. da Silva, J.P. Santos, C.A. Pessôa, K. Wohnrath, Nitrogen-doped carbon nanotubes towards electrochemical sensing: Effect of synthesis temperature, Diam. Relat. Mater. 110 (2020) 108093. https://doi.org/10.1016/j.diamond.2020.108093.
[149] N. Elgrishi, K.J. Rountree, B.D. McCarthy, E.S. Rountree, T.T. Eisenhart, J.L. Dempsey, A Practical Beginner's Guide to Cyclic Voltammetry, J. Chem. Educ. 95 (2018) 197–206. https://doi.org/10.1021/acs.jchemed.7b00361.
[150] T.R.L.C. Paixão, Measuring Electrochemical Surface Area of Nanomaterials versus the Randles−Ševčík Equation, ChemElectroChem. 7 (2020) 3414–3415. https://doi.org/10.1002/CELC.202000633.
[151] P. Wiench, Z. González, S. Gryglewicz, R. Menéndez, G. Gryglewicz,

Enhanced performance of pyrrolic N-doped reduced graphene oxide-modified glassy carbon electrodes for dopamine sensing, J. Electroanal. Chem. 852 (2019) 113547. https://doi.org/10.1016/J.JELECHEM.2019.113547.
[152] N. Zhou, N. Wang, Z. Wu, L. Li, Probing active sites on metal-free, nitrogen-doped carbons for oxygen electroreduction: A review, Catalysts. 8 (2018) 509. https://doi.org/10.3390/catal8110509.
[153] N. Li, E. Zheng, X. Chen, S. Sun, Y. Ruan, X. Weng, C. You, Layer-by-layer assembled multilayer films of nitrogen-doped graphene and polyethylenimine for selective sensing of dopamine, Int. J. Electrochem. Sci. 8 (2013) 6524–6534.
[154] D. Minta, Z. González, P. Wiench, S. Gryglewicz, G. Gryglewicz, N-doped reduced graphene oxide/gold nanoparticles composite as an improved sensing platform for simultaneous detection of dopamine, ascorbic acid, and uric acid, Sensors (Switzerland). 20 (2020) 1–13. https://doi.org/10.3390/s20164427.
[155] R. Chen, Y. Wang, Y. Liu, J. Li, Selective electrochemical detection of dopamine using nitrogen-doped graphene/manganese monoxide composites, RSC Adv. 5 (2015) 85065–85072. https://doi.org/10.1039/c5ra14328d.
[156] Z. Yang, X. Zheng, J. Zheng, A facile one-step synthesis of Fe2O3/nitrogen-doped reduced graphene oxide nanocomposite for enhanced electrochemical determination of dopamine, J. Alloys Compd. 709 (2017) 581–587. https://doi.org/10.1016/J.JALLCOM.2017.03.201.

LIST OF PUBLICATIONS INCLUDED IN THE THESIS

1. **R. Aukštakojytė**, J. Gaidukevič, J. Barkauskas, Thermal reduction of graphene oxide in the presence of carbon suboxide, Journal of Solid State Chemistry, 301, 2021, 122365, DOI: 10.1016/j.jssc.2021.122365 (IF = 3.2, Q2);
2. **R. Aukštakojytė**, J. Gaidukevič, G. Niaura, M. Skapas, V. Bukauskas, J. Barkauskas, Structural control and electrical behaviour of thermally reduced graphene oxide samples assisted with malonic acid and phosphorus pentoxide, Inorganics, 10(9), 2022, 142, DOI: 10.3390/inorganics10090142 (IF = 3.1, Q2);
3. J. Gaidukevic, **R. Aukstakojyte**, J. Barkauskas, G. Niaura, T. Murauskas, R. Pauliukaite, A novel electrochemical sensor based on thermally reduced graphene oxide for the sensitive determination of dopamine, Applied Surface Science, 592, 2022, 153257, DOI: 10.1016/j.apsusc.2022.153257 (IF = 6.3, Q1);
4. **R. Aukštakojytė**, G. Niaura, V. Bukauskas, J. Barkauskas, R. Pauliukaitė, J. Gaidukevič, Bismarck brown-assisted hydrothermal synthesis of nitrogen-modified reduced graphene oxide for selective electrochemical detection of dopamine, Surfaces and Interfaces, 46, 2024, 104041, DOI: 10.1016/j.surfin.2024.104041 (IF = 5.7, Q1).

PUBLICATIONS NOT INCLUDED IN THE THESIS

1. A. Popov, **R. Aukstakojyte**, J. Gaidukevic, V. Lisyte, A. Kausaite-Minkstimiene, J. Barkauskas, A. Ramanaviciene, Reduced graphene oxide and polyaniline nanofibers nanocomposite for the development of an amperometric glucose biosensor, Sensors, 21, 2021, 948, DOI: 10.3390/s21030948 (IF = 3.4, Q1);
2. J. Gaidukevič, **R. Aukštakojytė**, T. Navickas, R. Pauliukaitė, J. Barkauskas, A novel approach to prepare highly oxidized graphene oxide: structural and electrochemical investigations, Applied Surface Science, 567, 2021, 150883, DOI: 10.1016/j.apsusc.2021.150883 (IF = 6.3, Q1);
3. J. Gaidukevic, **R. Aukstakojyte**, M. Kozlowski, J. Barkauskas, R. Pauliukaite, A simple preparation of N-doped reduced graphene oxide as an electrode material for the detection of hydrogen peroxide and glucose, Electrochimica Acta, 446, 2023, 142113, DOI: 10.1016/j.electacta.2023.142113 (IF = 5.5, Q2).

ATTENDED CONFERENCES

Oral presentations:

1. **R. Aukštakojytė** (*presenter*), J. Gaidukevič, R. Pauliukaitė, J. Barkauskas. A dopamine electrochemical sensor based on N-doped reduced graphene oxide electrode. Functional inorganic materials 2022, October 6–8, 2022, Vilnius, Lithuania;
2. J. Gaidukevič, **R. Aukštakojytė**, M. Kozłowski, J. Barkauskas, R. Pauliukaitė (*presenter*). Can graphene be sensitive? Functional inorganic materials 2022, October 6–8, 2022, Vilnius, Lithuania;
3. **R. Aukštakojytė** (*presenter*), J. Gaidukevič, R. Pauliukaitė, J. Barkauskas. Nitrogen-modified reduced graphene oxide as a platform for sensitive and selective electrochemical detection of dopamine. Open Readings 2023, April 18–20, 2023, Vilnius, Lithuania;
4. R. Pauliukaitė (*presenter*), J. Gaidukevič, **R. Aukštakojytė**, J. Barkauskas. V. Žutautas, R. Trusovas, A. Sartanavičius. Differently functionalized graphene oxide for sensing applications. 74th annual meeting of the International Society of Electrochemistry (ISE), September 3–8, 2023, Lyon, France;
5. **R. Aukštakojytė** (*presenter*), G. Li, J. Kujawa, W. Kujawski, J. Gaidukevič. PDMS membranes modified with graphene-based materials for pervaporation processes. Membrane Materials-Modification and Separation (M3-S), September 26–28, 2023, Torun, Poland. ***The best oral presentation award***;
6. J. Gaidukevič (*presenter*), **R. Aukštakojytė**, M. Kozłowski, R. Pauliukaitė. Nitrogen-doped reduced graphene oxide for electrochemical sensing applications. EcoBalt 2023, October 9–11, 2023, Tallinn, Estonia;
7. J. Gaidukevič (*presenter*), **R. Aukštakojytė**, R. Pauliukaitė. Anglies alotropinių atmainų įvairovė ir jų panaudojimas. Chemija ir geomokslai 2024, March 22, 2024, Vilnius, Lithuania.

Poster presentations:

1. **R. Aukštakojytė** (*presenter*), J. Gaidukevič, J. Barkauskas. Thermal reduction of graphite oxide in the presence of malonic acid. Open Readings 2019, March 19–22, 2019, Vilnius, Lithuania;
2. **R. Aukštakojytė** *(presenter)*, J. Gaidukevič, J. Barkauskas. Malonic acid assisted reduction of graphite oxide: structural characterisation. Chemistry and Chemical Technology 2019, May 16, 2019, Vilnius, Lithuania;
3. **R. Aukštakojytė** *(presenter)*, J. Gaidukevič, J. Barkauskas. Structural characterization of thermally reduced graphene oxide in the presence of

malonic acid and phosphorus pentoxide. Functional materials and nanotechnologies 2020, November 23–24, 2020, Vilnius, Lithuania;
4. **R. Aukštakojytė** *(presenter)*, J. Gaidukevič, J. Barkauskas. Synthesis and structural characterization of graphene oxide and thermally reduced graphene oxide. Nanostructured bioceramic materials 2020, December 1–3, 2020, Vilnius, Lithuania;
5. **R. Aukštakojytė** *(presenter)*, J. Gaidukevič, J. Barkauskas. The thermal decomposition of graphene oxide in the presence of carbon suboxide. Open readings 2021, March 16–19, 2021, Vilnius, Lithuania;
6. J. Gaidukevič (*presenter*), R. Pauliukaitė, **R. Aukštakojytė**, J. Barkauskas. Novel synthesis of graphene oxide: structural and electrochemical investigation. Advanced materials and technologies 2021, August 23–27, 2021, Palanga, Lithuania;
7. **R. Aukštakojytė** *(presenter)*, J. Gaidukevič, J. Barkauskas. Thermal reduction of graphene oxide using carbon suboxide. Advanced materials and technologies 2021, August 23–27, 2021, Palanga, Lithuania;
8. **R. Aukštakojytė** *(presenter)*, J. Gaidukevič, J. Barkauskas. Kinetics of graphene oxide thermal decomposition in the presence of carbon suboxide. Chemistry and chemical technologies 2021, September 24, 2021, Vilnius, Lithuania;
9. J. Gaidukevič *(presenter)*, **R. Aukštakojytė**, J. Barkauskas, R. Pauliukaitė. A novel reduced graphene oxide based electrochemical sensor for the detection of dopamine. Chemistry and chemical technology 2021, September 24, 2021, Vilnius, Lithuania;
10. **R. Aukštakojytė** *(presenter)*, J. Gaidukevič, R. Pauliukaitė, J. Barkauskas. Synthesis and characterisation of thermally reduced graphene oxide and its application as a novel electrode material for dopamine detection. Open Readings 2022, March 15–18, 2022, Vilnius, Lithuania;
11. J. Gaidukevič *(presenter)*, **R. Aukštakojytė**, R. Pauliukaitė. New Bismarck Brown functionalized graphene oxide nanocomposite as electrode material for the electroanalysis of dopamine. 18th International conference on electroanalysis ESEAC 2022, June 5–9, 2022, Vilnius, Lithuania;
12. J. Gaidukevič *(presenter)*, **R. Aukštakojytė**, A. Bobrowski, A. Krolicka, R. Pauliukaitė. Electrochemical uric acid sensor based on P-doped graphene oxide. ISE: Regional Meeting International Society of Electrochemistry, August 15–19, 2022, Prague, Czech Republic;
13. **R. Aukštakojytė** *(presenter)*, J. Gaidukevič, R. Pauliukaitė, J. Barkauskas. Nitrogen-doped reduced graphene oxide as a sensitive platform for detection of dopamine. Chemistry and chemical technology 2022, October 14, 2022, Kaunas, Lithuania;

14. **R. Aukštakojytė** *(presenter)*, J. Gaidukevič, J. Barkauskas. Effect of B- and N-codoping on the structural and morphological properties of reduced graphene oxide. Chemistry and chemical technology 2023, March 10, 2023, Vilnius, Lithuania. ***The best poster presentation award***;
15. **R. Aukštakojytė** *(presenter)*, J. Gaidukevič, J. Barkauskas. Structural and morphological investigations of N-and B-modified reduced graphene oxide. EcoBalt 2023, October 9–11, 2023, Tallinn, Estonia;
16. **R. Aukštakojytė** (*presenter*), J. Gaidukevič, R. Pauliukaitė. Selective electrochemical detection of dopamine using nitrogen-modified reduced graphene oxide. Chemija ir geomokslai 2024, March 22, 2024, Vilnius, Lithuania;
17. **R. Aukštakojytė** (*presenter*), J. Gaidukevič, R. Pauliukaitė. Nitrogen-modified reduced graphene oxide: Bismarck brown-assisted hydrothermal synthesis and selective electrochemical sensing of dopamine. The first joint European MRS chapter workshop, March 19–22, 2024, Paris, France;
18. **R. Aukštakojytė** (*presenter*), R. Pauliukaitė, J. Gaidukevič. Synthesis and Characterization of Nitrogen-Modified Reduced Graphene Oxide. Open Readings 2024, April 23–26, 2024, Vilnius, Lithuania. ***The best poster presentation award***;
19. **R. Aukštakojytė** (*presenter*), R. Pauliukaitė, J. Gaidukevič. Phosphorus-Modified Reduced Graphene Oxide as a Platform for Simultaneous Electrochemical Detection of Dopamine and Uric Acid. 2024 IEEE 14th International conference Nanomaterials: Applications & Properties, September 8–13, 2024, Riga, Latvia.

CURRICULUM VITAE

Personal information	
Name, surname	Rūta Aukštakojytė
Email	ruta.aukstakojyte@chgf.vu.lt, ruta.aukstakojyte@gmail.com
Education	
2020–2024	PhD studies in Chemistry, Faculty of Chemistry and Geosciences, Vilnius University
2018–2020	Master of Science in Chemistry, Faculty of Chemistry and Geosciences, Vilnius University
2014–2018	Bachelor of Science in Chemistry, Faculty of Chemistry and Geosciences, Vilnius University
Work experience	
2024-09 – *present*	Junior assistant at the Faculty of Chemistry and Geosciences, Vilnius University
2020-07 – *present*	Study coordinator at the Faculty of Chemistry and Geosciences, Vilnius University
2018-12 – 2020-07	Administrator at the Faculty of Chemistry and Geosciences, Vilnius University
2014-09 – 2014-10	Professional practice at the Life Science Center, Vilnius University
Internships	
2023-01-15 – 2023-02-06	Nicolaus Copernicus University in Toruń (Toruń, Poland)
2022-06-23 – 2022-07-22	Biosensor, SRL (Formello, Italy)
Visits	
2022-05-22 – 2022-05-26	Arqus Twinning visit at Leipzig University (Leipzig, Germany)
2023-11-25 – 2023-11-29	Arqus Twinning visit at University of Wroclaw (Wroclaw, Poland)
Awards and scholarships	
2019-05	The nominal scholarship of the Faculty of Chemistry and Geosciences

2022-04	The one-time target scholarship of Vilnius University for scientific achievements (spring semester, 2021–2022 study years)
2022-07	The doctoral scholarship for active scientific research according to the call of Research Council of Lithuania (No P-DAP-22-322, 2021–2022 study years)
2022-11	The one-time target scholarship of Vilnius University for scientific achievements (autumn semester, 2022–2023 study years)
2022-12	The PROM project scholarship for academic internship in Toruń, Poland
2023-03	The best poster presentation award in the international conference "Chemistry and Chemical Technology 2023", March 10, 2023, Vilnius, Lithuania
2023-04	The one-time target scholarship of Vilnius University for scientific achievements (spring semester, 2022–2023 study years)
2023-06	The grant for doctoral academic visits according to the call of Research Council of Lithuania (No P-DAP-23-51, 2022–2023 study years)
2023-09	The best oral presentation award in the international conference "Membrane Materials – Modification and Separation" (M3-S), September 26–28, 2023, Toruń, Poland
2023-10	The doctoral scholarship for active scientific research according to the call of Research Council of Lithuania (No P-DAP-23, 2022–2023 study years)
2024-04	The best poster presentation award in the international conference "Open Readings 2024", April 23–26, 2024, Vilnius, Lithuania
2024-06	The grant for doctoral academic visits according to the call of Research Council of Lithuania (No P-DAK-24-12, 2023–2024 study years)

Memberships	
2022-09 – *present*	A member of Lithuanian Chemical Society (LChD)
Projects	
2019–2020	National Program "Students research and practice 2019–2020". Project "Thermal reduction of graphene oxide in the presence of the mixture of malonic acid and phosphorus pentoxide: investigation of synthesis conditions and structural properties" (LRC project No 09.3.3-LMT-K-712-16-0154; 2019–2020).

ACKNOWLEDGMENT

Norėčiau padėkoti savo doktorantūros vadovei doc. dr. Justinai Gaidukevič už suteiktas žinias, diskusijas, patarimus, vertingas įžvalgas, kurios leido man augti ir tobulėti kaip mokslininkei. Ačiū už visokeriopą pagalbą, skirtą laiką ir rūpestį visų studijų metu. Esu labai dėkinga už pasitikėjimą manimi ir galimybę tyrinėti anglinių medžiagų pasaulį. Ačiū už tai, kad nepavykus eksperimentams, visada išgirsdavau tik padrąsinimo žodį, kuris skatino nepasiduoti ir motyvavo siekti geresnių rezultatų. Visada jaučiau, kad esame komanda, kurioje abipusė pagalba, bendras darbas ir žinių sintezė vedė prie puikių pasiekimų.

Ačiū moksliniam konsultantui prof. dr. Jurgiui Barkauskui, kad pakvietėte prisijungti prie Anglinių medžiagų laboratorijos kolektyvo dar trečiame bakalauro studijų kurse. Dėkoju už vertingas pamokas, skirtą laiką ir žinias. Ačiū už pažintį su matematiniu modeliavimu ir kristalų chemija.

Ačiū prof. dr. Rasai Pauliukaitei už galimybę atlikti elektrocheminius tyrimus ir už skirtą laiką gautų rezultatų analizei. Ačiū už Jūsų akademinį profesionalumą ir gerą žodį.

Ačiū prof. dr. Gediminui Niaurai už galimybę atlikti Raman spektroskopijos tyrimus ir pagalbą analizuojant Raman spektrus. Dėkoju už vertingas pastabas ir siūlymus.

Ačiū dr. Virginijui Bukauskui už galimybę atlikti elektrinio laidumo matavimus. Dėkoju dr. Martynui Skapui už atliktus peršvietimo elektroninės mikroskopijos matavimus, dr. Andriui Pakalniškiui už skenuojančios elektroninės mikroskopijos matavimus ir dr. Tomui Murauskui – už atliktus Rentgeno fotoelektroninės spektroskopijos matavimus.

Ypatingas ačiū dr. Gretai, Gintarei, dr. Aleksandrai, dr. Andriui, Viktorijai, Lukui ir dr. Dovydui už Jūsų draugystę. Džiaugiuosi, kad Universitetas suvedė mūsų kelius.

Ačiū Vilniaus universiteto Chemijos ir geomokslų fakulteto administracijai už visokeriopą pagalbą.

Ačiū artimiesiems už tikėjimą manimi ir mano svajonėmis.

COPIES OF PUBLICATIONS

1st publication

“Thermal reduction of graphene oxide in the presence of carbon suboxide”

R. Aukštakojytė, J. Gaidukevič, J. Barkauskas

Journal of Solid State Chemistry, 301, 2021, 122365
DOI: 10.1016/j.jssc.2021.122365

Journal of Solid State Chemistry 301 (2021) 122365

Contents lists available at ScienceDirect

Journal of Solid State Chemistry

journal homepage: www.elsevier.com/locate/jssc

Thermal reduction of graphene oxide in the presence of carbon suboxide

Rūta Aukštakojytė *, Justina Gaidukevič, Jurgis Barkauskas

Vilnius University, Faculty of Chemistry and Geosciences, Naugarduko Str. 24, LT, 03225, Vilnius, Lithuania

ARTICLE INFO

Keywords:
Carbon suboxide
Thermal reduction
Kinetic analysis
Graphene oxide

ABSTRACT

This work focused on the kinetic analysis of the thermal reduction reaction of graphene oxide (GO) both with and without carbon suboxide (C_3O_2) by using Borchardt-Daniels, Kissinger, and Ozawa models. The effect of C_3O_2 on the thermal decomposition of GO was investigated by thermogravimetry (TG), derivative thermogravimetry (DTG), and differential scanning colorimetry (DSC) analysis. It was noticed that C_3O_2 tends to increase the chemical reactivity of GO due to the decreasing of the reaction activation energy E_a. The apparent reaction order is determined to be 0.7 for the thermal decomposition of both studied samples. This value evidences the complex mechanism of the thermal decomposition of GO that includes consecutive zero-order and first-order processes. Finally, by comparing the enthalpy values of GO thermal decomposition, it was determined that GO sample with the additive of C_3O_2 releases a lower amount of energy comparing to that of pure GO during the thermal reduction.

1. Introduction

Graphene is an allotrope of carbon with sp^2 hybridised carbon atoms arranged in a two-dimensional honeycomb-like structure. Remarkable electrical, chemical, optical, thermal, physical, and mechanical properties make it a promising material for various applications in electronics or electrochemical power sources such as fuel or solar cells [1,2], lithium ion batteries [3] and supercapacitors [1]. Nowadays, thermal reduction of GO is one of the potential synthesis methods for a simple, cost-effective, rapid, and bulk production of graphene and its derivatives [4]. However, GO is attributed to a class of energetic materials due to the high enthalpy of decomposition (ΔH). It is prone to decompose violently if not properly stored and handled, and cause irreversible damage [5,6]. Furthermore, the mechanism of thermal reduction of GO is complex and not yet fully understood because of the simultaneous stages of dehydration, oxygen functionalities removal, and extensive graphene network disruption occurring during the thermal exfoliation [7]. To date, research on the GO reduction process has mostly focused on the electrochemical properties and structural changes of the final product and the investigation of the influence of thermally reduced GO (rGO) properties on their applications [8–13]. Despite the potential technological importance of GO, there are only relatively few studies on the kinetic analysis of GO thermal decomposition [5,14–19]. Qui et al. have indicated that the decomposition of GO could be more precisely controlled by adding salts or chemical reducing agents. It was noticed that the addition of KOH or NaOH reduces the onset temperature for GO thermal decomposition because hydroxyl ion acts as a catalyst. Moreover, the authors have revealed that ascorbic acid, citric acid, and glutathione also reduce the enthalpy of thermal decomposition but increase the reactivity of GO [17]. In our previous study, dye additives containing aromatic moieties have been shown to inhibit the thermal decomposition reaction of GO effectively. Moreover, it has been demonstrated that the use of dyes changes the mechanism of the thermal reduction of GO due to the increase of the reaction order from 0.7 for pure GO up to 2.0 for GO-dye nanocomposites [19]. Despite the recent progress on the kinetics studies of the thermal reduction of GO, its detailed mechanism has not been known yet, especially at the initial stages or at low temperatures. Moreover, GO is a complex material, and more work is needed to comprehend the thermodynamic and kinetic parameters for GO thermal reduction reaction and the role of additives on the decomposition process. Besides, safety concerns also encourage a much closer look at the behaviour of GO as an energetic material under typical manufacturing and process conditions [17].

Although some research has been carried out on the impact of additives on the kinetics of GO thermal reduction, there is no evidence about the kinetic investigations of the thermal decomposition behaviour of GO in the presence of carbon suboxide (C_3O_2). It is a molecule of linear structure (O═C═C═C═O) and can be synthesised by the dehydration reaction between malonic acid and phosphorus pentoxide at 150 °C temperature [20]:

* Corresponding author.
E-mail address: ruta.aukstakojyte@chgf.vu.lt (R. Aukštakojytė).

https://doi.org/10.1016/j.jssc.2021.122365
Received 26 April 2021; Received in revised form 9 June 2021; Accepted 16 June 2021
Available online 19 June 2021

$$3C_3H_4O_4 + P_4O_{10} \rightarrow 3C_3O_2 + 4H_3PO_4 \quad (1)$$

C_3O_2 is stable below −35 °C, but it spontaneously polymerises under standard temperature and pressure (0 °C and 1 atm) [21,22]. Most importantly, C_3O_2 thermally decomposes to elemental carbon and two carbon monoxide molecules above 16 °C [23]. For this reason, it is used as a source of atomic carbon for the synthesis of carbon nanotubes [24]. H. B. Palmer et al. have demonstrated that C_3O_2 is also a suitable starting material for the successful preparation of carbon films due to its useful rate and lower temperature of decomposition comparing to most hydrocarbons [25]. Vigorous release of gases during the thermal decomposition of GO leads to disruption of the graphene basal-plane that limits the potential applications of rGO in energy storage devices [26]. According to the research reported by Y. Liang et al. the structural disorders of rGO can be effectively repaired by using the supplemental carbon source to obtain highly conductive graphene-based electrodes [27]. Therefore, C_3O_2 is expected to be an alternative source of atomic carbon in the thermal reduction of GO to restore the conjugated aromatic structure of rGO efficiently. We suppose that the detailed knowledge of the kinetics of thermal decomposition of GO in the presence of C_3O_2 will provide the safer, large-scale, and better-controlled synthesis of high-quality rGO with enhanced electronic and structural properties in future research. Therefore, the aim of this work was to evaluate the effect of carbon suboxide on the kinetics of GO thermal decomposition reaction.

In this research, we have systematically explored the thermochemistry, mechanism of energetic GO behaviour, and discussed its implications for safe GO processing. The non-isothermal decomposition kinetics and thermal stability of pure GO and GO with the additive of C_3O_2 have been studied by DSC and TG/DTG techniques. The activation energy E_a values of thermal reduction of GO have been determined using three kinetic models such as Kissinger, Ozawa, and Borchardt-Daniels. To the best of our knowledge, the determination of E_a for GO by using Ozawa model has not been reported yet. Besides, the reaction order n and decomposition enthalpy ΔH of GO thermal decomposition have been estimated. Finally, to evaluate the impact of C_3O_2 on the structural properties of reduced GO, the X-ray diffraction (XRD) and Raman spectroscopy studies have been carried out.

2. Experimental methods

2.1. Preparation of samples

GO synthesis was carried out according to the protocol described by Yan et al. [28]. In a typical experiment, natural graphite powder (6.0 g) was mixed with conc. H_2SO_4 (24.0 mL), $K_2S_2O_8$ (5.0 g), and P_2O_5 (5.0 g). Then, the obtained pre-oxidized graphite prepared in this way was subjected to oxidation, following the methodology reported by Hummers et al. [29]. The resulting GO brown powder was purified by dialysis and dried in ambient atmosphere to a constant weight. Later, GO (0.1 g), malonic acid (0.01 g), and phosphorus pentoxide (0.009 g) were grounded in an agate mortar for 10 min. The prepared mixture was named GO_MA_P.

The GO and GO_MA_P were thermally annealed in the tubular furnace under argon atmosphere (60 mL min^{-1}) at 250 °C temperature. Thermally exfoliated GO_MA_P was thoroughly washed with deionized water and dried in air. Finally, thermally reduced GO and GO_MA_P were denoted as rGO and rGO_C_3O_2, respectively.

2.2. Thermal analysis

TG/DTG and DSC experiments were performed using a Thermal analyser STA6000 from PerkinElmer under non-isothermal heating mode. The prepared samples were heated at three heating rates: 2.5 °C min^{-1}, 5 °C min^{-1}, and 10 °C min^{-1} from room temperature to 300 °C. The ambient nitrogen atmosphere was used with a flow rate of 20 mL min^{-1}. The average mass of the samples was about 5 mg.

2.3. Kinetic models

Kinetic analysis of the thermal reduction reaction of GO was performed using the obtained DSC curves and three different methods: Kissinger, Ozawa, and Borchardt-Daniels. Kissinger and Ozawa methods are model-free and based upon a series of experiments, in which solid samples are heated at several different heating rates while the reaction exothermic peak is recorded. The Kissinger method is based on the following equation:

$$\ln\left(\frac{\beta}{T_m^2}\right) = \ln\left(\frac{ZR}{E_a}\right) - \frac{E_a}{RT_m}, \quad (2)$$

where E_a is the activation energy, β – the heating rate, T_m – the peak temperature of DSC curve, Z – the Arrhenius frequency factor, R – the universal gas constant (8.314 J mol^{-1} K^{-1}). The E_a can be evaluated as a slope from Kissinger's $\ln(\beta/T_m^2)$ plot versus $1/T_m$ [30].

In the Ozawa method, a linear relation between heating rates and temperature can be expressed as:

$$\log(\beta) \cong 0.4567 \cdot \frac{E_a}{R} \cdot \frac{1}{T_m}, \quad (3)$$

where E_a is the activation energy, β – the heating rate, T_m – the peak temperature, and R – the universal gas constant. The apparent value of E_a can be determined from a slope by plotting $\log(\beta)$ versus $1/T_m$ [31].

The Borchardt-Daniels model allows a rapid determination of kinetic parameters based on a single scan by DSC. This approach considers that the reaction follows nth order kinetics and obeys Arrhenius behaviour. The Borchardt-Daniels method gives the following equation:

$$\ln\left(\frac{d\alpha}{dt}\right) = \ln(k(T)) + n \ \ln(1-\alpha), \quad (4)$$

where $d\alpha/dt$ is the reaction rate, α – the fractional conversion, $k(T)$ – the specific reaction rate constant at temperature T, and n – the reaction order. The activation energy E_a can be obtained from the slope of $\ln(k(T))$ versus $1/T$ by fitting the n values [32].

2.4. Structural characterization techniques

The crystallographic information of the obtained products was investigated using a MiniFlex II X-ray diffractometer (Rigaku). The XRD patterns were recorded in the 2θ range from 5° to 60° using CuKα λ = 1.5406 Å radiation with a step of 0.010°. The interlayer distance d was evaluated using Bragg's equation:

$$n\lambda = 2dsin\theta \quad (5)$$

where λ is the wavelength of the X-ray beam, n – the positive integer, d – the distance between the adjacent interlayers, and θ – the diffraction angle.

Raman spectra were recorded using an Alpha300R Raman spectrometer (WiTec) equipped with a thermoelectrically cooled (−61 °C) CCD camera in the range of 300–3300 cm^{-1}. The He–Ne gas laser was provided an excitation beam at 532 nm with power restricted to 1 mW. The integration time was selected as 100 s.

3. Results and discussion

The TG and DTG curves at three different heating rates of 2.5, 5.0, and 10.0 °C min^{-1} from room temperature to 300 °C are shown in Fig. 1. Thermal properties of GO under ambient atmosphere are presented in Fig. 1 (a) and (b). From the TG curves, it can be observed that the thermal reduction of GO occurs in three stages. These results are in good

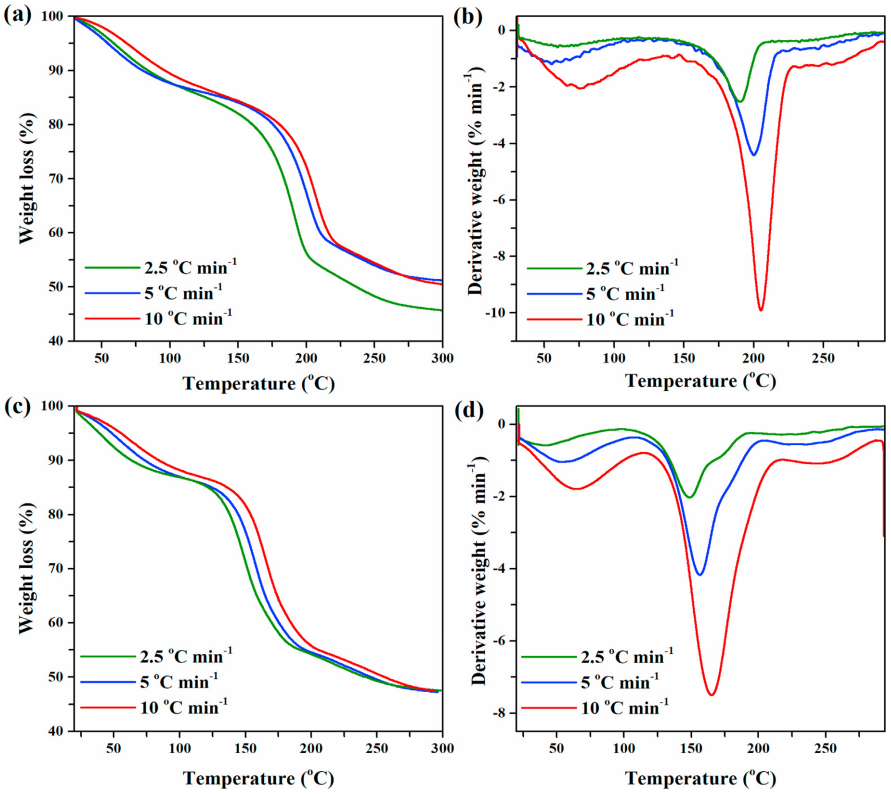

Fig. 1. TG curves of (a) GO and (c) GO_MA_P and DTG curves of (b) GO and (d) GO_MA_P at heating rates of 2.5, 5, and 10 °C min^{-1}.

agreement with those found in the literature [3,33]. The first stage (up to 100 °C) is associated with the evaporation of adsorbed or intercalated water molecules [3]. In the second step, the major loss of weight occurring between 100 °C and 250 °C results from the removal of labile oxygen functionalities (hydroxyl, lactone, carboxyl), forming CO and CO_2 gases [33]. The final step (>300 °C) could be attributed to the decomposition of stable oxygen-containing functional groups such as phenol, quinone, carbonyl and the degradation of graphitic GO network [3]. Moreover, it was noticed that the heating rate affects the thermal profile of samples by changing the position of the TG curve and the peak positions in DTG curves. Fig. 1 (a) shows that the residual weight after thermal decomposition of pure GO increases with increasing heating rate, which indicates the increase in thermal stability. Mass losses (measured at 240 °C) of 50.56%, 44.92%, and 44.42% were recorded for heating rates of 2.5, 5.0, and 10.0 °C min^{-1}, respectively. These observed differences are most likely due to the fact that the faster heating rate does not ensure the same temperature to the whole sample [34]. This trend suggests that the lower heating rate is more favourable for the production of high-quality rGO as the higher reduction degree is achieved. At higher heating rates, the decomposition process also slightly shifts towards the higher temperatures. This shift also could be assigned to the limitations of heat transfer [34].

The shapes of TG curves of the GO_MA_P sample are in general similar to that of pure GO. Nevertheless, each stage of decomposition of GO_MA_P is slightly shifted to lower temperatures. The shift can be more accurately observed using DTG curves (Fig. 1 (b) and (d)). The dehydration of the GO_MA_P sample starts at lower temperatures (50–90 °C) in comparison with that of pure GO (60–100 °C). The second stage, the deoxygenation of GO, occurs in the temperature range 90–200 °C, while the decomposition of pure GO starts at higher temperature (100–250 °C). Moreover, in TG curves of GO_MA_P sample, a decreasing trend in the mass loss with the increase in heating rate from 2.5 °C min^{-1} to 5.0 °C min^{-1} and then further to 10.0 °C min^{-1} was determined as in the case of pure GO. Mass losses (measured at 210 °C) of 46.86%, 46.40%, and 45.38% were recorded for heating rates of 2.5, 5.0, and 10.0 °C min^{-1}, respectively. Comparing the mass loss values and DTG curves of GO and GO_MA_P samples, one can conclude that the use of C_3O_2 additive in the reduction process can provide new possibilities in the decomposition of GO by reducing the temperature of the process. The successful low-temperature reduction of GO under ambient atmosphere could open new possibilities for the safe, large-scale production of graphene and the development of graphene-based composites.

In order to obtain a better understanding of the reaction that occurs during the thermal decomposition of pure GO and GO with C_3O_2 additive, the kinetic (activation energy, E_a; reaction order, n) and thermodynamic (reaction heat, ΔH) parameters were determined using the DSC

analysis. The DSC curves of GO, GO_MA_P, and the mixture of malonic acid and phosphorus pentoxide are displayed in Fig. 2.

DSC results of GO and GO_MA_P are in line with the studies obtained from TG/DTG. The faster heating rates β cause a marked shift in the peak maxima T_m of decomposition reaction to higher temperatures. As it was mentioned above, this shift is due to the heat transfer limitations at higher heating rates [34]. At a lower heating rate, the sample comes quickly into equilibrium with the external furnace temperature at any point with an increase in temperature. However, at a faster heating rate, equilibrium reaches slowly, and as such, the curve moves toward the high-temperature region. In addition, in the DSC results presented in Fig. 2 (b) the shoulder in the temperature range of 160–200 °C is observed. We are to assume that this shoulder in the DSC thermograms of GO_MA_P could correspond to the decomposition of non-reacted GO. We suppose that the amount of C_3O_2 reacted with GO was non-stoichiometric, since some part of gaseous C_3O_2 formed during the reaction between malonic acid and phosphorus pentoxide did not react with GO and was able to evaporate. Moreover, the amount of used mixture of malonic acid and phosphorous pentoxide was less comparing to the stoichiometric conditions. Thus, we consider that not the whole amount of GO reacts with C_3O_2 and the decomposition of the non-reacted amount of GO occurs in a different manner compared to that of pure GO without additives. The thermodynamic parameter (ΔH) and the temperatures (T_{onset} and T_m) at the peak of the DSC exotherm are summarized in Table 1. The value of T_{onset} specifies the practical start of thermal reduction of GO and it is reported to be in the range of 150–220 °C [17]. Moreover, in this study, a significant shift of T_{onset} to lower temperatures is observed using an additive. The addition of C_3O_2 can reduce the T_{onset} up to 125 °C at the heating rate of 2.5 °C min^{-1}, indicating the decreased reduction temperature of GO. Determined ΔH values of pure GO are similar to those reported in Refs. [5,35]. An average value of the enthalpy of the GO decomposition is 1487.18 J g^{-1}. In addition, from Table 1, it can be noted that the amount of energy released is reduced using C_3O_2 in the reaction mixture. As a result, the average ΔH of

Table 1
Parameters of DSC peaks and determined values of decomposition enthalpy at the heating rates of 2.5, 5, and 10 °C min^{-1}.

	β (°C min^{-1})	T_{onset} (°C)	T_m (°C)	ΔH (J g^{-1})
GO	2.5	166	190	1449.52
	5	173	201	1477.89
	10	186	207	1534.12
GO_MA_P	2.5	125	149	1083.47
	5	133	158	1169.65
	10	140	167	1296.88

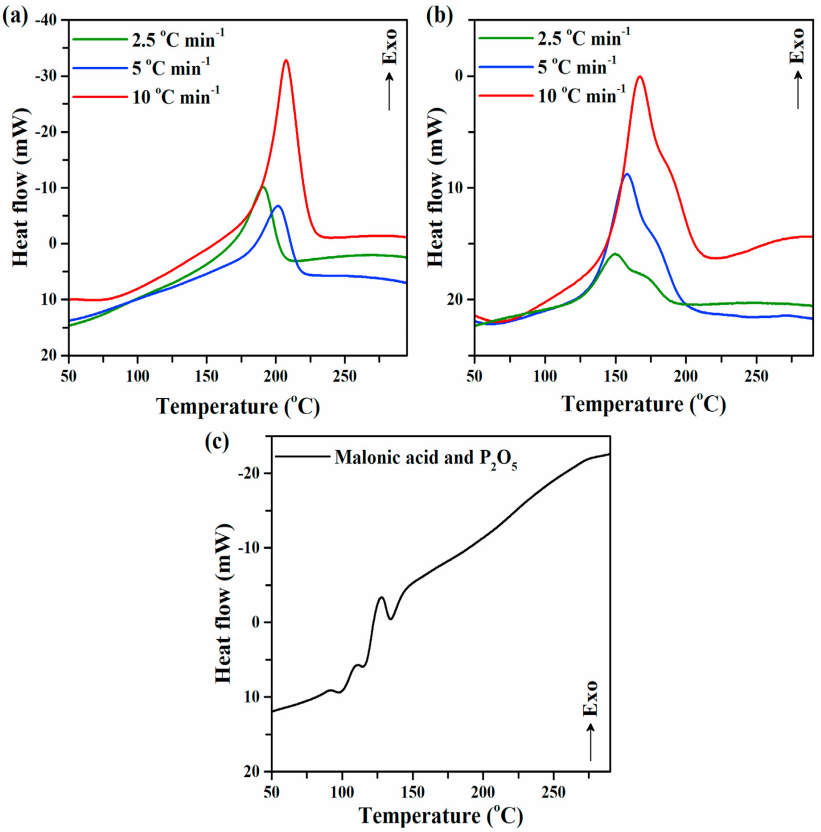

Fig. 2. DSC curves of (a) GO, (b) GO_MA_P at heating rates of 2.5, 5, and 10 °C min^{-1}, and (c) the mixture of malonic acid and P_2O_5 at the heating rate of 10 °C min^{-1}.

GO was decreased by 303.85 J g^{-1} with an additive of C_3O_2. Furthermore, these results show that heating rate affects the ΔH values and exhibits an important role for ensuring the safe process of thermal reduction of GO. The enthalpy increases with increasing the heating rate for pure GO and GO_MA_P samples. The enthalpy determined using heating rate range of 2.5 and 10 °C min^{-1} varied respectively between 1449.52 J g^{-1} and 1534.12 J g^{-1} for GO and between 1083.47 J g^{-1} and 1296.88 J g^{-1} for GO_MA_P. There might be various reasons for this increase. The first hypothesis is related to the instrumental property since the decomposition enthalpies linearly depends on to the heating rate. The heat flow (W) used in DSC is related to sample mass (m), the specific heat (C_p), and the heating rate (β) by equation $W = \beta \cdot m \cdot C_p$ [36]. Increasing the scanning rate during DSC measurements would increase the apparent intensity of endotherms or exotherms since DSC measures the heat flow as a function of time and temperature [36,37]. A second hypothesis that could clarify the increase of decomposition enthalpy with the heating rate is associated with GO structural changes occurring during thermal decomposition. In different stages of reduction process GO suffers complex restructurings such as endothermic dehydration, the release of CO, CO_2, and other carbon-containing gaseous products, the partial recovery of sp^2-hybridized carbon structure, and the rearrangement of carbon framework, where more complex carbonaceous structures and defects are formed [3,33]. All of these circumstances may vary the enthalpy value recorded during DSC analysis. Furthermore, the DSC curve of the mixture of malonic acid and phosphorus pentoxide presented in Fig. 2 (c) shows that this mixture does not have influence on the DSC of GO_MA_P. It could be explained by the positions of the peaks. The DSC peaks of the mixture of malonic acid and P_2O_5 observed in the temperature range of 85–140 °C are not visible in the DSC data of GO_MA_P. Furthermore, the amount of the mixture used in the investigation was relatively low that also reduced the possibility of system error during the DSC investigation.

Further, the Borchardt-Daniels model was applied with three heating rates (2.5, 5, and 10 °C min^{-1}) for the kinetic parameters (activation energy E_a and reaction order n) evaluation of the thermal decomposition of pure GO and GO_MA_P. The Borchardt-Daniels fitting plots of $\ln(k(T))$ vs. $1/T_m$ and kinetic parameters are shown in Fig. 3 and Table 2, respectively. These results show a positive relationship between heating rate and activation energy. The values of E_a increase with increasing the heating rate for both studied samples. This is because model fitting kinetic method, namely Borchardt-Daniels method, generally involves a single heating rate, and the disadvantage is that activation energy varies with heating rate. This discrepancy is likely due to the higher thermal lag appeared at the higher heating rate [38,39].

The most significant observation to emerge from the analysis was that, the addition of C_3O_2 to the reaction mixture results in a decrease of E_a by approximately 27 kJ mol^{-1} at all heating rates comparing to that of pure GO. Supposedly, it shows that carbon suboxide molecules catalyse the thermal decomposition reaction of GO and increase the reactivity of GO. Moreover, it should be noted that pure GO exhibits higher thermal stability than GO_MA_P due to the greater value of E_a for GO. The apparent reaction order for both GO and GO_MA_P is the same ($n = 0.7$), which is in agreement with the value of GO reported in Refs. [17,19]. The fractional value of n demonstrates a complex mechanism of the thermal reduction reaction of both GO and GO_MA_P. Also, the value $n = 0.7$ can be assigned to the fact that the extensive release of CO and CO_2 take place directly into the space between the basal planes of graphene. The mechanism of this operation can be designed including consecutive zero-order and first-order stages. The zero-order reaction could occur in the conditions when the energy consumed in the thermal reduction reaction comes through the basal graphene plane. Thus, the reaction rate should be constant and not depend on the reagent concentration (i.e., the concentration of oxygen functionalities). The first-order reaction could originate in the case when the energy is absorbed directly by an oxygen-containing functional group. In this situation the reaction rate linearly depends only on the concentration of the reagent [19]. The same reaction order for GO and GO_MA_P reduction reveals the same mechanism for both processes.

To compare the values of activation energy E_a for GO and GO_MA_P, the thermal decomposition is studied by other isoconversional (i.e., model-free) kinetic models such as Kissinger and Ozawa. The linear fitting plots of $\ln(\beta/T_m^2)$ vs $1/T_m$ and $\log(\beta)$ vs $1/T_m$ are displayed in Fig. 4. The activation energy E_a of GO and GO_MA_P can be evaluated as a slope from those displayed fitting plots. By comparing the results presented in Table 2, it is found that the E_a values obtained by both Kissinger and Ozawa method are quite similar. E_a values of GO from Kissinger and Ozawa approaches are estimated to be 141.5 kJ mol^{-1} and 142.1 kJ mol^{-1}, respectively. The difference between both values is 0.6 kJ mol^{-1}, which is acceptable in the error region. The error related to these models depends on the selected baseline to determine the peak temperature. Moreover, observed E_a values of pure GO are similar to those reported previously [15,17,18]. The values of E_a for GO_MA_P decomposition are found to be 114.0 kJ mol^{-1} and 115.2 kJ mol^{-1} from Kissinger and Ozawa methods, respectively. Also, it is noticed the same trend that the addition of C_3O_2 decreases the activation energy of GO by approximately 27 kJ mol^{-1} in both methods. Besides, it is observed that the activation energy evaluated by the Borchardt-Daniels' method is slightly different from those calculated by Ozawa and Kissinger's models. According to the literature [40], this variation of activation energy is due to assumptions made in these approaches and the simplicity of Borchardt-Daniels' method. This method is based on a single scan by DSC and it is assumed that the kinetic parameters depend on the heating rate. Nevertheless, it has the benefits of its straightforward and rapid determination of a broad kinetic information. Meanwhile, for the isoconversional methods, it is considered that the kinetic parameters do not depend on the heating rate, and the observed value of activation energy demonstrates the average value for the overall process.

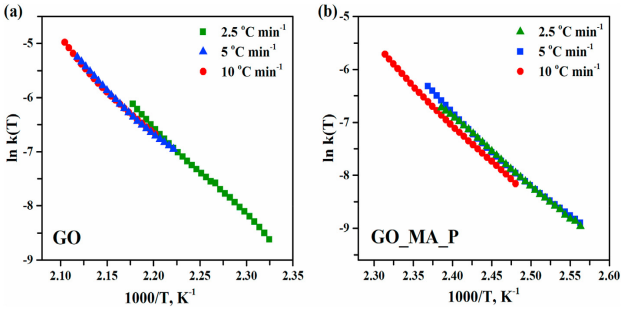

Fig. 3. The E_a determination for (a) GO and (b) GO_MA_P using the Borchardt-Daniels approach.

Table 2
Determined values of activation energy for GO and GO_MA_P by different kinetic models.

	Borchardt-Daniels			Kissinger		Ozawa	
	β (°C min $^{-1}$)	E_a (kJ mol $^{-1}$)	R^2	E_a (kJ mol^{-1})	R^2	E_a (kJ mol^{-1})	R^2
GO	2.5	134.9	0.9980	141.5	0.9682	142.1	0.9713
	5	137.8	0.9941				
	10	143.1	0.9931				
GO_MA_P	2.5	107.5	0.9991	114.0	0.9999	115.2	0.9999
	5	110.7	0.9948				
	10	115.8	0.9990				

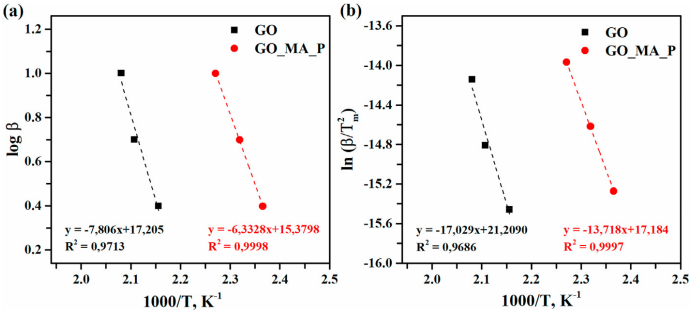

Fig. 4. The E_a determination of GO and GO_MA_P using (a) Ozawa and (b) Kissinger methods.

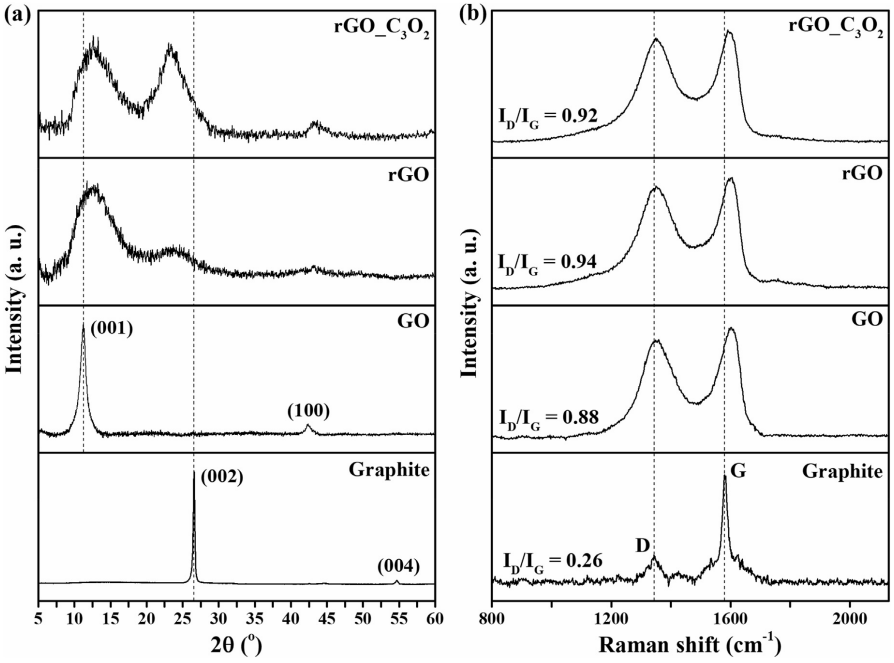

Fig. 5. (a) XRD patterns and (b) Raman spectra of graphite, GO, rGO, and rGO_C_3O_2.

GO and GO_MA_P samples were thermally annealed at 250 °C temperature to investigate the structural differences between reduced products with and without C_3O_2 additives. The reduction temperature of 250 °C has been selected for the primary structural analysis due to the fact that the thermal decomposition of GO and GO_MA_P occurs up to 250 °C. XRD patterns of graphite, GO, rGO, and rGO_C_3O_2 are presented in Fig. 5 (a). The diffractogram of pristine graphite powder exhibits a typical peak located at $2\theta = 26.60^\circ$ (002) with an interlayer spacing of 0.335 nm that reveals high crystallinity and well-ordered layer stacking of graphite. The diffraction peak at $2\theta = 54.70^\circ$ corresponding to the plane (004) is also observed in the XRD data of graphite. After oxidation, the peak at $2\theta = 26.60^\circ$ disappears, while two new diffraction reflections arise at $2\theta = 11.26^\circ$ (001) and $2\theta = 42.40^\circ$ (100). The interlayer distance of planes (001) is expanded to 0.785 nm due to the intercalated water and attached oxygen functionalities. The XRD pattern of GO is similar to the XRD results that have been reported in the work of C. Aumnate et al. [41]. The XRD data of rGO and rGO_C_3O_2 display noticeable changes in the structure crystallinity after thermal reduction. Both samples have amorphous structure that results from a decrease in the crystallite sizes. After GO annealing, the reflection (001) becomes wider and shifts to $2\theta = 12.55^\circ$ indicating the reduced interplanar distance (0.704 nm). The presence of this plane shows that the reduction of GO is not completely achieved at 250 °C temperature. Furthermore, in XRD pattern of rGO the new broad and non-intensive peak is determined at $2\theta = 23.70^\circ$ that should be related to the reflection (002) with the interlayer spacing of 0.375 nm. The XRD pattern of rGO_C_3O_2 also shows two peaks at $2\theta = 12.66$ and $2\theta = 23.27^\circ$ attributing to the planes (001) and (002), respectively. However, the second one is more intensive compared to that of rGO and has the d-spacing of 0.381 nm. The use of C_3O_2 in the thermal reduction of GO determines the more intensive conversion from GO to graphite structure due to the sharper and more expressed peak corresponding to the plane (002).

Raman spectroscopy is a common technique to characterize the structure of graphene-based materials. Recorded Raman spectra of graphite, GO, rGO, and rGO_C_3O_2 are shown in Fig. 5 (b). The spectrum of graphite exhibits a high-intensive G mode located at 1344 cm^{-1} representing the first order scattering of the E_{2g} mode of the sp^2 carbon domain, and the D band at 1580 cm^{-1} that is related to the defective sites of the structure [42]. In the spectrum of GO, the D and G bands becomes broader and shifts to 1350 cm^{-1} and 1602 cm^{-1}, respectively. Furthermore, the intensity of D peak is increased appreciably. These displacements of the modes and an increase of D intensity can be attributed to the surface defects caused by the disruption of the conjugated structure after the oxidation process. Moreover, the intensity ratio of D and G modes (I_D/I_G) determines the degree of disorders in the carbon materials, where a higher ratio defines more structural defects on the graphene sheet [42]. The calculated value of I_D/I_G alters from 0.24 in pristine graphite to 0.88 in GO that also confirms the presence of sp^3 carbon atoms, oxygen functional groups, vacancies, and edge defects in the GO structure [43, 44]. The position of D band in thermally reduced samples is the same as GO, but the G mode shifts to lower wavenumbers in both rGO (1600 cm^{-1}) and rGO_C_3O_2 (1594 cm^{-1}). Furthermore, the value of I_D/I_G ratio in the case of rGO and rGO_C_3O_2 is found to be 0.94 and 0.92, respectively. Thus, a more effective restoration of π-conjugated system in rGO_C_3O_2 than rGO is confirmed by the shift of G mode and a slight decrease in I_D/I_G ratio. The use of C_3O_2 has a positive effect on the structural properties of thermally reduced GO. Nevertheless, the higher values of reduction temperature should be applied in the investigation to efficiently repair structural defects of rGO_C_3O_2.

4. Conclusions

In this research, the determination of kinetic and thermodynamic parameters of GO decomposition is carried out using three kinetic models (Borchardt-Daniels, Ozawa, Kissinger). Our results demonstrate that the addition of carbon suboxide changes the thermal stability and chemical reactivity of GO. Furthermore, C_3O_2 lowers the enthalpy and activation energy but does not influence the reaction order of GO thermal decomposition. The reduction temperature of GO is successfully reduced up to 125 °C with the use of C_3O_2. The apparent reaction order of thermal reduction for GO and GO_MA_P is the same and equals 0.7. It reveals the complex mechanism of GO thermal decomposition that consists of simultaneous zero-order and first-order stages. Furthermore, it was observed that the kinetic parameters (E_a, ΔH) of GO thermal reduction reaction depend on the heating rate. The XRD and Raman spectroscopy results show a positive impact of C_3O_2 on the structural properties of reduced GO at relative low reduction temperature.

CRediT authorship contribution statement

Rūta Aukštakojytė: Investigation, Visualization, Writing – original draft, Writing – review & editing. **Justina Gaidukevič:** Writing – original draft, Writing – review & editing, Supervision. **Jurgis Barkauskas:** Conceptualization, Supervision.

Declaration of competing interest

The authors declare that they have no known competing financial interests or personal relationships that could have appeared to influence the work reported in this paper.

References

[1] Q. Ke, J. Wang, Graphene-based materials for supercapacitor electrodes – a review, J. Mater. 2 (2016) 37–54, https://doi.org/10.1016/j.jmat.2016.01.001.
[2] P. Fallahazad, N. Naderi, M.J. Eshraghi, Improved photovoltaic performance of graphene-based solar cells on textured silicon substrate, J. Alloys Compd. 834 (2020) 155123, https://doi.org/10.1016/j.jallcom.2020.155123.
[3] E. Aliyev, V. Filiz, M.M. Khan, Y.J. Lee, C. Abetz, V. Abetz, Structural characterization of graphene oxide: surface functional groups and fractionated oxidative debris, Nanomaterials 9 (2019), https://doi.org/10.3390/nano9081180.
[4] I. Sengupta, S. Chakraborty, M. Talukdar, S.K. Pal, S. Chakraborty, Thermal reduction of graphene oxide: how temperature influences purity, J. Mater. Res. 33 (2018) 4113–4122, https://doi.org/10.1557/jmr.2018.338.
[5] Y. Qiu, F. Guo, R. Hurt, I. Külaots, Explosive thermal reduction of graphene oxide-based materials: mechanism and safety implications, Carbon N. Y. 72 (2014) 215–223, https://doi.org/10.1016/j.carbon.2014.02.005.
[6] P. Lakhe, D.L. Kulhanek, W. Sun, B. Zhang, M.J. Green, M.S. Mannan, Calorimetry of explosive thermal decomposition of graphite oxide, J. Hazard Mater. 366 (2019) 275–281, https://doi.org/10.1016/j.jhazmat.2018.11.100.
[7] G.T.T. Le, J. Manyam, P. Opaprakasit, N. Chanlek, N. Grisdanurak, P. Sreearunothai, Divergent mechanisms for thermal reduction of graphene oxide and their highly different ion affinities, Diam. Relat. Mater. 89 (2018) 246–256, https://doi.org/10.1016/j.diamond.2018.09.006.
[8] C.Y. Ho, H.W. Wang, Characteristics of thermally reduced graphene oxide and applied for dye-sensitized solar cell counter electrode, Appl. Surf. Sci. 357 (2015) 147–154, https://doi.org/10.1016/j.apsusc.2015.09.016.
[9] R. Kumar, A. Kaur, Chemiresistive gas sensors based on thermally reduced graphene oxide for sensing sulphur dioxide at room temperature, Diam. Relat. Mater. 109 (2020) 108039, https://doi.org/10.1016/j.diamond.2020.108039.
[10] I. Šakinyte, J. Barkauskas, J. Gaidukevič, J. Razumiene, Thermally reduced graphene oxide: the study and use for reagentless amperometric d-fructose biosensors, Talanta 144 (2015) 1096–1103, https://doi.org/10.1016/j.talanta.2015.07.072.
[11] A.H. Lima, J.P. Mendonça, M. Duarte, F. Stavale, C. Legnani, G.S.G. De Carvalho, I.O. Maciel, F. Sato, B. Fragneaud, W.G. Quirino, Reduced graphene oxide prepared at low temperature thermal treatment as transparent conductors for organic electronic applications, Org, Electron 49 (2017) 165–173, https://doi.org/10.1016/j.orgel.2017.05.054.
[12] C. Rattanapan, C. Jankaenkaew, T. Sirithiwakorn, V. Loryuenyong, A. Buasri, Application of bioplastics and thermal reduced graphene oxide in electrochromic devices, Mater, Today Proc 5 (2018) 14868–14873, https://doi.org/10.1016/j.matpr.2018.04.021.
[13] M. Brycht, A. Leniart, J. Zavašnik, A. Nosal-Wiercińska, K. Wasiński, P. Półrolniczak, S. Skrzypek, K. Kalcher, Synthesis and characterization of the thermally reduced graphene oxide in argon atmosphere, and its application to construct graphene paste electrode as a naptalam electrochemical sensor, Anal. Chim. Acta 1035 (2018) 22–31, https://doi.org/10.1016/j.aca.2018.06.057.
[14] S. Chen, W. He, C.J. Luo, T. An, J. Chen, Y. Yang, P.J. Liu, Q.L. Yan, Thermal behavior of graphene oxide and its stabilization effects on transition metal complexes of triaminoguanidine, J. Hazard Mater. 368 (2019) 404–411, https://doi.org/10.1016/j.jhazmat.2019.01.073.

[15] K. Yin, H. Li, Y. Xia, H. Bi, J. Sun, Z. Liu, L. Sun, Thermodynamic and kinetic analysis of lowtemperature thermal reduction of graphene oxide, Nano-Micro Lett. 3 (2011) 51–55, https://doi.org/10.5101/nml.v3i1.p51-55.
[16] S.S. Mehetre, S.S. Maktedar, M. Singh, Understanding the mechanism of surface modification through enhanced thermal and electrochemical stabilities of N-doped graphene oxide, Appl. Surf. Sci. 366 (2016) 514–522, https://doi.org/10.1016/j.apsusc.2016.01.108.
[17] Y. Qiu, F. Collin, R.H. Hurt, I. Külaots, Thermochemistry and kinetics of graphite oxide exothermic decomposition for safety in large-scale storage and processing, Carbon N. Y. 96 (2016) 20–28, https://doi.org/10.1016/j.carbon.2015.09.040.
[18] I. Jung, D.A. Field, N.J. Clark, Y. Zhu, D. Yang, R.D. Piner, S. Stankovich, D.A. Dikin, H. Geisler, C.A. Ventrice, R.S. Ruoff, Reduction kinetics of graphene oxide determined by electrical transport measurements and temperature programmed desorption, J. Phys. Chem. C 113 (2009) 18480–18486, https://doi.org/10.1021/jp904396j.
[19] J. Barkauskas, J. Gaidukevič, G. Niaura, Thermal reduction of graphite oxide in the presence of nitrogen-containing dyes, Carbon Lett 1 (2021) 3, https://doi.org/10.1007/s42823-021-00228-3.
[20] O. Bortolini, L. Pandolfo, C. Tomaselli, P. Traldi, Ion-molecule chemistry of carbon suboxide in an ion-trap mass spectrometer, Int. J. Mass Spectrom. 190–191 (1999) 171–179, https://doi.org/10.1016/s1387-3806(98)14292-6.
[21] P.A. Gerakines, M.H. Moore, Carbon suboxide in astrophysical ice analogs, Icarus 154 (2001) 372–380, https://doi.org/10.1006/icar.2001.6711.
[22] N. Tsoureas, J.C. Green, F.G.N. Cloke, H. Puschmann, S.M. Roe, G. Tizzard, Trimerisation of carbon suboxide at a di-titanium centre to form a pyrone ring system, Chem. Sci. 9 (2018) 5008–5014, https://doi.org/10.1039/c8sc01127c.
[23] M. Allen, Carbon suboxide in Halley [6], Nature 354 (1991) 272, https://doi.org/10.1038/354272a0.
[24] M. Shao, D. Wang, G. Yu, B. Hu, W. Yu, Y. Qian, The synthesis of carbon nanotubes at low temperature via carbon suboxide disproportionation, Carbon N. Y. 42 (2004) 183–185, https://doi.org/10.1016/j.carbon.2003.10.010.
[25] H.B. Palmer, W.D. Cross, Carbon films from carbon suboxide decomposition. Inhibition by carbon monoxide and the heat of formation of C2O, Carbon N. Y. 3 (1966) 475–481, https://doi.org/10.1016/0008-6223(66)90033-9.
[26] R. Larciprete, S. Fabris, T. Sun, P. Lacovig, A. Baraldi, S. Lizzit, Dual path mechanism in the thermal reduction of graphene oxide, J. Am. Chem. Soc. 133 (2011) 17315–17321, https://doi.org/10.1021/ja205168x.
[27] Y. Liang, J. Frisch, L. Zhi, H. Norouzi-Arasi, X. Feng, J.P. Rabe, N. Koch, K. Müllen, Transparent, highly conductive graphene electrodes from acetylene-assisted thermolysis of graphite oxide sheets and nanographene molecules, Nanotechnology 20 (2009), https://doi.org/10.1088/0957-4484/20/43/434007.
[28] X. Yan, J. Chen, J. Yang, Q. Xue, P. Miele, Fabrication of free-standing, electrochemically active, and biocompatible graphene oxide-polyaniline and graphene-polyaniline hybrid papers, ACS Appl. Mater. Interfaces 2 (2010) 2521–2529, https://doi.org/10.1021/am100293r.
[29] W.S. Hummers, R.E. Offeman, Preparation of graphitic oxide, J. Am. Chem. Soc. 80 (1958) 1339, https://doi.org/10.1021/ja01539a017.
[30] R.L. Blaine, H.E. Kissinger, Homer kissinger and the kissinger equation, Thermochim. Acta 540 (2012) 1–6, https://doi.org/10.1016/j.tca.2012.04.008.
[31] N. Koga, Ozawa's kinetic method for analyzing thermoanalytical curves: history and theoretical fundamentals, in: J. Therm. Anal. Calorim., Springer, 2013, pp. 1527–1541, https://doi.org/10.1007/s10973-012-2882-5.
[32] H.J. Borchardt, F. Daniels, The application of differential thermal analysis to the study of reaction Kinetics1, J. Am. Chem. Soc. 79 (2002) 41–46, https://doi.org/10.1021/ja01558a009.
[33] K. Haubner, J. Murawski, P. Olk, L.M. Eng, C. Ziegler, B. Adolphi, E. Jaehne, The route to functional graphene oxide, ChemPhysChem 11 (2010) 2131–2139, https://doi.org/10.1002/cphc.201000132.
[34] M. Yahiaoui, H. Hadoun, I. Toumert, A. Hassani, Determination of kinetic parameters of Phlomis bovei de Noé using thermogravimetric analysis, Bioresour. Technol. 196 (2015) 441–447, https://doi.org/10.1016/j.biortech.2015.07.082.
[35] M.J. McAllister, J.L. Li, D.H. Adamson, H.C. Schniepp, A.A. Abdala, J. Liu, M. Herrera-Alonso, D.L. Milius, R. Car, R.K. Prud'homme, I.A. Aksay, Single sheet functionalized graphene by oxidation and thermal expansion of graphite, Chem. Mater. 19 (2007) 4396–4404, https://doi.org/10.1021/cm0630800.
[36] J.C. Van Miltenburg, M.A. Cuevas-Diarte, The influence of sample mass, heating rate and heat transfer coefficient on the form of DSC curves, Thermochim. Acta 156 (1989) 291–297, https://doi.org/10.1016/0040-6031(89)87197-7.
[37] P. Malumba, L. Doran, S. Danthine, C. Blecker, F. Béra, The effect of heating rates on functional properties of wheat and potato starch-water systems, LWT - Food Sci. Technol. (Lebensmittel-Wissenschaft -Technol.) 88 (2018) 196–202, https://doi.org/10.1016/j.lwt.2017.10.017.
[38] N. Kongkaew, W. Pruksakit, S. Patumsawad, Thermogravimetric Kinetic Analysis of the Pyrolysis of Rice Straw, Elsevier B.V., 2015, https://doi.org/10.1016/j.egypro.2015.11.552.
[39] Z. Yang, H. Peng, W. Wang, T. Liu, Crystallization behavior of poly(ε-caprolactone)/layered double hydroxide nanocomposites, J. Appl. Polym. Sci. 116 (2010) 2658–2667, https://doi.org/10.1002/app.
[40] M.V. Alonso, M. Oliet, J.M. Pérez, F. Rodríguez, J. Echeverría, Determination of curing kinetic parameters of lignin-phenol-formaldehyde resol resins by several dynamic differential scanning calorimetry methods, Thermochim. Acta 419 (2004) 161–167, https://doi.org/10.1016/j.tca.2004.02.004.
[41] C. Aumnate, P. Potiyaraj, C. Saengow, A.J. Giacomin, Reinforcing polypropylene with graphene-polylactic acid microcapsules for fused-filament fabrication, Mater. Des. 198 (2021) 109329, https://doi.org/10.1016/j.matdes.2020.109329.
[42] R. Sayyad, M. Ghambari, T. Ebadzadeh, A.H. Pakseresht, E. Ghasali, Preparation of Ag/reduced graphene oxide reinforced copper matrix composites through spark plasma sintering: an investigation of microstructure and mechanical properties, Ceram. Int. 46 (2020) 13569–13579, https://doi.org/10.1016/j.ceramint.2020.02.142.
[43] K. Tewatia, A. Sharma, M. Sharma, A. Kumar, Synthesis of graphene oxide and its reduction by green reducing agent, Mater. Today Proc. 44 (2020) 3933–3938, https://doi.org/10.1016/j.matpr.2020.09.294.
[44] J. Bin Wu, M.L. Lin, X. Cong, H.N. Liu, P.H. Tan, Raman spectroscopy of graphene-based materials and its applications in related devices, Chem. Soc. Rev. 47 (2018) 1822–1873, https://doi.org/10.1039/c6cs00915h.

2nd publication

“Structural control and electrical behaviour of thermally reduced graphene oxide samples assisted with malonic acid and phosphorus pentoxide”

R. Aukštakojytė, J. Gaidukevič, G. Niaura, M. Skapas, V. Bukauskas, J. Barkauskas

Inorganics, 10(9), 2022, 142
DOI: 10.3390/inorganics10090142

inorganics

MDPI

Article

Structural Control and Electrical Behavior of Thermally Reduced Graphene Oxide Samples Assisted with Malonic Acid and Phosphorus Pentoxide

Ruta Aukstakojyte [1], Justina Gaidukevic [1,*], Gediminas Niaura [2], Martynas Skapas [3], Virginijus Bukauskas [4] and Jurgis Barkauskas [1]

[1] Faculty of Chemistry and Geosciences, Vilnius University, Naugarduko Str. 24, LT-03225 Vilnius, Lithuania
[2] Department of Organic Chemistry, Center for Physical Sciences and Technology, Saulėtekio Ave. 3, LT-10257 Vilnius, Lithuania
[3] Department of Characterisation of Materials Structure, Center for Physical Sciences and Technology, Saulėtekio Ave. 3, LT-10257 Vilnius, Lithuania
[4] Department of Physical Technologies, Center for Physical Sciences and Technology, Saulėtekio Ave. 3, LT-10257 Vilnius, Lithuania
* Correspondence: justina.gaidukevic@chf.vu.lt

Abstract: We present a detailed study of the structural and electrical changes occurring in two graphene oxide (GO) samples during thermal reduction in the presence of malonic acid (MA) (5 and 10 wt%) and P_2O_5 additives. The morphology and de-oxidation efficiency of reduced GO (rGO) samples are characterized by Fourier transform infrared, X-ray photoelectron, energy-dispersive X-ray, Raman spectroscopies, transmission electron and scanning electron microscopies, X-ray diffraction (XRD), and electrical conductivity measurements. Results show that MA and P_2O_5 additives are responsible for the recovery of π-conjugation in rGO as the XRD pattern presents peaks corresponding to (002) graphitic-lattice planes, suggesting the formation of the sp^2-like carbon structure. Raman spectra show disorders in graphene sheets. Elemental analysis shows that the proposed reduction method in the presence of additives also suggests the simultaneous insertion of phosphorus with a relatively high content (0.3–2.3 at%) in rGO. Electrical conductivity measurements show that higher amounts of additives used in the GO reduction more effectively improve electron mobility in rGO samples, as they possess the highest electrical conductivity. Moreover, the relatively high conductivity at low bulk density indicates that prepared rGO samples could be applied as metal-free and non-expensive carbon-based electrodes for supercapacitors and (bio)sensors.

Keywords: thermally reduced graphene oxide; carbon suboxide; phosphorus doped reduced graphene oxide; structural analysis; electrical conductivity

Citation: Aukstakojyte, R.; Gaidukevic, J.; Niaura, G.; Skapas, M.; Bukauskas, V.; Barkauskas, J. Structural Control and Electrical Behavior of Thermally Reduced Graphene Oxide Samples Assisted with Malonic Acid and Phosphorus Pentoxide. *Inorganics* **2022**, *10*, 142. https://doi.org/10.3390/inorganics10090142

Academic Editor: Hiroshi Kageyama

Received: 29 August 2022
Accepted: 13 September 2022
Published: 16 September 2022

1. Introduction

Reduced graphene oxide (rGO) possesses properties between graphene oxide (GO) and graphene that makes it an attractive carbon material in the applications of energy storage systems, (bio)sensors, fuel cells, Li^+ ion batteries, supercapacitors, etc. [1–3]. Several synthesis strategies of rGO have been proposed, which could be mainly categorized into the chemical, electrochemical, and thermal reduction of GO. Chemical reduction is a fast and straightforward method to obtain rGO at low temperatures (below 90 °C). However, reducing agents (hydrazine, lithium aluminum hydride, hydroiodic acid) used are harmful and highly toxic [3,4]. Moreover, the complete removal of reductants is complicated due to their adsorption on the rGO lattice [5]. Electrochemical reduction of GO is considered a green synthesis approach, but it is not cost-effective in terms of large-scale production of rGO. As a scalable, eco-friendly, rapid, and inexpensive method, thermal reduction is more attractive than chemical and electrochemical treatments. The thermally reduced GO

exhibits a higher reduction degree, larger specific surface area as well as better electronic properties compared to rGO samples prepared by the chemical process. Furthermore, thermal reduction is a promising method for the industrial preparation of rGO with less damage to the environment [3].

However, the thermal reduction of GO is still challenging. Annealing of GO leads to high volumes of CO and CO_2 gases that cause structural disorders such as Stone–Wales defects, C vacancies, dislocations, grain boundaries, and sp^3 defects [6]. It is well known that these disorders alter the length of C–C bonds and induce the σ and π orbitals re-hybridization. They may cause the scattering of electron waves and the change of electrons trajectories resulting in a decrease of electron carrier mobility and electrical conductivity in the sample. The presence of distortions can also deteriorate physical properties such as the thermal conductivity and mechanical strength of the material [7]. For these reasons, it is essential to focus on the synthesis procedure to ensure the best recovery of the sp^2 carbon network in the rGO.

The final properties of rGO, including the C/O ratio, number of layers, surface area, and number of structural defects, could be controlled by changing thermal reduction conditions such as temperature, pressure, atmosphere, and oxidation degree of GO. The study reported by A. Kaniyoor et al. showed that the use of the H_2 and Ar mixture in the synthesis of rGO leads to a higher C/O ratio compared to that of the sample reduced only under Ar atmosphere [8]. Then, at higher temperatures (1000–2800 °C), the restoration of the sp^2 carbon network occurs more effectively than at lower temperatures due to the more pronounced decomposition of oxygen-containing functional groups and stimulation of graphitization [9,10]. The higher oxidation degree of GO influences the more efficient reduction process [11]. The substantial carbon source in thermal reduction of GO can also improve the restoration of the π-conjugated system, make a beneficial change in electrical properties, and decrease structural defects. For instance, Y. Liang et al. carried out thermal GO reduction in the presence of acetylene (C_2H_2) at 1000 °C temperature in order to prepare transparent graphene-based coatings for electrode materials. The sample obtained exhibited electrical conductivity more than four times higher than the compound in the absence of C_2H_2, representing the significant advantage of using additional carbon [12]. Following this, carbon suboxide (C_3O_2) may also be a good candidate as an atomic carbon source in the thermal reduction of GO. Formally, C_3O_2 is an anhydride of malonic acid ($CH_2(COOH)_2$); therefore, this carbon oxide could be produced by dehydration of malonic acid (MA) and a strong dehydrating agent, phosphorus pentoxide (P_2O_5), at 150 °C temperature [13]. C_3O_2 is gaseous and thermally decomposes into elemental carbon and two carbon monoxide molecules above 16 °C [14]. For this reason, this linear molecule has been successfully used as an atomic carbon source in the synthesis of carbon nanotubes and carbon coatings [15,16]. Additionally, our previous study showed the positive impact of C_3O_2 on the decomposition kinetics of GO and the structural properties of rGO obtained at relatively low temperatures (250 °C) [17]. Surprisingly, the use of the MA and P_2O_5 mixture could be beneficial in the thermal reduction of GO since the reaction between these two compounds produces C_3O_2 as well as H_3PO_4. According to the literature, phosphorus acid has been used as an effective dopant of phosphorus atoms in the chemical and thermal reduction of GO [18–21]. Modification with phosphorus can effectively modulate the electrical, catalytic, and electrochemical properties of rGO. The phosphorus atom has lower electronegativity than the carbon atom that changes charge densities in the graphene-based material resulting in enhanced capacitive performance and surface area of phosphorus-doped graphene compounds [21–23]. Moreover, the incorporation of phosphorus atoms increases the density of charge carries in the carbon sample due to the contribution of phosphorus electrons to the π-conjugated system of rGO. For this reason, the electrical conductivity is expected to increase [24]. Thus, we propose that this suggested thermal reduction technique with an additive of MA and P_2O_5 will provide new possibilities to achieve materials with restored sp^2 carbon network and improved electrochemical performance to successfully apply new phosphorus-doped rGO materials in (bio)sensors or supercapacitors. To the

best of our knowledge, the mixture of MA and P_2O_5 has been used for the first time as a reducing mixture and phosphorus-containing agent for the reduction and modification of GO. Moreover, the detailed structural characterization and electrical conductivity behavior of rGO obtained using the mixture of MA and P_2O_5 have not been investigated in depth yet.

The aim of this research was to evaluate the changes in the structure and electrical behavior of different rGO samples prepared using thermal reduction of GO in the absence and presence of MA and P_2O_5 mixture. Two GO samples with different oxidation degrees and functional groups were used to prepare rGO samples. We have demonstrated the enhanced successful restoration of the π-conjugated system, as well as the simultaneous incorporation of phosphorus atoms. The impact of C_3O_2 and the insertion of phosphorus atoms on structural properties and morphology was evaluated in detail using X-ray diffraction (XRD), energy dispersive X-ray spectroscopy (EDX), X-ray photoelectron spectroscopy (XPS), Fourier transform infrared spectroscopy (FTIR), scanning electron microscopy (SEM), transmission electron microscopy (TEM), and Raman spectroscopies. Electrical conductivity measurements of synthesized rGO samples with additives were also carried out.

2. Materials and Methods

2.1. Preparation of GO Samples

2.1.1. GO Synthesis Using Pre-Oxidation with $K_2S_2O_8$, P_2O_5, and H_2SO_4 Mixture

Pretreatment of graphite was performed by the synthesis protocol described in the work of Yan et al. [25]. In a typical experiment, natural graphite powder (6.0 g) was mixed with $K_2S_2O_8$ (5.0 g) and P_2O_5 (5.0 g) in the 98 wt% H_2SO_4 (24.0 mL) media. Subsequently, this pre-oxidized graphite obtained was subjected to oxidation, following the protocol reported by Hummers et al. [26]. The GO suspension formed in the reaction was transferred into a dialysis tubing cellulose membrane with a cut-off molecular weight of 10,000–20,000 Da for further purification and dialyzed against distilled water until the pH value of the dialysate became ~5. The brown powder obtained was dried in air at ambient temperature to a constant weight. The prepared powder sample was denoted as GO_1.

2.1.2. GO Synthesis Using Pre-Oxidation with H_2SO_4, H_3BO_3, and CrO_3 Mixture

In this study, pre-oxidation of graphite was carried out according to the new approach proposed in our laboratory [27]. In this method, graphite powder (2.0 g) was added to the mixture of 98 wt% H_2SO_4 (11.0 mL) and H_3BO_3 (0.78 g) with steady and vigorous stirring. Later, CrO_3 (2.1 g) was gradually added and the reaction mixture was maintained for 2 h at 45−55 °C. Afterwards, the resulting suspension was washed with warm distilled H_2O to remove the excess H_3BO_3. Further oxidation of this pre-oxidized graphite was performed using Hummers' method [26]. The GO suspension was purified by dialysis as previously described and dried in air to a constant weight. The product obtained was named as GO_2.

2.2. Thermal Reduction of GO Samples

Each synthesized GO sample (GO_1 and GO_2) mixed with MA and phosphorus pentoxide was ground in an agate mortar for 10 min. The weight ratios of GO and MA used in this mechanochemical synthesis were 1:0.05 and 1:0.10. The amount of phosphorus pentoxide was calculated according to the following equation:

$$3C_3H_4O_4 + P_4O_{10} \rightarrow 3C_3O_2 + 4H_3PO_4 \quad (1)$$

The solid mixtures prepared after grinding were reduced in the tubular furnace exposing them at 100 °C for 10 min. Later, the samples obtained were treated by thermal shock at 800 °C for 5 min. The whole heat treatment process (at 100 °C and 800 °C temperatures) was carried out under an argon atmosphere with a flow rate of 60 mL/min. After cooling, the thermally reduced GO samples were thoroughly washed with deionized water and dried in air. The thermal reduction of the GO samples without additives was also performed under the same synthesis conditions. The samples obtained were labelled

rGO_1 and rGO_2, respectively. Whereas, thermally reduced GO_1 and GO_2 samples with the addition of MA and phosphorus pentoxide were named according to the ratio of added MA. For example, if GO_1 was thermally reduced by adding 5 wt% or 10 wt% of MA, this synthesized product was denoted as rGO_1_5 or rGO_1_10, respectively.

2.3. Material Characterization

The crystallographic information of the synthesized products was obtained using a MiniFlex II X-ray diffractometer (Rigaku, Tokyo, Japan). XRD patterns were recorded in the 2θ range from 5° to 60° using CuKα λ = 1.5406 Å radiation with a step of 0.010°. The interlayer distance d of the prepared samples was evaluated using Bragg's equation:

$$n\lambda = 2dsin\theta \quad (2)$$

where λ is the wavelength of the X-ray beam, n is a positive integer, d is the interlayer distance, and θ is the diffraction angle. The average crystallite size D was calculated by determining the full-width at the half-maximum (FWHM) of the diffraction peaks using the Debye–Scherrer's equation as follows:

$$D = \frac{K\lambda}{\beta cos\theta} \quad (3)$$

where K is a constant (0.89), λ is the wavelength of the X-ray radiation, β is the FWHM of the peak, and θ is the diffraction angle. D for the graphite and rGO samples was determined from the (002) planes, while D for the GO samples was calculated from the (001) planes.

EDX analysis was performed by a scanning electron microscope (TM3000; Hitachi, Tokyo, Japan) equipped with an EDX detector.

XPS analysis was carried out with a Kratos Axis Supra (Kratos analytical, Manchester, UK) spectrometer. Monochromatic Al Kα radiation ($h\nu$ = 1486.69 eV) was used as an X-ray source. The XPS P2p spectrum was recorded at a pass energy of 20 eV and calibrated using the carbon 1 s line at 284.6 eV. The raw XPS spectrum was deconvoluted by curve fitting peak components using the software CASAXPS. Symmetric Gaussian–Lorentzian functions were used to approximate the line shapes of the fitting components after the Shirley-type background subtraction.

FTIR spectroscopy measurements were performed by an FTIR spectrometer (PerkinElmer, Inc., Waltham, MA, USA). Infrared spectra were recorded in the range of 700–4000 cm^{-1} using the KBr pellet technique in transmission mode. The spectral resolution was set at 4 cm^{-1}.

Raman spectra were recorded using an inVia Raman spectrometer (Renishaw, Wotton-under-Edge, UK) equipped with a thermoelectrically cooled (−70 °C) CCD camera in the range of 300–3300 cm^{-1}. The He-Ne gas laser provided an excitation beam at 532 nm with power restricted to 1 mW. The integration time was selected as 100 s. The average in-plane crystallite size $L\alpha$ was determined according to the following equation [28]:

$$L\alpha = 2.4 \times 10^{-10} \times \lambda_L^4 \times \left[\frac{I_D}{I_G}\right]^{-1} \quad (4)$$

where λ_L is the wavelength of the laser radiation used for the excitation of the Raman analysis, and I_D and I_G are the intensities of the D and G bands in the Raman spectra, respectively.

SEM imaging was carried out using a Hitachi SU-70 microscope at an accelerating voltage of 10.0 kV at magnifications of 50,000. The samples were coated with 10 nm of silver using a Q150T ES Turbo-Pumped Sputter Coater (Quorum, Washington, DC, USA) before SEM microscopy.

TEM analysis was performed using a TECNAI G2 F20 X-TWIN microscope equipped with an Orius SC1000B CCD camera (Gatan, Pleasanton, CA, USA) with a Schottky-type field emission electron source using an accelerating voltage of 200 kV. Selected area electron

diffraction (SAED) patterns on thermally reduced samples transferred on copper mesh were recorded using the SAED diaphragm.

A Keithley 2601 Source Meter (GlobalTech Sourcing, North Hampton, NH, USA) was applied for the conductivity measurement. The electrical conductivity of the rGO samples obtained was determined using a cell made in our laboratory. The experiments were carried out at room temperature (22 °C) and a relative humidity of 40%. Approximately 0.02 g of rGO powder samples were placed in a glass cylinder of 2.86 mm in diameter between two copper electrodes. We assume that the electrical contact area between the electrode and the powder was the same as the inner area of a cylinder. The sample was gradually pressed by reducing the distance between the electrodes, and the resistance was determined. The resistivity (ρ) was determined using the following equation:

$$\rho = R\frac{A}{l} \quad (5)$$

where, R is a resistance (Ω), A is a cross section area (m^2), and l is length of the sample (m). It is important to note that current-voltage characteristic curves were linear in a voltage range of ± 1 V for all tested samples.

3. Results and Discussion

The elemental composition of the synthesized GO and rGO samples is presented in Figure 1a,b. As can be seen in Figure 1a,b, GO_1 and GO_2 contain carbon, oxygen, and sulfur atoms. The origin of sulfur is associated with the presence of HSO_4^- and SO_4^{2-} residuals, introduced during the oxidation treatment of pristine graphite. Moreover, the C/O ratio of GO_2 is determined to be 1.66 indicating the higher oxidation degree compared to that of GO_1 (C/O = 1.95). After thermal treatment of GO samples without MA and P_2O_5 additives, only carbon and oxygen elements are identified for rGO_1 and rGO_2 and the ratio of C/O significantly increased up to 11.66 and 8.68 for rGO_1 and rGO_2, respectively. Besides, from Figure 1a,b, it can be noted that the relative concentration of oxygen has been reduced from 33.6 at% and 37.4 at% for GO_1 and GO_2, respectively, to 7.9 at% for rGO_1 and 9.6 at% for rGO_2, suggesting a partial reduction of the GO samples. On the contrary, the samples obtained after thermal reduction of GO using a mixture of MA and P_2O_5 consist of carbon, oxygen, and phosphorus atoms. The similar tendency of the increasing of C/O values is observed for all rGO samples obtained using additives in the reduction process. The determined C/O values for rGO_1_5, rGO_1_10, rGO_2_5, and rGO_2_10 are 8.68, 7.02, 7.71, and 6.24, respectively. Supposedly, phosphorus functionalities enter the structure of rGO samples due to the formation of H_3PO_4 in the reaction between MA and P_2O_5 (Equation (1)). As can be seen in Figure 1a,b, the content of phosphorus varies from 0.3 to 2.3 at%, while the highest content of P (2.3 at%) is determined in the rGO_2_10 sample. It should be noted that the phosphorus-doping level in this sample is much higher than other previously synthesized phosphorus-doped rGO samples reported in the literature [18,19,29,30]. Furthermore, the results obtained from the elemental analysis show that the amount of oxygen increases with an increase of the additives content used in the thermal reduction process. In the case of rGO_1 samples, the oxygen contents are 10.3 at% and 12.3 at% for rGO_1_5 and rGO_1_10, respectively, while in the case of rGO_2 samples, the oxygen contents are 11.4 at% and 13.5 at% for rGO_2_5 and rGO_2_10 samples, respectively. It could be a consequence of introducing oxygen-containing phosphate groups (O–P or O=P) into the graphene structure. The P2p XPS spectrum could provide detailed information on the phosphorus-containing functional groups presented on the surface of samples. As only two samples, rGO_1_10 and rGO_2_10, exhibited a higher amount of phosphorus, they were selected for a P2p peak deconvolution analysis, and the results are presented in Figure 1c,d. It can be noted that for both samples, deconvolution of the P2p region presents an inseparable doublet with $P2p_{1/2}$ and $P2p_{3/2}$ components at ΔBE = 0.8 eV and an area ratio of 1:2. A low energy doublet with the energy of the $P2p_{3/2}$ component of 132.6 eV is assigned to the C–P=O bonds. An intense doublet with the $P2p_{3/2}$ component located

at approximately 133.8 eV corresponds to the higher oxidation state of phosphorus [31]. Regarding the content of specific phosphorus-containing functionalities in the samples, it can be noticed that the reduction of GO in the presence of the MA and P_2O_5 additive leads to the formation of mainly the higher oxidation state of phosphorus (PO_x), as the relative concentration of these groups in the rGO_2_10 sample is 74.9 at% and in the case of the rGO_1_10 sample is 81.4 at%. The content of the C–P=O groups was considerably lower (25.1 at% for rGO_2_10 and 18.6 at% for rGO_1_10). Overall, these results confirm the partial reduction of GO samples and present a new kind of dopant for the successful insertion of phosphorus functionalities in the thermally reduced GO structure.

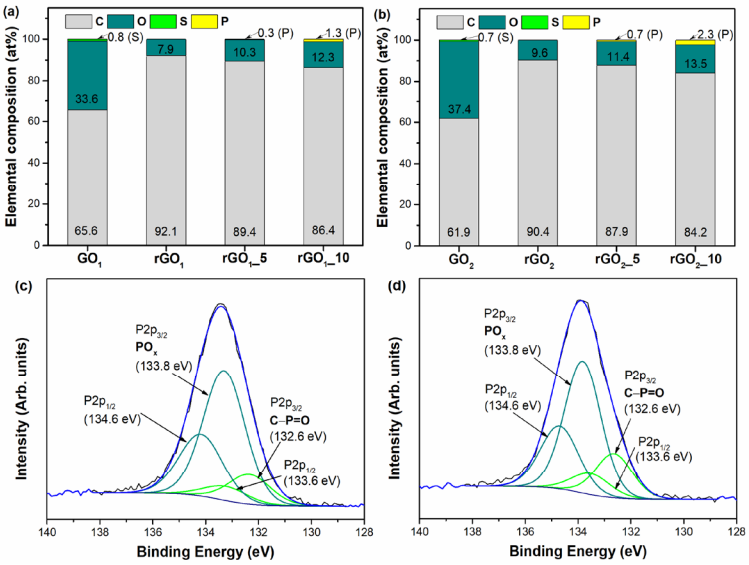

Figure 1. Elemental composition of GO_1 and thermally reduced samples derived from GO_1 (**a**), GO_2 and thermally reduced samples derived from GO_2 (**b**) based on EDX results. The P2p XPS spectra of rGO_1_10 (**c**) and rGO_2_10 (**d**) samples.

The functional groups on the surface of the samples obtained have been identified by FTIR spectroscopy. Figure 2 demonstrates the FTIR spectra of the graphite, GO_1, GO_2, and rGO samples. In the spectrum of pristine graphite (Figure 2a), the non-intensive absorption bands located at 2924 and 2853 cm^{-1} correspond to the symmetric and asymmetric stretching modes of the C–H bonds [32]. Then, a peak at 3444 cm^{-1} is attributed to the –OH bonds of adsorbed water molecules. The band at 1633 cm^{-1} arises due to the vibrations of aromatic C=C bonds, while the peaks at 1420 and 1052 cm^{-1} are ascribed to the vibrations of the phenolic (C–OH) and epoxy groups (C–O), respectively [33,34]. The FTIR spectra of the GO_1 and GO_2 samples (Figure 2a) exhibit quite a similar shape, which may reflect the similar surface composition of these materials. The width and intense band at 3444 cm^{-1} corresponds to –OH stretching vibration [35]. The new peak appearing at 1730 cm^{-1} could be attributed to C=O stretching vibrations in carboxyl or carbonyl groups, while the presence of the band at 1622 cm^{-1} could be related to the stretching of C=C bonds from unoxidized sp^2 carbon domains or C=O bonds in quinone groups [34]. The band centered at 1420 cm^{-1} is ascribed to –OH deformation vibrations of tertiary C–OH. The absorption modes at 1280 cm^{-1} and 1222 cm^{-1} are assigned to the C–O–C stretching vibrations in the epoxy functional group [33]. Moreover, two quite intense methylene group stretching bands at 2924 and 2853 cm^{-1} are identified in the spectrum of GO_2, indicating the presence

of sp^3 hybridized carbon regions [32]. Furthermore, the new absorption band centered at 800 cm^{-1} could be attributed to the deformation vibrations of C–H bonds of aromatic rings [33]. The above results demonstrate the presence of hydroxyl, carboxyl, quinone, and epoxy-functional groups and aromatic domains in the structure of GO samples, consistent with results reported elsewhere [34,36]. Most of these peaks are also present in the rGO_1 and rGO_2 samples (Figure 2b,c), but with significantly lower intensities. This notable decrease in the intensity confirms the partial decomposition of oxygen-containing functional groups during the thermal reduction of GO_1 and GO_2 samples. The non-intensive vibrational bands at 3440 cm^{-1} and in the range of 1730–950 cm^{-1} indicate the remaining hydroxyl, carbonyl, quinone, epoxy, and phenolic functional groups after annealing of GO samples.

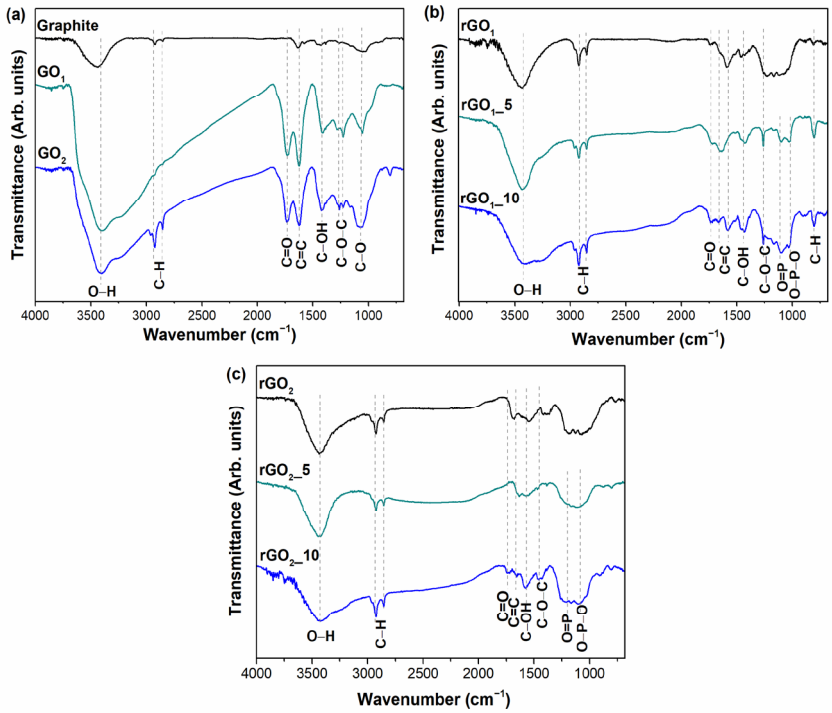

Figure 2. FTIR spectra of graphite, GO_1, and GO_2 (**a**); thermally reduced samples derived from GO_1 (**b**); and thermally reduced samples derived from GO_2 (**c**).

The thermal reduction of GO_1 with the mixture of MA (5 and 10 wt%) and P_2O_5 leads to the formation of the same functional groups as can be seen in the FTIR spectrum of rGO_1 (Figure 2b). Nevertheless, the new peaks appear at 1260, 1160, 1104, and 802 cm^{-1} that could be attributed to the formation of C–O–C, O=P, O–P–O, and C–H bonds on the surface of rGO_1_5 and rGO_1_10 samples, respectively [33,37]. The presence of phosphorus-containing bonds in those samples confirms the assumption of successful incorporation of P species into the structure of graphene. After thermal treatment of GO_2 with MA and P_2O additive, the FTIR spectra of the rGO_2_5 and rGO_2_10 samples (Figure 2c) exhibit quite similar spectra, which may reflect similar surface composition of these materials. The spectra of rGO_2_5 and rGO_2_10 contain a peak at 3440 cm^{-1} characterizing the vibrations of –OH bonds and bands at 2924 and 2853 cm^{-1} identifying the presence of C–H bonds [34]. However, the FTIR spectrum of rGO_2_5 exhibits two broad absorption bands in the ranges

of 1680–1440 cm^{-1} and 1310–950 cm^{-1}. The first wide band can be assigned to the stretching of the C=O and C=C bonds, while the second broad band may present the vibration of the C–O–C, C–OH, O=P, and O–P–O bonds [33,37]. The broad band in the range of 1310–950 cm^{-1} is also observed in the spectrum of the rGO_2_10 sample that indicates the phosphorus insertion in this sample [37]. Furthermore, the absorption band at 1580 cm^{-1} is related to C=C bonds from aromatic domains showing the partially restored sp^2 hybridized carbon structure in rGO_2_10. These data confirm the results of the XPS measurement showing the effective functionalization of rGO with phosphorus-containing functional groups.

The structural changes of the synthesized samples have been investigated by XRD analysis. The XRD patterns of the graphite, GO, and rGO samples are presented in Figure 3.

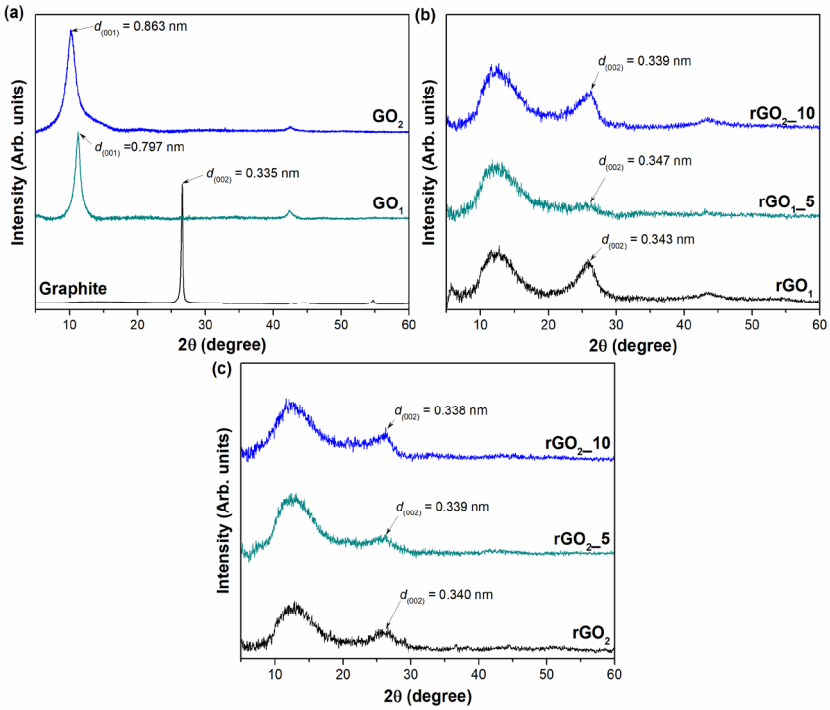

Figure 3. XRD patterns of graphite and synthesized GO samples (**a**), thermally reduced samples derived from GO_1 (**b**), and thermally reduced samples derived from GO_2 (**c**).

The XRD pattern of the pristine graphite powder (Figure 3a) exhibits a characteristic peak at 2θ = 26.60° corresponding to the (002) diffraction reflection and a low-intensity peak at 2θ = 54.70° that is related to the (004) plane of the hexagonal lattice. According to Bragg's equation, the interlayer distance $d_{(002)}$ is determined to be 0.335 nm, which is a typical d-spacing value of graphite. The crystallite size *D* reaches a value of about 31.98 nm. After the oxidation process, the (002) reflection disappears, while two new peaks arise in the ranges of 2θ = 10–11.5° (001) and at 2θ = 42.38° (100) in both cases of GO_1 and GO_2. The peaks of the (001) planes shift to lower 2θ angles of 11.28° and 10.24° for the GO_1 and GO_2 samples compared to that of graphite, respectively, due to intercalation of water and the attachment of oxygen-containing functional groups onto the graphitic carbon lattice. Moreover, this results in an increase of the interlayer distance from 0.335 nm in the case of graphite to 0.797 nm and 0.863 nm for the GO_1 and GO_2 samples, respectively. These

values are in good agreement with previous reports found in the literature [38,39]. The more significant expansion of the d-spacing for the GO_2 sample in comparison with that of GO_1 reveals that the higher oxidation degree of GO is achieved using a pre-oxidation step with the mixture of H_2SO_4, H_3BO_3, and CrO_3. The values of the crystallite size are estimated to be 8.41 nm and 4.50 nm for the GO_1 and GO_2 samples, respectively. It suggests that smaller crystallites are obtained during the synthesis of GO_2 because of the more substantial interruption of the structure due to the higher amount of oxygen-containing functional groups on the GO_2 surface.

Figure 3b,c presents the XRD results of thermally reduced GO_1 and GO_2 samples obtained with and without the use of MA and P_2O_5 additive, respectively. After annealing of GO_1, significant structural differences and changes in crystallinity are observed in all analyzed samples (Figure 3b). The XRD patterns of the samples produced become broader because of the breakdown of the long-range structure of the GO. Notably, a characteristic diffraction peak of GO (001) still remains in the XRD pattern of the rGO_1 samples (at approximately 2θ = 12.68–12.80°) and corresponds to interlayer spacing distances of 0.705 nm, 0.702 nm, and 0.692 nm for rGO_1, rGO_1_5, and rGO_1_10, respectively. This can support the conclusion of the elemental analysis, indicating that the reduction of graphene oxide to rGO is incomplete and that residual oxygen-containing functional groups are still present on the surface of rGO_1. It is important to note that the existence of the (001) plane in the rGO_1 samples may suggest the presence of thermally stable (at least at 800 °C) oxygen-containing functionalities, such as carbonyl, quinone, or pyrone groups, in the structure of the rGO samples. On the contrary, it is possible that the fraction of less stable functionalities may remain in the samples since the thermal shock time was relatively short. This could explain the reasons why rGO_1 samples are still high in oxygen [40]. Nevertheless, a characteristic (002) peak of graphite was observed at 2θ = 25.92° for the rGO_1, 2θ = 25.63° for the rGO_1_5, and 2θ = 26.23° for the rGO_1_10 samples, yielding an interlayer separation of 0.343 nm, 0.347 nm, and 0.339 nm for rGO_1, rGO_1_5, and rGO_1_10, respectively. This indicates that GO_1 reduction has occurred.

The XRD data of the annealed GO_2 samples with and without additives are presented in Figure 3c. The same trend is noticed that after the thermal reduction of GO_2, the peaks in the XRD patterns of the produced samples become broader. All samples exhibit a low degree of crystallinity, which implies that the graphene layers are randomly arranged along their stacking direction. Moreover, the peak of GO_2 can still be observed in the range of 2θ = 12.68–12.80°, denoting the coexistence of rGO and GO or the incompletion of the GO_2 reduction. Furthermore, as can be seen in Figure 3c, the diffraction reflections in the range of 2θ = 26.14–26.33° are attributed to the (002) plane. The determined values of $d_{(001)}$ are equal to 0.697 nm, 0.695 nm, and 0.691 nm, while the values of $d_{(002)}$ are 0.340 nm, 0.339 nm, and 0.338 nm, for rGO_2, rGO_2_5, and rGO_2_10, respectively. The smallest interlayer distance for the rGO_2_10 sample between all reduced products investigated in this research shows that the most efficient restoration of the π-conjugated system is obtained by using the GO_2 sample with the mixture of MA (10 wt%) and P_2O_5. Furthermore, XRD data showed that rGO samples derived from synthesized GO using the $H_2SO_4/H_3BO_3/CrO_3$ mixture exhibit lower *d*-spacing values compared to those of GO_1 reduced products. This tendency is probably related to the higher number of functional groups on the surface of GO_2 that during thermal treatment generates higher values of pressure and energy required for a more efficient reduction process of GO.

The behavior of the MA and P_2O_5 additive used to repair the π-conjugated system and defective sites of the graphene network during the annealing process were evaluated in detail by using Raman spectroscopy analysis. This technique was employed as a non-destructive, high-resolution, and fast tool to investigate the vibrational properties, the lattice structure, purity, defects, doping, and strain of carbon allotropes [39]. The Raman spectra of graphite, GO_1, GO_2, and thermally reduced GO_1 and GO_2 samples are shown in Figure 4.

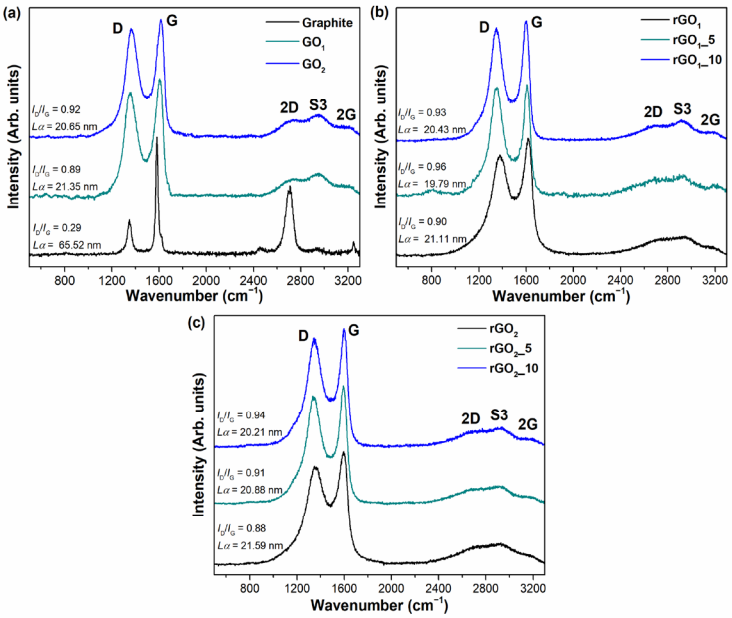

Figure 4. Raman spectra of graphite, GO_1, and GO_2 (**a**); thermally reduced samples derived from GO_1 (**b**); and thermally reduced samples derived from GO_2 (**c**). The excitation wavelength is 532 nm.

Figure 4 shows that recorded Raman spectra are similar between all synthesized samples. Each Raman spectrum consists of two dominant peaks located at ~1360 cm^{-1} and ~1600 cm^{-1}, corresponding to the D and G bands, which are typical modes of graphitic materials, respectively. The D band can be visualized as a breathing vibration of six-membered aromatic rings; defects and various disorders, such as carbon vacancies, grain boundaries, dislocations, sp^3 defects, armchair, or zigzag edges, are required for activation of this mode. The G band is associated with in-plane vibrations of pairs of sp^2 hybridized carbon atoms. This mode is always allowed in Raman spectra. The intensity ratio of the D and G modes (I_D/I_G) characterizes the degree of structural disorder in graphene-derived material. The number of defects decreases with a decrease in the I_D/I_G value [41–43]. Furthermore, the ratio of I_D/I_G could be used to determine an average crystallite size $L\alpha$ (Equation (4)) [28]. The second order bands are observed in the range of 2500–3300 cm^{-1}. The S3 peak located at ~2900 cm^{-1} is an overtone derived from the combination of D and G modes, while the 2G peak at ~3180 cm^{-1} is attributed to an overtone of the G band. The 2D band (also called the G′ band) at ~2700 cm^{-1} is a second-order band of the D peak. It is called the 2D band since it involves two of the same phonons responsible for the D band but it does not require the presence of the defects in the structure in contrast with the D band [44]. The value of I_{2D}/I_G (intensities ratio of 2D and G bands) defines the number of graphene layers in the structure. The number of layers increases with an increase of the G band intensity and the decrease of the 2D intensity [45]. In this study, the much higher intensity of the G peak is observed in all Raman spectra of synthesized samples compared to that of the 2D band. This suggests the multilayer structure in all obtained thermally reduced GO products.

As can be seen in Figure 4a, the ratio of I_D/I_G is found to be 0.89 and 0.92 for GO_1 and GO_2 samples, respectively. The higher I_D/I_G value for GO_2 indicates that this sample has a more defective structure than GO_1 due to the higher number of sp^3 defects and other disorders generated by the attachment of oxygen-containing functional groups to the graphene layers. Furthermore, the D and G bands in the GO_2 spectrum are shifted to higher

wavenumbers compared to that of GO_1, indicating a greater disruption of the conjugated structure after the oxidation process in the GO_2 sample. Meanwhile, Figure 4b,c indicates that the values of I_D/I_G for rGO samples obtained during thermal reduction of GO with MA and P_2O_5 additives varies from 0.91 to 0.96 and are slightly higher in comparison with those of pure GO. This increase might be due to the removal of functional groups and the high release of gaseous products during thermal reduction that causes disorders in the structure, such as vacancies, dislocations, armchair, and zigzag edges. Furthermore, from Figure 4b,c it can be noted that the thermal treatment of GO in the presence of additives causes a slightly higher I_D/I_G value than that of the thermal treatment of GO without additives. The value of the I_D/I_G could rise due to the presence of phosphorus atoms in the structure of the rGO samples, which were effectively introduced during thermal treatment of GO in the presence of the MA and P_2O_5 mixture. These phosphorus atoms could be attached to the graphene layer in the form of C–P–O or C–P=O bonds generating sp^3 defects and, also, may be able to replace carbon atoms creating new point defects in the structure due to the higher atomic radius of P than that of C atoms. Nonetheless, this slight increase of I_D/I_G does not detract from the benefits of the use of carbon suboxide in the thermal reduction of GO since lower values of I_D/I_G are obtained compared to the results investigated by other authors [18,29,45,46]. Furthermore, the values of $L\alpha$ vary from 19.79 to 21.59 nm between all synthesized samples showing that the crystallite size remains similar during the thermal treatment in the presence and absence of the addition of MA and P_2O_5 mixture.

The morphology of thermally reduced GO samples was studied using SEM analysis at 50,000× magnification (Figure 5). SEM images of the GO_1 and GO_2 samples (Figure 5a,e) present a well-ordered layered structure with folds and wrinkles. This is a consequence of the oxidative treatment of graphite by the attachment of oxygen functional groups. After thermal reduction of the pure GO_1 sample (Figure 5b), the layers agglomerate and form carbon derivatives of about 1 μm in size. The heat treatment of GO_1 with the mixture of MA (5 wt%) and P_2O_5 (Figure 5c) leads to irregular stacking of graphene layers with multiple folds. The further increase of additives in the thermal reduction of GO_1 creates a corrugated morphology, as can be seen in Figure 5d. These obtained folded sheets could be related not only to the reduction process but also to the insertion of phosphorus into the rGO_1_5 and rGO_1_10 structures, because the phosphorus atoms form a pyramid-like structure in the graphene sheet due to increased bond length and decreased bond angle [23,47]. After the reduction of pure GO_2 (Figure 5f), no agglomerates are observed, but the graphene layers are disrupted into smaller randomly arranged sheets. The rGO_2_10 sample is composed of numerous thin layers that are randomly stacked together, forming a porous network. Furthermore, as can be seen from Figure 5g,h, both reduced GO_2 samples in the presence of additives (rGO_2_5 and rGO_2_10) exhibit nanosheets with folded and crumpled features that could also be attributed to the doping of rGO with phosphorus atoms.

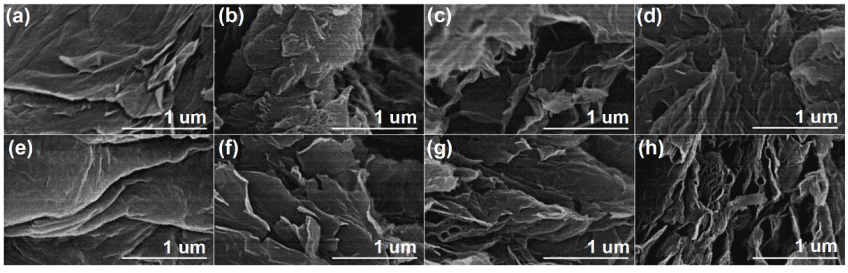

Figure 5. SEM images of GO_1 (**a**), rGO_1 (**b**), rGO_1_5 (**c**), rGO_1_10 (**d**), GO_2 (**e**), rGO_2 (**f**), rGO_2_5 (**g**), and rGO_2_10 (**h**) samples.

Electrical conductivity is one of the key characteristics determining the successful application of rGO in various electrochemical systems such as (bio)sensors, supercapacitors, fuel cells, etc. The electrical behavior of non-metallic powders, including carbonaceous compounds, could be estimated by monitoring the electrical conductivity of bulk materials under compression [48]. Consequently, in this study, the relationship between electrical conductivity (σ) on the logarithmic scale and bulk density (ρ_{bulk}) was determined. The results presented in Figure 6 reveal that the electrical conductivity of prepared carbon materials increases with the increasing of ρ_{bulk} value. This trend is in accordance with the electrical conductivity and resistivity results of graphene, graphite, graphite oxide, carbon black, and carbon nanotubes reported in [48–50]. By compressing a bulk material, closer contact between particles is achieved, leading to higher electrical conductivity because higher electron mobility is ensured in the sample. Following this, the highest electrical conductivity is established with maximum values of bulk density when the most compact arrangement of particles is obtained. The electrical conductivity of pristine graphite is dependent on the compression of the sample as well. From Figure 6a, it can be noted that graphite is a good electrical conductor. Log electrical conductivity varies in the range 1.47–3.53 S m^{-1}, approaching the theoretical values [50]. Besides, the maximum value of ρ_{bulk} for graphite powder is found to be 2.03 g cm^{-3}, which is a similar result to the theoretical value of its density reported in the literature (ρ = 2.26 g cm^{-3}) [51]. Meanwhile, the electrical conductivity of both synthesized GO_1 and GO_2 samples is significantly lower than that of graphite. This decrease is certainly due to the existence of a large number of oxygen-containing functional groups in the backbone of the graphene sheet. Upon oxidation treatment of graphite its band gap significantly broadens due to the disruption of the sp^2 carbon network and the attachment of numerous oxygen-containing functionalities to the surface that inhibit the effective electron transport. Furthermore, higher resistivity is estimated in the case of GO_2, which proves the higher degree of oxidation for GO_2 compared to that of GO_1.

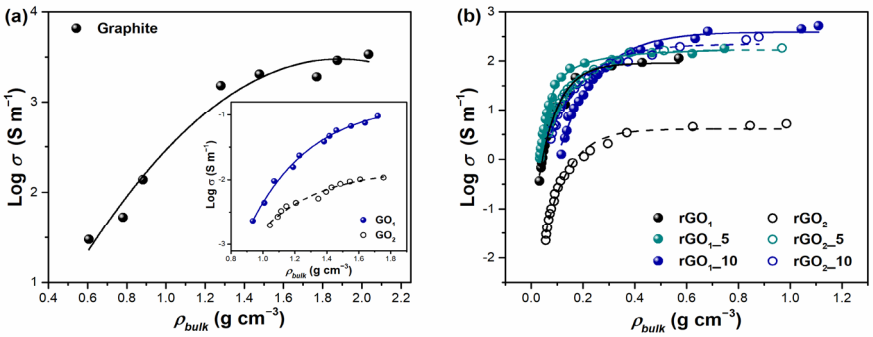

Figure 6. Electrical conductivity dependence on bulk density for graphite (**a**) and thermally reduced GO samples (**b**). The inset in (**a**) demonstrates the relationship between electrical conductivity and bulk density for GO_1 and GO_2 samples.

Figure 6b represents the dependence of electrical conductivity on bulk density for thermally reduced GO samples. It should be noted that the bulk density values for all annealed compounds are significantly decreased compared to those of their precursors (GO_1 and GO_2). This drastic change in density indicates the porous structure of products after thermal treatment. The highest bulk density corresponds to the rGO_1_10 sample (ρ_{bulk} = 1.11 g cm^{-3}), while the lowest density value is determined for the rGO_1 product (ρ_{bulk} = 0.57 cm^{-3}). Furthermore, a remarkable enhancement of electrical conductivity is observed after the thermal decomposition process of GO in the presence of the MA and

P_2O_5 mixture. The higher the amount of additives used in the thermal reduction reaction, the higher the conductivity achieved. In addition, higher electrical conductivity values in the case of rGO samples are achieved at lower densities than that of graphite. This makes these materials promising in the production of supercapacitor electrodes. Log conductivity (S m^{-1}) appears to be in the range of –0.43–2.05 for rGO_1, 0.01–2.25 for rGO_1_5, 0.09–2.72 for rGO_1_10, –1.65–0.71 for rGO_2, 0.53–2.26 for rGO_2_5, and 0.40–2.48 for rGO_2_10, showing the semi-conductor properties of samples. These electrical conductivity values of rGO are similar to previous reports found in the literature [49,52]. It should be highlighted that the most obvious advantage of the use of additives is observed in the set of thermally reduced GO_2 samples. As can be seen from Figure 6b, rGO_2 without additives shows the worst conductivity between all reduced products, but the addition of MA and P_2O_5 enhances electrical conductivity extremely in rGO_2_5 and rGO_2_10. These reduced samples exhibit values close to the reduced GO_1 products with additives indicating the achieved effective recovery of π-conjugated system. Moreover, it could be clearly seen that the addition of MA (10 wt%) and P_2O_5 in the thermal reduction of GO leads to the highest values of electrical conductivity between all reduced samples. This suggests that carbon suboxide used in the thermal reduction reaction of GO could repair the sp^2 hybridized carbon structure and improve electron mobility. However, the presence of phosphorus atoms observed by EDX and FTIR analysis could also influence the electrical behavior of the rGO_1_5, rGO_1_10, rGO_2_5, and rGO_2_10 samples because phosphorus atoms are capable of modulating the electronic structure and decreasing the resistivity of graphene-based derivatives. The incorporation of phosphorus species may increase the density of charge carries in the carbon product due to the contribution of phosphorus electrons to the graphene π-conjugated system [23]. Overall, the obtained electrical conductivity data indicate that the thermal reduction of GO with the use of the MA and P_2O_5 mixture has a positive impact on electronic properties of the final products. The relatively high conductivity at low values of bulk density demonstrates the possibility of applying thermally reduced GO samples for metal-free and cheap carbon-based electrode materials.

The samples having the highest values in electrical conductivity (rGO_1_10 and rGO_2_10) were analyzed using TEM analysis to compare their structure morphology and crystallinity in detail. Obtained TEM and SAED patterns are presented in Figure 7.

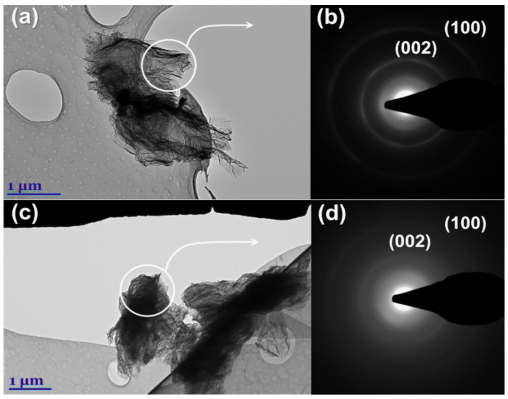

Figure 7. TEM images of—rGO_1_10 (**a**) and rGO_2_10 (**c**). SAED patterns of rGO_1_10 (**b**) and rGO_2_10 (**d**).

The TEM image of the rGO_1_10 specimen clearly shows several transparent reduced graphene oxide layers with wrinkled and folded features originated from the exfoliation process and incorporation of phosphorus atoms in the structure of graphene layer. However,

the existence of darker areas indicates thick stacking nanostructure in some regions. In contrast, rGO_2_10 consists of a remarkable multi-layered structure with corrugations that confirms the presence of structural defects in the nanosheets. The SAED images presented in Figure 7b,d show typical ring-like patterns indicating the polycrystalline nature of the rGO_1_10 and rGO_2_10 samples [53]. Nevertheless, the more obscure and featureless rings with unclear diffraction spots in the SAED image of rGO_2_10 are evidence of a more amorphous and disordered structure compared with that of rGO_1_10. For this reason, the rGO_2_10 sample may contain a larger number of sp^3 regions and phosphorus atoms in its structure. Based on obtained XRD analysis data it is determined that the inner ring shown in SAED images is associated with the diffraction of (002) planes and the outer ring describes (100) planes. This is in accordance with the study on the SAED patterns of reduced graphene oxide reported by Ngidi et al. [54]. The presence of both planes (002) and (100) confirms the partial restoration of sp^2 structure in both rGO_1_10 and rGO_2_10 samples.

4. Conclusions

In summary, we presented a novel and simple thermal reduction of a GO technique in the presence of malonic acid and phosphorus pentoxide that results in a repaired π-conjugated system and the incorporation of phosphorus atoms into the structure. It has been determined that structural and electrical properties or rGO samples depend on the amount of additive used and the type of GO. The best recovery of sp^2 hybridized carbon system was achieved using the mixture which has 10 wt% of malonic acid. Thermally reduced GO_1 samples in the presence of additives have higher values of electrical conductivity compared with those of annealed GO_2 samples. Furthermore, the investigation has showed the doping of phosphorus atoms in all rGO samples obtained using additives. The highest phosphorus content (2.3 at%) was achieved in rGO_2_10 compared to that of other samples synthesized. This suggests that samples prepared in this study could have a potential application in supercapacitors, biosensors, and fuel cells since the phosphorus-rich sites in rGO materials could act as electrochemical active regions, which can improve charge storage properties, increase charge carries, and enhance the capacity performance during electrochemical measurement. Moreover, the obtained findings set the direction for future research, suggesting that studies aimed at the full recovery of π-conjugated system and incorporation of high amounts of phosphorus-containing functionalities should focus on optimization of the GO-reduction process. It is still essential to test the effect of different temperatures, amount of additives, or pressure on the rGO structural changes.

Author Contributions: Conceptualization, J.B.; data curation, R.A.; funding acquisition, J.G.; investigation, R.A., G.N., M.S. and V.B.; methodology, J.B. and J.G.; supervision, J.B. and J.G.; visualization, R.A.; writing—original draft, R.A.; writing—review and editing, J.G., G.N., M.S., V.B. and J.B. All authors have read and agreed to the published version of the manuscript.

Funding: This research has received funding from European Social Fund (project No. 09.3.3-LMT-K-712-16-0154) under grant agreement with the Research Council of Lithuania (LMTLT).

Institutional Review Board Statement: Not applicable.

Informed Consent Statement: Not applicable.

Data Availability Statement: Data are contained within the article.

Conflicts of Interest: The authors declare no conflict of interest.

References

1. Ensafi, A.A.; Alinajafi, H.A.; Rezaei, B. Thermally reduced graphene oxide/polymelamine formaldehyde nanocomposite as a high specific capacitance electrochemical supercapacitor electrode. *J. Mater. Chem. A* **2018**, *6*, 6045–6053. [CrossRef]
2. Šakinyte, I.; Barkauskas, J.; Gaidukevič, J.; Razumiene, J. Thermally reduced graphene oxide: The study and use for reagentless amperometric d-fructose biosensors. *Talanta* **2015**, *144*, 1096–1103. [CrossRef]
3. Singh, R.K.; Kumar, R.; Singh, D.P. Graphene oxide: Strategies for synthesis, reduction and frontier applications. *RSC Adv.* **2016**, *6*, 64993–65011. [CrossRef]

4. Kurian, M. Recent progress in the chemical reduction of graphene oxide by green reductants–A Mini review. *Carbon Trends* **2021**, *5*, 100120. [CrossRef]
5. Barkauskas, J.; Gaidukevič, J.; Niaura, G. Thermal reduction of graphite oxide in the presence of nitrogen-containing dyes. *Carbon Lett.* **2021**, *31*, 1097–1110. [CrossRef]
6. Qiu, Y.; Collin, F.; Hurt, R.H.; Külaots, I. Thermochemistry and kinetics of graphite oxide exothermic decomposition for safety in large-scale storage and processing. *Carbon Lett.* **2021**, *31*, 1097–1110. [CrossRef]
7. Yang, G.; Li, L.; Lee, W.B.; Ng, M.C. Structure of graphene and its disorders: A review. *Sci. Technol. Adv. Mater.* **2018**, *19*, 613–648. [CrossRef]
8. Kaniyoor, A.; Baby, T.T.; Arockiadoss, T.; Rajalakshmi, N.; Ramaprabhu, S. Wrinkled graphenes: A study on the effects of synthesis parameters on exfoliation-reduction of graphite oxide. *J. Phys. Chem. C* **2011**, *115*, 17660–17669. [CrossRef]
9. Botas, C.; Álvarez, P.; Blanco, C.; Santamaría, R.; Granda, M.; Gutiérrez, M.D.; Rodríguez-Reinoso, F.; Menéndez, R. Critical temperatures in the synthesis of graphene-like materials by thermal exfoliation-reduction of graphite oxide. *Carbon* **2013**, *52*, 476–485. [CrossRef]
10. Zhang, P.; Li, Z.; Zhang, S.; Shao, G. Recent Advances in Effective Reduction of Graphene Oxide for Highly Improved Performance Toward Electrochemical Energy Storage. *Energy Environ. Mater.* **2018**, *1*, 5–12. [CrossRef]
11. Pei, S.; Cheng, H.M. The reduction of graphene oxide. *Carbon* **2012**, *50*, 3210–3228. [CrossRef]
12. Liang, Y.; Frisch, J.; Zhi, L.; Norouzi-Arasi, H.; Feng, X.; Rabe, J.P.; Koch, N.; Müllen, K. Transparent, highly conductive graphene electrodes from acetylene-assisted thermolysis of graphite oxide sheets and nanographene molecules. *Nanotechnology* **2009**, *20*, 434007. [CrossRef]
13. Bortolini, O.; Pandolfo, L.; Tomaselli, C.; Traldi, P. Ion-molecule chemistry of carbon suboxide in an ion-trap mass spectrometer. *Int. J. Mass Spectrom.* **1999**, *190–191*, 171–179. [CrossRef]
14. Allen, M. Carbon suboxide in Halley. *Nature* **1991**, *354*, 272. [CrossRef]
15. Palmer, H.; Cross, W. Carbon films from carbon suboxide decomposition. Inhibition by carbon monoxide and the heat of formation of C2O. *Carbon* **1966**, *3*, 475–481. [CrossRef]
16. Shao, M.; Wang, D.; Yu, G.; Hu, B.; Yu, W.; Qian, Y. The synthesis of carbon nanotubes at low temperature via carbon suboxide disproportionation. *Carbon* **2004**, *42*, 183–185. [CrossRef]
17. Aukstakojyte, R.; Gaidukevic, J.; Barkauskas, J. Thermal Reduction of Graphene Oxide in the Presence of Carbon Suboxide. *J. Solid State Chem.* **2021**, *301*, 122365. [CrossRef]
18. Li, R.; Wei, Z.; Gou, X.; Xu, W. Phosphorus-doped graphene nanosheets as efficient metal-free oxygen reduction electrocatalysts. *RSC Adv.* **2013**, *3*, 9978–9984. [CrossRef]
19. Niu, F.; Tao, L.-M.; Deng, Y.-C.; Wang, Q.-H.; Song, W.-G. Phosphorus doped graphene nanosheets for room temperature NH3 sensing. *New J. Chem.* **2014**, *38*, 2269–2272. [CrossRef]
20. Feng, L.; Qin, Z.; Huang, Y.; Peng, K.; Wang, F.; Yan, Y.; Chen, Y. Boron-, sulfur-, and phosphorus-doped graphene for environmental applications. *Sci. Total Environ.* **2019**, *698*, 134239. [CrossRef]
21. Poh, H.L.; Sofer, Z.; Nováček, M.; Pumera, M. Concurrent Phosphorus Doping and Reduction of Graphene Oxide. *Chem.—A Eur. J.* **2014**, *20*, 4284–4291. [CrossRef]
22. Hu, C.; Liu, D.; Xiao, Y.; Dai, L. Functionalization of graphene materials by heteroatom-doping for energy conversion and storage. *Prog. Nat. Sci.* **2018**, *28*, 121–132. [CrossRef]
23. Fan, X.; Xu, H.; Zuo, S.; Liang, Z.; Yang, S.; Chen, Y. Preparation and supercapacitive properties of phosphorus-doped reduced graphene oxide hydrogel. *Electrochim. Acta* **2019**, *330*, 135207. [CrossRef]
24. Kim, M.; Lee, J.; Jeon, Y.; Piao, Y. Phosphorus-doped graphene nanosheets anchored with cerium oxide nanocrystals as effective sulfur hosts for high performance lithium–sulfur batteries. *Nanoscale* **2019**, *11*, 13758–13766. [CrossRef]
25. Yan, X.; Chen, J.; Yang, J.; Xue, Q.; Miele, P. Fabrication of free-standing, electrochemically active, and biocompatible graphene oxide-polyaniline and graphene-polyaniline hybrid papers. *ACS Appl. Mater. Interfaces* **2010**, *2*, 2521–2529. [CrossRef]
26. Hummers, W.S., Jr.; Offeman, R.E. Preparation of Graphitic Oxide. *J. Am. Chem. Soc.* **1958**, *80*, 1339. [CrossRef]
27. Gaidukevic, J.; Aukstakojyte, R.; Navickas, T.; Pauliukaite, R.; Barkauskas, J. A novel approach to prepare highly oxidized graphene oxide: Structural and electrochemical investigations. *Appl. Surf. Sci.* **2021**, *567*, 150883. [CrossRef]
28. Cançado, L.G.; Takai, K.; Enoki, T.; Endo, M.; Kim, Y.A.; Mizusaki, H.; Jorio, A.; Coelho, L.N.; Magalhães-Paniago, R.; Pimenta, M.A. General equation for the determination of the crystallite size La of nanographite by Raman spectroscopy. *Appl. Phys. Lett.* **2006**, *88*, 163106. [CrossRef]
29. Zhang, C.; Mahmood, N.; Yin, H.; Liu, F.; Hou, Y. Synthesis of phosphorus-doped graphene and its multifunctional applications for oxygen reduction reaction and lithium ion batteries. *Adv. Mater.* **2013**, *25*, 4932–4937. [CrossRef]
30. MacIntosh, A.R.; Jiang, G.; Zamani, P.; Song, Z.; Riese, A.; Harris, K.J.; Fu, X.; Chen, Z.; Sun, X.; Goward, G.R. Phosphorus and Nitrogen Centers in Doped Graphene and Carbon Nanotubes Analyzed through Solid-State NMR. *J. Phys. Chem. C* **2018**, *122*, 6593–6601. [CrossRef]
31. Okotrub, A.; Kanygin, M.; Koroteev, V.; Stolyarova, S.; Gorodetskiy, D.; Fedoseeva, Y.; Asanov, I.; Bulusheva, L.; Vyalikh, A. Phosphorus incorporation into graphitic material via hot pressing of graphite oxide and triphenylphosphine. *Synth. Metals* **2019**, *248*, 53–58. [CrossRef]

32. Luceño-Sánchez, J.A.; Maties, G.; Gonzalez-Arellano, C.; Diez-Pascual, A.M. Synthesis and characterization of graphene oxide derivatives via functionalization reaction with hexamethylene diisocyanate. *Nanomaterials* **2018**, *8*, 870. [CrossRef] [PubMed]
33. Peng, W.; Li, H.; Hu, Y.; Liu, Y.; Song, S. Characterisation of reduced graphene oxides prepared from natural flaky, lump and amorphous graphites. *Mater. Res. Bull.* **2016**, *78*, 119–127. [CrossRef]
34. Ţucureanu, V.; Matei, A.; Avram, A.M. FTIR Spectroscopy for Carbon Family Study. *Crit. Rev. Anal. Chem.* **2016**, *46*, 502–520. [CrossRef]
35. Riahi, K.Z.; Sdiri, N.; Ennigrou, D.J.; Horchani-Naifer, K. Investigations on electrical conductivity and dielectric properties of graphene oxide nanosheets synthetized from modified Hummer's method. *J. Mol. Struct.* **2020**, *1216*, 128304. [CrossRef]
36. Verma, S.; Dutta, R.K. A facile method of synthesizing ammonia modified graphene oxide for efficient removal of uranyl ions from aqueous medium. *RSC Adv.* **2015**, *5*, 77192–77203. [CrossRef]
37. Zu, L.; Gao, X.; Lian, H.; Cai, X.; Li, C.; Zhong, Y.; Hao, Y.; Zhang, Y.; Gong, Z.; Liu, Y.; et al. High Electrochemical Performance Phosphorus-Oxide Modified Graphene Electrode for Redox Supercapacitors Prepared by One-Step Electrochemical Exfoliation. *Nanomaterials* **2018**, *8*, 417. [CrossRef]
38. Nie, L.; Wang, C.; Hou, R.; Li, X.; Sun, M.; Suo, J.; Wang, Z.; Cai, R.; Yin, B.; Fang, L.; et al. Preparation and characterization of dithiol-modified graphene oxide nanosheets reinforced alginate nanocomposite as bone scaffold. *SN Appl. Sci.* **2019**, *1*, 545. [CrossRef]
39. Sharma, N.; Sharma, V.; Vyas, R.; Kumari, M.; Kaushal, A.; Gupta, R.; Sharma, S.; Sachdev, K. A new sustainable green protocol for production of reduced graphene oxide and its gas sensing properties. *J. Sci. Adv. Mater. Devices* **2019**, *4*, 473–482. [CrossRef]
40. Gaidukevič, J.; Barkauskas, J.; Malaika, A.; Rechnia-Gorący, P.; Możdżyńska, A.; Jasulaitienė, V.; Kozłowski, M. Modified graphene-based materials as effective catalysts for transesterification of rapeseed oil to biodiesel fuel. *Chin. J. Catal.* **2018**, *39*, 1633–1645. [CrossRef]
41. Sengupta, I.; Chakraborty, S.; Talukdar, M.; Pal, S.K.; Chakraborty, S. Thermal reduction of graphene oxide: How temperature influences purity. *J. Mater. Res.* **2018**, *33*, 4113–4122. [CrossRef]
42. Stanford, V.L.; Vyazovkin, S. Thermal Decomposition Kinetics of Malonic Acid in the Condensed Phase. *Ind. Eng. Chem. Res.* **2017**, *56*, 7964–7970. [CrossRef]
43. Tuz Johra, F.; Lee, J.-W.; Jung, W.-G. Facile and safe graphene preparation on solution based platform. *J. Ind. Eng. Chem.* **2014**, *20*, 2883–2887. [CrossRef]
44. Ma, B.; Rodriguez, R.D.; Ruban, A.; Pavlov, S.; Sheremet, E. The correlation between electrical conductivity and second-order Raman modes of laser-reduced graphene oxide. *Phys. Chem. Chem. Phys.* **2019**, *21*, 10125–10134. [CrossRef] [PubMed]
45. Muzyka, R.; Drewniak, S.; Pustelny, T.; Chrubasik, M.; Gryglewicz, G. Characterization of graphite oxide and reduced graphene oxide obtained from different graphite precursors and oxidized by different methods using Raman spectroscopy. *Materials* **2018**, *11*, 1050. [CrossRef] [PubMed]
46. Kumar, R.; Kaur, A. Chemiresistive gas sensors based on thermally reduced graphene oxide for sensing sulphur dioxide at room temperature. *Diam. Relat. Mater.* **2020**, *109*, 108039. [CrossRef]
47. Wang, H.-M.; Chen, Y.; Liu, Y.-J.; Zhao, J.-X.; Cai, Q.-H.; Wang, X.-Z. Phosphorus-doped graphene and (8, 0) carbon nanotube: Structural, electronic, magnetic properties, and chemical reactivity. *Appl. Surf. Sci.* **2013**, *273*, 302–309. [CrossRef]
48. Marinho, B.; Ghislandi, M.; Tkalya, E.; Koning, C.E.; de With, G. Electrical conductivity of compacts of graphene, multi-wall carbon nanotubes, carbon black, and graphite powder. *Powder Technol.* **2012**, *221*, 351–358. [CrossRef]
49. Gaidukevič, J.; Pauliukaitė, R.; Niaura, G.; Matulaitienė, I.; Opuchovič, O.; Radzevič, A.; Astromskas, G.; Bukauskas, V.; Barkauskas, J. Synthesis of reduced graphene oxide with adjustable microstructure using regioselective reduction in the melt of boric acid: Relationship between structural properties and electrochemical performance. *Nanomaterials* **2018**, *8*, 889. [CrossRef]
50. Rattanaweeranon, S.; Limsuwan, P.; Thongpool, V.; Piriyawong, V.; Asanithi, P. Influence of Bulk Graphite Density on Electrical Conductivity. *Procedia Eng.* **2012**, *32*, 1100–1106. [CrossRef]
51. Ayyappadas, C.; Shanu, O.S.; Vijayan, A.; Mohammed, I.A.; Vishnu, V.; Shamnadh, M. Effect of graphene, SiC and graphite addition on hardness, microstructure and electrical conductivity of microwave sintered copper MMCs fabricated by powder metallurgy route. *J. Phy. Conf. Ser.* **2019**, *1355*, 012035. [CrossRef]
52. Park, H.; Lim, S.; Du Nguyen, D.; Suk, J.W. Electrical measurements of thermally reduced graphene oxide powders under pressure. *Nanomaterials* **2019**, *9*, 1387. [CrossRef] [PubMed]
53. Wilson, D.; Sheng, K.; Yang, W.; Jones, R.; Dunlap, N.; Read, P. Modern Electron Microscopy in Physical and Life Sciences: Electron Diffraction. 2016. Available online: https://www.intechopen.com/chapters/49537 (accessed on 28 August 2022).
54. Ngidi, N.P.D.; Ollengo, M.A.; Nyamori, V.O. Effect of Doping Temperatures and Nitrogen Precursors on the Physicochemical, Optical, and Electrical Conductivity Properties of Nitrogen-Doped Reduced Graphene Oxide. *Materials* **2019**, *12*, 3376. [CrossRef] [PubMed]

3rd publication

"A novel electrochemical sensor based on thermally reduced graphene oxide for the sensitive determination of dopamine"

J. Gaidukevic, **R. Aukstakojyte**, J. Barkauskas, G. Niaura, T. Murauskas, R. Pauliukaite

Applied Surface Science, 592, 2022, 153257
DOI: 10.1016/j.apsusc.2022.153257

Applied Surface Science 592 (2022) 153257

Contents lists available at ScienceDirect

Applied Surface Science

journal homepage: www.elsevier.com/locate/apsusc

Full Length Article

A novel electrochemical sensor based on thermally reduced graphene oxide for the sensitive determination of dopamine

Justina Gaidukevic [a,b,*], Ruta Aukstakojyte [b], Jurgis Barkauskas [b], Gediminas Niaura [c], Tomas Murauskas [b], Rasa Pauliukaite [a]

[a] Department of Nanoengineering, Center for Physical Sciences and Technology (FTMC), Savanoriu Ave. 231, LT-02300 Vilnius, Lithuania
[b] Vilnius University, Faculty of Chemistry and Geosciences, Institute of Chemistry, Naugarduko str. 24, LT-03225 Vilnius, Lithuania
[c] Department of Organic Chemistry, Center for Physical Sciences and Technology (FTMC), Sauletekio Ave. 3, LT-10257 Vilnius, Lithuania

ARTICLE INFO

Keywords:
Thermally reduced graphene oxide
Electrochemical sensor
Dopamine
Carbon suboxide
Structural analysis

ABSTRACT

In this paper, two different reduced graphene oxide samples rGO_H and rGO_M derived, respectively, from the graphene oxide (GO) obtained using traditional and modified Hummers methods were synthesized. Thermal reduction of GO was performed in the presence of malonic acid (MA) and P_2O_5 additives. The prepared rGO samples were investigated as active electrode materials for the electrochemical determination of dopamine (DA). The structural characterization using XPS demonstrated that the thermal treatment of GO with the mixture of MA and P_2O_5 leads to incorporation of phosphorus functional groups into the structure of graphene-based material, as evidenced by an increase in the phosphorus content in rGO_H (1.84%) and rGO_M (2.74%). Raman analysis confirms that a slightly larger number of defects are present in the rGO_M sample (I_D/I_G = 0.94) than in the rGO_H structure (I_D/I_G = 0.93). Electrochemical studies using CV and DPV showed that the rGO_M sample significantly improves the oxidation peak current of DA, demonstrating its higher sensitivity to the determination of dopamine than that on rGO_H. Also, it was determined that the proposed sensor based on rGO_M shows a low limit of detection value (0.11 μM) and high sensitivity (28.64 μA μM^{-1} cm^{-2}) toward DA detection.

1. Introduction

Because of the high demand of the world market, the number of electrochemical sensors suitable for commercial use is increasing regularly. However, there are a range of problems that hinder the widespread use of these sensors for the detection of analytes, and most of them are related to the design [1–3]. The general purpose is to get a reliable and strong analytical signal. In view of the above, current research is often focused on nanostructured carbon materials, which have tunable textural and chemical properties and can be easily obtained using simple and economically viable methods [4–6]. More recently, graphene and graphene-based materials, such as graphene oxide (GO), and reduced graphene oxide (rGO), have attracted much interest in sensing applications [7–10]. Incorporation of graphene and its related nanomaterials into sensor technologies has also attracted growing attention due to its high surface area, electrical conductivity, chemical stability, and its ability to immobilize a variety of different molecules [10–12].

Recently, the development of graphene-based sensors for dopamine (DA) detection has gained considerable attention because of the important role of dopamine in the human body. Dopamine is one of the most prominent neurotransmitters in our nervous system, also known as the neurotransmitter of pleasure [13,14]. The main function of dopamine is to transport signals from the brain to different organs and parts of the body. Moreover, dopamine is responsible for our emotional responses and for the control of the movements a person makes. Thus, brain function that controls mood, memory, learning, and focusing is affected by the concentration of dopamine in the body. Consequently, the normal balance of dopamine is vital not only for physical but also psychological well-being [14,15]. According to the literature, a common nervous disease that occurs in the deficiency of DA is depression, hallucinosis, Alzheimer's, and Parkinson's [14,16–18]. Therefore, the precise determination of DA, as well as the development of sensitive and selective platforms for the detection of DA, has become an important issue in clinical diagnosis, especially at a very low concentration.

Lately, the construction of carbonaceous or graphene-based sensors for the determination of neurotransmitters has been improved with the

* Corresponding author at: Department of Nanoengineering, Center for Physical Sciences and Technology (FTMC), Savanoriu Ave. 231, LT-02300 Vilnius, Lithuania.
E-mail address: justina.gaidukevic@chf.vu.lt (J. Gaidukevic).

https://doi.org/10.1016/j.apsusc.2022.153257
Received 2 February 2022; Received in revised form 21 March 2022; Accepted 29 March 2022
Available online 1 April 2022

incorporation of various nanomaterials such as metal oxides (Co_3O_4 [19,20], TiO_2 [21,22], Fe_2O_3 [23,24], etc.), polymeric materials [25–30], polyionic liquids [31,32], and metal nanoparticles (Au, Pd, Ag, or Pt) [31,33,34] due to their high electrical conductivity, high surface-to-volume ratio, thus contributing to the improvement of the analytical performance of sensors. However, although the aforementioned materials are promising in the support/transducer system, they still suffer from numerous drawbacks, for example poor stability and biomolecule adsorption, more complicated surface chemistry, and high cost [15]. Despite this, the research field of graphene-based sensors is rather dominated by the use of nanocomposites that combine graphene or graphene-related materials with other compounds. In contrast, the application of independent graphene materials is incomparably less common. For this reason, the area of the development of pristine graphene-based sensors has not been explored in depth and needs to be elaborated in order to eliminate the drawbacks mentioned above.

The aim of this work is to prepare highly electrocatalytically active graphene-based materials, as well as the characterization and testing of the electrochemical performance of the samples in dopamine detection. In this study, we present a prospective electrochemical sensing platform for the effective detection of dopamine based on thermally reduced graphene oxide. Thermal reduction of two different GO has been performed in the presence of malonic acid (MA) and P_2O_5 additives, which have also been used as a precursor to the synthesis of carbon suboxide (C_3O_2) [35,36]. The C_3O_2 obtained *in situ* could be an alternative source of atomic carbon in the thermal reduction of GO to repair the conjugated aromatic structure of rGO sheets. Moreover, we have shown for the first time, that the thermal treatment of GO in the presence of MA and the P_2O_5 mixture not only causes an effective restoration of the π-conjugated system of graphene layers, but also leads to an effective incorporation of the P element in the structure of the graphene-based material. Furthermore, to the best of our knowledge, the newly prepared samples have been applied for the first time in the development of electrochemical sensors for the detection of dopamine. Thus, this work makes a significant contribution to future developments in a new type of sensing platform that could enable the early detection of various neurological disorders and will inevitably focus on the technology of new conductive materials, especially the new graphene-based materials.

2. Experimental section

2.1. Materials

Graphite powder (purity ≥ 99.5%), potassium persulfate ($K_2S_2O_8$, purity 99.99%), sodium nitrate ($NaNO_3$, purity ≥ 99%), phosphorus pentoxide (P_2O_5, purity ≥ 99%), potassium permanganate ($KMnO_4$, purity ≥ 99%), malonic acid ($CH_2(COOH)_2$, purity 99%), chromium(VI) oxide (CrO_3, purity 99.99%), boric acid (H_3BO_3, purity ≥ 99.5%), dopamine hydrochloride ($(HO)_2C_6H_3CH_2CH_2NH_2 \cdot HCl$, purity 98%), and uric acid ($C_5H_4N_4O_3$, purity ≥ 99%) were purchased from Merck (Darmstadt, Germany). Phosphate buffer (PB) solution (pH 7.2, c = 0.1 mol L^{-1})) was prepared by sodium phosphate dibasic (Na_2HPO_4, purity ≥ 99%, Sigma-Aldrich, Steinheim, Germany) and sodium phosphate monobasic (NaH_2PO_4, purity ≥ 99%, Sigma-Aldrich, Steinheim, Germany). Sulphuric acid (H_2SO_4, purity ≥ 98%) and hydrogen peroxide (H_2O_2, 30% weight) were obtained from Eurochemicals (Bratislava, Slovakia). Nafion (5% weight) was purchased from Alfa Aesar (Kandel, Germany).

2.2. Synthesis of GO employing traditional Hummers' method

GO was derived from natural graphite by treating it with strong oxidizers in an acidic medium. The method used is as proposed by William S. Hummers and Richard E. Offeman. The detailed synthesis procedure has been reported in [37]. After this treatment, the sample obtained was washed with an aqueous solution of 10 wt% HCl, purified by dialysis tubing, filtered, and dried in a desiccator. The powder produced was marked as GO_H.

2.3. Preparation of GO by modified Hummers' method

The method used was previously proposed by our research group [38]. The alteration made to the Hummers and Offeman method was the preoxidation of pristine graphite powder using the H_2SO_4, H_3BO_3 and CrO_3 mixture. After the pre-oxidation step, the strong oxidation of the product obtained was carried out using the traditional Hummers' method. The resultant sample was denoted as GO_M.

2.4. Thermal reduction of GO samples in the presence of C_3O_2

The thermal reduction method used is as followed by our previous work [39]. The appropriate prepared GO samples were subjected to thermal reduction at 800 °C, in an argon atmosphere in the presence of MA (10 wt%) and P_2O_5 mixture. The details of the reduction protocol were as follows: 0.1 g of GO_H (or GO_M) powder, 0.01 g of malonic acid, and 0.009 g of P_2O_5 were mixed in agate mortar under ambient conditions for 10 min. Afterwards, the mixture was annealed in a horizontal tube furnace under Ar flow (60 mL min^{-1}) at a temperature of 800 °C for 1 h. The resulting carbons were denoted rGO_H and rGO_M, respectively. Thermal reduction of GO samples without additives was also performed following the protocol above. The samples were labeled rGO_H0 and rGO_M0, respectively.

2.5. Material characterization

Raman spectroscopy was performed using an inVia Raman spectrometer (Renishaw, Wotton-under-Edge, Gloucestershire, UK) equipped with a grating containing 1800 grooves mm^{-1} and a thermoelectrically cooled (−70 °C) CCD camera. Spectra were excited with 532 nm wavelength radiation with the diode-pumped solid-state (DPSS) laser. The integration time was 100 s. The 20×/0.40NA objective (Leica, Wetzlar, Germany) was used during the all measurements. Raman frequencies were calibrated by the silicon peak at 520.7 cm^{-1}. The crystallite size (L_α) was determined using the following equation [40]:

$$L_\alpha(nm) = \left(2.4 \times 10^{-10}\right) \times \lambda_L^4 \times \left[\frac{I(D)}{I(G)}\right]^{-1} \quad (1)$$

where L_a is the crystallite size and λ is the wavelength of the laser source (532 nm).

X-ray photoelectron spectroscopy (XPS) analysis was performed with a Kratos Axis Supra (Kratos analytical) spectrometer. Monochromatic Al $K\alpha$ radiation ($h\nu = 1486.69$ eV) was used as an X-ray source. The spectra were recorded at a pass energy of 20 eV and calibrated using the carbon 1 s line at 284.6 eV. The raw XPS spectra were deconvoluted by curve fitting peak components using the software CASAXPS. Symmetric Gaussian–Lorentzian functions were used to approximate the line shapes of the fitting components after a Shirley-type background subtraction.

Scanning electron microscope (SEM) images were obtained using a Hitachi SU-70 microscope (Tokyo, Japan) at an accelerating voltage of 10.0 kV at magnifications of 20,000.

2.6. Sensor construction

Electrochemical measurements were performed under ambient conditions at a temperature of 22 °C and a relative humidity of 40%, using a potentiostat/galvanostat CompactStat instrument (Ivium Technologies, The Netherlands). All electrochemical measurements were conducted in a three-electrode system composed of an auxiliary platinum wire electrode, a reference Ag/AgCl electrode, and working electrodes (Ø 3 mm). The working electrode was constructed by coating the

active material onto the surface of a glassy carbon electrode (GCE) previously polished with alumina powder (0.05 μm, Kemet, UK) and ultrasonicated in deionized water and ethanol for one hour. For the preparation of graphene-based active material/GCE modified electrodes, 1 mg of rGO_H (or rGO_M) sample was dispersed in 1 mL of the mixture of deionized water and Nafion (V_{water}:V_{Nafion} = 9:1) by sonicating in an ultrasonic bath for 2 h. Then 10 μL of the suspension (1.0 mg mL^{-1}) was drop-casted onto the GCE surface and left to dry at room temperature.

2.7. Electrochemical measurements

Cyclic voltammetry (CV) and differential pulse voltammetry (DPV) were used to investigate the electrochemical behaviour of dopamine at the modified GCE/rGO-based electrode. CV measurements were conducted cycling the potential from − 0.2 to + 0.8 V (vs Ag/AgCl) at a scan rate of 100 mV s^{-1} in a 0.1 M PB solution (pH = 7.2). The impact of the scan rate was also determined in the same buffer solution from 10 to 180 mV s^{-1}. The start potential of − 0.4 V, the end potential of + 0.6 V, the potential step of 5 mV, the scan rate 50 mV s^{-1}, the pulse time of 10 ms, and the pulse amplitude of 50 mV were used for the DPV electrochemical analysis.

In the interference study, 200 μM of uric acid (UA) and 1 mM of ascorbic acid (AA) were added to the electrochemical system. The selective detection of analytes was carried out by changing the concentrations of dopamine while keeping the UA and AA constant.

3. Results and discussion

3.1. Structural characterization of graphene-based materials

The elements occurring in the GO and thermally reduced GO samples as well as their chemical state have been determined by XPS analysis. Wide scan XPS spectra presented in Fig. 1 (a) show that elements including C, O, N, and S are found in the GO_H and GO_M samples, while carbon and oxygen, as well as a little content of the P element, are detected onto the surface of rGO_H and rGO_M. Fig. 1 (b) summarizes the elemental compositions of all reduced and non-reduced graphene-based samples. It is found that the content of each element in GO_H is C 68.33%, O 28.67%, N 1.21%, and S 1.79%, respectively. On the contrary, the GO_M sample has C 66.20%, O 32.29%, N 0.61%, and S 0.90%. Quantitative XPS analysis reveals that GO obtained by the modified Hummers' method using a pre-oxidation step with the $H_2SO_4/H_3BO_3/CrO_3$ mixture has a higher degree of oxidation (C/O = 2.05) than GO prepared by the traditional Hummers' method (C/O = 2.38).

Moreover, from the data shown in Fig. 1 (b), it is apparent that a small amount of nitrogen and sulphur is present in the GO_H and GO_M samples. The origin of these elements may be attributed to the presence of the residual substances (e.g. nitrates and sulphates) that have not been washed out thoroughly after the chemical treatment of pure or pre-oxidized graphite.

Furthermore, from Fig. 1 (b), it can be noted that thermal treatment of GO samples causes a significant decrease of the relative concentration of oxygen (from 28.67% and 32.29% observed in the case of GO_H and GO_M, respectively, even up to 9.64% for the rGO_H sample and up to 12.03% for the rGO_M), while it increases relative concentration of carbon (from 68.33% up to 88.52% in the case of GO_H and from 66.2% up to 85.22% in the case of GO_M). These observations suggest that the restoration of the π-conjugate structure of the reduced samples is only partial and that residual oxygen-containing functional groups are still present on the surface of rGO_H and rGO_M. Furthermore, sulphur and nitrogen are not detected in the rGO samples. This can be explained by the fact that residual ions (NO_3^- and SO_4^{2-}) intercalated between the GO graphene layers during GO preparation have been leached from the surface during thermal treatment at high temperature. The thermal treatment of GO in the presence of a mixture of MA and P_2O_5 leads to effective incorporation of the P element into the structure of the graphene-based material, as evidenced by an increase in the phosphorus content in rGO_H (1.84%) and rGO_M (2.74%).

In addition, to estimate the distribution of carbon and oxygen bonds, the C 1 s XPS spectra of the prepared samples have been deconvoluted into six components. Fig. 2 and Fig. 3 summarize the results of the deconvolution of the high-resolution C1s XPS spectra of the prepared graphene-based materials, showing the type and concentration of various carbon species.

After deconvolution of the GO_H and GO_M C1s XPS spectra (Fig. 2 (a) and (c)), two peaks presented at binding energies ~ 284.0 eV and ~ 285.2 eV correspond to the carbon sp^2 and sp^3 bonds [41]. The remaining three peaks with binding energies of approximately 286.7 eV, 287.3 eV, and 288.7 eV correspond to the hydroxyl/epoxy groups (C-OH/C-O-C), the carbonyl/quinone group (C = O), and the carboxylic (O-C = O) group, respectively [42,43]. The peak at 291 eV is due to π-π* shake-up, which is characteristic of sp^2 aromatic bonds [43]. Based on the results presented in Fig. 3, it can be noted that the hydroxyl/epoxy (50.72 at.%) and carboxyl (10.78 at.%) groups are the most abundant on the surface of GO_H. Also, smaller amounts of carbonyl and quinone (7.35 at.%) groups are present on its surface. Instead, the hydroxyl/epoxy (40.17 at.%) groups are also dominated onto the GO_M surface. However, compared to the traditional Hummers' method, pre-treatment with $H_2SO_4/H_3BO_3/CrO_3$ causes a considerable increase in the carbonyl and quinone (15.36 at.%) groups, while GO_M has a low number of carboxyl groups (3.58 at.%). Furthermore, the higher concentration of sp^3 bonds (21.37 at.%) on the surface of GO_M than GO_H (10.94 at.%) highlights that GO_M has a higher amount of oxygen-containing

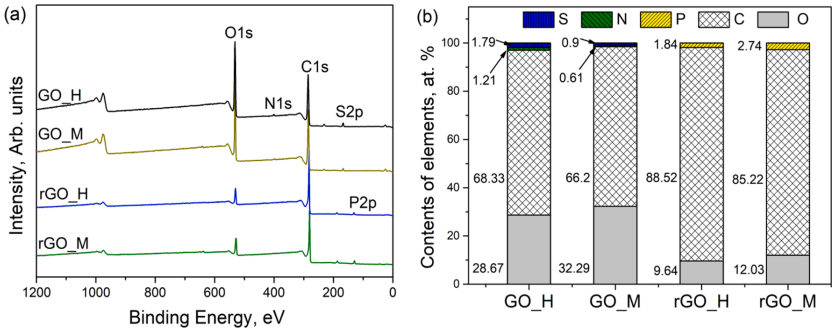

Fig. 1. The wide scan XPS spectrum (a) and surface elemental composition of GO and rGO samples determined by the XPS (b).

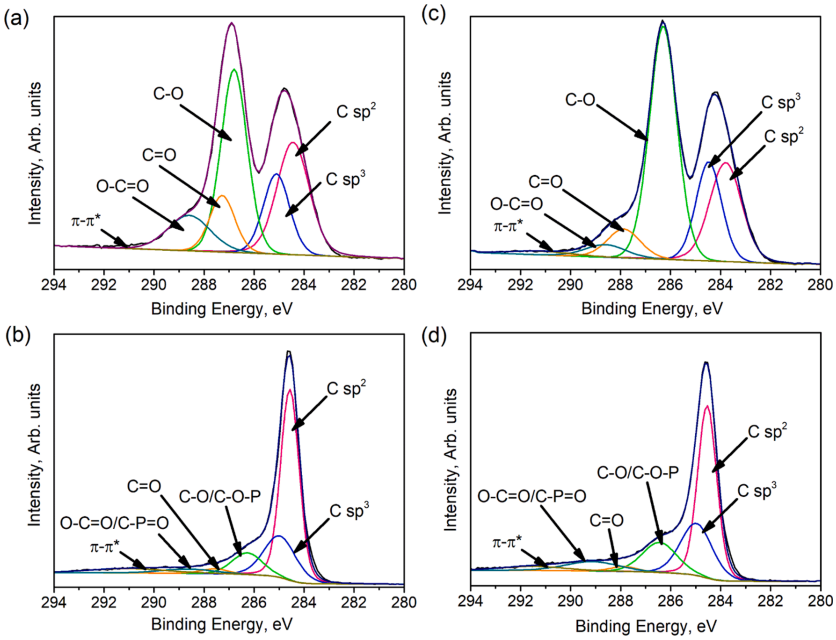

Fig. 2. C1s XPS spectra of GO_H (a), rGO_H (b), GO_M (c), and rGO_M (d) samples.

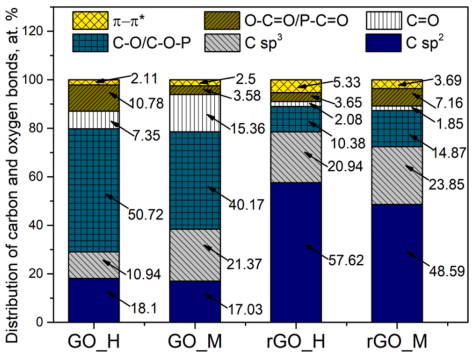

Fig. 3. Distribution and concentration (at.%) of carbon and oxygen bonds determined by XPS.

functional groups than GO prepared by the traditional Hummers' method.

Overall, rGO_H and rGO_M samples have the same oxygen-containing functional groups as graphene oxide, hence identical signals are presented in the C 1 s spectra (Fig. 2 (b) and (d)). However, after thermal treatment, the concentration of these groups in all cases considerably decreases, because of the decomposition of surface labile oxygen functionalities (carboxyl, phenol, carbonyl, and quinone) at a higher temperature, and the C = C bond becomes dominant in the reduced samples (see Fig. 3). Also, after thermal reduction, the peak at ~ 286.7 eV is slightly shifted to 286.2 eV (for rGO_H) and 286.4 eV (for rGO_M). Similarly, the peak at ~ 288.7 eV moves to 288.9 eV and 289.2 eV in the case of rGO_H and rGO_M, respectively. Moreover, the concentration of the C = O band in the case of rGO_M is slightly increased. Both facts suggest the presence of P-containing groups in the structure of the samples.

The P2p XPS spectra provided more detailed information on the types of P-containing functional groups present in the rGO_H and rGO_M samples (Fig. 4). Deconvolution of the P2p region shows an inseparable doublet with $2p_{1/2}$ and $2p_{3/2}$ components at ΔB.E. = 0.8 eV and area ratio of 1:2. The four peaks at 133.4 eV and 134.6 eV, and at 132.6 eV and 133.8 eV, correspond to the B.E. of P $2p_{1/2}$ and P $2p_{3/2}$, respectively. From Fig. 4 (a) and (b), it can be noted that for both samples, all the phosphorus signals can be assigned to the presence of phosphate groups (C-P, C-O-P, and C-P = O) [44], thus confirms the effectiveness of modification of the rGO surface.

Raman spectroscopy analysis has been performed to study the structural distortion and defects of graphene-based materials. The Raman spectra of the GO and rGO samples are shown in Fig. 5 (a).

Each of the Raman spectra obtained possesses the two typical bands at approximately 1345 cm^{-1} and 1600 cm^{-1}, corresponding to the D and G modes, which characterize the defective and the graphitic domains of graphene and its derived materials, respectively. The intensity ratio of the D to G bands (I_D/I_G) could be used to evaluate the degree of disorder in the structure of graphene-based material [45].

By comparing the I_D/I_G values for GO_H and GO_M, it can be concluded that there are some structural differences between the samples. The calculated ratio of I_D/I_G is 0.89 for GO_H. This value is slightly lower than that for GO_M (I_D/I_G = 0.91). The growth of I_D/I_G values is likely caused by the higher level of structural disorder and the greater number of defects in the graphene layers due to the more effective oxidation process during the modified Hummers' method. Moreover, the average aromatic cluster size ($L\alpha$) of GO_H is determined to be 21.60

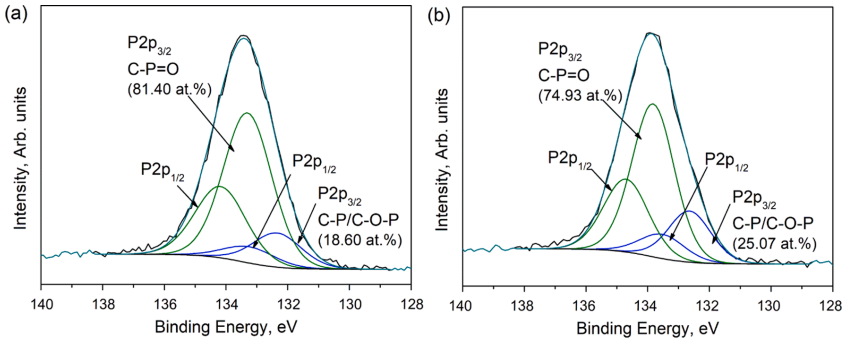

Fig. 4. P2p XPS spectra of rGO_H (a) and rGO_M (b) samples.

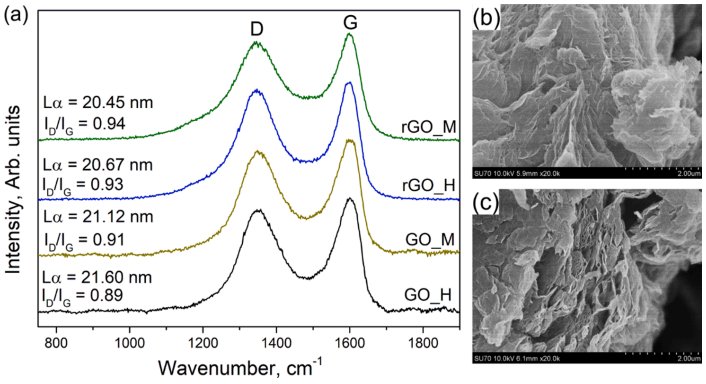

Fig. 5. Raman spectra of graphene-based samples (a). SEM images of rGO_H (b), and rGO_M (c).

nm, while *Lα* value for the sample GO_M is 21.12 nm. The larger *Lα* for GO_H suggests that it has larger graphitic domains with fewer structural defects. On the other hand, the decreasing aromatic cluster size in the GO_M sample reveals the increasing level of defects in the graphene layer due to the presence of a slightly greater amount of oxygen-containing functional groups.

Based on Fig. 5 (a), after the thermal treatment of GO, the I_D/I_G values show a significant change compared to the pristine GO. The I_D/I_G ratio varies from 0.89 to 0.93 for GO_H and from 0.91 to 0.94 for GO_M. The increase in I_D/I_G values is related to the removal of oxygen-containing functional groups and the formation of structural defects (vacancies, dislocations, roughness, etc.) during thermal treatment. This observation is in good agreement with the literature [46–48]. Moreover, the slightly higher I_D/I_G ratio obtained for the rGO_M sample confirms that a larger amount of defects and imperfections are present in this sample than in the rGO_H structure. The difference in results can be explained by the presence of a higher concentration of oxygen functionalities on the GO_M surface, which is related to a larger interlayer distance and a higher level of reduction. The SEM images prove that the rGO_M sample is characterized by much more irregular stacking and extensive disruption of graphene layers compared to rGO_H (Fig. 5 (b) and (c)).

In addition, the most significant observation emerging from our data is that a more effective restoration of the π-conjugated system of graphene layers is achieved using a carbon suboxide additive. The I_D/I_G ratio obtained up to 0.94 is obviously a lower value compared to other results based on thermally reduced GO. According to the literature, the I_D/I_G ratio of the thermally reduced GO products without additives is approximately at a rate of 1.2–2.8 [46,47,49]. These results indicate that the addition of carbon suboxide to the reduction system of GO has a positive effect on the structure and properties of thermally reduced GO. The creation of a novel reduction system as well as surface functionalization of graphene-based materials is extremely important for tailoring electronic properties, manipulating surface chemistry, and producing local changes to the elemental composition of host materials, which are essential for the development of highly sensitive and selective sensors.

3.2. Electrochemical response of dopamine on graphene-based active material/GCE modified electrodes

Electrochemical sensing of dopamine on three different electrodes, namely bare GCE, GCE/rGO_H, and GCE/rGO_M, has been studied by CV measurements in 0.1 M PB solution in the presence and absence of 52 μM dopamine. The CV results are depicted in Fig. 6. Besides, for the comparison of electrochemical parameters, the thermal reduction of two different GO samples without MA and P_2O_5 additives was also performed. The CV results of rGO_H0 and rGO_M0 are presented in Fig. S1 (Supplementary information).

A typical voltammogram obtained on the GCE in the presence of 52 μM DA is shown in Fig. 6 (a). A broad oxidation/reduction peak is

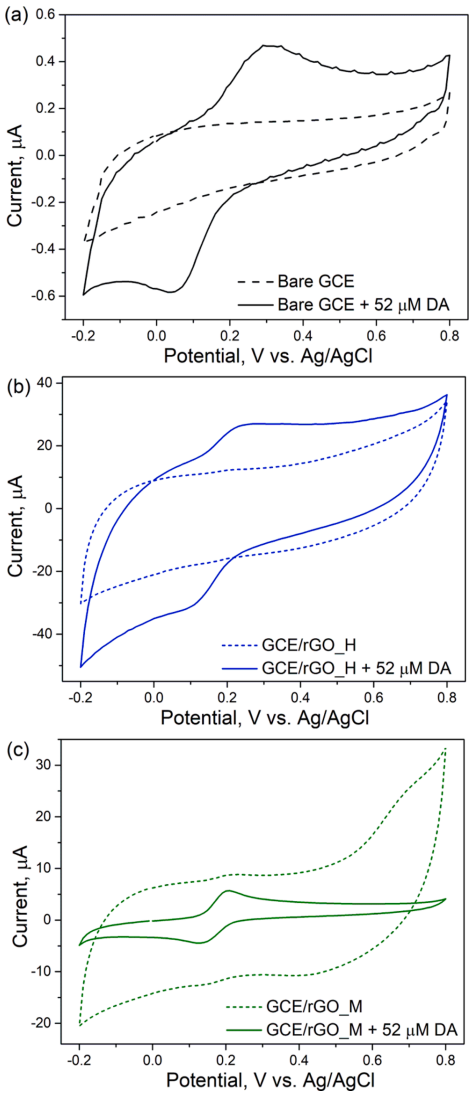

Fig. 6. CV curves of bare GCE (a), GCE/rGO_H (b), and GCE/rGO_M (c) in 0.1 M PB solution, in the absence and presence of 52 μM DA.

obtained with a large peak-to-peak separation (ΔE = 256 mV), suggesting that the present redox couple is irreversible [50]. Furthermore, the peak current values (I_{pa} = +0.15 μA; I_{pc} = − 0.37 μA) are very small, indicating a slow and sluggish electron transfer. In contrast, a couple of redox peaks are obtained on the GCE/rGO_H and GCE/rGO_M electrodes with a smaller peak separation and significantly enhanced peak currents compared with those of the GCE. From Fig. 6 (b), it can be seen that GCE/rGO_H exhibited a pair of broad and weakly expressed redox peaks. Obviously, GCE/rGO_H has a much higher sensitivity (I_{pa} = +5.31 μA; I_{pc} = − 6.73 μA) towards DA than GCE as the anodic and cathodic current values increase by almost 35 and 18 times, respectively. In addition, the calculated peak potential separation between the anodic and cathodic peaks of GCE/rGO_H is approximately two times lower (ΔE = 120 mV) than that obtained in bare GCE. However, the calculated values of ΔE exceeded 59/n mV, suggesting that the rate of electron transfer is moderate and the electrochemical reaction of dopamine is quasi-reversible [50]. The quasi-reversibility for this process has also been confirmed by the calculated ratio of reduction and oxidation currents, I_{pa}/I_{pc} = 0.79.

As seen in Fig. 6 (c), a prominent pair of redox peaks (oxidation peak at approximately + 0.20 V, reduction peak at approximately + 0.13 V) has appeared in the case of GCE/rGO_M, and the capacitive or non-faradaic current is decreased approximately by half after the addition of DA, demonstrating that the rGO_M sample has higher dopamine sensitivity than the bare GCE/Nafion electrode. The capacitive current indicates the capacitance of the double-layer, which is high in this case. The addition of DA, which due to its adsorption on the surface eases the charge transfer, decreases the capacitive current, and, therefore, well-defined redox peaks with a higher faradaic current are obtained. The calculated peak separation (ΔE = 63.5 mV) allows us to assume the reversible electrochemical behaviour of DA on this electrode. The values of ΔE are very close to the theoretical peak separation for a single electron transfer reaction of 59 mV [50]. In addition, the peak current values of the cathodic (I_{pc} = − 4.31 μA) and anodic (I_{pa} = +4.82 μA) are similar, giving I_{pa}/I_{pc} = 1.1, which is close to the absolute value of 1 for a perfectly reversible process [51].

The GCE modified with rGO_H0 and rGO_M0 samples, which were obtained during the thermal reduction of GO without additives of MA and P_2O_5, showed a poor electrocatalytic response toward the DA redox process, making them a non-suitable electrode material. As can be seen in Fig. S1, both electrodes are incapable to detect low concentrations of DA. In the case of GCE/rGO_H0, the non-intensive and the well-resolved redox peak appeared in the presence of 291 μM of DA, while in the case of GCE/rGO_M0, the redox peaks appeared in the presence of 100 μM of DA. Moreover, after the addition of DA, the capacitive current decreases. This decrease is due to the adsorption of analyte in the active site of the electrode and the increased charge transfer.

In summary, these results show that the obtained rGO_H and rGO_M modified electrodes have exhibited better electrocatalytic activity toward the DA redox reactions than the bare GCE, rGO_H0, and rGO_M0 samples. A significant improvement in the electrochemical response at the modified GCE with rGO_H and rGO_M could be attributed to P-atom doping. The incorporation of P atoms into graphene layers could provide the formation of topological defects and many active sites for electron transfer to DA. Also, this increase in the electrochemical response of modified electrodes might be due to the higher effective surface area of 0.2020 cm^2 and 0.1244 cm^2 for the rGO_M and rGO_H based electrode, respectively. The electroactive area was estimated by the Randles–Sevcik equation [52]. In comparison, the value of effective surface of pure GCE is 0.0670 cm^2. The electroactive surface area of the rGO modified electrode increased about 3 and 2 times compared to GCE, which provided an effective evidence for the good electrochemical response of the rGO based electrode to dopamine detection. Besides, this increase in the electrochemical performance of GCE after coating it with rGO_H and rGO_M samples could be due to the good conductivity of these samples as, during a thermal reduction in the presence of the MA and P_2O_5 mixture, the π-conjugate structure of the GO samples is restored. Finally, during the thermal reduction/exfoliation of GO, small molecule species such as water, CO_2, and CO is evolved [53]. As a consequence, the increased internal pressure could force the graphene sheets apart, resulting in a substantial increase in the volume and high surface area of the material, which could be favourable for the DA reaction on the electrode.

Furthermore, the effect of the potential scan rate on the redox reaction of DA has been investigated. The results are presented in Fig. 7.

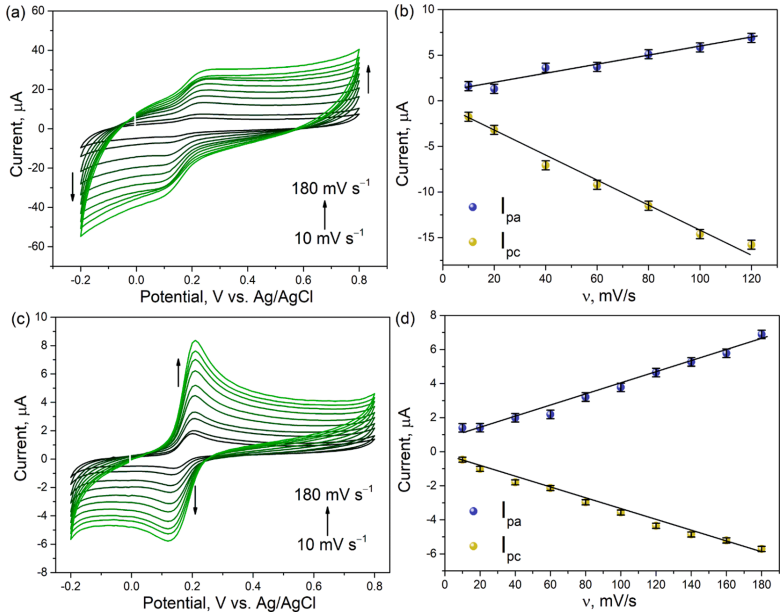

Fig. 7. CV curves at different scan rates and linear variation of anodic and cathodic peak currents vs. scan rates of GCE/rGO_H (a, b) and GCE/rGO_M (c, d). Supporting electrolyte: 0.1 M PB pH = 7.2, c(DA) = 52 μM.

Fig. 7 (a) shows the CVs of 52 μM DA on the surface of the GCE/rGO_H electrode at different potential scan rates from 10 to 180 mV s^{-1}. As seen, the anodic and cathodic peak currents of the DA gradually enhance with the increase in the scan rate. Moreover, the E_{pc} is slightly shifted toward lower potential values, while the anodic peak, corresponding to oxidation of DA, is slightly shifted toward higher potential values, which indicates that the electron transfer is a rather slow process than the high scan rates. A minor increase in the separation of cathodic and anodic peak potentials (ΔE_p), suggests a quasi-reversible redox system. The calculated ΔE_p value of GCE/rGO_H at a scan rate of 180 mV s^{-1} is approximately 136 mV. The graphs of the cathodic and anodic peak currents against the scan rate (Fig. 7 (b)) have shown linear relationships in the range of 10 to 120 mV s^{-1}, with regression equations of $I_{pa}(\mu A) = 0.050 \times + 0.943$ ($R^2 = 0.963$) and I_{pc} (μA) = − 0.1303 × − 1.006 ($R^2 = 0.986$), which proves that the electrochemical process is a surface adsorption-controlled reaction. Later, at higher scan rates, the relationships became non-linear, suggesting that the mechanism of the redox reaction of DA has been changed, probably because of the transition from reversible to irreversible dependence.

From Fig. 7 (c), it can be seen that the GCE/rGO_M electrode demonstrates the same trend of the increase in anodic and cathodic peak currents with the increasing scan rate as in the case of the rGO/rGO_H modified electrode. Moreover, the plots of the cathodic and anodic peak currents against the scan rate (Fig. 7 (d)) have linear relationships the entire tested scan rate range, indicating an adsorption-controlled mechanism. The linear equation for GCE/rGO_M is $I_{pa}(\mu A) = 0.0305 \times + 0.8203$ ($R^2 = 0.973$) and I_{pc} (μA) = − 0.0286 × − 0.5392 ($R^2 = 0.976$). Furthermore, as Fig. 7 (c) shows, there is no shift in the position of the redox peaks. The separation of the cathodic and anodic peak potentials (ΔE_p) of the voltammograms is independent of the scan rates, demonstrating the electrochemical reversibility of the process and fast electron transfer.

The DPV study has been performed for the quantitative analysis of DA on GCE/rGO_H and GCE/rGO_M modified electrodes because of the higher sensitivity and selectivity than CV [54]. The DPV responses of the prepared GCE/rGO_H and GCE/rGO_M sensors with various concentrations of DA (0 μM – 500 μM) are depicted in Fig. 8. Besides, Fig. S2 (Supplementary information) shows the DPV response of the GCE/rGO_H0 and GCE/rGO_M0 electrodes. The GCE/rGO_H0 sensor response for DA has changed chaotically, indicating poor electrochemical performance. Similarly, the GCE/rGO_M0 sensor exhibited a high limit of detection (LOD) value (18.95 μM) and low sensitivity (0.56 μA μM^{-1} cm^{-2}) toward DA detection. From the data shown in Fig. 8 (a), it is apparent that in the case of the GCE/rGO_H sensor, one peak at approximately + 0.19 V is presented and can be attributed to the oxidation of DA. Also, it must be noted that with the increase in the DA concentration, the peak at + 0.19 V gradually increases in a range from 0 μM to 42 μM and reaches a plateau after the addition of a higher amount of DA (Fig. 8 (c)). The linear regression equation is $I_{pc}(\mu A) = 0.1515 \times - 0.7021$ ($R^2 = 0.976$). The sensitivity is 2.14 μA μM^{-1} cm^{-2}. The LOD is 0.27 μM based on a 3σ/s. Moreover, at higher concentrations of dopamine (104 – 500 μM), oxidation peak shifts toward higher potential values (+0.19 V to + 0.31 V). One reasonable explanation for this shift can be explained by the adsorption of dopamine or its by-products on the electrode surface. This might result in an increase in the thickness of a layer, and a higher voltage is acquired for electron transfer [55].

Fig. 8 (b) shows the DPV curves of DA with a variety of different concentrations (from 0 to 500 μM) recorded on the GCE/rGO_M sensor. It is clearly visible that the current responses increase with the rise of the DA concentration in the range of 0 μM to 42 μM. Fig. 8 (d) displays excellent linearity of the calibration curve obtained from the oxidation peak current and at different concentrations of dopamine ranging from 5 μM to 42 μM. The linear regression equation is $I_{pc}(\mu A) = 2.0232 \times - 10.876$ ($R^2 = 0.993$). The estimated LOD of DA is 0.11 μM, while the sensitivity is 28.64 μA μM^{-1} cm^{-2}. Whereas, at higher concentrations of DA (from 104 μM to 500 μM), the intensity of the anodic peak decreases

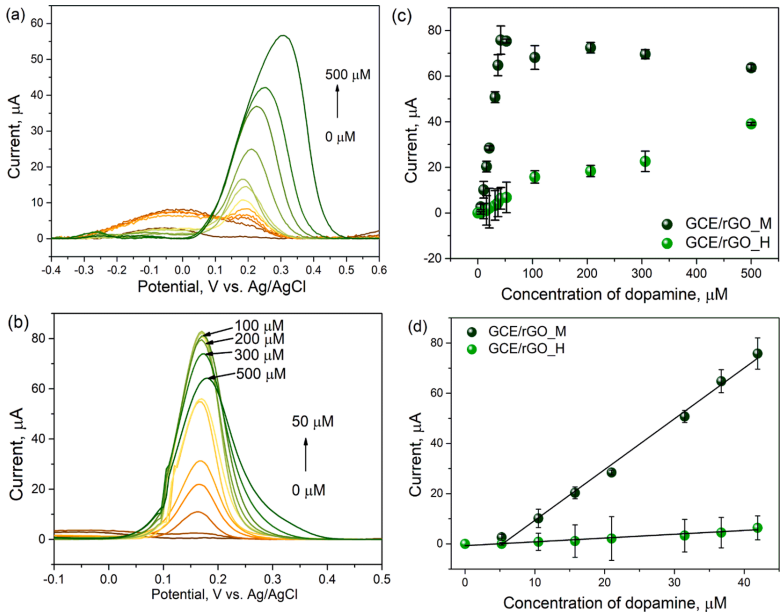

Fig. 8. DPV responses of successive additions of DA into PB solution pH 7.2 on GCE/rGO_H (a) and GCE/rGO_M (b). Typical calibration plots corresponding to DA additions (c). Calibration curves in low concentration range (d).

and the oxidation peak moves slightly to higher potential values. This shift in potential and decrease in peak current can be explained by the increase in the layer thickness due to the adsorption of DA, its by-products, or impurities on the catalyst surface, and increased blockage of the rGO-based electrode pores and active sites, which are responsible for the electrode kinetics. Similar trends have been reported by Wei Sun et al. in their work on methanol sensors [56].

To sum up, DPV results are in line with CV ones and prove that rGO_H and rGO_M samples are promising electrode materials for DA sensing. However, the determined LOD of DA and sensitivity of GCE/rGO_M are much better than those of GCE/rGO_H. The difference in results can be explained by a slightly higher amount of P-containing functional groups on the rGO_M surface. It has been published that a great number of defective/active sites created by doped heteroatoms strongly contribute to improving the sensing performance of modified graphene-based electrodes [57]. Moreover, the proposed GCE/rGO_M electrode possesses a comparable or impressively lower LOD than other previously developed rGO-based sensors. A comparison of some analytical properties with other works from the literature is presented in Table 1. On the contrary, in comparison to some rGO/metal nanoparticle or rGO/polymer modified electrodes, the GCE/rGO_M electrode exhibits worse analytical characteristics [58–60]. Functionalization of rGO-based electrode materials with various nanomaterials such as metal oxides, quantum dots, and metal nanoparticles effectively improved the analytical performance of sensors. Nonetheless, the development of pure metal-free rGO electrodes for the sensing of neurotransmitters has drawn the most attention in the past few years. The main reason is that rGO/metal nanoparticles or rGO/polymers modified electrodes suffer from numerous disadvantages, e.g. adsorption of the analyte, high-cost, toxicity, environmentally harmful, and complicated surface chemistry.

Table 1
Comparison of the analytical performance for the determination of DA at various modified graphene-based electrodes.

Material	Linear range (μM)	LOD (μM)	Sensitivity (μA μM^{-1} cm^{-2})	Reference
rGO_H	0 – 42	0.27	2.14	This work
rGO_M	5 – 42	0.11	28.6	This work
Au-Cu_2O/rGO	10 – 90	3.90	0.29	[13]
LIG	5 – 40	3.40	4.39	[61]
Au/rGO/GCE	6.8 – 41	1.40	25.71	[51]
ErGO/GCE	0.5 – 60	0.50	15.4	[62]
AG-NA	0.5 – 35	0.33	33.1	[58]
GCE/ZnO-rGO	1 – 70	0.33	4.69	[63]
Pd/rGO	0.45 – 71	0.18	0.896	[64]
MgO/Gr/Ta	0.1 – 7	0.15	–	[65]

3.3. Electrochemical behaviour of dopamine in presence of uric acid

The selectivity of the GCE/rGO_M electrode has been evaluated using DPV carried out in the presence of uric acid. According to the literature, the oxidation process of UA occurs at the potential similar to that of DA [66]. As a result, the presence of UA in the electrochemical cell may influence the results of the analysis. Unfortunately, the GCE/rGO_H sensor response for dopamine has changed chaotically and decreased in the presence of UA (data not shown). Consequently, Fig. 9 shows the DPV responses of the GCE/rGO_M sensor towards DA and UA when the concentration of dopamine changes with the other analyte kept constant (200 μM).

DPV peaks for DA and UA occur at approximately + 0.17 V and + 0.31 V, respectively. Also, it can be observed that the oxidation peaks of DA and UA are well-separated and the peak current of UA almost stays constant when the concentration of DA increases up to 104 μM, suggesting a non-significant interference for the simultaneous detection of DA and UA. Conversely, at higher concentrations of DA, both peaks become broad and begin to coalesce. In addition, the corresponding calibration plot of the DA is presented in the Fig. 9 (a) insert and Fig. 9

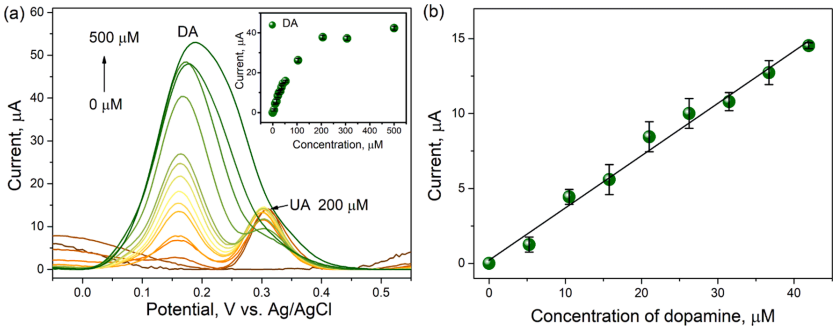

Fig. 9. DPV responses of selective detection of DA in presence of 200 μM of UA on GCE/rGO_M in 0.1 M PB (pH = 7.2) (a). Calibration plot is depicted in inset. Calibration curves in low concentration range (b).

(b). The peak current of DA increased linearly with DA concentrations in the range of 5 – 42 μM. The linear regression equation is $I_{pc}(\mu A) = 0.3488 \times + 0.2136$ ($R^2 = 0.987$). The estimated LOD of DA is 0.13 μM, while the sensitivity is 4.94 μA μM^{-1} cm^{-2}. According to these results, it is assumed that the presence of UA in the electrochemical cell causes a slightly lower sensor response to DA. Nonetheless, the GCE/rGO_M sensor still exhibits good electrochemical performance toward DA detection in the presence of common interference.

The selectivity of the GCE/rGO_M electrode has been evaluated in the presence of ascorbic acid (AA) as well. The DPV responses of the GCE/rGO_M sensor towards DA, UA, and AA were obtained when the concentration of dopamine changes with the other analytes were kept constant (the concentration of UA was 200 μM, while the concentration of AA was 1 mM). The results obtained are presented in Fig. S3 (Supplementary information). After the addition of such a high concentration of AA (1 mM) into the electrochemical cell, no additional peaks were observed, resulting in the conclusion that this analyte may not influence the results. Therefore, the simultaneous determination of only two molecules (DA and UA) was performed.

The contemporaneous determination of DA and UA has been carried out at GCE/rGO_M changing the concentrations of both molecules from 0 μM to 306 μM. The DPV curves for DA and UA simultaneous sensing are presented in Fig. 10.

As seen, the oxidation peaks of these two analytes remain well-separated when the concentration is increasing, showing that there is no mutual disturbance for the DA and UA contemporaneously detection. Moreover, even in the presence of higher concentrations of UA, the DA oxidation peak is still well developed. The results of this study indicate that the GCE/rGO_M sensor shows effective detection of DA with good selectivity. Also, the current signals of DA and UA are linearly enhanced with the increase of their concentration in the range of 5 – 52 μM (Fig. 9 (b)). The linear regression equations for DA and UA are $I_{DA} = 0.5984 \times + 11.167$ ($R^2 = 0.990$) and $I_{UA} = 0.0985 \times + 0.2035$ ($R^2 = 0.980$), respectively. Meanwhile, the LODs of simultaneous determination is 0.12 μM and 0.15 μM for DA and UA, respectively. The sensitivity of GCE/rGO_M to DA and UA in the binary mixture is 8.47 μA μM^{-1} cm^{-2} and 1.40 μA μM^{-1} cm^{-2}, respectively. The sensitivity at the GCE/rGO_M modified electrode in the presence of UA (8.47 μA μM^{-1} cm^{-2}) decreases approximately three times from the sensitivity at GCE/rGO_M in the absence of interferant (28.64 μA μM^{-1} cm^{-2}). This indicates that the presence of UA in the same mixture has an effect on the detection of DA. On the other hand, these results suggest that the GCE/rGO_M sensor still possesses acceptable selectivity for the simultaneous determination of DA and UA species.

3.4. Stability of the GCE/rGO_M modified electrode

The long-term stability of the GCE/rGO_M modified electrode has also been investigated. The electrode has been stored dry at room temperature between measurements. Fig. 11 shows the current response obtained after the addition of 21 μM of dopamine to PB (pH 7.2). Measurements have been made during 15 days of the electrode storage period. The GCE/rGO_M modified electrode activity has decreased by around 5.27% and 40.24% after 2 days and 3 days of storage,

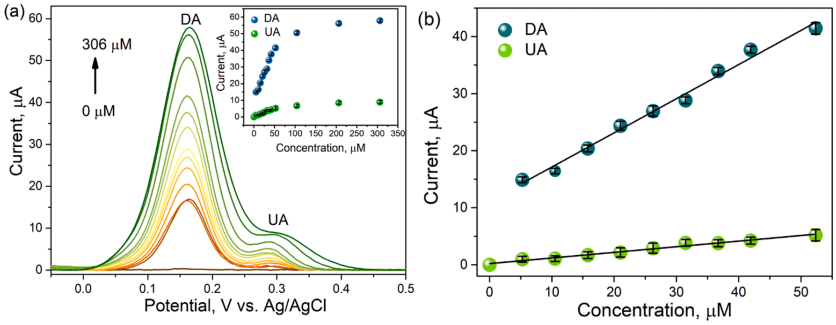

Fig. 10. DPV responses of simultaneous additions of DA and UA into PB solution pH 7.2 on GCE/rGO_M (a); Calibration plot is depicted in inset. Calibration curves in low concentration range (b).

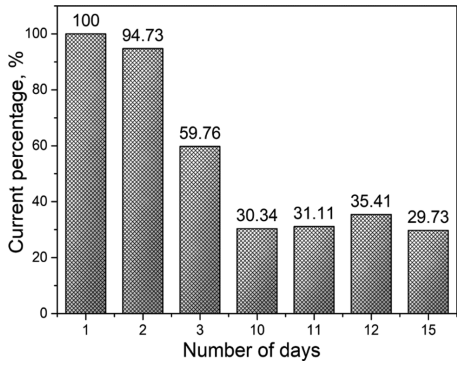

Fig. 11. Stability of the GCE/rGO_M sensor tested over 15 days period.

respectively. After 10 days of electrode storage, the current has dropped by 69.66%. Additionally, it is seen that the electrode retained approximately 32% of the original current at the end of two weeks. The loss of activity (~69.66%) during 10 days of storage could be a consequence of poisoning of the electrode surface by adsorbed dopamine or intermediate species on its surface. One more reasonable explanation for this decrease can be attributed to the insufficient adhesion of the active material onto the GCE, and after the consecutive washing of the electrode, the active material could be partially leach from the surface. The relative standard deviation of the oxidation peak currents by three successive measurements is 2.28%. This result revealed a good reproducibility of the GCE/rGO_M modified electrode.

4. Conclusions

In summary, this study underlines that during the thermal reduction of GO in the presence of the MA and P_2O_5 mixture, the pristine GO plays a crucial role in controlling the defects on the surface, the amount and nature of oxygen functionalities, the level of surface doping, and the electrochemical properties of the final rGO products. Quantitative XPS analysis has shown that the thermal treatment of GO with the mixture of MA and P_2O_5 leads to the incorporation of phosphorus-containing functional groups into the structure of graphene-based material, as evidenced by an increase in the phosphorus content in rGO_H (1.84%) and rGO_M (2.74%). Raman spectroscopy has indicated that rGO samples contain an increased number of defects compared to that of pristine GO. It is determined that the I_D/I_G ratio varies from 0.89 to 0.93 in the case of GO_H and from 0.91 to 0.94 in the case of GO_M. Moreover, it is shown that a slightly larger number of defects are present in the rGO_M sample (I_D/I_G = 0.94) than in the rGO_H structure (I_D/I_G = 0.93). Electrochemical studies using CV and DPV showed that the rGO_M sample significantly improves the oxidation peak current of DA, demonstrating its higher sensitivity to the determination of dopamine than that on rGO_H. From the DPV studies, it is determined that the GCE/rGO_M modified electrode shows a fairly wide linear range (5 – 42 μM), low LOD value (0.11 μM) and high sensitivity (28.64 μA μM^{-1} cm^{-2}) toward detection of DA. Moreover, it is observed that the presence of UA in the electrochemical cell causes a slightly lower sensor response for DA. Nonetheless, the proposed GCE/rGO_M modified electrode still possesses acceptable selectivity and is capable of detecting DA simultaneously. Simultaneous LOD (0.12 μM) and sensitivity (8.47 μA μM^{-1} cm^{-2}) are obtained for DA, while for UA the corresponding values are 0.15 μM and 1.40 μA μM^{-1} cm^{-2}, respectively. Overall, the obtained results have suggested that rGO_M active material could become a prospective candidate for the construction of other progressive sensing devices and could have promising applications of multi-analyte simultaneous detection.

CRediT authorship contribution statement

Justina Gaidukevic: Methodology, Data curation, Writing – original draft, Project administration, Funding acquisition. **Ruta Aukstakojyte:** Investigation, Writing – review & editing. **Jurgis Barkauskas:** Conceptualization, Writing – review & editing. **Gediminas Niaura:** Writing – review & editing. **Tomas Murauskas:** Visualization, Writing – review & editing. **Rasa Pauliukaite:** Writing – review & editing, Supervision.

Declaration of Competing Interest

The authors declare that they have no known competing financial interests or personal relationships that could have appeared to influence the work reported in this paper.

Acknowledgments

This project has received funding from European Social Fund (project No 09.3.3-LMT-K-712-19-0050) under grant agreement with the Research Council of Lithuania (LMTLT).

Appendix A. Supplementary data

Supplementary data to this article can be found online at https://doi.org/10.1016/j.apsusc.2022.153257.

References

[1] F. Otero, E. Magner, Biosensors-recent advances and future challenges in electrode materials, Sensors (Basel) 20 (2020) 3561.
[2] K. Štulík, Challenges and promises of electrochemical detection and sensing, Electroanalysis 11 (1999) 1001–1004.
[3] C. Ferrag, K. Kerman, Grand challenges in nanomaterial-based electrochemical sensors, Frontiers in Sensors 1 (2020).
[4] A. Ansón-Casaos, E. García-Bordeje, A.M. Benito, W.K. Maser, Nanostructured Carbon Materials: Synthesis and Applications, Springer, Netherlands, Dordrecht, 2018, pp. 177–191.
[5] G. Speranza, Carbon Nanomaterials: Synthesis, Functionalization and Sensing Applications, Nanomaterials (Basel, Switzerland), 11 (2021).
[6] A.C. Power, B. Gorey, S. Chandra, J. Chapman, Carbon nanomaterials and their application to electrochemical sensors: a review, Nanotechnol. Rev. 7 (1) (2018) 19–41.
[7] A.D. Silva, W.J. Paschoalino, J.P.V. Damasceno, L.T. Kubota, Structure, properties, and electrochemical sensing applications of graphene-based materials, ChemElectroChem 7 (22) (2020) 4508–4525.
[8] M. Coroş, S. Pruneanu, R.-I. Stefan-van Staden, Review—recent progress in the graphene-based electrochemical sensors and biosensors, J. Electrochem. Soc. 167 (3) (2020) 037528, https://doi.org/10.1149/2.0282003JES.
[9] D. Chen, L. Tang, J. Li, Graphene-based materials in electrochemistry, Chem. Soc. Rev. 39 (8) (2010) 3157, https://doi.org/10.1039/b923596e.
[10] P. Suvarnaphaet, S. Pechprasarn, Graphene-based materials for biosensors: a review, Sensors 17 (10) (2017) 2161, https://doi.org/10.3390/s17102161.
[11] C.N.R. Rao, A.K. Sood, K.S. Subrahmanyam, A. Govindaraj, Graphene: the new two-dimensional nanomaterial, Angew. Chem. Int. Ed. 48 (42) (2009) 7752–7777.
[12] T. Sattar, Current review on synthesis, composites and multifunctional properties of graphene, Top. Curr. Chem. 377 (2019) 10.
[13] T.K. Aparna, R. Sivasubramanian, M.A. Dar, One-pot synthesis of Au-Cu2O/rGO nanocomposite based electrochemical sensor for selective and simultaneous detection of dopamine and uric acid, J. Alloy. Compd. 741 (2018) 1130–1141.
[14] R. Franco, I. Reyes-Resina, G. Navarro, Dopamine in health and disease: much more than a neurotransmitter, Biomedicines 9 (2021) 109.
[15] S. Lakard, I.-A. Pavel, B. Lakard, Electrochemical biosensing of dopamine neurotransmitter: a review, Biosensors 11 (6) (2021) 179, https://doi.org/10.3390/bios11060179.
[16] T.C. Napier, A. Kirby, A.L. Persons, The role of dopamine pharmacotherapy and addiction-like behaviors in Parkinson's disease, Prog. Neuro-Psychopharmacol. Biol. Psychiatry 102 (2020), 109942.
[17] X. Liu, J. Liu, Biosensors and sensors for dopamine detection, VIEW 2 (2021) 20200102.
[18] K.L. Davis, R.S. Kahn, G. Ko, M. Davidson, Dopamine in schizophrenia: A review and reconceptualization, Am. J. Psychiatry 148 (1991) 1474–1486.
[19] G. Vinodhkumar, R. Ramya, I.V. Potheher, M. Vimalan, A.C. Peter, Synthesis of reduced graphene oxide/Co3O4 nanocomposite electrode material for sensor application, Res. Chem. Intermed. 45 (2019) 3033–3051.

[20] A. Numan, M.M. Shahid, F.S. Omar, K. Ramesh, S. Ramesh, Facile fabrication of cobalt oxide nanograin-decorated reduced graphene oxide composite as ultrasensitive platform for dopamine detection, Sens. Actuators, B 238 (2017) 1043–1051.

[21] G.T.S. How, A. Pandikumar, H.N. Ming, L.H. Ngee, Highly exposed 001 facets of titanium dioxide modified with reduced graphene oxide for dopamine sensing, Sci. Rep. 4 (2014) 5044.

[22] T. Joseph, N. Thomas, A facile electrochemical sensor based on titanium oxide (TiO2)/reduced graphene oxide (RGO) nano composite modified carbon paste electrode for sensitive detection of epinephrine (EP) from ternary mixture, Mater. Today:. Proc. 41 (2021) 606–609.

[23] G. Li, P. Zhong, Y. Ye, X. Wan, Z. Cai, S. Yang, Y. Xia, Q. Li, J. Liu, Q. He, A highly sensitive and stable dopamine sensor using shuttle-like α-Fe2O3 nanoparticles/electro-reduced graphene oxide composites, J. Electrochem. Soc. 166 (15) (2019) B1552–B1561.

[24] Z. Yang, X. Zheng, J. Zheng, A facile one-step synthesis of Fe2O3/nitrogen-doped reduced graphene oxide nanocomposite for enhanced electrochemical determination of dopamine, J. Alloy. Compd. 709 (2017) 581–587.

[25] D.B. Gorle, M.A. Kulandainathan, Electrochemical sensing of dopamine at the surface of a dopamine grafted graphene oxide/poly(methylene blue) composite modified electrode, RSC Adv. 6 (24) (2016) 19982–19991.

[26] W. Al-Graiti, J. Foroughi, Y. Liu, J. Chen, Hybrid graphene/conducting polymer strip sensors for sensitive and selective electrochemical detection of serotonin, ACS Omega 4 (26) (2019) 22169–22177.

[27] J.G. Manjunatha, B.E.K. Swamy, M. Deraman, G.P. Mamatha, Simultaneous determination of ascorbic acid, dopamine and uric acid at poly (aniline blue) modified carbon paste electrode: A cyclic voltammetric study, Int. J. Pharmacy and Pharmaceutical Sci. 5 (2013) 355–361.

[28] N. Hareesha, J.G. Manjunatha, Fast and enhanced electrochemical sensing of dopamine at cost-effective poly(DL-phenylalanine) based graphite electrode, J. Electroanal. Chem. 878 (2020) 114533, https://doi.org/10.1016/j.jelechem.2020.114533.

[29] J.G. Manjunathaa, M. Deraman, N.H. Basri, I.A. Talib, Selective detection of dopamine in the presence of uric acid using polymerized phthalo blue film modified carbon paste electrode, Adv. Mater. Res. 895 (2014) 447–451.

[30] J. Manjunatha, Poly (Nigrosine) modified electrochemical sensor for the determination of dopamine and uric acid: a cyclic voltammetric study, Int. J. ChemTech Res. 9 (2016) 136–146.

[31] A. Pandikumar, G.T. Soon How, T.P. See, F.S. Omar, S. Jayabal, K.Z. Kamali, N. Yusoff, A. Jamil, R. Ramaraj, S.A. John, H.N. Lim, N.M. Huang, Graphene and its nanocomposite material based electrochemical sensor platform for dopamine, RSC Adv. 4 (108) (2014) 63296–63323.

[32] J. Li, Y. Wang, Y. Sun, C. Ding, Y. Lin, W. Sun, C. Luo, A novel ionic liquid functionalized graphene oxide supported gold nanoparticle composite film for sensitive electrochemical detection of dopamine, RSC Adv. 7 (4) (2017) 2315–2322.

[33] M.M. Rahman, J.-J. Lee, Electrochemical dopamine sensors based on graphene, J. Electrochem. Sci. Technol. 10 (2019) 185–195.

[34] A. Cernat, G. Ştefan, M. Tertis, C. Cristea, I. Simon, An overview of the detection of serotonin and dopamine with graphene-based sensors, Bioelectrochemistry 136 (2020) 107620, https://doi.org/10.1016/j.bioelechem.2020.107620.

[35] S. Keßel, D. Cabrera-Perez, A. Horowitz, P.R. Veres, R. Sander, D. Taraborrelli, M. Tucceri, J.N. Crowley, A. Pozzer, C. Stönner, L. Vereecken, J. Lelieveld, J. Williams, Atmospheric chemistry, sources and sinks of carbon suboxide, C3O2, Atmos. Chem. Phys. 17 (2017) 8789–8804.

[36] J.E. House, Chapter 13 - Chemistry of nonmetallic elements I. Hydrogen, boron, oxygen, and carbon, in: J.E. House (Ed.) Inorganic Chemistry (Third Edition), Academic Press2020, pp. 465-516.

[37] W.S. Hummers, R.E. Offeman, Preparation of graphitic oxide, J. Am. Chem. Soc. 80 (1958).

[38] J. Gaidukevic, R. Aukstakojyte, T. Navickas, R. Pauliukaite, J. Barkauskas, A novel approach to prepare highly oxidized graphene oxide: structural and electrochemical investigations, Appl. Surf. Sci. 567 (2021) 150883, https://doi.org/10.1016/j.apsusc.2021.150883.

[39] R. Aukštakojytė, J. Gaidukevič, J. Barkauskas, Thermal reduction of graphene oxide in the presence of carbon suboxide, J. Solid State Chem. 301 (2021), 122365.

[40] L.G. Cançado, K. Takai, T. Enoki, M. Endo, Y.A. Kim, H. Mizusaki, A. Jorio, L. N. Coelho, R. Magalhães-Paniago, M.A. Pimenta, General equation for the determination of the crystallite size La of nanographite by Raman spectroscopy, Appl. Phys. Lett. 88 (2006), 163106.

[41] A. Carvalho, M.C.F. Costa, V.S. Marangoni, P.R. Ng, T.L.H. Nguyen, A.H. Castro Neto, The degree of oxidation of graphene oxide, Nanomaterials 11 (2021) 560.

[42] E. Aliyev, V. Filiz, M.M. Khan, Y.J. Lee, C. Abetz, V. Abetz, Structural characterization of graphene oxide: surface functional groups and fractionated oxidative debris, Nanomaterials 9 (2019) 1180.

[43] M.P. Araújo, O.S.G.P. Soares, A.J.S. Fernandes, M.F.R. Pereira, C. Freire, Tuning the surface chemistry of graphene flakes: new strategies for selective oxidation, RSC Adv. 7 (2017) 14290–14301.

[44] J. Bassil, S. Roualdès, V. Flaud, J. Durand, Plasma-polymerized phosphonic acid-based membranes for fuel cell, J. Membr. Sci. 461 (2014) 1–9.

[45] D. López-Díaz, M. López Holgado, J.L. García-Fierro, M.M. Velázquez, Evolution of the Raman spectrum with the chemical composition of graphene oxide, J. Phys. Chem. C 121 (2017) 20489–20497.

[46] S. Eigler, C. Dotzer, A. Hirsch, Visualization of defect densities in reduced graphene oxide, Carbon 50 (2012) 3666–3673.

[47] J.C. Silva Filho, E.C. Venancio, S.C. Silva, H. Takiishi, L.G. Martinez, R.A. Antunes, A thermal method for obtention of 2 to 3 reduced graphene oxide layers from graphene oxide, SN Appl. Sci. 2 (2020) 1450.

[48] Kurniasari, A. Maulana, A.Y. Nugraheni, D.N. Jayanti, S. Mustofa, M.A. Baqiya, Darminto, Defect and Magnetic Properties of Reduced Graphene Oxide Prepared from Old Coconut Shell, IOP Conference Series: Materials Science and Engineering, 196 (2017) 012021.

[49] I. Šakinytė, J. Barkauskas, J. Gaidukevič, J. Razumienė, Thermally reduced graphene oxide: The study and use for reagentless amperometric d-fructose biosensors, Talanta 144 (2015) 1096–1103.

[50] N. Elgrishi, K.J. Rountree, B.D. McCarthy, E.S. Rountree, T.T. Eisenhart, J. L. Dempsey, A practical beginner's guide to cyclic voltammetry, J. Chem. Educ. 95 (2018) 197–206.

[51] C. Wang, J. Du, H. Wang, C.e. Zou, F. Jiang, P. Yang, Y. Du, A facile electrochemical sensor based on reduced graphene oxide and Au nanoplates modified glassy carbon electrode for simultaneous detection of ascorbic acid, dopamine and uric acid, Sens. Actuators B: Chem., 204 (2014) 302-309.

[52] R.P. Bacil, L. Chen, S.H.P. Serrano, R.G. Compton, Dopamine oxidation at gold electrodes: mechanism and kinetics near neutral pH, Phys.Chem.Chem.Phys. 22 (2) (2020) 607–614.

[53] A. Mtibe, T.H. Mokhothu, M.J. John, T.C. Mokhena, M.J. Mochane, Chapter 8 - Fabrication and Characterization of Various Engineered Nanomaterials, in: C. Mustansar Hussain (Ed.) Handbook of Nanomaterials for Industrial Applications, Elsevier2018, pp. 151-171.

[54] G. Hussain, D.S. Silvester, Comparison of voltammetric techniques for ammonia sensing in ionic liquids, Electroanalysis 30 (2018) 75–83.

[55] A.u.H.A. Shah, A. Inayat, S. Bilal, Enhanced Electrocatalytic Behaviour of Poy (aniline-co-2-hydroxyaniline) Coated Electrodes for Hydrogen Peroxide Electrooxidation, Catalysts, 9 (2019) 631.

[56] W. Sun, G. Sun, W. Yang, S. Yang, Q. Xin, A methanol concentration sensor using twin membrane electrode assemblies operated in pulsed mode for DMFC, J. Power Sources 162 (2006) 1115–1121.

[57] X. Wang, G. Sun, P. Routh, D.-H. Kim, W. Huang, P. Chen, Heteroatom-doped graphene materials: syntheses, properties and applications, Chem. Soc. Rev. 43 (2014) 7067–7098.

[58] D. Kim, S. Lee, Y. Piao, Electrochemical determination of dopamine and acetaminophen using activated graphene-Nafion modified glassy carbon electrode, J. Electroanal. Chem. 794 (2017) 221–228.

[59] S.-S. Choo, E.-S. Kang, I. Song, D. Lee, J.-W. Choi, T.-H. Kim, Electrochemical detection of dopamine using 3D porous graphene oxide/gold nanoparticle composites, Sensors 17 (2017) 861.

[60] L. Gao, J. Ma, J. Zheng, Solvothermal synthesis of Sb2S3-graphene oxide nanocomposite for electrochemical detection of dopamine, J. Electrochem. Soc. 167 (2020), 107503.

[61] F. Mahmood, Y. Sun, C. Wan, Biomass-derived porous graphene for electrochemical sensing of dopamine, RSC Adv. 11 (2021) 15410–15415.

[62] L. Yang, D. Liu, J. Huang, T. You, Simultaneous determination of dopamine, ascorbic acid and uric acid at electrochemically reduced graphene oxide modified electrode, Sens. Actuators, B 193 (2014) 166–172.

[63] X. Zhang, Y.-C. Zhang, L.-X. Ma, One-pot facile fabrication of graphene-zinc oxide composite and its enhanced sensitivity for simultaneous electrochemical detection of ascorbic acid, dopamine and uric acid, Sens. Actuators, B 227 (2016) 488–496.

[64] J. Wang, B. Yang, J. Zhong, B. Yan, K. Zhang, C. Zhai, Y. Shiraishi, Y. Du, P. Yang, Dopamine and uric acid electrochemical sensor based on a glassy carbon electrode modified with cubic Pd and reduced graphene oxide nanocomposite, J. Colloid Interface Sci. 497 (2017) 172–180.

[65] L. Zhao, H. Li, S. Gao, M. Li, S. Xu, C. Li, W. Guo, C. Qu, B. Yang, MgO nanobelt-modified graphene-tantalum wire electrode for the simultaneous determination of ascorbic acid, dopamine and uric acid, Electrochim. Acta 168 (2015) 191–198.

[66] P.-S. Hung, G.-R. Wang, W.-A. Chung, T.-T. Chiang, P.-W. Wu, Green synthesis of Ni@PEDOT and Ni@PEDOT/Au (Core@Shell) inverse opals for simultaneous detection of ascorbic acid, dopamine, and uric acid, Nanomaterials 10 (2020) 1722.

Supplementary material

A novel electrochemical sensor based on thermally reduced graphene oxide for the sensitive determination of dopamine

Justina Gaidukevic[a,b,*], Ruta Aukstakojyte[b], Jurgis Barkauskas[b], Gediminas Niaura[c], Tomas Murauskas[b], Rasa Pauliukaite[a]

[a]Department of Nanoengineering, Center for Physical Sciences and Technology (FTMC), Savanoriu Ave. 231, LT-02300 Vilnius, Lithuania.

[b]Vilnius University, Faculty of Chemistry and Geosciences, Institute of Chemistry, Naugarduko str. 24, LT – 03225, Vilnius, Lithuania.

[c]Department of Organic Chemistry, Center for Physical Sciences and Technology (FTMC), Sauletekio Ave. 3, LT-10257 Vilnius, Lithuania.

*Corresponding Author

E-mail: justina.gaidukevic@chf.vu.lt (J. Gaidukevic)

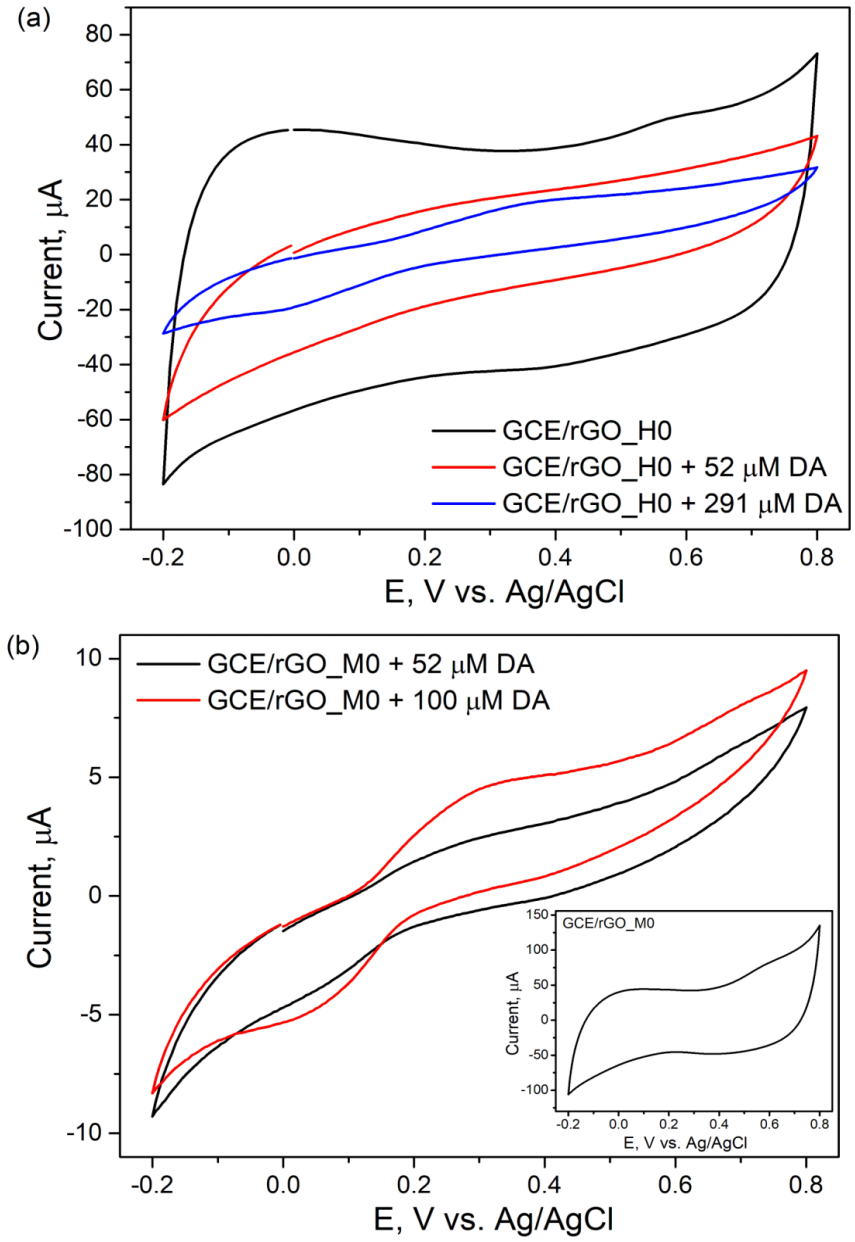

Fig. S1 CV curves of bare GCE/rGO_H0 (a), and GCE/rGO_M0 (b) in the presence and absence of dopamine. Supporting electrolyte: 0.1 M PB pH = 7.2, potential scan rate: 100 mV s^{-1}.

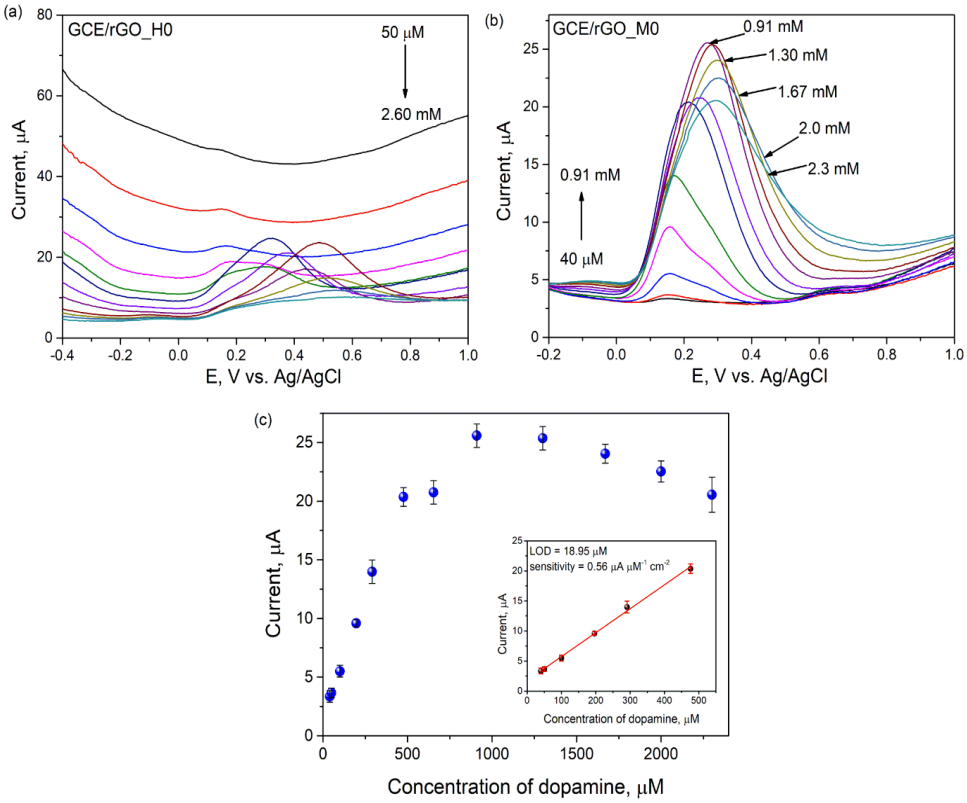

Fig. S2 DPVs at various DA concentrations (40, 50, 100, 196, 291, 476, 654, 910, 1300, 1670, 2000, 2300, and 2600 μM) at GCE/rGO_H0 (a) and GCE/rGO_M0 (b) in 0.1 M PB, pH 7.2. Relationship between peak currents and DA concentrations for GCE/rGO_M0 sensor (c). Calibration curves in low concentration range (insert).

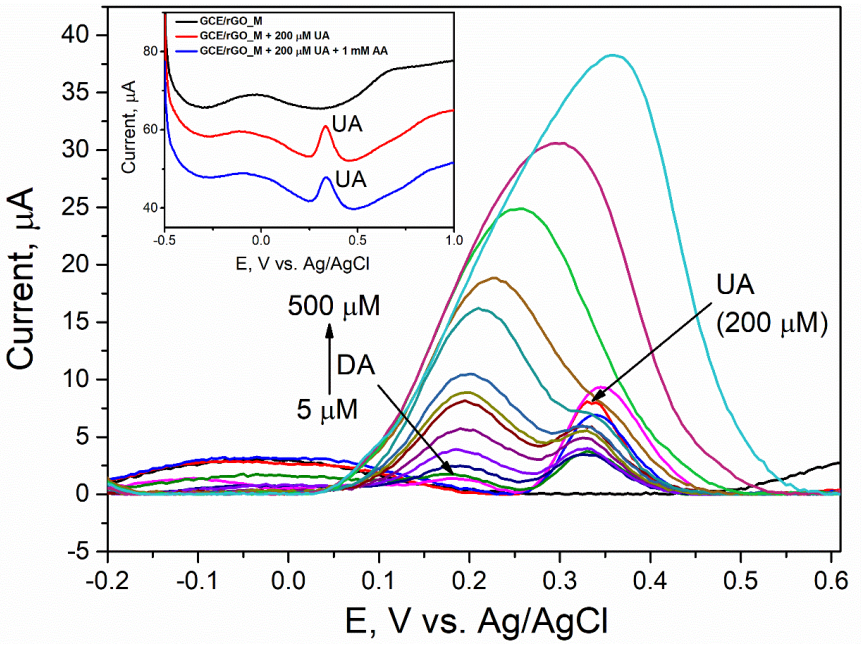

Fig. S3 DPV responses of selective detection of DA in presence of 200 μM of UA and 1 mM of AA on GCE/rGO_M in 0.1 M PB (pH = 7.2).

4th publication

“Bismarck brown-assisted hydrothermal synthesis of nitrogen-modified reduced graphene oxide for selective electrochemical detection of dopamine”

R. Aukštakojytė, G. Niaura, V. Bukauskas, J. Barkauskas, R. Pauliukaitė, J. Gaidukevič

Surfaces and Interfaces, 46, 2024, 104041
DOI: 10.1016/j.surfin.2024.104041

Surfaces and Interfaces 46 (2024) 104041

Contents lists available at ScienceDirect

Surfaces and Interfaces

journal homepage: www.sciencedirect.com/journal/surfaces-and-interfaces

Bismarck brown-assisted hydrothermal synthesis of nitrogen-modified reduced graphene oxide for selective electrochemical detection of dopamine

Rūta Aukštakojytė [a], Gediminas Niaura [b], Virginijus Bukauskas [c], Jurgis Barkauskas [a], Rasa Pauliukaitė [d], Justina Gaidukevič [a,d,*]

[a] Institute of Chemistry, Faculty of Chemistry and Geosciences, Vilnius University, Naugarduko str. 24, LT, 03225, Vilnius, Lithuania
[b] Department of Organic Chemistry, Center for Physical Sciences and Technology, Saulėtekio Ave. 3, LT, 10257, Vilnius, Lithuania
[c] Department of Physical Technologies, Center for Physical Sciences and Technology, Saulėtekio Ave. 3, LT, 10257, Vilnius, Lithuania
[d] Department of Nanoengineering, Center for Physical Sciences and Technology, Savanorių Ave. 231, LT, 02300, Vilnius, Lithuania

ARTICLE INFO

Keywords:
N-modified reduced graphene oxide
Metal-free
Structural and morphological analysis
Dopamine
Electrochemical sensor

ABSTRACT

Metal-free nitrogen-modified reduced graphene oxide (N-rGO) samples were prepared by convenient and cost-effective hydrothermal treatment of graphene oxide using two different concentrations of Bismarck Brown, namely 20 wt.% (rGO_BB20) and 50 wt.% (rGO_BB50). The synthesized N-rGO samples served as an electroactive platform for the highly selective electrochemical detection of dopamine (DA). Structural characterization using XPS demonstrated that Bismarck Brown-assisted hydrothermal treatment of GO leads to incorporation of nitrogen functional groups into the structure of graphene-based material, as evidenced by an increase in the nitrogen content in rGO_BB20 (3.8 at.%) and rGO_BB50 (10.6 at.%). Raman spectroscopy revealed increased FWHM(G) values for both samples, indicating interrupted carbon lattices and higher defective degrees due to nitrogen incorporation. Notably, rGO_BB20 exhibited a higher concentration of quaternary nitrogen species (6.1%), a larger specific surface area (52 $m^2\ g^{-1}$), and higher electrical conductivity compared to rGO_BB50. This led to superior electrochemical performance, with rGO_BB20 demonstrating a lower detection limit (45 nM), higher sensitivity (0.61 $\mu A\ \mu M^{-1}\ cm^{-2}$) in a 0–15 μM linear range, and 0.39 $\mu A\ \mu M^{-1}\ cm^{-2}$ sensitivity in a wider 15–476 μM linear detection range compared to rGO_BB50. The proposed sensor displayed exceptional selectivity, reproducibility, repeatability, and stability.

1. Introduction

Dopamine (DA) functions as a neurotransmitter, which irregular levels in the human blood result in the progression of nervous system disorders such as senile dementia, schizophrenia, attention deficit hyperactivity syndrome, Parkinson's, and Alzheimer's diseases [1,2]. For this reason, rapid, sensitive, and accurate measurement of DA is of particular importance for the precocious diagnosis and treatment of the aforementioned diseases. To date, a variety of highly sensitive techniques, including mass spectrometry [3], fluorescence spectrophotometry [4], fluorimetry [5], capillary electrophoresis [6], and high-performance liquid chromatography [7] have been utilized for the determination of DA. On the other hand, these methods also require well-qualified staff, tedious sample preparation methods, expensive and complex instrumentation setups, which extend the detection time of analytes [8]. In contrast, considering the fast determinations of redox-active molecules, electrochemical sensors have attracted considerable attention as an alternative methodology to detect DA due to a range of benefits such as high sensitivity, rapid response time, reproducibility, time-saving, cost-effectiveness, and simple operating procedure [9].

Recently, graphene-based derivatives, such as graphene oxide (GO) and reduced graphene oxide (rGO), have displayed significant promise as active electrode materials for electrochemical devices. This is attributed to their long-term stability, affordability, biocompatibility, and eco-friendly nature [10]. Pure graphene in nature is an inert carbon material that restricts its electrochemical performance and limits applications in sensing devices [11]. However, modifying the graphene

* Corresponding author at: Institute of Chemistry, Faculty of Chemistry and Geosciences, Vilnius University, Naugarduko str. 24, LT, 03225, Vilnius, Lithuania.
E-mail address: justina.gaidukevic@chf.vu.lt (J. Gaidukevič).

https://doi.org/10.1016/j.surfin.2024.104041
Received 23 October 2023; Received in revised form 19 January 2024; Accepted 4 February 2024
Available online 9 February 2024

and rGO matrix with heteroatoms (N, P, S, and B) is able to tailor the electronic structure, physicochemical and textural characteristics as well as enhance surface catalytic active sites, resulting in the improved charge transfer at the interface between an electrode and electrolyte [12]. In particular, nitrogen-modified rGO (N-rGO) has attracted great interest as a potential candidate for the electrochemical detection due to its relatively high electrical conductivity, high binding ability, mechanical strength, and large surface area [13]. N-containing bonding configurations, such as pyridinic-N and pyrrolic-N, are capable of increasing the catalytic activity, wettability, and biocompatibility of graphene-based derivatives, when graphitic-N accelerates the mobility of the charge carrier, all of which favor improved electrochemical performance [14]. Consequently, a variety of sensors based on N-rGO have been successfully fabricated to detect the different types of analytes such as H_2O_2 [15], glucose [16], uric acid [17], methyl parathion [14], nitrite [18], guanine [19], catechol [20], methylene blue [21], and hemoglobin [22]. N-rGO also demonstrates efficient catalytic activity in supercapacitors Li^+ ion batteries, solar cells, and fuel cells [23–25].

In the case of DA determination, N-rGO-based sensors are generally designed with noble/transition metal nanoparticles (Au, Pd) or their oxides (MnO, NiO, CoO, Fe_2O_3, ZnO, and $CuCo_2O_4$) [26–34]. Even with the high efficiency and excellent electrochemical sensing ability of N-rGO/metal nanocomposites, the high cost and toxic effects discourage the use of metal nanoparticles or their combination with graphene-based derivatives when it comes to the sustainability parameters. The present studies show only several works regarding the electrochemical detection of DA using metal-free N-rGO working electrodes [13,35–38]. Furthermore, most of the proposed sensors exhibit a narrow linear range of detection and poor selectivity, since the simultaneous responses for interfering species such as ascorbic acid (AA) and uric acid (UA) are still detected [13,37]. For example, Z. H. Sheng et al. have prepared N-doped rGO by thermal reduction of GO with the addition of melamine as a nitrogen-containing precursor and designed the DA sensor with a linear range of 0.5–170 μM and a limit of detection (LOD) of 250 nM for DA in the presence of AA and UA [35]. H. Zhang and co-workers have also presented the DA sensor based on N-rGO with a LOD of 0.1 μM in the detection range of 1–60 μM toward DA, simultaneously determining AA and UA [13]. Furthermore, the study reported by S. Ai et al. has revealed that the non-metal N-doped rGO aerogel synthesized by the hydrothermal reduction of GO with aniline exhibits excellent electrochemical characteristics toward DA (LOD = 0.1 μM; the linear range of 1–250 μM), confirming the highly promising sensing abilities of the metal-free N-rGO-modified electrode [38]. Nonetheless, an examination of the available literature reveals that the task of acquiring graphene-based materials for DA sensors without metal impurities, which may demonstrate enhanced electrochemical parameters, including a wide linear range, low LOD values, excellent sensitivity, stability, and selectivity, remains a formidable challenge. Furthermore, the scarcity of studies focusing on electrochemical sensors solely based on N-rGO shows that more efforts must be devoted to the synthesis and investigation of sustainable, low-cost, and metal-free electrocatalytically active N-rGO materials for the development of sensors endowed with superior characteristics.

This paper has been motivated to prepare non-metal, sensitive, and selective electrode materials for the detection of DA. N-rGO materials have been prepared via a simple and facile one-step hydrothermal reduction of GO in the addition of the cationic dye Bismarck Brown (BB) that, to the best of our knowledge, has been the first-ever used as a nitrogen agent in modifying rGO. The resulting N-rGO materials have been studied in detail by X-ray photoelectron spectroscopy (XPS), Raman spectroscopy, scanning electron microscopy (SEM), and Brunauer-Emmett-Teller (BET) analysis. The electrical conductivity has also been examined under compression of the samples. Electrochemical techniques, including cyclic voltammetry (CV), chronoamperometry (ChA), and interference studies, have been used to analyze the activity of N-rGO materials toward DA.

2. Experimental

2.1. Materials and reagents

The all materials and reagents used in this research are of analytical grade. Their purity and origin is given in the Supplementary material.

2.2. Synthesis of GO

The modified Hummers' synthesis was employed to prepare GO [39]. Primarily, using a magnetic stirrer, 6.0 g of natural graphite powder, 5.0 g of potassium persulfate, and 5.0 g of phosphorus pentoxide were combined in a solution of 98 wt.% sulfuric acid (24.0 mL). Afterward, the resulting sample underwent oxidative treatment in accordance with the methodology documented by Hummers et al. [40]. After the reaction, the GO suspension was placed into a cellulose membrane dialysis tubing to undergo additional purification till the dialysate became sulfate-free and achieved pH = 4.5. The resultant brown powder was utilized for additional reduction stages after being dried to a constant weight in air at room temperature.

2.3. Hydrothermal reduction of GO

GO was reduced by one-pot hydrothermal treatment. To prepare a homogeneous suspension, GO (500 mg) was dispersed in 50 mL of DI water in the presence of 20 wt.% or 50 wt.% Bismarck Brown and ultrasonicated for 1 h. The chemical structure of dye was presented in Fig. S1 (Supplementary material). The prepared suspensions were transferred to Teflon-lined stainless-steel autoclaves with a capacity of 90 mL and were heated at a temperature of 180 °C for 12 h. After the reaction time, the autoclaves were kept for cooling at room temperature. The resulting black powders were extensively washed with DI water and dried in air at the ambient atmosphere. Samples synthesized with 20 wt.% and 50 wt.% of BB were denoted as rGO_BB20 and rGO_BB50, respectively. Pure rGO in the absence of BB was also prepared under the same synthesis conditions.

2.4. Material characterization

A Kratos Axis Supra spectrometer (Kratos analytical, Kyoto, Japan) was used for the XPS analysis. A monochromatic Al Kα source with an energy of 1486.69 eV was installed in the spectrometer. The carbon 1 s line at 284.6 eV was used to calibrate the XPS spectra, which were obtained at a pass energy of 20 eV Using the CASAXPS program, curve fitting peak components were used to deconvolute the raw XPS spectra. Following the Shirley-type background subtraction, the line forms of the fitting components were approximated using symmetric Gaussian-Lorentzian functions.

Raman spectroscopy was performed using inVia Raman (Renishaw, Wotton-under-Edge, Gloucestershire, UK) spectrometer equipped with thermoelectrically cooled (−70 °C) CCD camera and microscope. The excitation wavelength was 532 nm. A 20x/0.40 NA objective lens and 1800 lines/mm grating were used during measurements. The accumulation time was 100 s. The laser power at the sample was limited to 0.4 mW in order to prevent sample damage. The polystyrene standard was used to calibrate the Raman frequencies. Using GRAMS/A1 8.0 (Thermo Scientific) software, the experimental spectra were fitted with Gaussian and Lorentzian-Gaussian shape components to estimate the band parameters.

Scanning electron micrographs were taken with a Hitachi SU-70 microscope (Tokyo, Japan) at an accelerating voltage of 5.0 kV at the magnification of 50,000. Prior to SEM, the specimens underwent a coating process involving 10 nm of silver using a Quorum Q150T ES Turbo-Pumped Sputter Coater.

The N_2 adsorption-desorption measurements were performed using a BET analyzer TriStar II 3020 (Micromeritics, Norcross, GA, USA) at 77 K.

All materials were outgassed for two hours at 120 °C in a N_2 environment prior to gas sorption experiments. The BET model was applied to determine the specific surface area S_{BET}, while the pore volume distribution was estimated using the Barrett-Joyner-Halenda (BJH) method.

For the conductivity measurement, a Keithley 2601 Source Meter (Keithley Instruments, Solon, OH USA) was used. As per our earlier research [41], the electrical properties of the carbon-based samples were ascertained.

The methodology of electrochemical experiments performed in this study is provided in the Supplementary material.

3. Results and discussion

In the present work, XPS analysis has been carried out to examine the chemical nature, composition, and nitrogen-doping configurations of graphene-based materials synthesized. The results of the elemental composition presented in Fig. 1 show that GO contains C (66.4 at.%), O (31.9 at.%), S (0.9 at.%), and N (0.8 at.%) elements. The presence of sulfur and nitrogen in the GO structure could be associated with residual substances such as nitrates and sulfates used in the chemical oxidation of graphite. Hydrothermal treatment of GO results in a notable decrease in oxygen content (from 31.9 at.% for GO to 12.1 at.% for rGO), indicating a partial reduction of oxygen-containing functionalities in rGO. On the contrary, hydrothermal treatment of GO using BB leads to the simultaneous reduction process as well as the incorporation of N species into the structure of the rGO_BB20 and rGO_BB50 samples. From Fig. 1 it is observed that the content of N-containing functionalities increases in accordance with N-precursor concentration (3.8 at.% for rGO_BB20 and 10.6 at.% for rGO_BB50). The similar N content in the hydrothermally reduced GO samples has also been reported by other authors (Table S1), revealing the effectiveness of the BB additive as a nitrogen source in modifying rGO.

Although the C/O ratio has increased drastically from 2.08 for GO to 6.5 for rGO_BB20 and 8.1 for rGO_BB50 after hydrothermal treatment in the presence of BB, residual oxygen-containing functional groups still remain in the structure. Nevertheless, the presence of oxygen species might induce the appropriate wettability of the N-rGO material, which is favorable for the suitable accessibility of an electrolyte during the electrochemical measurements. Furthermore, the existence of oxygen-containing functional groups with the negative charge on the N-rGO surface can assist in the attraction of cationic DA molecules, which may have a beneficial impact on the sensor performance [42].

The oxygen and nitrogen-containing functionalities on the surface of graphene derivatives have been studied in detail using the high resolution C1s and N1s XPS spectra. The high resolution C1s of the GO and rGO samples are provided in Fig. 2. After the deconvolution of the GO C1s XPS spectrum (Figure 2(a)), the components presented at the binding energies of 284.5 eV and 285.7 eV correspond to the C=C (sp^2) and C–C (sp^3) bonds, respectively. The remaining peaks located at 287.2 eV, 287.7 eV, and 288.9 eV are attributed to hydroxy/epoxy (C–O), carbonyl (C=O), and carboxylic groups (O–C=O), respectively [43–45]. After hydrothermal reduction of pure GO, the intensity of peaks corresponding to oxygen-containing functionalities and sp^3 carbon drastically decreases and sp^2 carbon becomes dominant. Also, the new component appears at the binding energy of 290.9 eV that is associated with π–π* due to the partially recovered π-conjugated system in rGO (Figure 2(b)) [44]. The same peaks are observed in the C1s XPS spectra of the rGO_BB20 and rGO_BB50 samples (Figure 2(c), (d)). However, after the Bismarck Brown-assisted hydrothermal modification, the peaks at 286.6 eV and 287.9 eV are slightly shifted to the lower values of binding energy compared to that of rGO. This change in energy could be a result of nitrogen element incorporation in the structure of modified samples. In this case, the presence of N species such as C=N and C–N in rGO_BB20 and rGO_BB50 could be confirmed by peaks located at ~286.2 eV and ~287.4 eV, respectively, overlapping with the C–O and C=O components [43]. The aforementioned shift also aligns with the heightened structural disorder observed in the materials, resulting from disturbances in the sp^2 carbon framework following the introduction of nitrogen [46].

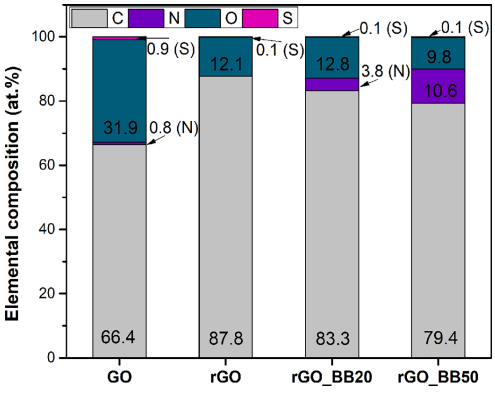

Fig. 1. Surface elemental composition (at.%) for GO, rGO, rGO_BB20, and rGO_BB50 samples determined by the XPS analysis.

In order to provide further insights into the structural differences between the rGO_BB20 and rGO_BB50 samples, the N1s XPS spectra have been deconvoluted into five components, as shown in Fig. 3. The assignment of the first component aligns with pyridinic-N (398.0 eV), the second one covers amide-N or pyridone (399.1 eV), when the remaining peaks are attributed to pyrrolic- (400.5 eV), graphitic-N (402.6 eV), and nitrogen oxides (404.8 eV) [47]. As could be seen from the relative amount of nitrogen bands presented in Fig. 3, in the rGO_BB20 sample nitrogen primarily exists as the pyridinic groups (45.0%), whereas the rGO_BB50 sample demonstrates both pyridinic (40.7%) and amine groups (35.7%) as prevailing nitrogen configurations. Furthermore, the rGO_BB20 sample exhibits a higher amount of pyrrolic-N (16.1%) and graphitic-N (6.1%) groups compared to those of rGO_BB50. The graphitic nitrogen is doped into the graphitic basal plane and replaces one of the carbon atoms in the six-numbered ring. This kind of bond configuration is able to improve the electrical conductivity in the rGO material as a result of the induced electron transfer rate. The pyrrolic and pyridinic nitrogen are mainly located at the edges of graphene nanosheets, forming five- and six-membered rings, respectively. The presence of these structural defects in the graphene sheet has the potential to improve electron transfer rates in redox reactions and consequently enhance the electrochemical capabilities for dopamine detection [14].

Raman spectroscopy is a highly sensitive technique to identify the microstructure of graphene-based derivatives. Therefore, Raman spectra for graphite, GO, and reduced GO samples have been recorded and presented in Fig. 4. Each spectrum exhibits two characteristic peaks located around 1350 cm^{-1} and 1600 cm^{-1}, corresponding to the D and G bands, respectively. The D band is associated with defects (vacancies, edges, sp^3-hybridized carbon, heteroatom doping and functionalities) and the G band represents the in-plane vibrations of sp^2 hybridized carbon domains [48]. Important quantitative information about the structure of carbon material can be extracted from the analysis of full width at half maximum of G band, FWHM(G) [49–52]. Therefore, the Raman spectra in the frequency range from 1000 to 1800 cm^{-1} have been fitted by 3–5 Gaussian or Lorentzian-Gaussian form components (Fig. 4). Besides the well-known D and G components (Lorentzian-Gaussian form), an additional Gaussian form bands located at 1275 cm^{-1} (D*) and 1520 cm^{-1} (D") have been introduced [52,53]. The D" band has been previously related with amorphization of carbon

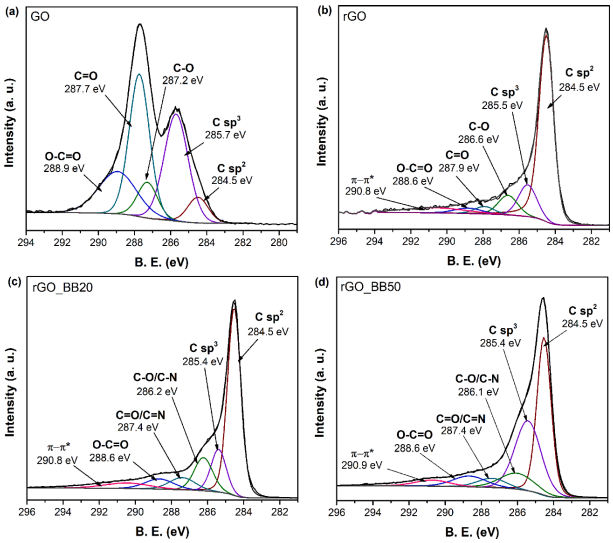

Fig. 2. The C1s XPS spectra for GO (a), rGO (b), rGO_BB20 (c), and rGO_BB50 (d) samples.

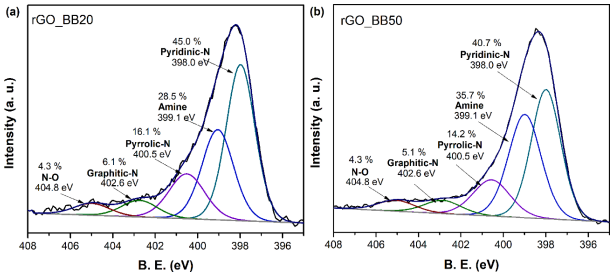

Fig. 3. The N1s XPS spectra for rGO_BB20 (a) and rGO_BB50 (b) samples.

material [54,55]. Fitting the Raman spectra from samples rGO_BB20 and rGO_BB50 has required to introduce additional bands at 1160 and 1166 cm^{-1}, respectively (Fig. 4(d) and (e)). The important structural parameter in sp^2-hybridization layered carbon material is an average in-plane crystallite size L_a [50,52]. The experimentally obtained FWHM(G) value can be used to determine the L_a [49,52,55]:

$$L_a = \frac{l_c}{2} ln\left[\frac{C}{FWHM(G) - FWHM(G_0)}\right] \quad (1)$$

where photon coherence length $l_c = 32$ nm, C = 95 cm^{-1}, and FWHM(G) and FWHM(G_0) are the widths of the G band of sample under investigation and undoped pristine graphene (15 cm^{-1}), respectively. The equation is valid for measuring the L_a dawn to 2.8 nm [52]. The parameters of G band and estimated L_a values are given in Table 1. As could be seen in Table 1, after oxidative treatment of pristine graphite, the FWHM(G) value increases significantly from 21.2 cm^{-1} for graphite to 71.4 cm^{-1} for GO. Higher values of FWHM(G) mean the higher sp^3 defects as well as reduction in particle size, due to the attachment of an abundance of oxygen-containing groups such as hydroxyl, epoxy, carboxyl, and carbonyl groups. Following the hydrothermal reduction of GO, the decrease of the FWHM(G) value from 71.4 cm^{-1} to 62.7 cm^{-1} reflects the partial restoration of the sp^2 hybridization due to the removal of oxygen moieties. The modification with nitrogen results in the further increase of FWHM(G) values to 67.2 cm^{-1} and 72.4 cm^{-1} for rGO_BB20 and rGO_BB50, respectively, indicating the interrupted carbon lattice and induced higher defective degrees due to the incorporation of nitrogen species in the structure. These results are in a good agreement with the studies reported elsewhere [13,56]. Moreover, a slight red shift of the G band (from 1602 to 1594 cm^{-1}) for both nitrogen-modified rGO samples provides additional evidence for the formation of chemical bonds between C and N in the carbon honeycomb network [57]. Depending on the sample treatment the L_a varies from 8.1 to 43.7 nm. The largest in-plane crystallite size values have been obtained for graphite (43.7 nm). High L_a values are also characteristic for rGO sample (11.0 nm). The intensity ratio $I(D'') / I(G)$ can be employed to probe amorphization of studied carbon samples (Table 1). The highest content of amorphous phase has been found in the sample rGO_BB50 (0.72).

Not only elemental composition but also the surface morphology of materials considerably impacts their application in electrochemical

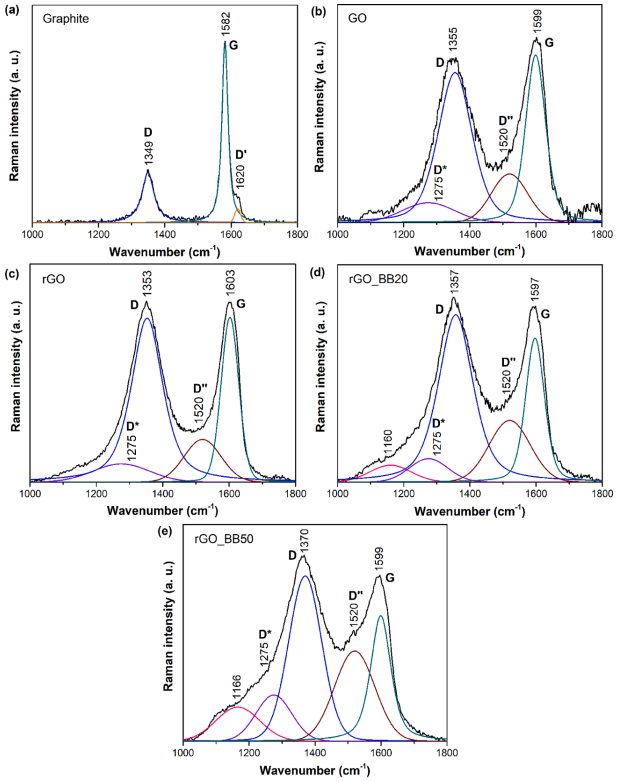

Fig. 4. Raman spectra for graphite with fitted Lorentzian-Gaussian (D and G bands) and Gaussian (D' band) form components (a), GO with fitted Gaussian (D* and D" bands) and Lorentzian-Gaussian (D and G bands) form components (b), rGO with fitted Gaussian (D* and D" bands) and Lorentzian-Gaussian (D and G bands) form component (c), rGO_BB20 with fitted Gaussian (D*, D", and 1160 cm^{-1} bands) and Lorentzian-Gaussian (D and G bands) form components (d), and rGO_BB50 with fitted Gaussian (D*, D", and 1160 cm^{-1} bands) and Lorentzian-Gaussian (D and G bands) form components (e) samples. Excitation wavelength is 532 nm (0.4 mW).

Table. 1
G-peak full with at half maximum FWHM(G), average crystallite size L_a, and intensity ratio $I(D'')$ / $I(G)$ of carbon-based samples.

Sample	FWHM(G) (cm^{-1})	L_a (nm)	$I(D'')$ / $I(G)$
GO	71.4	8.3	0.29
rGO	62.7	11.0	0.26
Graphite	21.2	43.7	0
rGO_BB20	67.2	9.6	0.43
rGO_BB50	72.4	8.1	0.72

sensing devices, as electrochemical reactions, including adsorption and diffusion, take place specifically on the surface of the electrode. Fig. 5 shows SEM micrographs of the GO, rGO, rGO_BB20, and rGO_BB50 samples. Fig. 5(a) represents a typical morphology of GO with irregular, wrinkled layers and multiple folds. After hydrothermal reduction of GO (Fig. 5(b)), the resultant material forms a highly porous structure with a wide range of pore sizes. From Fig. 5(c) and (d) it could be seen that the morphology of N-rGO samples is corrugated due to the presence of foreign nitrogen atoms and is highly dependent on the BB content used during the hydrothermal synthesis. In the case of rGO_BB20, the pores have become larger compared to that of rGO and their consistent formation between the layers is not observed in all areas of the surface. On the contrary, in the presence of 50 wt.% BB graphene nanosheets partially aggregate and form a small number of pores. The restacking of layers could be associated with a high content of nitrogen (10.6 at.%) since the similar trend has been noticed in other studies [58].

The differences in porous nature and surface area between reduced GO samples have been further investigated by BET analysis. Fig. 5(e) and (f) show N_2 adsorption-desorption isotherms at 77 K and pore distribution curves for the rGO, rGO_BB20, and rGO_BB50 samples, respectively. As can be seen in Fig. 5(e), N_2 adsorption-desorption curves of reduced GO samples can be characterized by IV-type isotherms, according to the classification defined by IUPAC, which is a typical signature of mesopores [47]. The hysteresis loop (H2-type) for rGO indicates the ink-bottle-shaped pores, while hysteresis loops (H3-type) for rGO_BB20 and rGO_BB50 suggest the presence of slit type pores between parallel layers of graphene. The pore distribution curves obtained by the BJH model (Fig. 5(f)) also confirm the presence of mesopores with predominant pore widths in the range of 2.5–5 nm for all reduced GO samples. The value of the BET surface area (S_{BET}) is determined to be 241 $m^2 g^{-1}$ for pure rGO which is significantly lower than the theoretical value for fully exfoliated and isolated graphene sheets (2630 $m^2 g^{-1}$) [59]. After BB-assisted hydrothermal treatment of GO, S_{BET} drastically decreases to 52 $m^2 g^{-1}$ and 29 $m^2 g^{-1}$ for rGO_BB20 and rGO_BB50, respectively. This drastic reduction in the BET surface area for the

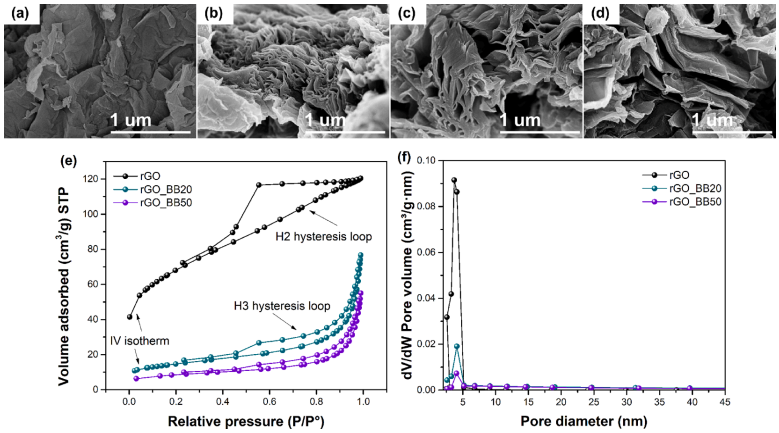

Fig. 5. SEM micrographs for the GO (a), rGO (b), rGO_BB20 (c), and rGO_BB50 (d) samples. N_2 adsorption-desorption curves (e) and pore distribution curves (f) for the rGO, rGO_BB20, and rGO_BB50 samples.

nitrogen-modified rGO samples is probably attributed to the inability of N_2 molecules to access the interlamellar space of the samples because of the aggregation of graphene sheets [60]. The aggregated layers are clearly observed in the SEM image of rGO_BB50 (Fig. 5(d)). The divergence in S_{BET} could also be a result of a possible adsorption of the BB dye on the rGO surface or the blocking of some pores between the graphene layers. Despite the low surface area, the rGO_BB20 and rGO_BB50 samples still provide a great advantage for electrochemistry studies due to their mesoporous characteristics.

The conductive properties of electrode materials are crucial in electrochemical sensing devices. This study assesses the electrical performance of the synthesized materials by observing changes in electrical conductivity during compression. Fig. 6 shows the calculated electrical conductivity against bulk density for GO and reduced GO samples in the presence and absence of BB. The findings indicate that as bulk densities increase for the carbon-based materials synthesized, there is a corresponding rise in electrical conductivity. When a bulk substance is compressed, the enhanced particle-to-particle contact leads to greater electrical conductivity, as denser samples facilitate electron transfer more effectively [61]. Consequently, the highest electrical conductivity occurs when achieving the most compact arrangement of particles, leading to the peak values in bulk density. A similar trend of the results is observed in studies of other bulk carbon-based derivatives such as carbon foam, reduced GO, carbon nanotubes, P-doped rGO, and graphene [41,60,62,63]. From Fig. 6(a) it could be seen that the determined log conductivity for GO varies from –2.24 to –1.77 S m $^{-1}$, indicating electrically insulating behavior of GO. GO becomes an insulator since the π-conjugated system is interrupted due to the alteration suffered by the hybridization of carbon atoms from sp^2 to sp^3 during the oxidation. The hydrothermal reduction of pure GO leads to the partially recovered π-conjugation that results in an enhanced log electrical conductivity from 0.46 S m^{-1} to 1.91 S m^{-1} with increasing of bulk density. The relationships presented in Fig. 6 (b) also show that rGO samples in the presence of BB exhibit electrical conductivity in the ranges of 0.40 – 1.79 S m^{-1} and –1.26 – 0.76 S m^{-1} for rGO_BB20 and rGO_BB50, respectively. The negligible reduction in conductivity for rGO_BB20 compared to that of unmodified rGO is related to the insertion of pyridinic-N in the basal plane and the creation of disorders in the structure. Although N-doping provides additional energy levels, thus favoring a higher number of electrons for conductivity, it also creates defects throughout the graphene layer, hampering the electron motion [64]. Following this, the most drastic change in conductivity has been established for rGO_BB50 as a result of a highest number of defects due to the nitrogen insertion in the structure as well as a relatively low concentration of graphitic-N species.

Structural and morphological studies have shown that the nitrogen-modified rGO materials prepared in this study exhibit appropriate and promising characteristics for their successful application in the electrochemical sensing of DA. Therefore, the electrochemical characteristics of the four individual electrodes (the bare GCE, GCE/rGO, GCE/rGO_BB20, and GCE/rGO_BB50) has been initially investigated via CV using 476 μM DA in 0.1 M PB solution at a fixed scanning rate of 50 mV s^{-1}, as

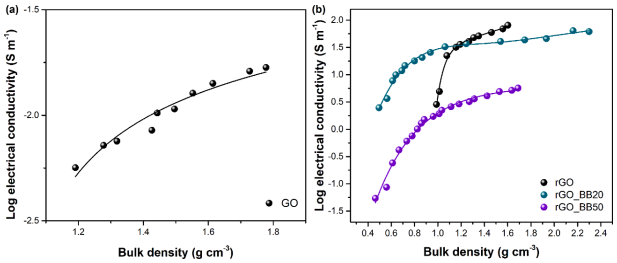

Fig. 6. The relationship between electrical conductivity and bulk density for GO (a) rGO, rGO_BB20, and rGO_BB50 (b).

presented in Fig. 7.

As seen in the CV results, the oxidation of DA to dopamine quinone (DAQ) is indicated by anodic (E_{pa1}) peaks, whereas the cathodic (E_{pc1}) peaks show a reduction of DAQ to DA. Also, the voltammograms show another two additional peaks. The cathodic peak (E_{pc2}) around –0.33 V could be because an oxidised DA molecule contains electron deficient ring and an electron-donation amine. When amine is deprotonated, the molecule undergoes cyclisation resulting to the formation of lucodopachrome. An additional oxidation peak (E_{pa2}) was found around –0.19 V because of the lucodopachrome oxidised to dopachrome [65]. The likely mechanism is illustrated in Fig. S2 (Supplementary material).

The bare GCE shows weak current responses (I_{pa1} = +9.16 μA and I_{pc1} = –8.35 μA at +0.30 and +0.10 V, respectively), suggesting a slow and sluggish electron transfer. The GCE coated with pure rGO exhibits slightly higher current values (I_{pa1} = +17.56 μA and I_{pc1} = –13.50 μA at +0.22 and +0.15 V, respectively). In contrary, a remarkable improvement in electrochemical performance is evident following the modification of the bare electrode with rGO_BB20, which contains 3.8 at.% of nitrogen (Fig. 7(c)).

The GCE/rGO_BB20 electrode shows a pair of highly expressed redox peaks at +0.36 V and +0.09 V with approximately 5 and 7 times higher anodic and cathodic current intensities (I_{pa1} = +45.40 μA, I_{pc1} = –47.56 μA), respectively, compared to those of the bare electrode. Although a higher number of N-containing functionalities and structural defects has been determined in rGO_BB50 (10.6 at.% of N; FWHM(G) = 72.4 cm^{-1}), GCE/rGO_BB50 possesses 1.5 times lower peak current values (I_{pa1} = +27.65 μA, I_{pc1} = –28.17 μA) and the higher peak-to-peak potential separation (ΔE_{p1} = 389 mV) compared to that of GCE/rGO_BB20 (ΔE_{p1} = 270 mV). The results indicate that defects were not the only contributing factor for fast electron transfer. It shows that the GCE/rGO_BB20 electrode has higher sensitivity and stronger electrocatalytic oxidation ability toward DA than GCE/rGO_BB50, mostly because of the greater surface area and enhanced charge transfer. It is well known that N-containing species are able to improve electrochemical performance, however, according to the CV data, the relatively high content of N in GCE/rGO_BB50 may have led to a surface passivation of the working electrode due to the adsorption of by-products of the redox reaction that has influenced the decrease in the electrochemical response. It suggests that the content of N in rGO must be controlled to reach the optimal electrocatalytic performance with these electrodes.

CV data have also shown that the electrochemical reaction of DA is quasi-reversible on the surface of both N-modified GCE electrodes since the values of ΔE_{p1} between redox peaks are higher than 59/n mV. The quasi-reversibility for this process has been revealed as well by the determined ratio of reduction and oxidation currents since I_{pa1}/I_{pc1} is around unity (I_{pa1}/I_{pc1} = 0.95 for GCE/rGO_BB20 and I_{pa1}/I_{pc1} = 0.98 for GCE/rGO_BB50). To sum up the CV results, it could be concluded that electron transfer kinetics is more effective in the GCE/rGO_BB20 electrode, leading to a better sensitivity and reversibility of the process in the comparison of GCE/rGO_BB50. Although GCE modified with pure rGO possesses the lower values of Faradaic current, further electrochemical investigations have been performed only for the N-modified electrodes, since they exhibit higher current values compared to those of GCE and GCE/rGO.

The impact of the scan rate (ν) on the electrochemical behavior of the N-modified electrodes toward DA detection has been analyzed, and the results obtained are shown in Fig. 8. Fig. 8 (a, b) present CV curves at different scanning rates from 10 to 120 mV s^{-1} with 99 μM DA for both N-modified GCE. It is determined that all anodic and cathodic peaks show the enhancement in current response in correspondence of increasing scanning rate, implying a high charge transfer occurred between the redox reaction centers and the surface of the N-modified electrodes. As the scan rate rises, the anodic current increases alongside a slight shift in the peak potential toward the positive side. Simultaneously, the cathodic current rises with a slight shift in the peak potential toward the negative side, indicating a deceleration in the charge transfer process due to the increased scanning rate [66].

For a more circumstantial comprehension of the process controlling the electrochemical reaction, the current dependence on the scanning rate (not shown) and the square root of scanning rate has been plotted (Fig. 8 (c, d)). It demonstrates the linear dependence was obtained only in the case of the square root of the scanning rate in the range of 10–120 mV s^{-1} with linear regression equations of $I_{pa}(\mu A) = 2.0293\nu - 1.6466$ (R^2 = 0.9905) and $I_{pc}(\mu A) = -0.8077\nu + 0.8492$ (R^2 = 0.9839) for GCE/rGO_BB20, as well as $I_{pa}(\mu A) = 1.471\nu + 0.024$ (R^2 = 0.9965) and I_{pc} = –0.3901ν – 0.2276 (R^2 = 0.9874) for GCE/rGO_BB50. These results

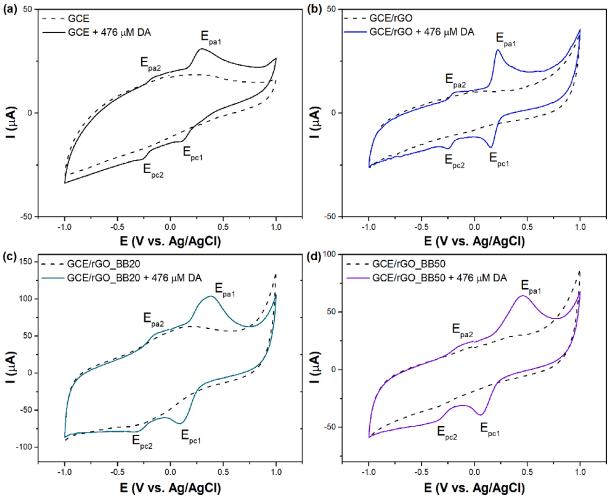

Fig. 7. Cyclic voltammograms of the GCE (a), GCE/rGO (b), GCE/rGO_BB20 (c), and GCE/rGO_BB50 (d) electrodes recorded in N_2-saturated PB solution (0.1 M, pH = 7.0) in the absence and presence of 476 μM dopamine.

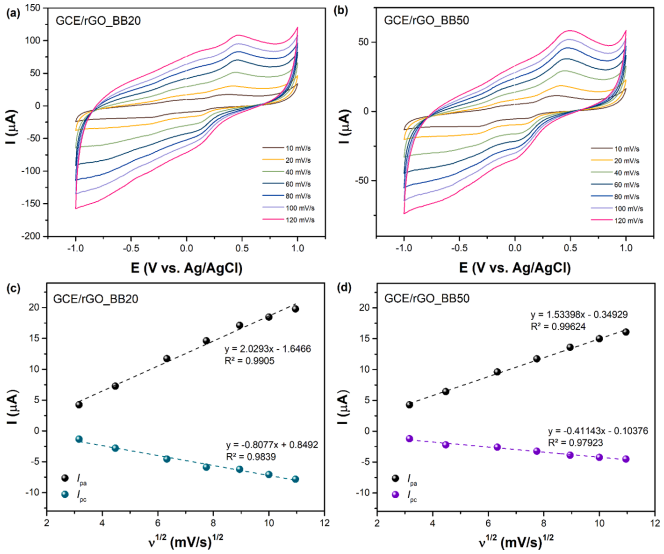

Fig. 8. CV curves at different scan rates and linear variation of anodic and cathodic peak currents vs. square root of scan rate for GCE/rGO_BB20 (a, c) and GCE/rGO_BB50 (c, d) in 0.1 M PB (pH = 7.0) with 99 μM dopamine.

suggest that the kinetics of the electrochemical reactions on the GCE/rGO_BB20 and GCE/rGO/BB50 electrodes is a diffusion-controlled process. The electrochemically active surface area (ECSA) of the N-modified electrodes has been determined by the linear regression curves derived from the Randles-Sevcik equation [67]. The electroactive area is found to be 0.3092 cm^2 and 0.2336 cm^2 for GCE/rGO_BB20 and

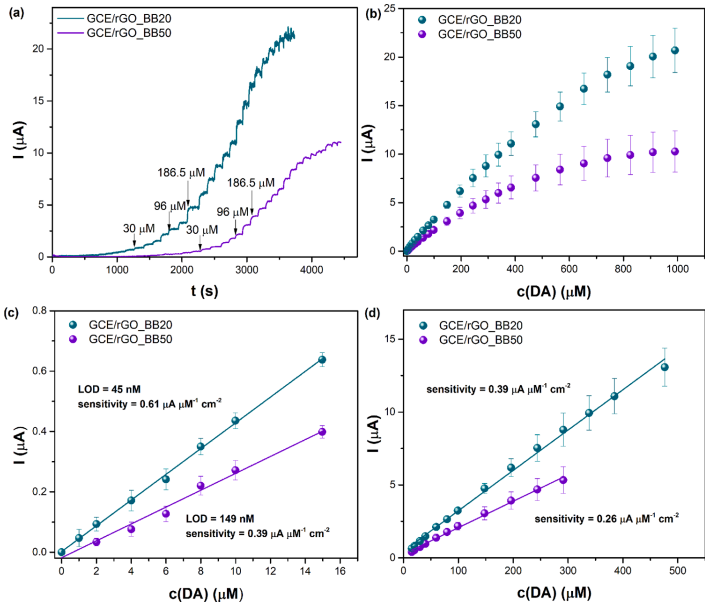

Fig. 9. Chronoamperograms (a) and calibration curves in different concentration ranges (b, c, d) for GCE/rGO_BB20 and GCE/rGO_BB50 in 0.1 M PB (pH = 7.0). The applied potential of +0.3 V, 300 rpm.

GCE/rGO_BB50, respectively, which was larger than the geometric area in four and three times. ECSA is correlated with the results of the BET surface area, since the higher value of surface area has been determined for the sample with a lower content of nitrogen.

The analytic performance of the GCE/rGO_BB20 and GCE/rGO_BB50 electrodes has been further examined using chronoamperometry. This involved successive additions of DA to the 0.1 M PB solution under an applied potential of +0.3 V. This optimal potential has been determined through chronoamperometry measurements conducted at various applied potentials (data not shown). As presented in Fig. 9(a), the anodic current progressively increases with the addition of DA and reaches stability within a few seconds using both N-modified electrodes. Nevertheless, much higher current responses are recorded for GCE/rGO_BB20, confirming its suitability for the determination of DA compared to that of GCE/rGO_BB50. Two linear calibration curves corresponding to the lower and higher concentration regions could be obtained for both proposed modified electrodes, as presented in Fig. 9 (c, d). In the lower concentration range (0–15 μM), GCE/rGO_BB20 and GCE/rGO_BB50 exhibit linear regression equations, which could be represented as $I(\mu A) = 0.04264c(DA) + 0.00216$ ($R^2 = 0.998$) and $I(\mu A) = 0.02795c(DA) - 0.01823$ ($R^2 = 0.986$), respectively. In the linear range of 0–15 μM, LOD is estimated to be 45 nM with a sensitivity of 0.61 μA μM^{-1} cm^{-2} for GCE/rGO_BB20 and 149 nM with a sensitivity of 0.39 μA μM^{-1} cm^{-2} for GCE/rGO_BB50.

Fig. 9 (b and d) distinctly illustrates that GCE/rGO_BB20 possesses a much wider linear detection range (15–476 μM), compared to that of the GCE/rGO_BB50 electrode (15–291 μM) and N-rGO-based sensors reported elsewhere [13,35,37]. The calibration plot in $c(DA) = 15–476$ μM follows the equation of $I(\mu A) = 0.02767c(DA) + 0.46357$ ($R^2 = 0.996$) with a sensitivity of 0.39 μA μM^{-1} cm^{-2} for GCE/rGO_BB20. In the range of 15–291 μM, GCE/rGO_BB50 exhibits $I(\mu A) = 0.01813c(DA) + 0.25497$ ($R^2 = 0.995$) with a sensitivity = 0.26 μA μM^{-1} cm^{-2}. All these observations show that the electrode modified with rGO_BB20 exhibits higher sensitivity and a lower limit of detection compared to those of GCE/rGO_BB50. Several reasons for the better sensing performances of GCE/rGO_BB20 can be distinguished. First, the higher surface area and ECSA for the GCE/rGO_BB20 electrode increases the adsorption capacities toward DA. Second, the higher electrical conductivity ensures a higher charge transfer between the redox reaction center and the electrode's surface. Third, the GCE/rGO_BB20 electrode demonstrates the highest sensitivity, since the protonated groups in DA molecules are more attracted to the surface of the electrode as a result of the larger concentration of electronegative oxygen-containing functional groups. One more reasonable explanation for the enhanced electrochemical response at the GCE/rGO_BB20 sensor could be attributed to the elevated content of graphitic-N groups on its surface.

As reported in the literature, the increased nucleophilicity of the carbon atom neighboring graphitic-N in a material brings forth several advantages for electrochemical sensing. This phenomenon fosters increased adsorption of analyte molecules on the electrode surface, enhances electrical conductivity, and consequently results in superior electrochemical activity, thereby improving sensing performance [68]. Comparing the existing N-rGO sensors with and without metal particles (Table S2), the rGO_BB20-modified sensor also exhibits preferable analytical characteristics in terms of LOD and linear range than non-metal electrodes (GCE/NG, GCE/N-rGO-Ur, GCE/N-rGO-180–8/NH_3, and GCE/N-rGO/polyethylenimine) or even metal-assisted materials (GCE/N-rGO-Au, GCE/N-RGO/MnO, and GCE/Fe_2O_3/N-rGO). Our results represent a notable improvement in the electrochemical performance since sensors with high sensitivity usually operate within an especially restricted linear range, while GCE/rGO_BB20 presented in this report possesses two linear ranges of 0–15 μM and 15–476 μM with a detection limit of 45 nM. Therefore, the results achieved suggest promising applications of GCE/rGO_BB20 to detect DA in a wider linear concentration range that is important in the medicine and food industry.

Determining the interference of different compounds at identical oxidation potentials is a key aspect in assessing selectivity. In this study, the selectivity of the prepared GCE/rGO_BB20 and GCE/rGO_BB50 electrodes toward DA has been investigated by recording the chronamperometric current response of DA with various interfering molecules such as AA, CA, H_2O_2, and UA. The results obtained are depicted in Fig. 10. As illustrated in Fig. 10, the well-defined chronamperometric responses using both modified electrodes have been recorded only with the additions of 0.05 mM DA, while no significant changes in current have been observed in the presence of 0.05 mM AA, 0.05 mM CA, 0.05 mM H_2O_2, and 0.05 mM UA at regular intervals at the working potential of +0.3 V. It indicates that GCE/rGO_BB20 and GCE/rGO_BB50 exhibit outstanding selectivity and anti-interference property for the DA detection. The strong electrostatic attraction between DA and N-rGO materials, which causes more DA molecules to absorb on the surface of the sensor, results in an amplified and specific response of DA, which may be the most possible cause of the selective detection of DA. Additionally, Nafion is a cation-exchanger polymer which could increase the selectivity of DA by deflecting electronegative AA, CA, and UA away from the sensor [30].

Finally, the stability of the GCE/rGO_BB20 sensor has been explored by assessing the current response following the introduction of 30 μM DA into the PB solution (pH = 7.0) over a 13-day period. The sensor has been kept in the air at room temperature during the intervals between measurements. As seen in Fig. 10(c), the peak current remains at 94% of its initial current response after 3 days of measurements, showing a slight decrease in electrochemical activity. Although the sensing performance of the proposed sensor further decreases by 17%, 33%, and 36% after 6, 7, and 13 days, respectively, the active sites are still exposed for the detection of DA. The decline in observed activity during measurements might be due to the active electrode sites getting blocked by adsorbed analytes or intermediate substances on their surface. Additionally, this reduction is likely a result of the active material being washed away from the GCE surface during electrode cleaning. Nevertheless, these results confirm that the GCE/rGO_BB20 electrode demonstrates great stability in the detection of DA over a period of six days, which would be extended in changing polymers used for rGO_BB20 immobilization on the electrode surface.

The repeatability of the GCE/rGO_BB20 electrode has also been determined as the relative standard deviation (RSD) of the DA oxidation signal by repeating measurements three times using a PB solution (pH = 7.0) containing 10 μM DA. The RSD is found to be 2.73%, revealing excellent repeatability for the proposed sensor based on rGO_BB20. Finally, the reproducibility of the GCE/rGO_BB20 electrode has been tested by measuring the current response for three electrodes prepared under the same conditions. The rGO_BB20 based sensor offers satisfactory reproducibility with an RSD of 5.33% in three successive measurements of the chronoamperometric response to 10 μM DA.

4. Conclusion

We have demonstrated a facile hydrothermal synthesis of N-rGO materials (rGO_BB20 and rGO_BB50) using GO and the Bismarck Brown additive as a nitrogen source. Quantitative XPS analysis shows the successful incorporation of nitrogen-containing functional groups into the structure of graphene-based material, as evidenced by an increase in the nitrogen content in rGO_BB20 (3.8 at.%) and rGO_BB50 (10.6 at.%). Notably, the rGO_BB20 sample exhibits a higher concentration of pyrrolic-N (16.1%) and graphitic-N (6.1%) groups compared to rGO_BB50. Raman spectroscopy analysis reveals that the sample rGO_BB50 exhibits the highest content of amorphous phase and an increased number of defects. Electrical conductivity measurements demonstrate that the pure rGO sample exhibits the highest electrical conductivity among both N-rGO samples. The slight decrease in conductivity for rGO_BB20 and rGO_BB50 compared to unmodified rGO can be attributed to the higher structural disorders in the basal plane.

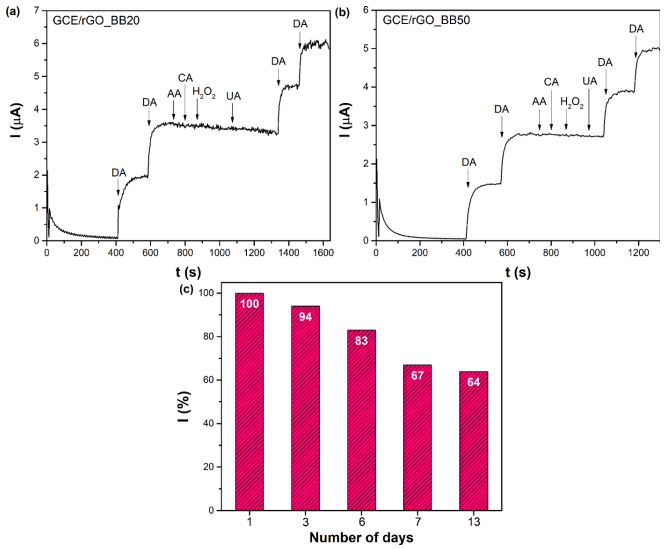

Fig. 10. Interference of 0.05 mM AA, 0.05 mM CA, 0.05 mM H_2O_2, and 0.05 mM UA on the response of 0.05 mM DA in 0.1 PB solution at +0.3 V for GCE/rGO_BB20 (a) and GCE/rGO_BB50 (b). Stability of GCE/rGO_BB20 tested over the 13 days of electrode storage period (c).

Electrochemical measurements have revealed that both GCE modified with rGO_BB20 and rGO_BB50 possess outstanding selectivity towards the detection of DA in the presence of AA, UA, CA and H_2O_2. However, compared to the rGO_BB50 modified GC electrode, the proposed GCE/rGO_BB20 electrode exhibits superior electrochemical performance in terms of DA sensing as it shows a low value of LOD (45 nM) and a high sensitivity (0.61 μA μM^{-1} cm^{-2}) in a linear detection range (0–15 μM), and the sensitivity of 0.39 μA μM^{-1} cm^{-2} in the wide linear detection range of 15–476 μM. Considering the facile preparation route and excellent experimental results, rGO_BB20 may be used as an alternative metal-free electrode material in the construction of a sensing platform for the determination of DA. After further improvements of the rGO_BB20 attachment to the electrode, the long-term stability might be extended significantly.

CRediT authorship contribution statement

Rūta Aukštakojytė: Writing – original draft, Visualization, Investigation, Data curation. **Gediminas Niaura:** Writing – review & editing, Investigation. **Virginijus Bukauskas:** Writing – review & editing, Investigation. **Jurgis Barkauskas:** Writing – review & editing, Conceptualization. **Rasa Pauliukaitė:** Writing – review & editing, Supervision. **Justina Gaidukevič:** Writing – original draft, Supervision, Project administration, Methodology, Funding acquisition.

Declaration of competing interest

The authors declare that they have no known competing financial interests or personal relationships that could have appeared to influence the work reported in this paper.

Data availability

Data will be made available on request.

Acknowledgment

This project has received funding from European Social Fund (project No 09.3.3-LMT-K-712–19–0050) under grant agreement with the Research Council of Lithuania (LMTLT).

Supplementary materials

Supplementary material associated with this article can be found, in the online version, at doi:10.1016/j.surfin.2024.104041.

References

[1] Z.N. Huang, Jiao Zou, J. Teng, Q. Liu, M.M. Yuan, F.P. Jiao, X.Y. Jiang, J.G Yu, A novel electrochemical sensor based on self-assembled platinum nanochains - Multi-walled carbon nanotubes-graphene nanoparticles composite for simultaneous determination of dopamine and ascorbic acid, Ecotoxicol. Environ. Saf. 172 (2019) 167–175.
[2] R. Darabi, H. Karimi-Maleh, M. Akin, K. Arikan, Z. Zhang, R. Bayat, M. Bekmezci, F. Sen, Simultaneous determination of ascorbic acid, dopamine, and uric acid with a highly selective and sensitive reduced graphene oxide/polypyrrole-platinum nanocomposite modified electrochemical sensor, Electrochim. Acta. 457 (2023) 142402.
[3] A. Scalbert, L. Brennan, O. Fiehn, T. Hankemeier, B.S. Kristal, B. van Ommen, E. Pujos-Guillot, E. Verheij, D. Wishart, S. Wopereis, Mass-spectrometry-based metabolomics: limitations and recommendations for future progress with particular focus on nutrition research, Metabolomics 5 (2009) 435–458.
[4] Z. Miao, W. Hou, M. Liu, Y. Zhang, S. Yao, BSA capped bi-functional fluorescent Cu nanoclusters as pH sensor and selective detection of dopamine, New J. Chem. 42 (2018) 1446–1456.
[5] Y. Liu, X. He, P. Ma, Y. Huang, X. Li, Y. Sun, X. Wang, D. Song, Fluorometric detection of dopamine based on 3-aminophenylboronic acid-functionalized AgInZnS QDs and cells imaging, Talanta 217 (2020) 121081.
[6] A. Roychoudhury, K.A. Francis, J. Patel, S. Kumar, J. Ab, S. Basu, A decoupler-free simple paper microchip capillary electrophoresis device for simultaneous detection of dopamine, epinephrine and serotonin †, RSD Adv 10 (2020) 25487–25495.
[7] A. Gottås, Ripel, F. Boix, V. Vindenes, J. Mørland, E.L. Øiestad, Determination of dopamine concentrations in brain extracellular fluid using microdialysis with short sampling intervals, analyzed by ultra high performance liquid chromatography tandem mass spectrometry, J. Pharmacol. Toxicol. Methods. 74 (2015) 75–79.
[8] Z. Liao, Y. Ma, S. Yao, J. Zhang, Y. Han, K. Xu, Honeycomb-patterned porous graphene film for electrochemical detection of dopamine, Appl. Surf. Sci. 605 (2022) 154725.

[9] S.K. Arumugasamy, S. Govindaraju, K. Yun, Electrochemical sensor for detecting dopamine using graphene quantum dots incorporated with multiwall carbon nanotubes, Appl. Surf. Sci. 508 (2020) 145294.
[10] S. Lakard, I.A. Pavel, B. Lakard, Electrochemical Biosensing of Dopamine Neurotransmitter: a Review, Biosensors 11 (2021) 179.
[11] Y.S. Chang, F.K. Chen, D.C. Tsai, B.H. Kuo, F.S. Shieu, N-doped reduced graphene oxide for room-temperature NO gas sensors, Sci. Rep. 11 (2021) 20719.
[12] A.F. Quintero-Jaime, J. Quílez-Bermejo, D. Cazorla-Amorós, E. Morallón, Metal free electrochemical glucose biosensor based on N-doped porous carbon material, Electrochim. Acta. 367 (2021) 137434.
[13] H. Zhang, S. Liu, Electrochemical sensors based on nitrogen-doped reduced graphene oxide for the simultaneous detection of ascorbic acid, dopamine and uric acid, J. Alloys Compd. 842 (2020) 155873.
[14] Z. Chen, Y. Zhang, Y. Yang, X. Shi, L. Zhang, G. Jia, Hierarchical nitrogen-doped holey graphene as sensitive electrochemical sensor for methyl parathion detection, Sensors Actuators B Chem 336 (2021) 129721.
[15] J. Gaidukevic, R. Aukstakojyte, M. Kozlowski, J. Barkauskas, R. Pauliukaite, A simple preparation of N-doped reduced graphene oxide as an electrode material for the detection of hydrogen peroxide and glucose, Electrochim. Acta. 446 (2023) 142113.
[16] W. Raza, K. Ahmad, H. Kim, Nitrogen-doped graphene as an efficient metal-free catalyst for ammonia and non-enzymatic glucose sensing, J. Phys. Chem. Solids. 160 (2022) 110359.
[17] G. Song, T. Wu, F. Liu, B. Zhang, X. Liu, Electrochemical Detection of Xanthine and Study for the Inhibition of Uric Acid Based on Chitosan/Nitrogen Doped Reduced Graphene Oxide Modified Electrode, Acta Chim. Sin. 78 (2020) 82–88.
[18] D. Chen, J. Jiang, X. Du, Electrocatalytic oxidation of nitrite using metal-free nitrogen-doped reduced graphene oxide nanosheets for sensitive detection, Talanta 155 (2016) 329–335.
[19] G. Song, R. Zhang, X. Jiang, F. Liu, X. Liu, Nitrogen-doped reduced graphene oxide as a sensing platform for detection of guanine and application in cell necrosis, Chem. Pap. 74 (2020) 89–98.
[20] Z. Lu, D. Li, Q. Zhang, J. Wei, Facile simultaneous determination of hydroquinone and catechol using nitrogen-doped graphene modified electrode, Int. J. Electrochem. Sci. 11 (2016) 10607–10619.
[21] S. Sharma, R. Kumar, R.M. Yadav, Polyacrylonitrile/N-doped graphene quantum dots nanocomposite activity as SERS nanosensors for detection of methylene blue, Mater. Today Commun. 36 (2023) 106860.
[22] J. Lavanya, A. Subbiah, S. Neogi, N. Gomathi, Direct electron transfer of hemoglobin at nitrogen incorporated reduced graphene oxide obtained by radio frequency ammonia plasma treatment, Sensors Actuators B Chem 255 (2018) 536–543.
[23] R. Kumar, A. Pérez del Pino, S. Sahoo, R.K. Singh, W.K. Tan, K.K. Kar, A. Matsuda, E. Joanni, Laser processing of graphene and related materials for energy storage: state of the art and future prospects, Prog. Energy Combust. Sci. 91 (2022) 100981.
[24] R. Kumar, S. Sahoo, E. Joanni, R.K. Singh, W.K. Tan, K.K. Kar, A. Matsuda, Recent progress in the synthesis of graphene and derived materials for next generation electrodes of high performance lithium ion batteries, Prog. Energy Combust. Sci. 75 (2019) 100786.
[25] R. Kumar, S. Sahoo, E. Joanni, R.K. Singh, K. Maegawa, W.K. Tan, G. Kawamura, K. K. Kar, A. Matsuda, Heteroatom doped graphene engineering for energy storage and conversion, Mater. Today. 39 (2020) 47–65.
[26] D. Minta, Z. González, P. Wiench, S. Gryglewicz, G. Gryglewicz, N-doped reduced graphene oxide/gold nanoparticles composite as an improved sensing platform for simultaneous detection of dopamine, ascorbic acid, and uric acid, Sensors (Switzerland) 20 (2020) 1–13.
[27] R. Chen, Y. Wang, Y. Liu, J. Li, Selective electrochemical detection of dopamine using nitrogen-doped graphene/manganese monoxide composites, RSC Adv 5 (2015) 85065–85072.
[28] Z. Lu, Y. Li, T. Liu, G. Wang, M. Sun, Y. Jiang, H. He, Y. Wang, P. Zou, X. Wang, Q. Zhao, H. Rao, A dual-template imprinted polymer electrochemical sensor based on AuNPs and nitrogen-doped graphene oxide quantum dots coated on NiS2/biomass carbon for simultaneous determination of dopamine and chlorpromazine, Chem. Eng. J. 389 (2020) 124417.
[29] L. Zhang, J. Tang, J. Li, Y. Li, P. Yang, P. Zhao, J. Fei, Y. Xie, A novel dopamine electrochemical sensor based on 3D flake nickel oxide/cobalt oxide @ porous carbon nanosheets/carbon nanotubes/electrochemical reduced of graphene oxide composites modified glassy carbon electrode, Colloids Surfaces A Physicochem. Eng. Asp. 666 (2023) 131284.
[30] Z. Yang, X. Zheng, J. Zheng, A facile one-step synthesis of Fe2O3/nitrogen-doped reduced graphene oxide nanocomposite for enhanced electrochemical determination of dopamine, J. Alloys Compd. 709 (2017) 581–587.
[31] X. Chen, G. Zhang, L. Shi, S. Pan, W. Liu, H. Pan, Au/ZnO hybrid nanocatalysts impregnated in N-doped graphene for simultaneous determination of ascorbic acid, acetaminophen and dopamine, Mater. Sci. Eng. C. 65 (2016) 80–89.
[32] S. Yasmin, M.S. Ahmed, D. Park, S. Jeon, Nitrogen-Doped Graphene Supported Cobalt Oxide for Sensitive Determination of Dopamine in Presence of High Level Ascorbic Acid, J. Electrochem. Soc. 163 (2016) B491–B498.
[33] F. Tadayon, Z. Sepehri, A new electrochemical sensor based on a nitrogen-doped graphene/CuCo2O4 nanocomposite for simultaneous determination of dopamine, melatonin and tryptophan, RSC Adv 5 (2015) 65560–65568.
[34] A. Brouzgou, E. Gorbova, Y. Wang, S. Jing, A. Seretis, Z. Liang, P. Tsiakaras, Nitrogen-doped 3D hierarchical ordered mesoporous carbon supported palladium electrocatalyst for the simultaneous detection of ascorbic acid, dopamine, and glucose, Ionics (Kiel) 25 (2019) 6061–6070.
[35] Z.H. Sheng, X.Q. Zheng, J.Y. Xu, W.J. Bao, F.Bin Wang, X.H Xia, Electrochemical sensor based on nitrogen doped graphene: simultaneous determination of ascorbic acid, dopamine and uric acid, Biosens. Bioelectron. 34 (2012) 125–131.
[36] R. Soni, K. Palit, M. Soni, R. Kumar, S.K. Sharma, Highly sensitive electrochemical sensing of neurotransmitter dopamine from scalable UV irradiation-based nitrogen-doped reduced graphene oxide-modified electrode, Bull. Mater. Sci. 43 (2020) 1–11.
[37] P. Wiench, Z. González, S. Gryglewicz, R. Menéndez, G. Gryglewicz, Enhanced performance of pyrrolic N-doped reduced graphene oxide-modified glassy carbon electrodes for dopamine sensing, J. Electroanal. Chem. 852 (2019) 113547.
[38] S. Ai, Y. Chen, Y. Liu, Q. Zhang, L. Xiong, H. Huang, L. Li, X. Yu, L. Wei, Facile synthesis of nitrogen-doped graphene aerogels for electrochemical detection of dopamine, Solid State Sci 86 (2018) 6–11.
[39] X. Yan, J. Chen, J. Yang, Q. Xue, P. Miele, Fabrication of free-standing, electrochemically active, and biocompatible graphene oxide-polyaniline and graphene-polyaniline hybrid papers, ACS Appl. Mater. Interfaces. 2 (2010) 2521–2529.
[40] W.S. Hummers, R.E. Offeman, Preparation of Graphitic Oxide, J. Am. Chem. Soc. 80 (1958) 1339.
[41] R. Aukstakojyte, J. Gaidukevic, G. Niaura, M. Skapas, V. Bukauskas, J. Barkauskas, Structural Control and Electrical Behavior of Thermally Reduced Graphene Oxide Samples Assisted with Malonic Acid and Phosphorus Pentoxide, Inorganics 2022 10 (2022) 142. *Page10*, 142.
[42] P. Wiench, Z. González, R. Menéndez, B. Grzyb, G. Gryglewicz, Beneficial impact of oxygen on the electrochemical performance of dopamine sensors based on N-doped reduced graphene oxides, Sensors Actuators B Chem 257 (2018) 143–153.
[43] T.R. Gengenbach, G.H. Major, M.R. Linford, C.D. Easton, Practical guides for x-ray photoelectron spectroscopy (XPS): interpreting the carbon 1s spectrum, J. Vac. Sci. Technol. A. 39 (2021) 13204.
[44] M.P. Araújo, O.S.G.P. Soares, A.J.S. Fernandes, M.F.R. Pereira, C. Freire, Tuning the surface chemistry of graphene flakes: new strategies for selective oxidation, RSC Adv 7 (2017) 14290–14301.
[45] R. Al-Gaashani, A. Najjar, Y. Zakaria, S. Mansour, M.A. Atieh, XPS and structural studies of high quality graphene oxide and reduced graphene oxide prepared by different chemical oxidation methods, Ceram. Int. 45 (2019) 14439–14448.
[46] J. Gaidukevič, J. Barkauskas, A. Malaika, V. Jasulaitienė, M. Kozlowski, Preparation and characterization of basic graphene-based catalysts and their application in biodiesel synthesis, Appl. Surf. Sci. (2021) 554.
[47] M. Ayiania, M. Smith, A.J.R. Hensley, L. Scudiero, J.S. McEwen, M. Garcia-Perez, Deconvoluting the XPS spectra for nitrogen-doped chars: an analysis from first principles, Carbon N. Y. 162 (2020) 528–544.
[48] D. Li, X. Duan, H. Sun, J. Kang, H. Zhang, M.O. Tade, S. Wang, Facile synthesis of nitrogen-doped graphene via low-temperature pyrolysis: the effects of precursors and annealing ambience on metal-free catalytic oxidation, Carbon N. Y. 115 (2017) 649–658.
[49] A. Jorio, A.G. Souza Filho, Raman Studies of Carbon Nanostructures, Annu. Rev. Mater. Res. 46 (2016) 357–382.
[50] A. Jorio, L.G. Cançado, Perspectives on Raman spectroscopy of graphene-based systems: from the perfect two-dimensional surface to charcoal, Phys. Chem. Chem. Phys. 14 (2012) 15246–15256.
[51] J. Ribeiro-Soares, L.G. Cançado, N.P.S. Falcão, E.H. Martins Ferreira, C.A. Achete, A. Jorio, The use of Raman spectroscopy to characterize the carbon materials found in Amazonian anthrosoils, J. Raman Spectrosc. 44 (2013) 283–289.
[52] J. Ribeiro-Soares, M.E. Oliveros, C. Garin, M.V. David, L.G.P. Martins, C. A. Almeida, E.H. Martins-Ferreira, K. Takai, T. Enoki, R. Magalhães-Paniago, A. Malachias, A. Jorio, B.S. Archanjo, C.A. Achete, L.G. Cançado, Structural analysis of polycrystalline graphene systems by Raman spectroscopy, Carbon N. Y. 95 (2015) 646–652.
[53] S. Claramunt, A. Varea, D. López-Díaz, M.M. Velázquez, A. Cornet, A. Cirera, The importance of interbands on the interpretation of the raman spectrum of graphene oxide, J. Phys. Chem. C. 119 (2015) 10123–10129.
[54] A.C. Ferrari, J. Robertson, Resonant Raman spectroscopy of disordered, amorphous, and diamondlike carbon, Phys. Rev. B Condens. Matter Mater. Phys. 64 (2001) 1–13.
[55] R. Trusovas, K. Ratautas, G. Račiukaitis, G. Niaura, Graphene layer formation in pinewood by nanosecond and picosecond laser irradiation, Appl. Surf. Sci. 471 (2019) 154–161.
[56] H. Zhang, T. Kuila, N.H. Kim, D.S. Yu, J.H. Lee, Simultaneous reduction, exfoliation, and nitrogen doping of graphene oxide via a hydrothermal reaction for energy storage electrode materials, Carbon N. Y. 69 (2014) 66–78.
[57] F.Y. Kong, L. Yao, R.F. Li, H.Y. Li, Z.X. Wang, W.X. Lv, W. Wang, Synthesis of nitrogen-doped reduced graphene oxide loading with Au-Ag bimetallic nanoparticles for electrochemical detection of daunorubicin, J. Alloys Compd. 797 (2019) 413–420.
[58] P. Bharathidasan, M.B. Idris, D.W. Kim, S.R. Sivakkumar, S. Devaraj, Enhanced capacitance properties of nitrogen doped reduced graphene oxide obtained by simultaneous reduction and nitrogen doping, FlatChem 11 (2018) 24–31.
[59] B.D. Ossonon, D. Bélanger, Synthesis and characterization of sulfophenyl-functionalized reduced graphene oxide sheets, RSC Adv 7 (2017) 27224–27234.
[60] J. Gaidukevič, R. Pauliukaitė, G. Niaura, I. Matulaitienė, O. Opuchovič, A. Radzevič, G. Astromskas, V. Bukauskas, J. Barkauskas, Synthesis of reduced graphene oxide with adjustable microstructure using regioselective reduction in the melt of boric acid: relationship between structural properties and electrochemical performance, Nanomaterials 8 (2018) 889.

[61] Y. Cheng, S. Zhou, P. Hu, G. Zhao, Y. Li, X. Zhang, W. Han, Enhanced mechanical, thermal, and electric properties of graphene aerogels via supercritical ethanol drying and high-Temperature thermal reduction, Sci. Rep. 7 (2017) 1–11.
[62] M. Ghislandi, E. Tkalya, B. Marinho, C.E. Koning, G. De With, Electrical conductivities of carbon powder nanofillers and their latex-based polymer composites, Compos. Part A Appl. Sci. Manuf. 53 (2013) 145–151.
[63] Q. Yan, R. Arango, J. Li, Z. Cai, Fabrication and characterization of carbon foams using 100% Kraft lignin, Mater. Des. 201 (2021) 109460.
[64] M. Steinmetz, D. Lima, R.R.L. Machado, U. Sundararaj, M. Arjmand, A.B. da Silva, J.P. Santos, C.A. Pessôa, K. Wohnrath, Nitrogen-doped carbon nanotubes towards electrochemical sensing: effect of synthesis temperature, Diam. Relat. Mater. 110 (2020) 108093.
[65] U. Chandra, B.E.K. Swamy, M. Kumar, A.W. Gebisa, M. Praveen, Simple flame etching of pencil electrode for dopamine oxidation in presence of ascorbic acid and uric acid, Int. J. Nanotechnol. 14 (2017) 739–751.
[66] N. Elgrishi, K.J. Rountree, B.D. McCarthy, E.S. Rountree, T.T. Eisenhart, J. L. Dempsey, A Practical Beginner's Guide to Cyclic Voltammetry, J. Chem. Educ. 95 (2018) 197–206.
[67] T.R.L.C. Paixão, Measuring Electrochemical Surface Area of Nanomaterials versus the Randles–Ševčík Equation, ChemElectroChem 7 (2020) 3414–3415.
[68] N. Zhou, N. Wang, Z. Wu, L. Li, Probing active sites on metal-free, nitrogen-doped carbons for oxygen electroreduction: a review, Catalysts 8 (2018) 509.

Supplementary material

Bismarck Brown-Assisted Hydrothermal Synthesis of Nitrogen-Modified Reduced Graphene Oxide for Selective Electrochemical Detection of Dopamine

Rūta Aukštakojytė [1], Gediminas Niaura [2], Virginijus Bukauskas [3], Jurgis Barkauskas [1], Rasa Pauliukaitė [4], Justina Gaidukevič [1, 4, *]

[1] Institute of Chemistry, Faculty of Chemistry and Geosciences, Vilnius University, Naugarduko str. 24, LT-03225 Vilnius, Lithuania

[2] Department of Organic Chemistry, Center for Physical Sciences and Technology, Saulėtekio Ave. 3, LT-10257 Vilnius, Lithuania

[3] Department of Physical Technologies, Center for Physical Sciences and Technology, Saulėtekio Ave. 3, LT-10257 Vilnius, Lithuania

[4] Department of Nanoengineering, Center for Physical Sciences and Technology, Savanorių Ave. 231, LT-02300 Vilnius, Lithuania

[*] corresponding author: justina.gaidukevic@chf.vu.lt (J.G.)

Materials and reagents

Graphite powder (particle size ≤ 50 μm; purity ≥ 99.5%), potassium persulfate ($K_2S_2O_8$, purity 99.99%), sodium nitrate ($NaNO_3$, purity ≥ 99%), phosphorus pentoxide (P_2O_5, purity ≥ 99%), potassium permanganate ($KMnO_4$, purity ≥ 99%), dopamine hydrochloride ($(HO)_2C_6H_3CH_2CH_2NH_2 \cdot HCl$, purity 98%), ascorbic acid ($C_6H_8O_6$, ≥ 99%), citric acid ($C_6H_8O_7$, ≥ 99.5%), and uric acid ($C_5H_4N_4O_3$, purity ≥ 99%) were purchased from Merck (Darmstadt, Germany). Phosphate buffer (PB) solution (pH = 7.0; c = 0.1 mol L^{-1}) was prepared by sodium phosphate dibasic (Na_2HPO_4, purity ≥ 99%, Sigma-Aldrich, Steinheim, Germany) and sodium phosphate monobasic (NaH_2PO_4, purity ≥ 99%, Sigma-Aldrich, Steinheim, Germany). Sulfuric acid (H_2SO_4, purity ≥ 98%) and hydrogen peroxide (H_2O_2, 30% weight) were purchased from Eurochemicals (Bratislava, Slovakia). Bismarck Brown ($C_{18}H_{18}N_8 \cdot 2HCl$, ≥ 99%). Nafion (5% weight) was purchased from Alfa Aesar (Kandel, Germany).

Electrochemical characterization

Electrochemical experiments were performed carried out at room temperature using the potentiostat/galvanostat CompactStat (Ivium Technologies, The Netherlands). Electrochemical measurements were carried out in a three-electrode cell composed of a modified glassy carbon

electrode (GCE) as the working electrode (0.07065 cm^2), a platinum wire as the counter electrode, and the Ag/AgCl electrode as the reference electrode. The GCE was first polished with Al_2O_3 powder (0.05 μm, Kemet, UK) and ultrasonicated in DI water and ethanol for one minute before the working electrode modification. For the preparation of GCE/modified reduced GO working electrodes, 1 mg of rGO_BB20 or rGO_BB50 was dispersed in 1 mL of the mixture of DI water and Nafion (in volume ratio of 9:1) under ultrasonication for 1 hour. Subsequently, 10 microliters of the resulting suspension were dropped onto the GCE surface and allowed to air dry for an hour at room temperature.

Utilizing both chronoamperometry (ChA) and cyclic voltammetry (CV), the electrochemical behavior of DA at the modified rGO-based/GCE electrodes was examined. CV experiments were investigated by cycling the applied potential from –1.0 to +1.0 V (vs Ag/AgCl) at a scanning rate of 50 mV s^{-1} in a 0.1 M PB solution (pH = 7.0) for 5 cycles in the presence of 476 μM DA. In the same buffer solution, the effect of the scanning rate was also noted between 10 and 120 mV s^{-1}. ChA measurements were carried out in 0.1 M PB (pH = 7.0) by gradually adding DA while stirring continuously at 300 rpm. A constant voltage of +0.3 V was used to measure the chronoamperometric response. Ascorbic acid (AA), citric acid (CA), uric acid (UA), and H_2O_2 were added to the electrochemical system at 0.05 mM concentrations for the interference research.

The limit of detection of DA has been calculated according to the equation (S1):

$$LOD = 3\,\sigma / s \qquad (S1)$$

σ is a standard deviation of the anodic peak current of the blank signal, and s signifies the slope of the calibration plot obtained using chronoamperometry results. The sensitivity of the electrodes toward DA has been determined by the following equation (S2):

$$sensitivity = s / A \qquad (S2)$$

where *A* is the geometric area (cm^2) of the GCE electrode.

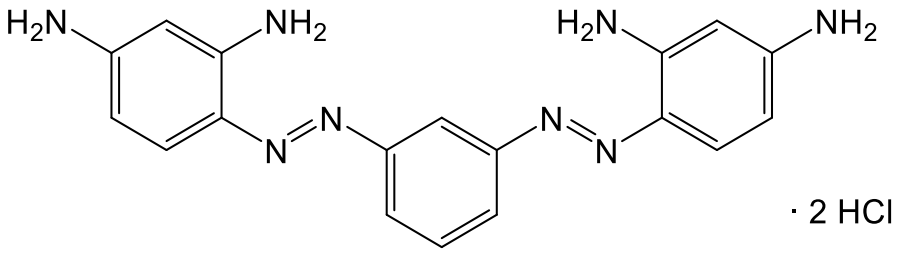

Figure S1. Chemical structure of Bismarck Brown.

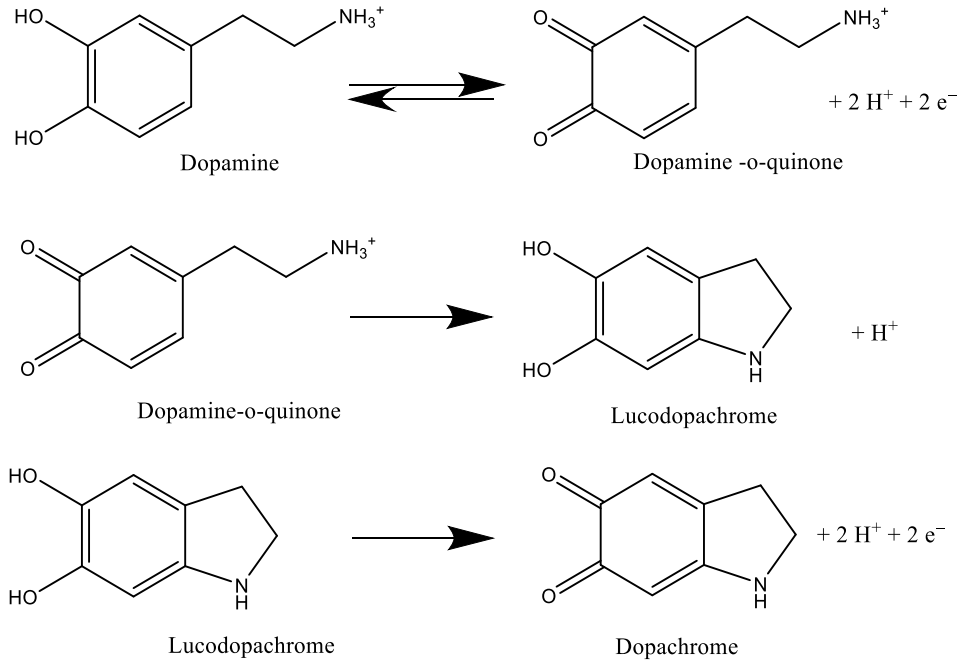

Figure S2. Probable electro-oxidation mechanism of dopamine

Table S1. The nitrogen content (at.%) in nitrogen-modified rGO samples by hydrothermal treatment of GO.

Nitrogen source	Nitrogen content (at.%)	Reference
Ammonium formate	~5.2	[1]
$(NH_4)_2CO_3$	6.8–10.1	[2]
Urea	3.98–6.57	[3]
Amitrole	8.1–10.5	[4]
Hexamethylenetetramine	8.62	[5]
Tetraethylenepentamine and hydrazine hydrate	8.03	[6]
Hydrazine	3.5	[7]
Bismarck Brown	3.8	This work
Bismarck Brown	10.6	This work

Table S2. Comparison of sensors modified with metal-free N-rGO or metal/N-rGO for the determination of DA.

Electrode	LOD (nM)	Linear range (μM)	Reference
GCE/N-rGO	100	1–60	[8]
GCE/NG	250	0.5–170	[9]
GCE/N-rGO-Ur	335	0.5–85	[10]
GCE/N-rGO-180-8/NH_3	410	0.5–150	[11]
NG600/SPCE	930	100–450	[12]
GCE/N-rGO/polyethyleneimine	500	1–130	[13]
GCE/N-rGO-Au	2400	3–100	[14]
GCE/N-RGO/MnO	3000	10–180	[15]
GCE/Fe_2O_3/N-rGO	490	0.5–340	[16]
GCE/rGO_BB20	45	0–15 15–476	This work

References

1. Song, M.; Zhao, J.; Meng, Y.; Riekehr, L.; Hou, P.X.; Grennberg, H.; Zhang, Z. Bin Nitrogen-Doped Reduced Graphene Oxide Hydrogel Achieved via a One-Step Hydrothermal Process. *ChemNanoMat*. **2019**, *5*, 1144–1151.
2. Zhang, H.; Kuila, T.; Kim, N.H.; Yu, D.S.; Lee, J.H. Simultaneous reduction,

exfoliation, and nitrogen doping of graphene oxide via a hydrothermal reaction for energy storage electrode materials. *Carbon N. Y.* **2014**, *69*, 66–78.

3. Miao, H.; Li, S.; Wang, Z.; Sun, S.; Kuang, M.; Liu, Z.; Yuan, J. Enhancing the pyridinic N content of Nitrogen-doped graphene and improving its catalytic activity for oxygen reduction reaction. *Int. J. Hydrogen Energy*. **2017**, *42*, 28298–28308.
4. Sanchez-Padilla, N.M.; Benavides, R.; Gallardo, C.; Fernandez, S.; De-Casas, E.; Morales-Acosta, D. Influence of doping level on the electrocatalytic properties for oxygen reduction reaction of N-doped reduced graphene oxide. *Int. J. Hydrogen Energy*. **2021**, *46*, 26040–26052.
5. Lee, J.W.; Ko, J.M.; Kim, J.D. Hydrothermal preparation of nitrogen-doped graphene sheets via hexamethylenetetramine for application as supercapacitor electrodes. *Electrochim. Acta*. **2012**, *85*, 459–466.
6. Jayabal, E.; Natarajan, A.; Rengarajan, V. One-pot hydrothermal synthesis of nitrogen-doped reduced graphene oxide for the highly sensitive and simultaneous determination of dihydroxy benzene isomers. *J. Appl. Electrochem.* **2021**, *51*, 1189–1205.
7. Phattharasupakun, N.; Wutthiprom, J.; Ma, N.; Suktha, P.; Sawangphruk, M. High-Performance Supercapacitors of N-Doped Graphene Aerogel and Its Nanocomposites with Manganese Oxide and Polyaniline. *J. Electrochem. Soc.* **2018**, *165*, A1430–A1439.
8. Zhang, H.; Liu, S. Electrochemical sensors based on nitrogen-doped reduced graphene oxide for the simultaneous detection of ascorbic acid, dopamine and uric acid. *J. Alloys Compd.* **2020**, *842*, 155873.
9. Sheng, Z.H.; Zheng, X.Q.; Xu, J.Y.; Bao, W.J.; Wang, F. Bin; Xia, X.H. Electrochemical sensor based on nitrogen doped graphene: Simultaneous determination of ascorbic acid, dopamine and uric acid. *Biosens. Bioelectron.* **2012**, *34*, 125–131.
10. Wiench, P.; González, Z.; Gryglewicz, S.; Menéndez, R.; Gryglewicz, G. Enhanced performance of pyrrolic N-doped reduced graphene oxide-modified glassy carbon electrodes for dopamine sensing. *J. Electroanal. Chem.* **2019**, *852*, 113547.
11. Wiench, P.; González, Z.; Menéndez, R.; Grzyb, B.; Gryglewicz, G. Beneficial impact of oxygen on the electrochemical performance of dopamine sensors based on N-doped reduced graphene oxides. *Sensors Actuators B Chem.* **2018**, *257*, 143–153.
12. Li, S.M.; Yang, S.Y.; Wang, Y.S.; Lien, C.H.; Tien, H.W.; Hsiao, S.T.; Liao, W.H.; Tsai, H.P.; Chang, C.L.; Ma, C.C.M.; Hu, C.C. Controllable synthesis of nitrogen-doped graphene and its effect on the simultaneous electrochemical determination of ascorbic acid, dopamine, and uric acid. *Carbon N. Y.* **2013**, *59*, 418–429.

13. Li, N.; Zheng, E.; Chen, X.; Sun, S.; Ruan, Y.; Weng, X.; You, C. Layer-by-layer assembled multilayer films of nitrogen-doped graphene and polyethylenimine for selective sensing of dopamine. *Int. J. Electrochem. Sci.* **2013**, *8*, 6524–6534.
14. Minta, D.; González, Z.; Wiench, P.; Gryglewicz, S.; Gryglewicz, G. N-doped reduced graphene oxide/gold nanoparticles composite as an improved sensing platform for simultaneous detection of dopamine, ascorbic acid, and uric acid. *Sensors (Switzerland)*. **2020**, *20*, 1–13.
15. Chen, R.; Wang, Y.; Liu, Y.; Li, J. Selective electrochemical detection of dopamine using nitrogen-doped graphene/manganese monoxide composites. *RSC Adv.* **2015**, *5*, 85065–85072.
16. Yang, Z.; Zheng, X.; Zheng, J. A facile one-step synthesis of Fe2O3/nitrogen-doped reduced graphene oxide nanocomposite for enhanced electrochemical determination of dopamine. *J. Alloys Compd.* **2017**, *709*, 581–587.

NOTES

Vilnius University Press
Saulėtekio Ave. 9, Building III, LT-10222 Vilnius
Email: info@leidykla.vu.lt, www.leidykla.vu.lt
bookshop.vu.lt, journals.vu.lt
Print run copies 20.